IOWA STATE UNIVERSITY
Digital Repository

Graduate Theses and Dissertations | Graduate College

2011

Studies of long range order and excitations in the iron arsenide superconductors

Daniel Keith Pratt
Iowa State University

Follow this and additional works at: http://lib.dr.iastate.edu/etd

 Part of the Physics Commons

Recommended Citation

Pratt, Daniel Keith, "Studies of long range order and excitations in the iron arsenide superconductors" (2011). *Graduate Theses and Dissertations*. 10177.
http://lib.dr.iastate.edu/etd/10177

This Dissertation is brought to you for free and open access by the Graduate College at Iowa State University Digital Repository. It has been accepted for inclusion in Graduate Theses and Dissertations by an authorized administrator of Iowa State University Digital Repository. For more information, please contact digirep@iastate.edu.

Studies of long range order and excitations in the iron arsenide superconductors

by

Daniel K. Pratt

A dissertation submitted to the graduate faculty

in partial fulfillment of the requirements for the degree of

DOCTOR OF PHILOSOPHY

Major: Condensed Matter Physics

Program of Study Committee:

Robert J. McQueeney, Co-Major Professor

Alan I. Goldman, Co-Major Professor

Andreas Kreyssig

Bruce N. Harmon

Lee Anne Willson

Vitalij K. Pecharsky

Iowa State University

Ames, Iowa

2011

Copyright © Daniel K. Pratt, 2011. All rights reserved.

TABLE OF CONTENTS

LIST OF TABLES v

LIST OF FIGURES vi

Chapter 1. Thesis overview 1

1.1 Introduction and motivation . . . 1

1.2 Summary of key results . . . 2

1.2.1 Effects of pressure application on antiferromagnetism and superconductivity in $CaFe_2As_2$ . . . 2

1.2.2 Effects of Co doping on magnetism and SC in $Ba(Fe_{1-x}Co_x)_2As_2$ . . . 3

1.3 Thesis layout . . . 5

Chapter 2. Introduction to iron arsenides 6

2.1 Discovery of superconductivity in iron pnictide compounds . . . 6

2.2 General comments about iron pnictide compounds . . . 7

2.2.1 Superconductivity . . . 12

2.3 Iron pnictide and iron chalogenide family of compounds . . . 14

2.4 Characterization of the 122 superconductors . . . 18

2.4.1 Crystal structure . . . 19

2.4.2 Magnetic structure . . . 21

2.4.3 Studies of the p-T phase diagram of $CaFe_2As_2$ . . . 22

2.4.4 Cobalt doping of $BaFe_2As_2$ . . . 28

Chapter 3. Discussion of analysis and experimental methods 34

3.1 Introduction . . . 34
3.2 Nuclear scattering . . . 34
3.2.1 Scattering cross section . . . 34
3.2.2 Expressing $\frac{d^2\sigma}{d\Omega dE}$ for nuclear scattering . . . 37
3.2.3 Bragg scattering . . . 40
3.3 Magnetic scattering . . . 41
3.3.1 Elastic magnetic scattering . . . 46
3.4 Spin waves and relaxational dynamics . . . 47
3.4.1 Scattering function using the generalized dynamic magnetic susceptibility 48
3.4.2 Superconducting resonance . . . 56
3.5 The triple axis spectrometer . . . 58
3.5.1 Elements of the triple axis spectrometer . . . 58
3.5.2 Triple axis data analysis . . . 64

Chapter 4. Effects of pressure application on structure and magnetism in $CaFe_2As_2$ 73

4.1 Introduction . . . 73
4.2 The pressure-temperature (p-T) phase diagram . . . 75
4.2.1 Magnetism . . . 79
4.3 Investigation of magnetism in the cT phase with polarized neutron scattering . 82
4.4 Pressure medium dependence of the p-T phase diagram . . . 90
4.5 Evidence from neutron diffraction for superconductivity in the stabilized tetragonal phase of $CaFe_2As_2$ under uniaxial pressure . . . 94
4.6 Electronic density of states and $\chi(q)$ calculations in T and cT phases . . . 98
4.7 Suppression of antiferromagnetic spin fluctuations in the cT phase of $CaFe_2As_2$ 101
4.8 Summary . . . 108

Chapter 5. Investigation of structure, magnetic excitations, and superconductivity in $Ba(Fe_{1-x}Co_x)_2As_2$ 110

5.1 Introduction . . . 110

5.2 Experimental details of the of neutron and x-ray scattering measurements on $Ba(Fe_{1-x}Co_x)_2As_2$ . . . 111
5.2.1 Neutron and x-ray diffraction measurements $Ba(Fe_{1-x}Co_x)_2As_2$ . . . 111
5.2.2 Inelastic neutron scattering measurements on $Ba(Fe_{0.953}Co_{0.047})_2As_2$ . . 112
5.3 Coexistence and competing antiferromagnetic and superconducting phases in the underdoped $Ba(Fe_{0.953}Co_{0.047})_2As_2$ compound studied by x-ray and neutron scattering techniques . . . 113
5.4 Unconventional pairing in iron arsenide superconductors . . . 119
5.4.1 Experimental results for $\mathbf{M}(x,T)$ . . . 120
5.4.2 Phenomenological model . . . 121
5.4.3 Microscopic model . . . 124
5.4.4 Application to $Ba(Fe_{1-x}Co_x)_2As_2$ . . . 129
5.4.5 Further theoretical investigations in superconducting gap symmetry . . 130
5.4.6 Conclusions from the unconventional pairing study . . . 133
5.5 Dispersion of the SC resonance in $Ba(Fe_{0.953}Co_{0.047})_2As_2$ . . . 133

Chapter 6. Summary and future work **142**
6.1 Summary . . . 142
6.2 Future work . . . 145

BIBLIOGRAPHY **147**

LIST OF TABLES

Table 2.1 Representative crystal symmetries 16

Table 2.2 Representative Fe-moment value 17

Table 2.3 List of critical temperatures 18

Table 4.1 Results of moment prediction in O-AFM phase 85

Table 4.2 Results of moment prediction in cT phase 90

LIST OF FIGURES

Figure 2.1 (a) The layered structure of electron doped $La(O_{1-x}F_x)FeAs$ (b) The structural and magnetic phase diagram determined by neutron scattering measurements. (c) The spin stripe arrangement of the Fe spins. Figures 2.4(a) and (b) were taken from ref (59) while figure 2.4(c) was taken from (30) 7

Figure 2.2 (a) Schematic of electron dispersion of hole (red) and electron (blue) bands displaced by the magnetic ordering vector $\mathbf{Q}_{\mathrm{AFM}}$ (b) Schematic of Fermi surface along with the nesting vector $\mathbf{Q}_{\mathrm{AFM}}$. 9

Figure 2.3 (a) Electron distribution at the Fermi level determined by ARPES (27) (b) Hole Fermi surface (empty circles) at the zone center and the electron Fermi surface displaced by $\mathbf{Q}_{\mathrm{AFM}}$ (filled circles) to demonstrate the level of nesting in $Ba(Fe_{1-x}Co_x)_2As_2$ x = 0.038, 0.058, 0.073, and 0.114. . . . 10

Figure 2.4 The layered structure of La_2CuO_4. Please note the crystal structure shown is not representative of Nd_2CuO_4. (b) The arrangement of the Cu spins in the Cu-O plane(reproduced figure from ref (35)). (c) A simple cartoon of the copper oxide phase diagram showing electron doped and hole doped compounds (reproduced figure from ref (36)). 11

Figure 2.5 (a) The gap structure around the Fermi surface for $d_{x^2-y^2}$ pairing symmetry appropriate for describing the gap structure in copper oxide superconductors. The light grey regions represent the portion of the gap that is positive while the black portions are negative. For different directions the gap changes sign and also varies in magnitude. (b) A diagram of the multiband isotropic s+- gap structure demonstrating gaps around the electron and hole bands, which are separated by $\mathbf{Q}_{\mathrm{AFM}}$, have different sign and constant magnitude around the Fermi surface. 14

Figure 2.6 The iron containing layer in iron based superconductors along with a summary of the classes of compounds that have been discovered since the beginning of this field in 2006. (from ref (44)) In the figure the atoms (and colors) are Fe(red), chalogen or pnictogen(orange), rare earth atom (green), alkaline earth atom (dark blue), and alkali metal (grey) 15

Figure 2.7 The tetragonal unit cell for the 122 system. The light cyan spheres represent the alkaline earth atom, the orange spheres represent Fe atoms, and the dark blue spheres represent the As atoms 20

Figure 2.8 The orthorhombic unit cell for the 122 system. The light cyan spheres represent the alkaline earth atom, the orange spheres represent Fe atoms, and the dark blue spheres represent the As atoms. The antiferromagnetic Fe spin structure is represented by the pattern of red arrows. 21

Figure 2.9 (a) The simple square lattice that makes up the base of the tetragonal unit cell is bounded by the dashed brown line along with the base of the orthorhombic cell (in the absence of orthorhombic distortion) bounded by the solid blue line. The directions in the **a**-**b** plane are labeled along with the lattice parameter. This figure is a reproduction of figure 7 from ref (24) (b) The reciprocal lattice associated with the square the crystal lattice shown in (a). The filled circles represent allowed Bragg reflections. 22

Figure 2.10 The temperature dependent resistivity of $CaFe_2As_2$ with $\mathbf{H} \parallel \mathbf{c}$ with $H = 0$ (open circles) and $H = 140$ Oe (filled triangles). The inset demonstrates the hysteresis in temperature around 170 K. (from ref (9)) 24

Figure 2.11 Temperature dependent magnetic susceptibility of $CaFe_2As_2$ for applied field parallel to the **a**-**b** plane (filled triangles) and applied field parallel to the **c** axis. This inset highlights the transition region. (from ref (9))) 25

Figure 2.12 The in plane, electrical resistivity of $CaFe_2As_2$ as a function of pressure for $p = 0$, 2.3, 3.5, 5.1, 5.5, 8.6, 12.7, 16.8, and 19.3 kbar. The downward and upward arrows indicate transition temperatures.(4) 26

Figure 2.13 p-T phase diagram for $CaFe_2As_2$ from ref. (4) determined from resistivity measurements 27

Figure 2.14 The change in scattering angle of the (002) peak as the pressure was changed from ambient pressure to 0.6 GPa at 50 K. The inset demonstrates the loss of magnetic order(5) 28

Figure 2.15 (a) and (b)Resistivity measurements on $CaFe_2As_2$ as a function of temperature and hydrostatic pressure.(68) 29

Figure 2.16 In-plane resisitivity (top), magnetization for fields applied in-plane and along **c** (middle), and heat capacity measurements on the compound $BaFe_2As_2$ (taken from ref (48)) 30

Figure 2.17 Electrical resistivity of $Ba(Fe_{1-x}Co_x)_2As_2$ single crystals normalized to their room temperature value. The inset highlights the low temperature behavior.(69)] 31

Figure 2.18 The temperature derivative of the heat capacity (top panel), the room temperature normalized resistivity (blue) along with its derivative (middle panel) and the magnetic susceptibility for a field along c (magenta) along with its temperature derivative (bottom panel) for the compound $Ba(Fe_{1-x}Co_x)_2As_2$ with $x = 0.038$ [taken from ref (69)] 32

Figure 2.19 The x-T phase diagram. The solid symbols represent the T-O transition. The open symbols represent the transition the AFM ordered state. The half filled squares and asterisks represent the superconducting transitions.(48) 33

Figure 3.1 Geometry for Scattering Experiment. (reproduction from ref (70)) . . . 36

Figure 3.2 Relation between $\mathbf{S}$ and $\mathbf{S}_{\perp}$. (reproduction from ref (70)) 44

Figure 3.3 Physical picture of a spin wave where the static moment direction is perpendicular to the plane which includes the spin motions represented as the circular trajectory. (reproduction from ref (70)) 50

Figure 3.4 The spin arrangement and the coupling constants used in the Heisenburg spin Hamiltonian (Taken from ref (76)) 50

Figure 3.5 Contour plot of $\mathcal{S}(\mathbf{Q},\omega)$ based on measurements on $Ba(Fe_{0.953}Co_{0.047})_2As_2$ along the (a) $(h01)$ and (b) $(10l)$ directions. The sold lines represent the spin-wave dispersion. Please note the different energy scales. 53

Figure 3.6 Conical Dispersion 54

Figure 3.7 This schematically shows the effect of SC on $\chi_0''(\mathbf{Q},\omega)$ along with the resulting trend of $\chi_0'(\mathbf{Q},\omega)$ as determined from Kramers-Kronig relations. A condition for the resonance peak at ω_{res} in the RPA $\chi_0(\mathbf{Q},\omega)$ is that $\chi_0'(\mathbf{Q},\omega) = 1/\text{V}(\mathbf{Q})$ while $\chi_0''(\mathbf{Q},\omega)$ simultaneously equals zero. 59

Figure 3.8 Schematic of a triple axis spectrometer 61

Figure 3.9 Schematic of a nuclear reactor that produces thermal neutrons (taken from ref (85) 61

Figure 3.10 The triple axis spectrometer configuration in (a) Three-axis mode and in (b) Two-axis mode 65

Figure 3.11 The path in reciprocal space followed during longitudinal scans and rocking scans which are commonly performed during a triple-axis experiment 66

Figure 3.12 Example resolution ellipsoid where the solid lines represent the cross section of the ellipse in plane and the dashed lines show the projection into the plane. The spectrometer parameters are discussed in the text. This figure was taken from ref (88) 69

Figure 3.13 (a) The resulting S($\mathbf{Q}$,ω) from a fitting a magnetic excitation in using Reslib (b) The observed intensity along with the curve representing the resolution convolution with the results shown in (a). 71

Figure 3.14 Focused and unfocused (a) $\mathbf{Q}$ scans and (b) energy scans. 71

Figure 3.15 Transverse lattice excitations (motion transverse to the (1 1 0) direction) were measured in regions of -space where the triple axis was focused ($\mathbf{Q}$ = $(2\ 2\ -0.6)_{\mathrm{T}}$) and defocused ($\mathbf{Q}$ = $(2\ 2\ 0.6)_{\mathrm{T}}$). The lines are guides to the eye. 72

Figure 4.1 Magnetic structures for $CaFe_2As_2$ shown in the orthorhombic unit cell to facilitate comparison. (a) The AF2 magnetic structure realized at ambient pressure below 170 K (92). (b) Representation of the AF1 G-type antiferromagnetic structure with antiferromagnetic ordering along the $\mathbf{c}$ axis. (c) Representation of the AF1 C-type antiferromagnetic structure with ferromagnetic ordering along the c axis. 74

Figure 4.2 (a) Pressure-temperature phase diagram of $CaFe_2As_2$ under hydrostatic pressure. Filled and open circles (squares) denote phase boundaries determined upon heating and cooling at a set pressure for the O-T (cT-T) phase transition. Filled and open triangles denote phase boundaries determined upon decreasing and increasing pressure at a fixed temperature. The shading denotes hysteresis. The inset of (a) shows the lattice constants near the T-cT transition at 300 K. In (b)(i), the color codes denote measurements of the T phase (blue), O phase (green), or cT phase (red) diffraction peak positions. (b) Ω-2θ scans of the $(0\ 0\ 4)_{cT}$ peak at 0.47 GPa on increasing temperature. (c) Ω-2θ scans of the $(0\ 0\ 4)_{T}$ peak at 0.47 GPa on decreasing temperature. (d) Temperature dependence of the peak intensities of the $(0\ 0\ 4)_{T}$ as the temperature is decreased at p=0.47 GPa and the $(0\ 0\ 4)_{cT}$ as the temperature is increased at p=0.47 GPa. (e) Ω scans through the $(0\ 0\ 4)_{O}$ peak at 92 K as the pressure is increased from 0.375 to 0.400 GPa. (f) Ω scans through the $(004)_{cT}$ peak at 92 K as the pressure is decreased from 0.250 to 0.225 GPa. (g) Ω-2θ scans through the expected position of the $(\frac{1}{2}\ \frac{1}{2}\ 3)_{T}$ magnetic peak in the tetragonal phase. (h) Ω-2θ scans through the observed position of the $(1\ 0\ 3)_{O}$ magnetic peak. (i) Ω-2θ scans through the expected position of the $(\frac{1}{2}\ \frac{1}{2}\ 3)_{cT}$ magnetic peak. 76

Figure 4.3 Phase fractions of the O and cT phases as a function of pressure upon increasing pressure (top panel) at 75 K and decreasing pressure (bottom panel) at 50 K. The integrated intensity of the magnetic $(1\ 0\ 3)_{O}$ reflection remains constant in the O phase. Uncertainties are statistical in origin and represent one standard deviation. 81

Figure 4.4 (top panel) θ-2θ scan through the nuclear $(0\ 0\ 4)_{O}$ peak in the non spin-flip channel. (bottom panel) θ-2θ scan through the magnetic $(1\ 0\ 1)_{O}$ peak in the spin-flip channel. 86

Figure 4.5 (top left) Corrected θ-2θ scan through the nuclear $(0\ 0\ 4)_{cT}$ peak in the non spin-flip channel. (bottom left) Corrected θ-2θ scan through the nuclear $(0\ 0\ 4)_{cT}$ peak in the spin-flip channel. Not that the counts are at background level. (top right) θ-2θ scan through the nuclear $(1\ 0\ 1)_{cT}$ peak in the non spin-flip channel. (bottom right) θ-2θ scan through the proposed magnetic $(1\ 0\ 1)_{cT}$ peak in the spin-flip channel. This peak is clearly displaced from the nuclear $(1\ 0\ 1)_{cT}$ peak which is suggestive that this is an impurity peak. 88

Figure 4.6 (top panel) Rocking scans through the nuclear $(1\ 0\ 1)_{cT}$ peak in the non spin-flip channel. (bottom panel) Rocking scans through the proposed magnetic $(1\ 0\ 1)_{cT}$ in the spin-flip channel. These scans provide allow for"fast" estimate of an upper limit of the proposed magnetic moment magnitude. 89

Figure 4.7 Measurement of the (0 0 2) nuclear reflection from $CaFe_2As_2$ with an area detector on the E4 diffractometer using a Be-Cu clamp-type cell. For an initial pressure of 0.83 GPa, at room temperature, the T phase transforms to a mixture of the cT and O phases below approximately 100 K. 93

Figure 4.8 (Taken from K. Prokěs *et al.* (129)) Temperature dependence of the integrated intensity around the (0 0 2) position in the T (filled triangles), T' (open triangles), O (filled circles), and cT (filled stars) phases. . . . 96

Figure 4.9 (Taken from K. Prokěs *et al.* (129)) Color map showing the intensity near the (002) reflection of CaFe2As2 under uniaxial pressure (0.1 GPa) upon (a) cooling and (b) warming. It is important to note that the color map intensity in (a) ranges from 20-260 while in (b) the range is 60-220. (c) Two probe resistance measurements taken simultaneously with diffraction measurements upon cooling (filled triangles) and warming (open triangles). The lower right inset shows a low temperature range highlighting the onset of SC at ∼10 K. The panel on the upper left shows the weight fraction of the stabilized T' phase as pressure is varied. The dotted line is a guide to the eye. 97

Figure 4.10 (a) Calculated DOS near the Fermi energy for the T (red line) and cT (blue line) phases of $CaFe_2As_2$. (b) The generalized susceptibility $\chi(\mathbf{q})$ for the T (red line) and cT (blue line) phases of $CaFe_2As_2$. 100

Figure 4.11 (a) Coaligned single crystals of $CaFe_2As_2$. Approximately 300 crystals were mounted on both sides of five Al plates that were stacked to produce the measurement sample (shown on a millimeter grid). (b) Schematic of the reciprocal lattice plane probed in these measurements. The dashed lines denote scans along the $[h\ h\ 0]_T$ and $[0\ 0\ l]_T$ directions. (c) The p-T phase diagram of $CaFe_2As_2$ (after ref. (8)). The shaded area represents hysteretic regions, and the numbers correspond to the measurement sequence as described in the text. 103

Figure 4.12 Constant energy $\mathbf{q}$ scans at 3 and 7 meV energy transfer through the $(\frac{1}{2}\ \frac{1}{2}\ 1)_T$ antiferromagnetic wave vector along the in-plane $[h\ h\ 0]_T$ direction at T=180 K and p= .5 GPa for (a) and (b); T=100 K and p=0.5 GPa for (c) and (d). Panels (e) and (f) show the data taken at T=180 K and p =0.5 GPa after passing through the T-cT transition twice (upon cooling and warming). The open squares denote the empty can background measurements. The dashed vertical line denotes the position of the $(\frac{1}{2}\ \frac{1}{2}\ 1)_T$. Each data point in this figure represents 6 min of counting time (8000 monitor counts). 105

Figure 4.13 Constant energy **q** scans, after background subtraction, at 3 meV energy transfer through the $(\frac{1}{2}\ \frac{1}{2}\ 1)_{\mathrm{T}}$ antiferromagnetic wave vector along the $[h\ h\ 0]_{\mathrm{T}}$ [panels (a), (c), and (e)] and the $[0\ 0\ l]_{\mathrm{T}}$ directions [panels (b), (d), and (f)]. The numbers in the shaded circles correspond to the points indicated in Fig. 4.11(c). The heavy lines through the data are fits to a single Gaussian line shape. The thin lines provide a guide to the eyes. The dashed vertical line denotes the position of the $(\frac{1}{2}\ \frac{1}{2}\ 1)_{\mathrm{T}}$). The instrumental resolution is shown at the bottom of panels (a) and (b). . 107

Figure 5.1 (a) Magnetization (dots) and its temperature derivative (line), and (b) resistivity and its temperature derivative for $Ba(Fe_{0.953}Co_{0.047})_2As_2$ as a function of temperature. (c) The integrated intensity of the $(2\ 2\ 0)_{\mathrm{T}}$ nuclear reflection (circles) and the $(\frac{1}{2}\ \frac{1}{2}\ 1)_{\mathrm{T}}$ magnetic reflection (squares) as a function of temperature. Hollow symbols indicate warming and filled symbols cooling. The solid line shows the power law fit to the magnetic order parameter. Vertical lines through all three panels indicate the structural (T_{S}), magnetic (T_N), and superconducting (T_{c}) transitions. 115

Figure 5.2 (Right) Images of the x-ray diffracted intensity of the $(2\ 2\ 0)_{\mathrm{T}}$ peak for $x = 0.047$ showing a single spot above T_{S} and two spots below T_{S} due to orthorhombic splitting. (Left) The temperature evolution of the $(1\ 1\ 10)_{\mathrm{T}}$ reflection for $x = 0.038$, showing T-O phase transition. 116

Figure 5.3 Phase diagram for $Ba(Fe_{1-x}Co_x)_2As_2$ showing paramagnetic tetragonal (T), paramagnetic orthorhombic (O), AFM ordered orthorhombic (AFM O), and superconducting (SC). AFM O and SC phases coexist between $x = 4\%$ and 6%. The vertical line shows the position of the $x = 0.047$ sample studied here. The data points for the phase lines have been taken from ref. (9). 117

Figure 5.4 (a) The reduction in intensity of the $(\frac{1}{2}\ \frac{1}{2}\ 1)_{\mathrm{T}}$ peak compared to the fit of the magnetic order parameter to a power law [shown in Fig. 1(c)] and the intensity ratio of $(\frac{1}{2}\ \frac{1}{2}\ 1)_{\mathrm{T}}$ and $(\frac{1}{2}\ \frac{1}{2}\ 3)_{\mathrm{T}}$ as a function of temperature. (b) Energy scan at $(\frac{1}{2}\ \frac{1}{2}\ 1)_{\mathrm{T}}$ for T = 25 K (empty circles) and 5 K (solid circles). (c) Scans along [110] at 2.5 meV for 25 K and 5 K. Lines are guides to the eye. 118

Figure 5.5 (a) Experimentally determined x-T phase diagram based on observed magnetic neutron and x-ray scattering as well as bulk thermodynamic and transport measurements. (b) The moment trend versus reduced temperature T/T_{N} The maximum moment value of the undoped compound is 0.87 $\mu_{\mathrm{B}}(23)$ 121

Figure 5.6 The experimentally determined moment trend with temperature for 5.4% Co doped $BaFe_2As_2$. The line shows an extrapolation to the T = 0 K moment value in the absence of SC. 122

Figure 5.7 Schematic $x - T$ phase diagrams for the Co doped $BaFe_2As_2$ system with (a) homogeneous coexistence of SC and AFM and (b) heterogeneous coexistence of SC and AFM. 123

Figure 5.8 Schematic representation of the hole band at $\mathbf{k} = 0$ and the electron band at $\mathbf{k} = \mathbf{Q}$. The maxima of the hole bands and minima of the electron bands are labeled $\epsilon_{1,0}$ and $\epsilon_{2,0}$ respectively. The dashed line indicates the position of the chemical potential μ. 125

Figure 5.9 Extrapolated zero temperature ordered moment M(T=0,x) as function of doping x (panel a) and as function of T_{N} (panel b) for $Ba(Fe_{1-x}Co_x)_2As_2$. Points correspond to experimental data whereas the solid line is the result of the calculation described in the text. In the insets, the red circle (blue ellipse) denotes the hole (electron) Fermi pocket. 129

Figure 5.10 (a) Experimentally determined x-T phase diagram. (b) AFM order parameter squared determined by neutron scattering measurement. [(c) and (d)] Theoretically determined phase diagram and AFM order parameter squared for s+- pairing state. [(e) and (f)] Theoretically determined phase diagram and AFM order parameter squared for s++ pairing state. 131

Figure 5.11 Summary of the resulting g-parameters which parameterize the band dispersions and SC states 132

Figure 5.12 (a) Monitor-normalized neutron intensity I($\mathbf{Q}$,ω) for x =4.7% including background measurement for energy scans at $\mathbf{Q}_{\mathrm{AFM}}$=($\frac{1}{2}$ $\frac{1}{2}$ 1)$_{\mathrm{T}}$ both above (25 K, open circles) and below T_{c} (5 K, filled circles). The arrow shows the location of the resonance. The dark gray shading highlights regions of increased intensity related to the resonance while the light gray shading highlights a loss of intensity.(b) Energy dependence of $\chi''(\mathbf{Q}_{\mathrm{AFM}},\omega)$ at 5 and 25 K. The solid line is a fit to spin waves described in the text. (c) [h h 0]$_{\mathrm{T}}$ scans and (d) [0 0 l]$_{\mathrm{T}}$ scans through ($\frac{1}{2}$ $\frac{1}{2}$ 1) at 5, 7, and 10 meV. In (c) and (d) solid lines represent fits to the spin-wave model in the normal state. The inset to (d) shows [0 0 l]$_{\mathrm{T}}$ scans for x =8.0% both above (30 K, open triangles) and below T_{c} (10 K, filled triangles) at an energy transfer of 9.5 meV (close to the resonance peak) taken from Lumsden et al., Ref. (18). 135

Figure 5.13 (a) Dispersion of the resonance shown by monitor-normalized constant-$\mathbf{Q}$ energy scans at ($\frac{1}{2}$ $\frac{1}{2}$ l)$_{\mathrm{T}}$ for x =4.7% for several values of l at temperatures above and below T_{c}. (b) Difference of scattering intensity between temperatures 5 K and 25 K above and below T_{c}, respectively, for both x =4.7% (open circles) and 8.0% (filled triangles) at l=0, $\frac{1}{2}$, and 1. (c) Comparison of the dispersion of the resonance peak energies along the l direction for x =4.7% and 8.0%. The x =8.0% data are taken from Ref. (18). 138

Figure 5.14 Contour plots of the magnetic susceptibility as a function of $\hbar\omega$ and l=1 to 2. (a) Measured data at 25 K. The line shows the fitted normal-state spin-wave dispersion. This line also appears in panels (b) and (c). (b) Normal-state damped spin-wave fitting results which have been convoluted with the experimental resolution. (c) Measured data below T_c at 5 K. The lower solid line is a fit to the square data points which represents the peak in the resonance. (d) The measured resonance susceptibility obtained from the difference of the data at 5 K [panel (c)] and 25 K [panel (a)]. . 140

CHAPTER 1. Thesis overview

1.1 Introduction and motivation

The study of iron based superconductors began in 2006 when the compound LaOFeP was found to have a superconducting transition at a modest temperature (T_c) of 3.2 K (1). Because elemental iron is a strong ferromagnet and magnetic moments are generally associated with magnetic pair breaking and the loss of superconductivity, this discovery was a great surprise.(2) Soon after this discovery, variations of these superconductors were made through chemical substitutions and the T_c rose to 55 K two years later(3). The explosion of research that has followed these discoveries has led to the synthesis of several families of iron based superconductors whose high values of T_c are second only to the cuprates, bringing them into the field of high temperature superconductivity (SC).

The purpose of this thesis is to answer questions about how pressure and electron doping affect the crystallographic and magnetic properties of the iron based superconductors (Ca,Ba)Fe_2As_2 which are part of a group of compounds known as 122s. Upon cooling, these compounds undergo a dual structural-magnetic transition from a tetragonal paramagnetic state to an orthorhombic and antiferromagnetic state. By tuning the pressure or dopant concentration knob, we have been able to show clearly that this has the effect of suppressing the magnetism and associated structural transition observed in un-doped or ambient pressure compounds. For the case of doping, it is clear that a sufficient suppression of structural and magnetic ordering transitions is necessary for the appearance and optimization of superconductivity while the conditions for superconductivity under pressure remain an open question.

The experiments associated with this work were performed at a variety of neutron scattering facilities using a triple axis spectrometer. The majority were performed at Oak Ridge National

Laboratory's (ORNL) High Flux Isotope Reactor (HFIR) in Oak Ridge, TN. Additionally, experiments were performed at the National Institute of Standards (NIST) Center for Neutron Research (NCNR) in Gaithersburg MD, as well as at the Institut Laue-Langevin (ILL) in Grenoble, France. The neutron and x-ray scattering studies presented in this work have provided important information about the microscopic structural and magnetic properties of the iron based superconductors. In particular, neutron scattering measurements have provided key information about the static magnetic ordering and the associated magnetic excitations, and have allowed for the attempt to address questions about the nature of magnetism in these materials and what role magnetism plays in the appearance of superconductivity.

1.2 Summary of key results

1.2.1 Effects of pressure application on antiferromagnetism and superconductivity in $CaFe_2As_2$

Prior to the work described in this thesis, it was demonstrated that pressure application to the compound $CaFe_2As_2$ can produce the necessary conditions for superconductivity(4). Also, it was clear that $CaFe_2As_2$ stood out amongst the other 122 superconductors as it transitioned to what is known as a collapsed tetragonal (cT) phase with very modest pressures (< 1 GPa). The details of this phase were reported in ref.(5) which showed that upon transitioning to the cT phase, the c-lattice parameter decreased by $\approx$9.5% and volume decreased by 5%. Several groups revealed p-T phase diagrams for $CaFe_2As_2$ with different superconducting, magnetic, and structural phase lines(4; 6; 7). This work has discovered the reason for this. A variety of pressure application methods failed to apply identical pressure to all surfaces, and thus did not achieve the hydrostatic condition. Only through the use of a He gas medium (or hydrostatic pressure) did a clear and consistent picture of the equilibrium p-T phase diagram develop. When a true hydrostatic pressure medium is used, SC is absent in the p-T phase diagram of $CaFe_2As_2$ as SC is disrupted by transition to a cT phase.

One of the most exciting results involved the complete loss of Fe moments in the cT phase. Neutron scattering experiments revealed both the loss of antiferromagnetic order and magnetic

excitations in the cT phase.(5; 8) Investigations employing both unpolarized and polarized neutron scattering searched for the existence of a variety of predicted magnetic ordering structures, and nothing was found. Inelastic neutron scattering showed that paramagnetic fluctuations observed at high temperatures and low pressures also disappear in the cT phase. These results, which were predicted by band structure calculations presented in this work, provide a potential explanation for the absence of superconductivity in the cT phase as there are no mediating magnetic fluctuations to assist in the formation of Cooper pairs.

Finally, some clues as to how the observed SC (Figure 4.9) did develop were found through experiments which maximized non-hydrostatic pressure. $CaFe_2As_2$ samples were pressurized in a clamp cell which only pressed along the **c**-direction. Using this procedure multiple co-existing phases were formed including a previously unobserved tetragonal phase at high pressure and low temperature which was stabilized by non-hydrostatic pressure. *In situ* resistivity measurements performed during the scattering measurements revealed the onset of SC along with this new phase. As it had been established that SC was not present in the equilibrium p-T diagram, these results provide compelling evidence that the appearance of this newly discovered non-hydrostatic pressure stabilized tetragonal phase is responsible for the reports of SC under pressure.

1.2.2 Effects of Co doping on magnetism and SC in $\mathbf{Ba(Fe_{1-x}Co_x)_2As_2}$

At the beginning of this work, various groups were demonstrating the ability to grow high quality single crystals of electron doped $Ba(Fe_{1-x}Co_x)_2As_2$(9; 10) which resulted in published phase diagrams based on anomalies (specifically sudden changes in the slope upon cooling or warming) observed during thermodynamic and transport measurements . Figure 2.19 shows the evolution of anomalies observed in resistivity measurements. The anomalies in magnetization suggested that the magnetic transition was suppressed with doping and after sufficient doping, SC appeared in these x-T phase diagrams. This is reminiscent of other unconventional superconductors such as the cuprates and suggests some commonality between them. These exciting results motivated the further investigation of the microscopic details of these transitions by neutron and x-ray scattering.

A combined neutron and x-ray scattering study revealed that a dual magnetic and structural transition (from a tetragonal paramagnetic to an orthorhombic antiferromagnet) occurred in the undoped (parent) compound $BaFe_2As_2$ with the same magnetic structure observed in $CaFe_2As_2$. Upon doping, the transitions split as the magnetic transition was suppressed more than the structural transition. The onset of SC can be observed by magnetic neutron diffraction which revealed that below T_c the ordered moment was suppressed (due to the competition for electrons which contribute to SC and AFM). This result is further supported magnetization, NMR, μSR (9; 11; 12) which show the entire volume of the material is simultaneously magnetized and superconducting, providing evidence for homogenous co-existence of competing AFM and SC for a range of doping.

The observed co-existence and competition of AFM and SC is rather significant because it allows for the narrowing down of possible SC gap symmetries as well as SC pairing mechanisms. The co-existence and competition of AFM and SC was studied for selected compositions ranging from the undoped compound to optimally doped (highest T_c) by neutron and x-ray scattering. A mean field theory was developed and discussed in chapter 5 to study the effects of competing AFM and SC phases and it was revealed that conventional pairing was not consistent with the observed co-existence and competition. The current consensus is that pairing symmetry is s+- (including two sign changing isotropic SC gaps located on two different bands)(13). This study demonstrated that the trends in magnetization observed in the x-T phase diagram including a re-entrance to paramagnetism for $Ba(Fe_{1-x}Co_x)_2As_2$ with $x = 0.059$, could be reproduced by a theory including s+- pairing symmetry. This suggests that conventional electron-phonon pairing is not suitable to describe SC in the arsenides.

Another challenge in the field of high temperatures superconductors in which neutron scattering has made a significant impact is the study of the SC resonance. The SC resonance refers to the redistribution of low energy magnetic excitations below T_c. The SC resonance has been observed previously in unconventional superconductors such as the cuprates (14), and heavy fermion compounds(15; 16; 17). For superconducting compositions of $Ba(Fe_{1-x}Co_x)_2As_2$, this resonance appears near the wave vector $\mathbf{Q}_{\mathrm{AFM}}$ of the AFM ordered structure. In optimal doped compounds where long range AFM order is absent(18), the intensity is independent of

the **c** component of **Q** (perpendicular to the Fe layers), indicating 2-dimensional (2D) behavior. However, in underdoped compounds, where long range AFM order exists, it is observed that the resonance also depends on $\mathbf{Q}_c$ providing yet another connection between AFM and SC in these compounds. These results also highlight the fact that future theoretical descriptions which will describe the origin of the resonance and the connection to superconductivity will need to consider a 3-D system for underdoped $Ba(Fe_{1-x}Co_x)_2As_2$.

1.3 Thesis layout

In chapter 2, I briefly review the state of the field and describe some key properties of iron based superconductors that are useful for understanding the studies that follow. In chapter 3, the appropriate neutron scattering cross sections are described as well as important technical considerations for the use of a triple axis spectrometer, which was the primary experimental tool. Chapter 4 summarizes my work along with a wide range of research performed on $CaFe_2As_2$ and shows how studies with modest pressure application has provided insight into the interplay of structure, magnetism, and superconductivity. The main results are (1) a mapping of the structure and magnetic order in a p-T phase diagram and (2) the demonstration that pressure results in the suppression of not only long range magnetic order, but also magnetic excitations. Chapter 5 explores the doping of Co for Fe in series of compounds $Ba(Fe_{1-x}Co_x)_2As_2$ and includes three main sections. The first section discusses neutron and x-ray scattering measurements involved in mapping out the x-T phase diagram. The second section summarizes an important combined experimental and theoretical work which investigates potential candidates for the electron pairing mechanism and demonstrates how important neutron scattering has been for understanding this mechanism. This section includes a summary of the theory which was developed by Rafael Fernandes and Jörg Schmalian based upon my experimental results. The final section discusses a feature in the magnetic excitation spectrum known as the magnetic resonance which supports the work by Rafael Fernandes(19) and also demonstrates that future models of superconductivity need to consider electronic interactions in all three dimensions and not just in the Fe-planes as is typically done. Finally, chapter 6 will summarize the results and discuss future work.

CHAPTER 2. Introduction to iron arsenides

2.1 Discovery of superconductivity in iron pnictide compounds

For their work in 2006, Y. Kamihara *et al.* (1) are credited with discovery of the first iron based superconductor. This work showed that in LaFeOP, resistivity measurements indicated the transition to state with zero resistance and negative magnetic susceptibility, the signatures of superconductivity, at 3.2 K. It was shown in this same work that through the 6% chemical substitution of fluorine at the oxygen site (electron doping), the superconducting transition temperature (T_c) was raised by 2 K.

The same group of researchers followed this result with a systematic study of fluorine doping the compound LaFeAsO which was published in 2008.(20) Through the characterization of LaFeAs($O_{1-x}F_x$) with doping levels ranging from $x = 0.04 - 0.12$, an optimized T_c of 26 K was found for LaFeAs($O_{0.89}F_{0.11}$), which was five times larger than the previous result on LaFeOP. The transition temperatures of the iron superconductors were rapidly approaching the level of "high temperature superconductivity status" demarcated by an upper limit of 30 K estimated from BCS theory of superconductivity(21). Since their discovery, an immediate flurry of research in this field occurred which has relied heavily on the knowledge and experimental techniques gained from previously discovered superconductors such as the cuprates and heavy fermion compounds. In particular, the ability to create a wide variety of novel iron superconductors through chemical substitution, as will be discussed in the next section, has allowed for the optimization of superconducting temperature so that iron superconductors can now be added to the field of high temperature superconductivity with T_c reaching 55 K in $SmFeAsO_{1-\delta}$ (3).

2.2 General comments about iron pnictide compounds

As is shown in Figure 2.1(a), the RFeAs($O_{1-x}F_x$), where R refers to rare earth elements, are layered compounds. As Figure 2.1(b) shows, for a range of doping, a structural transition occurs from a high temperature tetragonal state (space group P4/nmm) to a low temperature orthorhombic state (Cmma) which is followed by a transition to an orthorhombic/antiferromagnetic state. Figure 2.1(c) shows the antiferromagnetic arrangement of static spins located on the iron atoms. Neutron scattering measurements on RFeAs($O_{1-x}F_x$) found that the structure and magnetic ordering was suppressed as increased amounts of fluorine were substituted for oxygen. The trend in the ordered Fe-moment is shown in the upper right of Figure 2.1(b). Once AFM order as well as the structural transition is suppressed, SC appears along with dynamic spin fluctuations which may support the development of SC.(22).

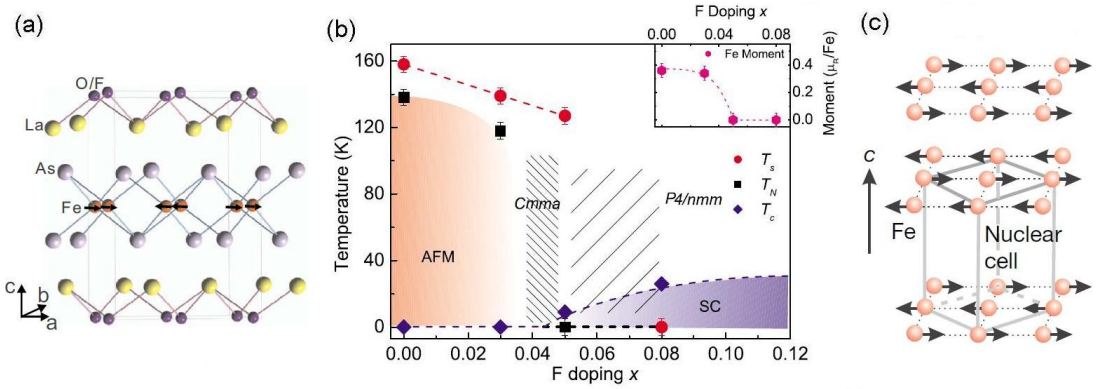

Figure 2.1 (a) The layered structure of electron doped La($O_{1-x}F_x$)FeAs (b) The structural and magnetic phase diagram determined by neutron scattering measurements. (c) The spin stripe arrangement of the Fe spins. Figures 2.4(a) and (b) were taken from ref (59) while figure 2.4(c) was taken from (30)

It is now established that RFeAs($O_{1-x}F_x$) is characterized as a semi-metal(24). A semimetal can be understood when considering the filling and relative positions of the conduction and valence bands. For example, metals have a partially filled conduction band (or nearly filled valence band) leading to a large number of charge carriers at the Fermi level which can conduct at the lowest reachable temperatures. Insulators (or semiconductors) have a filled valence band and empty conduction band, and electrical conductance can occur if electrons are thermally

excited to the conduction band. The band gap can be direct, where no momentum transfer is required to reach the conduction band, or indirect where both a momentum and energy transfer to the electron is required to reach the conduction band. Semimetal can be understood as a compound which is on the verge of being an indirect semiconductor. Because there is a small overlap between the valence and conduction band, there is a small density of charge carriers at the Fermi level. A typical semimetal such as graphite has a density of charge carriers that is four orders of magnitude smaller than metallic copper.(25)

LDA calculations on LaFeAsO have revealed band structure of a semi-metal with a Fermi surface consisting of hole bands at the zone center and electron bands displaced by a momentum transfer $(\frac{\pi}{a}, \frac{\pi}{a})$ where a is the in-plane lattice parameter(26). The density of states at the Fermi level is dominated by Fe-d states (24) and electronic susceptibility calculations have revealed itinerant electrons are important for the formation of magnetic order(26). Fermi surface nesting (which refers to the condition that two portions of the Fermi surface are parallel and separated by a common wavevector) leads to a peak in the susceptibility at the magnetic momentum transfer $(\frac{\pi}{a}, \frac{\pi}{a})$. A simple picture of the band structure is shown in Figure 2.2(a) and (b). Figure 2.2(a) shows the dispersion of the hole band (in red) at the zone center which is separated from the electron band by $\mathbf{Q}_{\mathrm{AFM}} = (\frac{\pi}{a}, \frac{\pi}{a})$. Figure 2.2(b) shows a cartoon of the Fermi surface which represents the predicted circular hole band and an elliptical electron band. The nesting vector has been drawn to show portions of the Fermi surface which are nested. An itinerant picture for AFM order (spin density wave) is consistent with the fact that the measured moment of LaFeAsO is 0.36 μ_{B}. For the expected oxidation state of Fe^{2+}, a high spin state of 4 μ_{B} would be observed if the electrons were localized around the Fe site(24).

Angle Resolved Photoemission Spectroscopy (ARPES) measurements have provided some confirmation of the details of the band structure and the degree of nesting in the iron arsenides superconductors (27) and show good agreement with the theoretical predictions of band structure. ARPES experiments allow for the direct measurement of the kinetic energy and angular distribution of the electrons photoemitted from a sample illuminated with sufficiently high-energy radiation. From ARPES measurements, one can gain information on both the energy and momentum of the electrons inside a material(28). Figure 2.3(a) shows a map

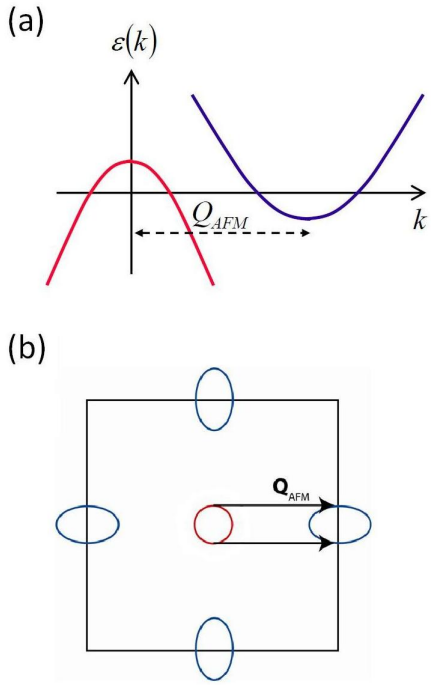

Figure 2.2 (a) Schematic of electron dispersion of hole (red) and electron (blue) bands displaced by the magnetic ordering vector $\mathbf{Q}_{\mathrm{AFM}}$ (b) Schematic of Fermi surface along with the nesting vector $\mathbf{Q}_{\mathrm{AFM}}$.

of the electron distribution at the Fermi surface of an electron doped iron arsenide compound $Ba(Fe_{1-x}Co_x)_2As_2$ with $x = 0.047$ in the paramagnetic state ref (27). One can see that there are two bands. The central band is a hole band (with increasing binding energy the size of the FS increases) and the band shifted by momentum $\mathbf{Q} = \mathbf{Q}_{\mathrm{AFM}} = (\frac{\pi}{a}, \frac{\pi}{a})$, is an electron band (with increasing binding energy the size of the FS decreases). The data points in Figure 2.3(b) show the peak of the hole (empty circles) and the electron (filled circles) distribution and indicate the shape of the Fermi surface. In can be clearly seen that the hole band is close to circular in shape while the electron band has an elliptical shape. In Figure 2.3(b), the "Fermi pockets" have been shifted by the wave vector $\mathbf{Q}_{\mathrm{AFM}}$ to highlight where nesting occurs.

The data in Figure 2.2(b) reveal that there are four regions where the circular hole and elliptical electron band cross each other. But, even with this non-perfect nesting (where perfect nesting refers to a complete overlap of bands after displacement of $\mathbf{Q}_{\mathrm{AFM}}$), the nesting can lead to a spin density wave instability and push the system into a state which exhibits the

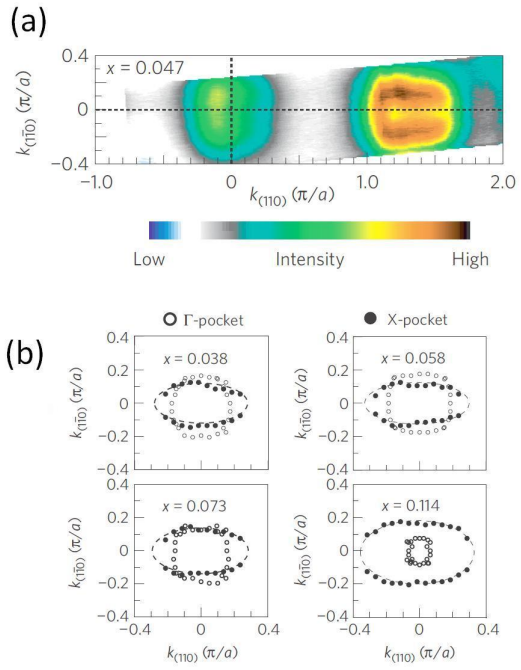

Figure 2.3 (a) Electron distribution at the Fermi level determined by ARPES (27) (b) Hole Fermi surface (empty circles) at the zone center and the electron Fermi surface displaced by $\mathbf{Q}_{\mathrm{AFM}}$ (filled circles) to demonstrate the level of nesting in $Ba(Fe_{1-x}Co_x)_2As_2$ x = 0.038, 0.058, 0.073, and 0.114.

observed long range antiferromagnetism in compounds with low levels of doping(29)

Further research on the electronic phase diagram of RFeAs$(O_{1-x}F_x)$ (R = La, Ce, Pr) (30; 31; 32) excited researchers, as it seemed there was some similarities between these compounds and the thoroughly studied copper oxide high temperature superconductors that were discovered in 1986(33). In what follows, I will discuss some important properties of the cuprates, in particular La_2CuO_4 and Nd_2CuO_4 so I can compare the cuprates and the iron arsenide compounds.

The layered crystal structure of the copper oxide superconductors is shown for La_2CuO_4 in figure 2.4(a). The parent copper oxide compounds are Mott insulators which differ from conventional insulators which have low conductivity because of filled orbitals which inhibit electron motion because of Pauli's exclusion principal. Undoped copper oxides have an unpaired electron in its unit cell and therefore should be conductors. An explanation for the unexpected

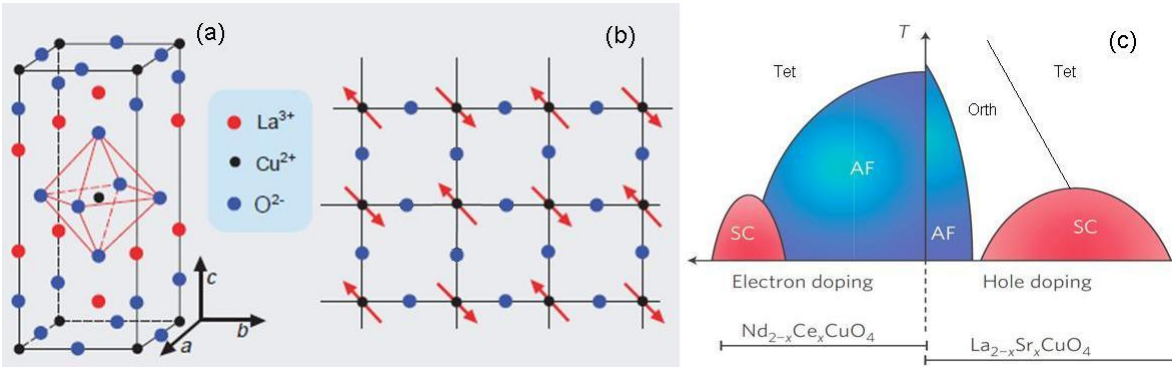

Figure 2.4 The layered structure of La_2CuO_4. Please note the crystal structure shown is not representative of Nd_2CuO_4. (b) The arrangement of the Cu spins in the Cu-O plane(reproduced figure from ref (35)). (c) A simple cartoon of the copper oxide phase diagram showing electron doped and hole doped compounds (reproduced figure from ref (36)).

insulating behavior was first proposed by Nevile Mott in 1949 where electron conduction in these compounds is based on the formula $(Cu^{2+}O^{2-})_2 \rightarrow Cu^{3+}O^{2-} + Cu^{1+}O^{2-}$ which costs energy in the form of Coulomb repulsion of electrons on doubly occupied Cu^+ and therefore is inhibited(34). At low temperatures, the system exhibits long range antiferromagnetic order where neighboring Cu spins are anti-aligned (antiferromagnetic) in the Cu-O plane (35) which is shown in Fig 2.1(b). Figure 2.4(c) reveals a generic phase diagram for the copper oxides which shows the presence of antiferromagnetism and its suppression with both electron and hole doping where electron doping (i.e. Ce^{3+} for Nd^{4+}) refers to the substitution of an element which adds electrons to the parent system and hole doping refers the substitution of an element that lowers the electron number in the parent system (i.e. Sr^{3+} for La^{2+}). The act of doping alters the number of electrons in unit cell and these compounds become metallic. However, the large Coulomb repulsion results in strongly correlated motion of charge carriers. Electron and hole doping causes the weakening of AFM order as is seen by the suppression of the antiferromagnetic transition temperature or the Néel Temperature (T_N). Also for $La_{2-x}Sr_xCuO_4$ there exists a structural transition where the crystal structure changes from high temperature tetragonal state to a low temperature orthorhombic state. The appearance of superconductivity occurs over a range of both electron and hole doping only after AFM order (as well as the structural transition for the case of $La_{2-x}Sr_xCuO_4$) is sufficiently suppressed. In the SC state, static long

range AFM order is suppressed and the moments are dynamical. As will be discussed in the next section, it is commonly thought that these spin fluctuations are key for the development of SC but the exact microscopic mechanism for SC in the cuprates remains an open question.

The details of the cuprates can now be compared to the $RFeAs(O_{1-x}F_x)$ compounds. It is clear from this comparison that there are many similarities between the cuprates and the $RFeAs(O_{1-x}F_x)$. These similarities are surprising when considering that the parent compounds have very different electronic properties with the cuprates being insulators and RFeAsO metallic. Even though the structural and magnetic order differs, they both are layered structures with long range antiferromagnetic order. In both compounds, doping causes a suppression of structural and antiferromagnetic order and after sufficient suppression superconductivity appears. The proximity of the superconductivity to the magnetic and structural phase transitions in the phase diagram suggests that SC may have a common microscopic origin in both compounds.

2.2.1 Superconductivity

Superconductivity was discovered in 1911 by H. Kamerlingh Onnes (37) where after cooling metals such as mercury, lead, or tin, it was observed that the electrical resistance dropped to zero at the critical temperature $T_{\rm C}$ indicating perfect conductivity. In 1933, a study by Meissner and Ochsenfeld revealed that superconductors show perfect diamagnetism(37). For the decades that followed, a theoretical picture to describe this phenomenon eluded scientists until 1957 when a theory proposed by Bardeen, Cooper, and Schrieffer known as the BCS theory was published(38). This theory describes the pairing of electrons through the over screening of the electron's charge by the small displacement of positively charged heavy ions toward the electron. Therefore, the electron indirectly attracts other electrons through the ionic motion, i.e. through the electron-phonon coupling. The pairs themselves are bosons and can condense into a SC state akin to superfluidity. The energy to break this attraction is $2\Delta_{\rm SC}$ where $\Delta_{\rm SC}$ is a gap in the electronic excitation spectrum at the Fermi level that develops because of the small phonon mediated attraction. Superconductors described by BCS theory are known as conventional superconductors which have a $\mathbf{Q}$ independent gap structure and are predicted to

have a maximum T_c of around 30 K(21).

In 1986, a clear problem arose with BCS theory after the discovery of superconductivity at a record T_c of 35 K in $La_{1.85}Ba_{0.15}CuO_4$ (39). Such a high T_c was difficult to reconcile with BCS theory and marked the beginning of high temperature superconductivity (HTSC). In 1987, the record rose to 93 K in $YBa_2Cu_3O_{7-y}$ (40) and because it was above the liquid nitrogen boiling point, these compounds brought the possibility of taking advantage of HTSC for technological applications. Currently, the ambient pressure record T_c is the compound $HgBa_2Ca_2Cu_3O_{1-x}$ at 135 K (41).

Cuprates have dominated the field of high temperature superconductivity until the iron arsenide high temperature superconductors were discovered in 2008 and the pairing mechanism in both high temperature superconductors (HTSC) is under debate. The leading candidate is a spin fluctuation mediated pairing. A key issue for understanding the pairing mechanism is the determination the symmetry of the superconducting order parameter Δ_{SC}. There has been extensive experimental work on the cuprates which has allowed for understanding the momentum dependence of Δ_{SC} and an understanding the pairing symmetry(42). This work is important because, even though understanding of the pairing symmetry does not specify a mechanism for high-temperature superconductivity, it does provide some constraints on possible pairing mechanisms. For example, if the Cooper pairing involves scattering to different portions of the Fermi surface where the Cooper pair wave function (or Δ_{SC} as well) has opposite sign, then a repulsive interaction such as electron-electron interaction may be appropriate. In the cuprates, there is overwhelming evidence in favor of what is known as d-wave pairing which favors repulsive interaction(42). A representation of d-wave gap structure is shown in Figure 2.5(a).

In the arsenides, a candidate for the SC order parameter involves isotropic gaps (or wave-functions) on the hole and electron bands with a phase difference between the gaps causing them to have opposite signs as is demonstrated in figure 2.5(b). This pairing symmetry is known as s+-. Confirmation of the s+- symmetry would indicate that the superconductivity is unconventional (not electron-phonon mediated) and repulsive, and potentially mediated through spin fluctuations as described in ref. (13). Still, other mechanisms such as electron-phonon

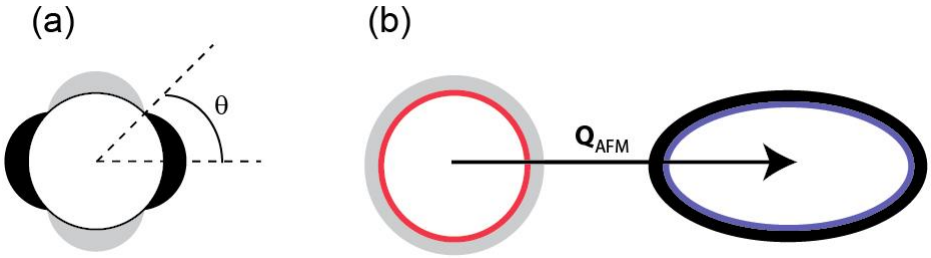

Figure 2.5 (a) The gap structure around the Fermi surface for $d_{x^2-y^2}$ pairing symmetry appropriate for describing the gap structure in copper oxide superconductors. The light grey regions represent the portion of the gap that is positive while the black portions are negative. For different directions the gap changes sign and also varies in magnitude. (b) A diagram of the multiband isotropic s+- gap structure demonstrating gaps around the electron and hole bands, which are separated by $\mathbf{Q}_{\mathrm{AFM}}$, have different sign and constant magnitude around the Fermi surface.

coupling cannot be ruled out as having some role in pairing electrons(43).

Gaining an understanding the microscopic details of high temperature superconductivity has proven to be an extremely difficult endeavor. In the iron arsenides, the proximity of both structural and magnetic phase transitions is suggestive that each may play an important role. In this thesis, the main focus is to systematically study static magnetic order as well as the magnetic excitation spectrum through doping and pressure application to understand the details of the antiferromagnetism. These studies have also indirectly allowed for further understanding of the microscopic details of superconductivity as well.

2.3 Iron pnictide and iron chalogenide family of compounds

The family of iron based superconductors can be divided into four classes of layered compounds as shown in fig. 2.6. All of the classes contain a layer composed of a square lattice of iron atoms with layers either a chalogen (Ch) atom (such as Se or Te) or a pnictogen (Pn) atom (such as P or As) above and below the iron containing layer as shown in the left panel of fig 2.6.

As discussed above, the first class includes RFeAsO compounds where R refers to a rare earth element and the chemical formula for these compounds are abbreviated as (1111) because

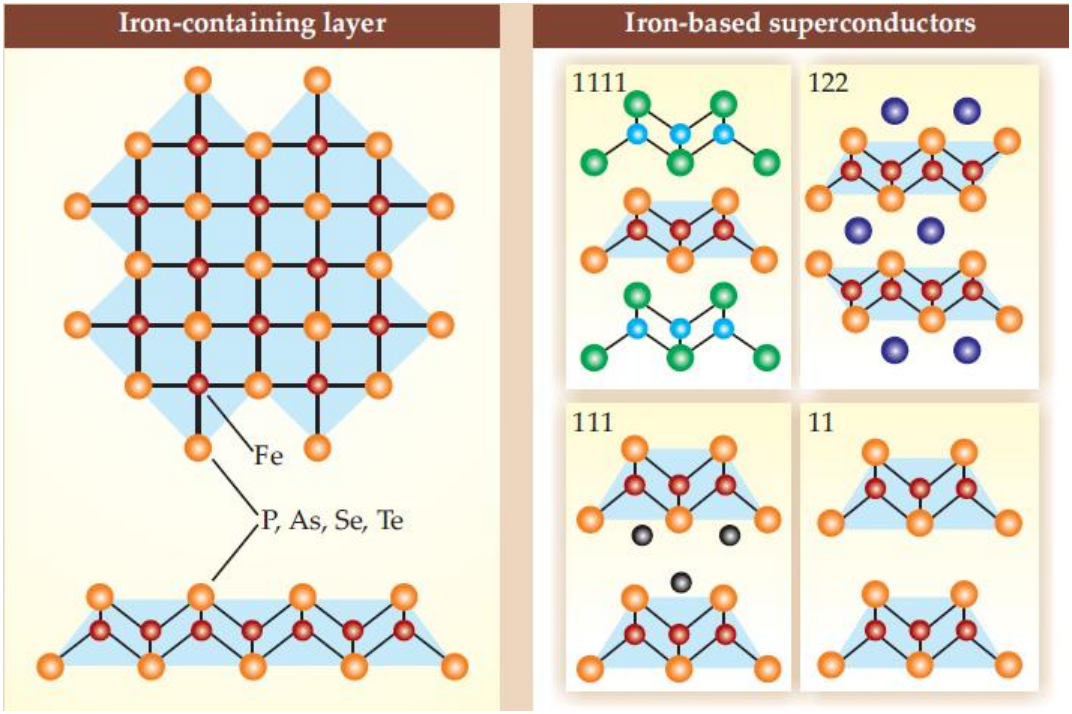

Figure 2.6 The iron containing layer in iron based superconductors along with a summary of the classes of compounds that have been discovered since the beginning of this field in 2006. (from ref (44)) In the figure the atoms (and colors) are Fe(red), chalogen or pnictogen(orange), rare earth atom (green), alkaline earth atom (dark blue), and alkali metal (grey)

there are four single elements in the chemical formula. These compounds consist of alternating iron containing layers FePn and R-O layers. Variations of (1111) systems include electron doping by rare earth elemental substitution such as $Sm_{1-x}Th_xFeAsO$ (45), or F replacement of oxygen as in $SmFeAsO_{1-x}F_x$ (46). The next class are the (122) superconductors with chemical formula $AeFe_2As_2$ (where Ae refers to an alkaline earth element), with an Fe-As layer and layers consisting of only Ae atoms. Doped (122) have been synthesized by substitution of alkaline earth elements with potassium(47), and an extensive exploration of iron substitution by other transition metal (Tm) elements. The compounds $Ba(Fe_{1-x}Tm_x)_2As_2$ with Tm = (Co, Ni, Cu, Pd, and Rh) are discussed in ref (48). A third class is the (111) superconductors (including compounds such as LiFeAs(49), NaFeAs(50), and LiFeP(51)) which have an alkali metal layer separating the Fe-As layers. The fourth class referred to as (11)s shown in Fig. 2.6 includes only FeCh layers. Examples of the (11)s are $Fe_{1+y}Ch$ such as $Fe_{1+y}Se_{1+x}Te_x$.(24)

There is slight variation of the crystal structure across these compounds. The (1111) and the (122) phase diagrams show a transition from a high temperature tetragonal structure to a low temperature orthorhombic. The (111) and undoped (11) do not have a structural transition but doped (11) such as $Fe_{1+y}Te_{1-x}Se_x$ can be orthorhombic or monoclinic at low temperatures depending on the chemical makeup (52). The high and low temperature crystal structures for representative compounds are shown in Table 2.1.

Table 2.1 Representative crystal symmetries

Compound (reference)	High temperature symmetry	Low temperature symmetry
$BaFe_2As_2$(53)	I4/mmm	Fmmm
LaFeAsO(23)	P4/nmm	Cmma
$Fe_{1+y}Te_{1-x}Se_x$(52)	P4/nmm	P4/nmm,Pmmn,$P2_1$m
LiFeAs(54)	P4/nmm	P4/nmm

A comparison of the electronic properties such as carrier concentration, magnetism, band structure can provide an additional idea of the similarities and differences in the various compounds. In the following I will compare some characteristic compounds within each family.

As discussed earlier, to classify a compound as a semimetal, the Fermi surface must include an electron and hole band where the electron band is nearly filled and the hole band is nearly empty. As discussed in ref (24), the appropriate measurement to confirm semi-metallic behavior are Hall resistance or thermelectric power but these measurements have been inconclusive which is typical of studies of multiband conductors(24). The band structure calculations have predicted carrier concentrations between around 0.2-2.5 $\times 10^{21}$ cm^{-3} which can be compared to copper metal with 85 $\times 10^{21}$ cm^{-3}(55). This is not proof that these compounds are semimetallic but when considering the multibands predicted from band structure calculations, the ARPES results which demonstrate the presence of hole and electron bands near the Fermi level, together with the small carrier concentrations, there exists sufficient evidence to categorized these compounds as semimetals.

Because of the small ordered moments (Table 2.2) observed in these compounds, an itinerant picture is a good starting point for describing the long range magnetic order. The undoped (122), (1111), and (11) have a similar nested band structure so one would expect spin density

wave order to be an appropriate description for all these compounds (24). For the case of stoichiometric LiFeAs, ARPES measurements claim an absence of Fermi surface nesting (56) and also refer to the observed absence of magnetic order in this compound based on μSR measurements(57). An understanding of the (11) band structure would lead one to expect the propagation vector to be identical to what is observed in (122), (1111)(58), but instead it is rotated 45 degrees to $\mathbf{Q}_{\mathrm{AFM}} = (\frac{\pi}{a},0)$ and the mechanism for AFM is not well understood. It was shown in ref (52) that the compound $Fe_{1+y}Te$ has a tunable incommensurate propagation vector $\mathbf{Q}_{\mathrm{AFM}} = (\delta\ 0)$ which depends on the excess iron. Also, the large moment observed in Table 2.2 for $Fe_{1.05}Te$ may be an indicator that local moment magnetism may also play a role in this compound.

Table 2.2 Representative Fe-moment value

Compound (reference)	Measured Moment (μ_{B})
$BaFe_2As_2$ (23)	0.87
LaFeAsO(59)	0.4
$Fe_{1.05}Te$(60)	2.54
LiFeAs(61)	0

Finally, all of these compounds show superconductivity where as mentioned earlier the highest T_{c} is observed through doping (1111) compounds. Table 2.3 (which was taken from ref. (24)) lists some observed T_{c}s in these materials at ambient pressure.

This comparison suggests a clear connection between the (1111), (111), and (122) compounds but the (11) compounds stand out a bit because of the large moment and unique magnetic structure. What is in common amongst all these compounds is the low electrical conductivity along with band structure that suggests they are semi metals, nesting appears important for static AFM order, and superconductivity is observed through doping and pressure application.

It has been a challenge for theorists to capture all of the details of experimental doping phase diagrams as doping simultaneously changes the number of charge carriers, induces steric effects, and introduces disorder. As will be discussed in chapter 5, there has been success in understanding the 122 diagram in a rigid band model and explaining how electron and hole

Table 2.3 List of critical temperatures

Compound (reference)	T_c (K)
$LaFeAsO_{0.89}F_{0.11}$(20)	26
$SmFeAsO_{1-x}F_x$(3)	55
$Ba_{0.6}K_{0.4}Fe_2As_2$(47)	38
KFe_2As_2(62)	3.8
LiFeAs(49)	18
$Fe_{1.03}Te_{0.43}Se_{0.57}$ (63)	13.9

doping changes the ordered moment. Alternatively, studies involving pressure application have also made important contributions to the field because it has been shown experimentally the application of pressure can also suppress AFM order in a similar manner to doping(64) with the benefit that pressure application avoids the complication of doping induced chemical disorder. Both doping and pressure effects are explored in this work.

2.4 Characterization of the 122 superconductors

This thesis focuses on studies of the structure and magnetism of the (122) systems in part because of the availability of high quality and large single crystal samples which have been synthesized at the Ames Laboratory. Because of the similarities amongst these compounds, studies on the (122) compounds can potentially provide some general understanding of the entire family of compounds. The samples studied in the work were grown using a solution growth technique (9). Single crystal growth of the iron arsenide compounds result in plate like crystals with typical dimensions which are commonly several millimeters in length and with a thickness less than a millimeter. A typical mass for a sample used in a neutron scattering experiment is around 100 mg. In rare cases, the samples can grow to approximately a centimeter in length, which is limited diameter of the solution container, and have masses close to 1 gram. The specific compounds studied were $CaFe_2As_2$ and a series of compounds $Ba(Fe_{1-x}Co_x)_2As_2$ with $x = 0$ to 0.063.

2.4.1 Crystal structure

As is summarized in chapter 3, the pattern of Bragg scattering intensity that occurs from elastic scattering of x-rays or neutrons can provide information about the arrangements of the atoms in the repeating unit cell which comprises the crystal lattice. For example, one can easily see how information from scattering experiments can provide information about a unit cell's lattice parameters through the use of Bragg's Law ($n\lambda = \frac{4\pi}{\mathbf{G}_{h,k,l}} \sin\theta$) where n is an integer, λ is the wavelength of incident wave, and θ is the angle between the incident ray and the scattering planes. In this formula, $\mathbf{G}_{h,k,l} = \frac{2\pi h}{a}\hat{x} + \frac{2\pi k}{b}\hat{y} + \frac{2\pi l}{c}\hat{z}$ is the reciprocal lattice vector for an orthogonal system ($\alpha = \beta = \gamma = 90°$) where the integers h, k, and l are the Miller indices and the crystal unit cell has length of a along the **x**-direction, b along the **y**-direction, and c along the **z**-direction. The set of reciprocal lattice vectors correspond to the Fourier transform of the set of direct lattice vectors defining the crystal lattice

Several scattering studies (104; 23; 92) showed that the observed discontinuities in resistivity, magnetization, and heat capacity at temperature T_S correspond to a transition from a tetragonal unit cell as shown in Fig. 2.7 (where tetragonal refers to an orthogonal unit cell where $a = b \neq c$)to an orthorhombic structure shown in Fig. 2.8 (or an orthogonal unit cell where $a \neq b \neq c$).

Above the structural transition T_S, the $AeFe_2As_2$ compounds adopt the $ThCr_2Si_2$-type crystal structure which is described by the body centered tetragonal space group I4/mmm. Below T_S the crystal structure is described by the face centered orthorhombic space group Fmmm. Fig. 2.8 shows the larger orthorhombic cell with the lattice parameters $a_O = \sqrt{2}a_T + \delta$ and $b_O = \sqrt{2}a_T - \delta$ (where δ refers to the orthorhombic distortion of the tetragonal lattice) and is rotated 45° relative to the original tetragonal lattice directions.

Throughout this thesis, crystal planes will be indexed using both the tetragonal and orthorhombic unit cell. The relationship between these structures and the indexing of reciprocal space should be explained. This can be done with the assistance of Figure 2.9. A projection of the **a**-**b** plane of the crystal lattice from Figs. 2.7 and 2.8, is shown in Fig, 2.9(a) which for both systems is a square lattice in the absence of orthorhombic distortion δ of the

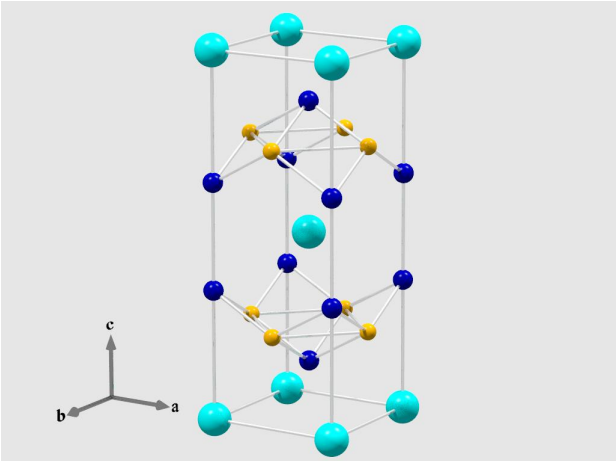

Figure 2.7 The tetragonal unit cell for the 122 system. The light cyan spheres represent the alkaline earth atom, the orange spheres represent Fe atoms, and the dark blue spheres represent the As atoms

O-phase. The smaller tetragonal square base is shown as a dashed red line while the larger orthorhombic base, ignoring orthorhombic distortion, is shown as a solid blue line. Note the 45° rotation between crystal systems and the enlarged lattice parameters of the orthorhombic cell noted earlier. The corresponding reciprocal lattice is shown in fig. 2.9(b). The region of the reciprocal lattice associated the base of the tetragonal unit cell is bounded by the dashed brown line and the boundary associated with the orthorhombic unit cell base is the solid blue line. Figure 2.9(b) also demonstrates the relationship between the two reciprocal lattices. The Miller indices for each reciprocal lattice vector are labeled. The brown Miller indices are for the tetragonal reciprocal lattice and the blue indices are for the orthorhombic reciprocal lattice. The conversion of Miller indices between crystal systems can be done with equation 2.1.

$$\begin{aligned} h_{\mathrm{O}} &= h_{\mathrm{T}} + k_{\mathrm{T}} \\ k_{\mathrm{O}} &= k_{\mathrm{T}} - h_{\mathrm{T}} \\ l_{\mathrm{O}} &= l_{\mathrm{T}} \end{aligned} \tag{2.1}$$

Systematic absences of Bragg scattering will occur for both crystal systems due to body-centered tetragonal and face centered orthorhombic space groups. In figure 2.9(b), the filled circles are positions in the reciprocal lattice where Bragg scattering will occur and open circles denote reciprocal lattice points where scattering is absent. For I4/mmm, the general require-

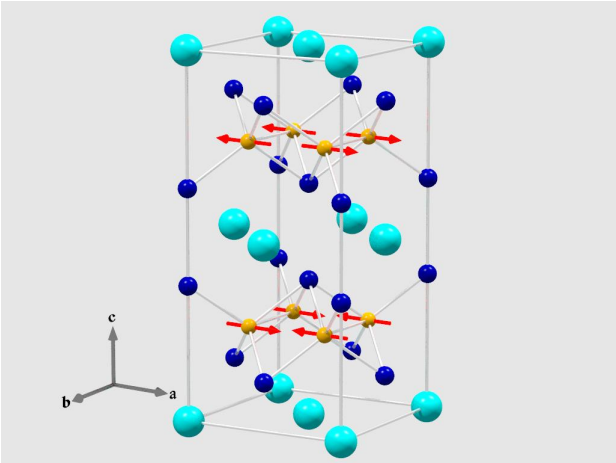

Figure 2.8 The orthorhombic unit cell for the 122 system. The light cyan spheres represent the alkaline earth atom, the orange spheres represent Fe atoms, and the dark blue spheres represent the As atoms. The antiferromagnetic Fe spin structure is represented by the pattern of red arrows.

ment for the observation of Bragg scattering is that the Miller indices obey the condition for body-centered lattices $h_T + k_T + l_T = 2n$ where n is an integer and for face centered Fmmm the general requirement is that $h_O + k_O = 2n$, $h_O + l_O = 2n$, and $k_O + l_O = 2n$ are simultaneously met (or that indices are all even or all odd). As an alternative, from this point on, the reflections for the (122) tetragonal system will be indexed $(h\ k\ l)_T$ and the orthorhombic reflections will be labeled $(h\ k\ l)_O$

2.4.2 Magnetic structure

It was shown in references (23) and (92), when $CaFe_2As_2$ is cooled below 170 K, antiferromagnetic ordering is observed. The magnetic moment of the iron atoms point along the $\mathbf{a}_O$-direction and form ferromagnetic spin stripes along the orthorhombic $\mathbf{b}_O$-direction which are antiferromagnetically coupled (or anti-aligned) along the $\mathbf{a}_O$ and $\mathbf{c}_O$-directions. This is represented by the pattern of spins shown in Fig. 2.8. As is discussed in chapter 3, because the neutron interacts with the electronic magnetic moment through a dipole-dipole interaction, a periodic pattern of electronic spins (i.e. the magnetic structure) can be found through neutron scattering experiments. As is demonstrated in chapters 4 and 5, magnetic Bragg scattering in $AeFe_2As_2$ appears with propagation vector $(\frac{h}{2}\ \frac{k}{2}\ l)_T$ where h, k, and l are odd integers or

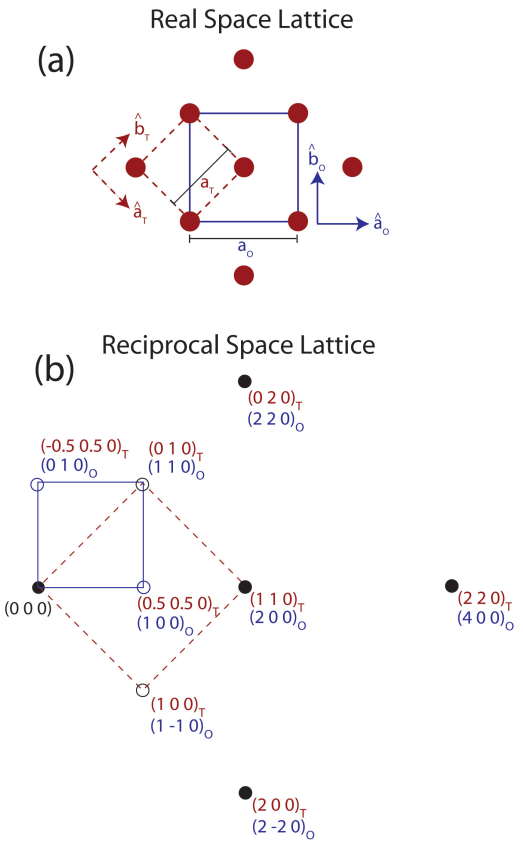

Figure 2.9 (a) The simple square lattice that makes up the base of the tetragonal unit cell is bounded by the dashed brown line along with the base of the orthorhombic cell (in the absence of orthorhombic distortion) bounded by the solid blue line. The directions in the **a**-**b** plane are labeled along with the lattice parameter. This figure is a reproduction of figure 7 from ref (24) (b) The reciprocal lattice associated with the square the crystal lattice shown in (a). The filled circles represent allowed Bragg reflections.

$(h\ 0\ l)_{\mathrm{O}}$ where h and l are odd integers. Therefore an antiferromagnetic or Néel transition also occurs at $\mathrm{T_N}$. The fact that $T_{\mathrm{S}} = T_{\mathrm{N}}$ in the undoped compound indicates an intimate connection between structure and magnetism and the observed orthorhombic distortion.

2.4.3 Studies of the *p*-*T* phase diagram of $CaFe_2As_2$

It was demonstrated in section 2.2 that doping the iron pnictide compounds suppresses the structural and magnetic transitions, and after sufficient suppression, superconductivity appears. As I will discuss in this section, pressure application has also proven to suppress

the structural and magnetic transitions and potentially induce superconductivity without the induced disorder and steric effects associated with doping. However, it became clear is that pressurizing $CaFe_2As_2$ in particular was problematic because of a new phase that exists at modest pressures which has proven to be disruptive to superconductivity.

Initial characterization measurements, including resistivity and magnetization taken on single crystal samples of the parent compound $CaFe_2As_2$ (9), are shown in Figs. 2.10 and 2.11. These figures reveal some important characteristics of the (122) compounds. The resistivity values increase with increasing temperature which is metallic behavior. The most striking feature in the resistivity and magnetization data is the discontinuity observed at $T \approx 170$ K. This sharp feature is consistent with a first order phase transition as evidenced by the observed hysteresis. Magnetization measurements in Figure 2.11 shows there is a magnetic character to the transition, but at the time when this measurement was made, the microscopic details of the low temperature magnetic order were not verified. The lack of understanding of the crystalline and magnetic structure provided the motivation for scattering measurements. Neutron and x-ray scattering measurements revealed that this transition was from the high temperature tetragonal (T) and paramagnetic state to a low temperature orthorhombic (O) and antiferromagentic (AFM) state.(65)

Figure 2.12 shows a series of resistivity measurements performed under applied pressure. Pressure application was performed using a Be-Cu clamp cell with a fluorocarbon-based fluid known as Florinert FC-75 used as a pressure medium as described in ref (4). Pressure ranges explored in this study ranged from ambient pressure to 19.3 kbar.

Some important observations can be made from figure 2.12. First, the resistive anomalies observed in figure 2.12, which are highlighted by the black arrows, are an indication that the dual first order structural / magnetic phase transition is suppressed with pressure. Signatures of superconductivity appear after the suppression of dual structural and magnetic transition. At high pressure, a new feature appears in the data associated with a drop in resistivity as highlighted by the red arrows. This is associated with a transition to a new unidentified phase. From warming and cooling through these transitions, it was apparent that this new phase transition was extremely hysteretic with offsets as high as 30 K(4). Lastly, it is important to

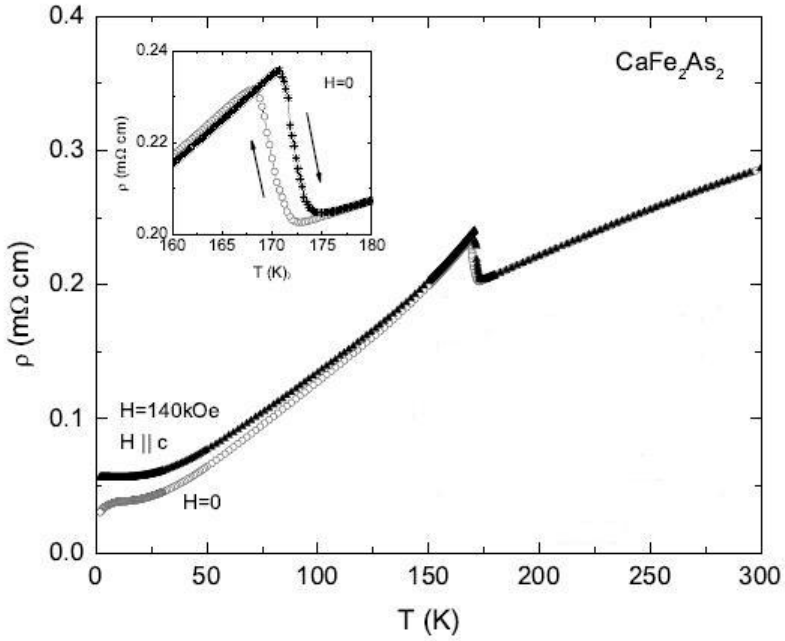

Figure 2.10 The temperature dependent resistivity of $CaFe_2As_2$ with $\mathbf{H} \parallel \mathbf{c}$ with $H = 0$ (open circles) and $H = 140$ Oe (filled triangles). The inset demonstrates the hysteresis in temperature around 170 K. (from ref (9))

note that the data in Figure 2.12 is not offset. The observation that for a given temperature, the resistivity drops monotonically with pressure and neutron scattering measurements revealed that this is associated with the loss of magnetism.

A phase diagram was constructed based on the anomalies in resistivity and is shown in figure 2.13. The black dots represent the break in the slope at the temperature of the resistivity upturn while the red dots indicate the positions of maximum slope magnitude at the resistance drop observed at high pressure. The green dots represent the onset superconductivity with a maximum at 12 K and 5 kbar(4). Zero resistance is observed at 3.5, 5.1, and 5.5 kbar. The onset of superconductivity was observed at 2.3 and 8.6 kbar and the superconducting dome is shown to only exist between these two extremes. The drop in resistivity at 15 K with pressure is shown by the blue stars. This figure demonstrates this loss of resistance can be associated with the establishment of the high pressure phase. Questions into the nature of this high pressure phase motivated a neutron scattering measurement to gain an understanding of the

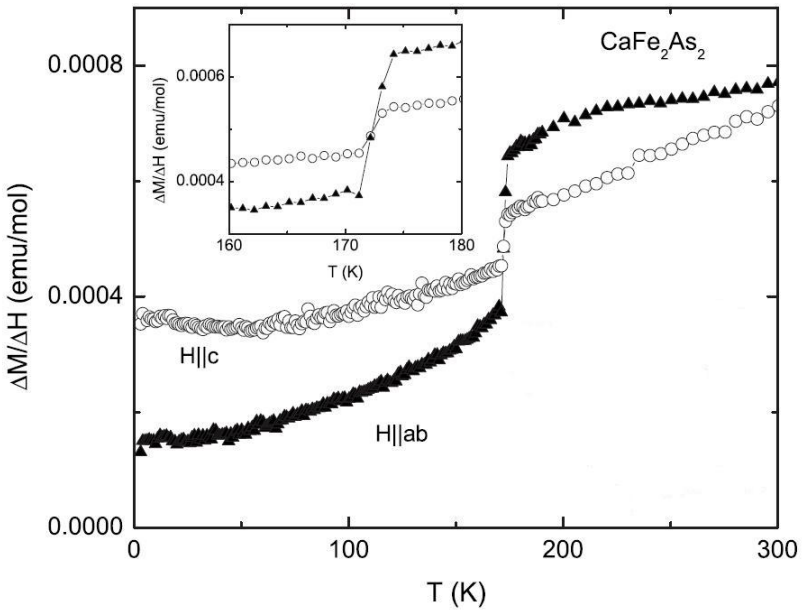

Figure 2.11 Temperature dependent magnetic susceptibility of $CaFe_2As_2$ for applied field parallel to the **a-b** plane (filled triangles) and applied field parallel to the **c** axis. This inset highlights the transition region. (from ref (9)))

crystallographic and magnetic properties of the new phase.

Neutron scattering measurements which employed He gas to pressurize the sample were performed at the NIST Center for Neutron Research(5). The experiment involved the measurement of collection of $\approx$ 500 randomly oriented small single crystals ($\approx$ 1-2 mm in length and less that 0.5 mm in thickness). Preferred orientation was dealt with in part by the rotation of the crystal assembly by 36 degrees during each measurement. Figure 2.14 shows some important results. The figure shows the behavior of the (002) structural peak and the $(121)_O$ magnetic peak upon pressurizing from ambient pressure to 0.63 GPa (6.3 kbar) at $T = 50$ K. The increase in the scattering angle of the (002) peak is a signature of the 9.5% reduction of the c-lattice parameter. Also, an approximately 2% expansion of the in-plane lattice parameters was observed at high pressures. Overall, a volume reduction of 5% is observed. The new high pressure phase has the same I4/mmm structure as the ambient pressure phase but with different lattice parameters. In sum, a collapsed tetragonal (cT) phase was discovered. The volume collapse transition is not unique to $CaFe_2As_2$ but is observed in other compounds which crystallize in the $ThCr_2Si_2$ structure(8). The conditions for a transition to a cT phase

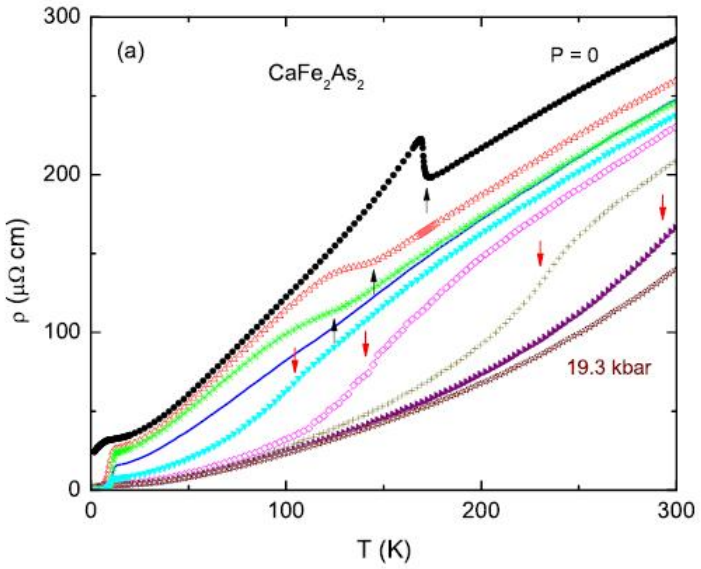

Figure 2.12 The in plane, electrical resistivity of $CaFe_2As_2$ as a function of pressure for p = 0, 2.3, 3.5, 5.1, 5.5, 8.6, 12.7, 16.8, and 19.3 kbar. The downward and upward arrows indicate transition temperatures.(4)

is determined by a competition between the rare earth cation packing, the As-As bonding energy, and the Coulomb or Madelung energy between ionic Ca^{2+} and $(Fe_2As_2)^{2-}$ layers.(66) An important factor for realizing the cT phase in $CaFe_2As_2$ is the size of the relatively small Ca^{2+} cations(64).

The inset of Figure 2.14 demonstrates that stripe AFM order disappears in the cT phase. Spin-polarized total energy calculations from ref (5) predicted a non magnetic state for the observed c/a ratio in the cT phase and provided an explanation for the loss of long range magnetic order. As will be discussed in chapter 5, additional magnetic structures proposed by Yildrim et al. (67) for the cT phase were not found, providing further evidence that the cT phase does not host long range magnetic order.

As is further described in chapter 4, a phase diagram contradicting figure 2.13 was published by H. Lee *et al.* (7) which showed superconductivity existing up to 15 kbar and where the high pressure cT phase was claimed to appear at approximately 2.5 kbar. This study employed a clamp cell with a fluid silicone pressure medium. What was clear after this work was that due to the extreme sensitivity of $CaFe_2As_2$ to applied pressure, the solidifying pressure medium was

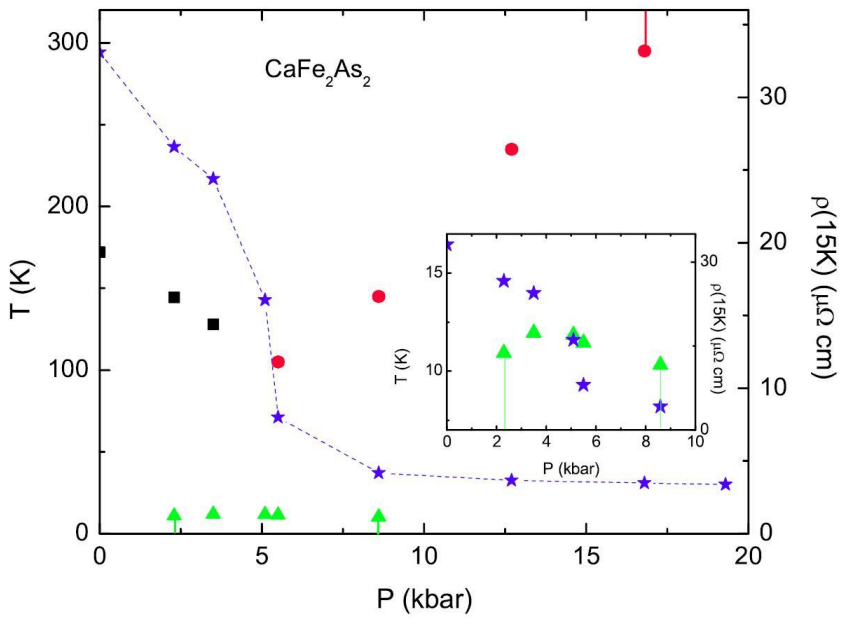

Figure 2.13 p-T phase diagram for $CaFe_2As_2$ from ref. (4) determined from resistivity measurements

freezing around the samples, placing the material in a complex pressure environment. These complicated medium specific pressure gradients can explain the conflicting phase diagrams especially when considering that a typical pour point for the medium discussed is approximately 150 K at ambient pressures, placing the samples in frozen medium for the majority of the p-T phase diagram.

He gas provides a truly hydrostatic environment for a large range of pressures (except when it freezes at 1.2 K at ambient pressure and up to 50 K at 0.7 GPa) and when the resistivity measurements were performed using He gas, it was found that the cT phase did not host superconductivity. This is demonstrated in figure 2.15(a) and (b), which was taken from ref (68). From these measurements it can be seen that the T-O transition consistently remained sharp. For pressures greater than 0.4 GPa, a sharp and hysteretic transition is observed which is associated with the transition. Finally, as seen in figure 2.15(b), superconductivity is absent when hydrostatic pressure is used. Chapter 4 discusses the scattering measurements that also employed a He pressure cell, which have shed light on the microscopic details of these phases observed in the p-T phase diagram.

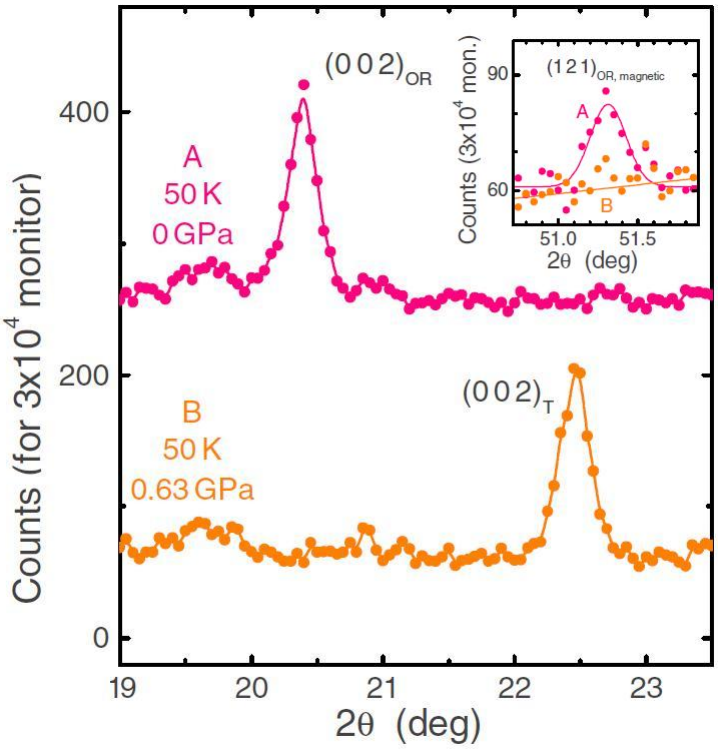

Figure 2.14 The change in scattering angle of the (002) peak as the pressure was changed from ambient pressure to 0.6 GPa at 50 K. The inset demonstrates the loss of magnetic order(5)

2.4.4 Cobalt doping of $BaFe_2As_2$

Another major focus of our studies is the phase diagram of electron doped $Ba(Fe_{1-x}Co_x)_2As_2$. Figure 2.16(48) shows a stack plot of some of the initial characterization measurements of $BaFe_2As_2$. It displays in-plane resisistivity, magnetization for fields applied in the **a**-**b** plane as well as along the **c**-direction, and heat capacity as a function of temperature. This demonstrates the first order T-O and AFM phase transition at 130 K and there is a clear magnetic signature to this transition as seen in the magnetization in the center panel figure 2.15.

Systematic study of these characterization measurements was performed for $Ba(Fe_{1-x}Co_x)_2As_2$(69). The resistivity measurements from this study are shown in figure 2.17 (69) for compounds with doping levels ranging from $x = 0$ to 0.114. As the doping level is increased, the sharp feature is broadened and suppressed in temperature and is not observable at or above $x = 0.058$. The inset provides a clear picture of the developed superconductivity for compounds above $x =$

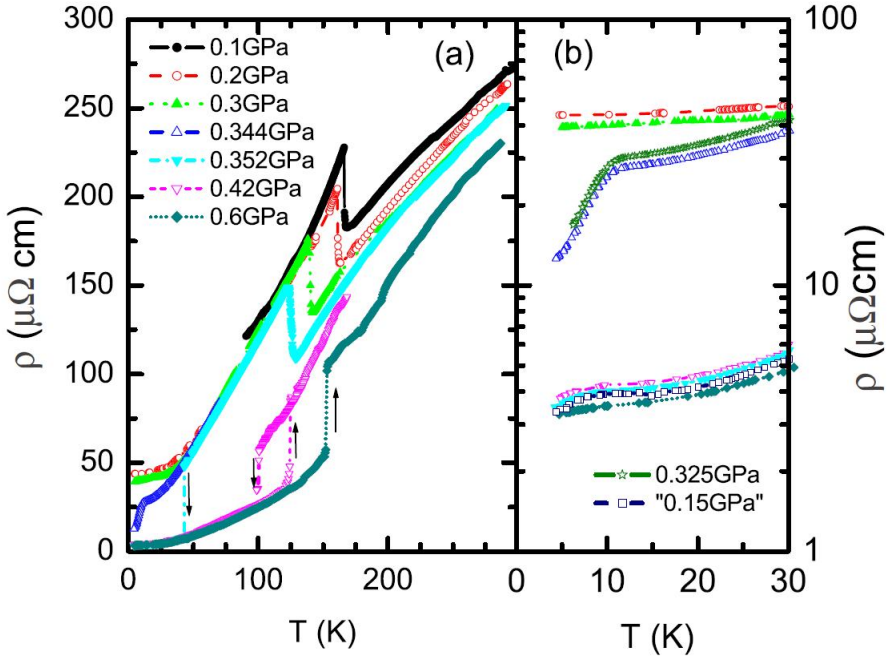

Figure 2.15 (a) and (b)Resistivity measurements on $CaFe_2As_2$ as a function of temperature and hydrostatic pressure.(68)

0.038.

Corresponding anomalies were also observed in heat capacity and magnetization. Through differentiating of the resistivity, magnetization and heat capacity data from all compositions with respect to temperature, Ni Ni *et al.*(69) observed the first evidence that the dual structural and magnetic transition was split into two transitions. An example of this is shown in figure 2.18 for $Ba(Fe_{1-x}Co_x)_2As_2$, with $x = 0.038$, which covers a temperature range that captures the broad feature in resistivity shown in figure 2.17 just before the sample becomes superconducting. There are two prominent features in each of the data sets. From this data alone, it was not clear if these features were due to a spread in composition where both features are related to a dual structural/magnetic phase transition for different compositions, or, if a single composition had two transitions.

Combined neutron and x-ray scattering measurements described in chapter 5 revealed that the dual transition observed in the parent compound did split. A phase diagram was constructed based on the observations from characterization measurements and scattering mea-

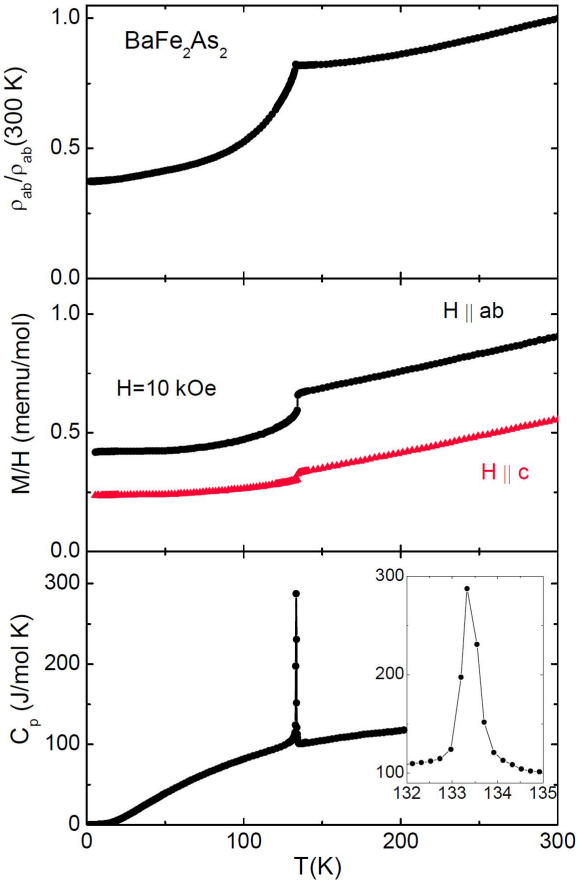

Figure 2.16 In-plane resisitivity (top), magnetization for fields applied in-plane and along **c** (middle), and heat capacity measurements on the compound $BaFe_2As_2$ (taken from ref (48))

surements. Our current understanding of the phase diagram for $Ba(Fe_{1-x}Co_x)_2As_2$ with x as high as 0.16 is shown in figure 2.19.

An interesting feature of the phase diagram is the coexistence of SC and AFM (indicated by purple shaded region in figure 2.19 but it was not clear if the coexistence was homogeneous or heterogeneous. The measurements discussed up to this point could not definitively answer this question. Experimental techniques such as NMR(11) and μSR(12), which allows investigation of the local environments around specific atoms in a crystal, provided some important clues. NMR measurements on a Co doped sample ($x = 0.05$) showed that the paramagnetic signal in a superconducting sample was completely lost indicating the full volume was magnetically

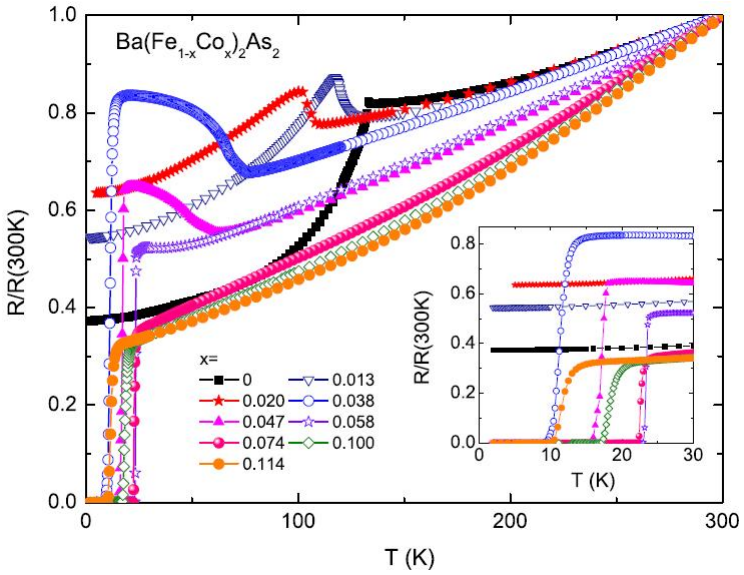

Figure 2.17 Electrical resistivity of $Ba(Fe_{1-x}Co_x)_2As_2$ single crystals normalized to their room temperature value. The inset highlights the low temperature behavior.(69)]

ordered. μSR measurements on a Co doped sample ($x = 0.06$) provide an indication of the magnetic field distribution inside the sample. This distribution proved to be very narrow showing that all of the muon sites throughout the entire sample experience similar magnetic fields. Together with the susceptibility measurements during both experiments which indicated a 100% superconducting volume fraction, these results provide compelling evidence for homogeneous co-existence of SC and long range AFM order. Neutron scattering measurements discussed in chapter 5 investigated the microscopic details in this region of the x-T phase diagram where homogenous co-existence occurs.

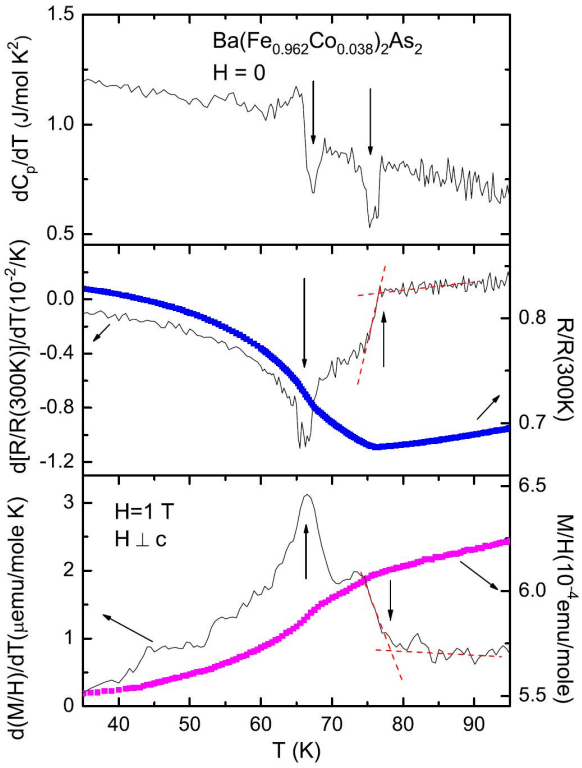

Figure 2.18 The temperature derivative of the heat capacity (top panel), the room temperature normalized resistivity (blue) along with its derivative (middle panel) and the magnetic susceptibility for a field along c (magenta) along with its temperature derivative (bottom panel) for the compound $Ba(Fe_{1-x}Co_x)_2As_2$ with $x = 0.038$ [taken from ref (69)]

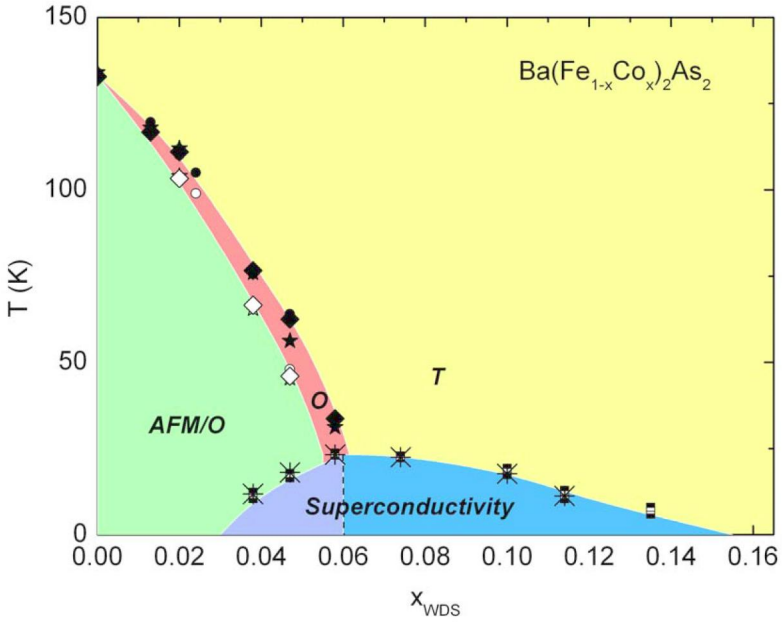

Figure 2.19 The x-T phase diagram. The solid symbols represent the T-O transition. The open symbols represent the transition the AFM ordered state. The half filled squares and asterisks represent the superconducting transitions.(48)

CHAPTER 3. Discussion of analysis and experimental methods

3.1 Introduction

Neutron scattering has proven to be an extremely important tool for the study of condensed matter due to the various phenomenon that can be easily probed including long range chemical and magnetic order in solids and associated excitations such as phonons (vibrational excitations) and magnons (magnetic excitations). This chapter discusses the basic theoretical description of neutron scattering cross sections from static order as well as excitations. There are several references (70; 71; 72) which thoroughly cover these derivations, so the reader is urged to read these references if more detail is needed.

3.2 Nuclear scattering

3.2.1 Scattering cross section

In general, the neutron scattering cross section is measure of how, and with what strength, the neutron interacts with a collection of atoms in the scattering system. The cross section is represented by the symbol σ. During an experiment, only a small portion of σ is measured due to the limited size of the detector or small solid angle ($d\Omega$) actually covered. Additionally, various scattering processes may involve no energy transfer (elastic processes) or may involve some finite energy transfer (inelastic processes). The experimenter can select which process is studied by defining an energy window represented by the differential dE. In sum, a measurement during a scattering experiment is related to the partial differential cross section shown in equation (3.1). Fig. 3.1 shows the geometry of a scattering experiment using spherical polar coordinates. (70)

$$\frac{d^2\sigma}{d\Omega dE} = (\text{number of neutrons scattered per second into a small solid angle d}\Omega \text{ in the direction } \theta, \phi \text{ with final energy between } E \text{ and } E + dE)/\Phi d\Omega dE \tag{3.1}$$

In equation (3.1), Φ is the flux of incident neutrons with units of neutron number per area per second. Through unit analysis it can be seen that the unit of a cross section is an area. The total cross section σ can be found by the measuring the number of neutrons scattered per second for a given flux for all scattering processes and at all angles or over a solid angle of 4π.

As is discussed in the next section, the nuclear cross section can be expressed in terms of a scattering length 'b' as shown in equation (3.2) which typically have units of femtometers (fm) which results in a cross section represented by an area.

$$\sigma = 4\pi b^2 \tag{3.2}$$

This expression can be understood by considering the simple case of a neutron being scattered by a fixed nucleus. The range of the nuclear force is 10^{-15} meters and the chosen de Broglie wavelength for neutrons used to probe condensed matter is near the interatomic spacing which is around 10^{-10} meters. In this case we are probing distances much greater than the range of the strong nuclear force and therefore the observed scattering will be spherically symmetric. The incoming and outgoing wave functions are shown in equation (3.3)

$$\begin{aligned} \Psi_{\text{in}} &= e^{ikz} \\ \Psi_{\text{out}} &= \frac{be^{ikr}}{r} \end{aligned} \tag{3.3}$$

If the scattering is elastic, the incoming and outgoing neutron velocities (v) are unchanged. The scattered neutron current (neutrons/second) passing through the small area dA is $vdA\left|\Psi_{\text{out}}\right|^2$. Using the spherically symmetric Ψ_{out}, the outgoing or scattered neutron current is $\frac{vdAb^2}{r^2}$ or $vb^2d\Omega$. The incoming flux (Φ) is $v\left|\Psi_{\text{in}}\right|^2$ which can be simplified to v neutrons per unit area

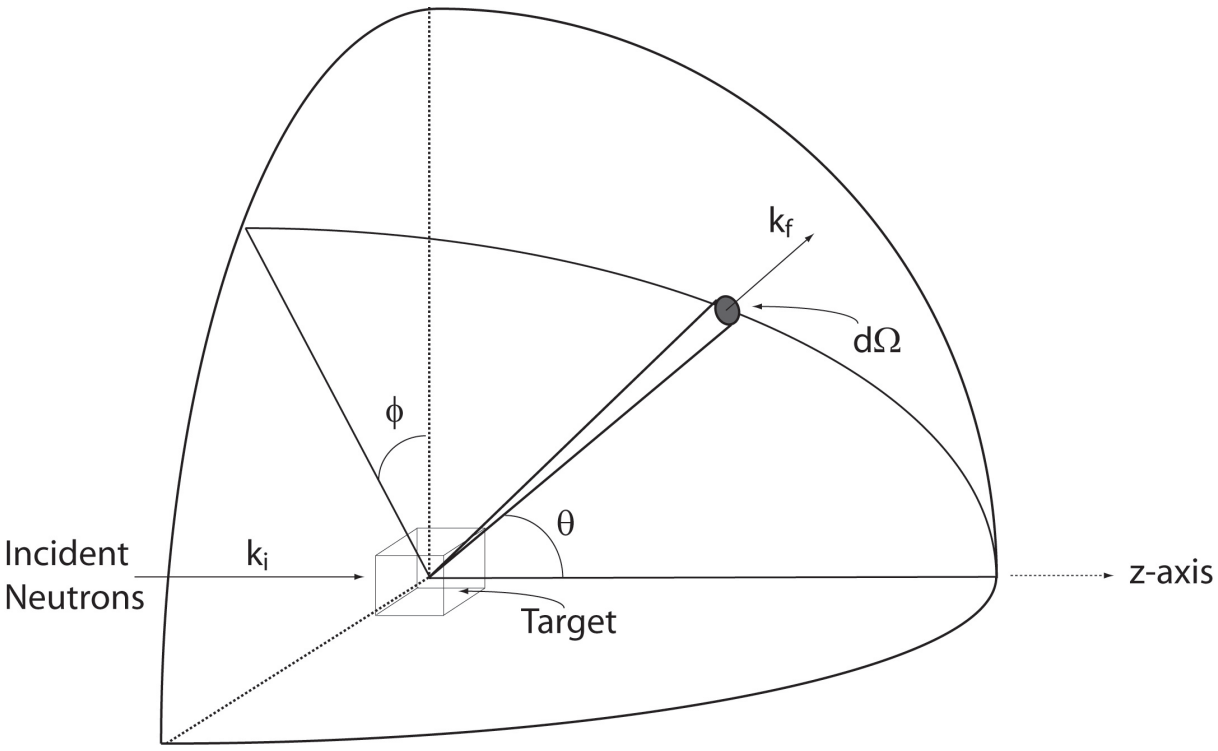

Figure 3.1 Geometry for Scattering Experiment. (reproduction from ref (70))

per second. If the energy is not analyzed, the differential cross section shown in equation shown in equation (3.1) can be simplified as shown in equation (3.4).

$$\frac{d\sigma}{d\Omega} = (\text{neutron current in the direction of } \theta, \phi) \ / \Phi d\Omega \tag{3.4}$$

Plugging in the outgoing neutron current and flux into equation (3.4) yields

$$\begin{aligned} \frac{d\sigma}{d\Omega} &= \frac{vb^2 d\Omega}{v d\Omega} \\ &= b^2 \end{aligned} \tag{3.5}$$

When integrated over solid angle equation (3.2) is derived.

The physical interpretation of the scattering length (equation (3.6)) is that 'b' indicates strength and nature of the interaction of the neutron with a nucleus. The scattering length can be approximated through calculations of the stability of a compound nucleus composed of the original nucleus with an additional neutron. Due to the fact that there exists an absence of a fundamental understanding of the nuclear force, there has been great difficulties in understanding the structure and stability of a nucleus. But, simple models such as the shell model which mirrors atomic physics has been developed and can account for many properties nuclear matter. If, for example, the nucleus has a number of nucleons that fills the nuclear shell, the addition of another nucleon will create an unstable nucleus and the neutron may be quickly re-emitted. This process is connected with α in equation (3.6).

$$b = \alpha + i\beta \tag{3.6}$$

On the other hand if the additional neutron fills a nuclear shell, the neutron will likely be absorbed which will be indicated by a large β and connected to a large probability of absorption.

3.2.2 Expressing $\frac{d^2\sigma}{d\Omega dE}$ for nuclear scattering

Symbolically, we can represent the energy integrated differential cross section $\frac{d\sigma}{d\Omega}$ which transitions from an initial state labeled λ to a final state λ' as equation (3.7)

$$(\frac{d\sigma}{d\Omega})_{\lambda\to\lambda'} = \frac{1}{\Phi}\frac{1}{d\Omega}\sum_{\substack{k' \\ \text{in d}\Omega}} W_{k,\lambda\to k'\lambda'} \tag{3.7}$$

This equation represents the sum of all processes which transition the system from state λ to λ'. In this equation the neutron state changes from $\mathbf{k}$ which is set by the experiment to $\mathbf{k}'$. The term $W_{k,\lambda\to k'\lambda'}$ represents the number of transitions the compound system undergoes per second or in other words, as in equation (3.4), the number of scattered neutrons from the sum of general scattering processes. Due to the fact that the neutrons are only weakly perturbing the system, Fermi's Golden Rule can be used such that the sum in equation (3.7) is replaced using the relation shown in equation (3.8).

$$\sum_{\substack{k' \\ \text{in d}\Omega}} W_{k,\lambda\to k'\lambda'} = \frac{2\pi}{\hbar}\rho_{k'}\left|\langle k'\lambda'\left|V\right|k\lambda\rangle\right|^2 \tag{3.8}$$

The expression for the density of states is $\rho_{k'}$, using the fact that $\rho_{k'}dE$ is the number of momentum states in $d\Omega$. The matrix element involves an integration over volume elements surrounding each atom as well as the neutron. Considering the neutron wave function as a box normalized plane wave, the differential cross section is simplified further to equation (3.9)

$$(\frac{d\sigma}{d\Omega})_{\lambda\to\lambda'} = \frac{k'}{k}(\frac{m_{\text{n}}}{2\pi\hbar^2})^2\left|\langle k'\lambda'\left|V\right|k\lambda\rangle\right|^2 \tag{3.9}$$

Conservation of energy can be mathematically be represented as $\int\delta(E_\lambda - E_{\lambda'} + E - E')dE' = 1$ where E and E' are the initial and final states of the neutron while E_λ and $E_{\lambda'}$ are the initial and final states of the system, the partial differential cross section can be expressed as equation (3.10).

$$(\frac{d\sigma}{d\Omega dE'})_{\lambda\to\lambda'} = \frac{k'}{k}(\frac{m_{\text{n}}}{2\pi\hbar^2})^2\left|\langle k'\lambda'\left|V\right|k\lambda\rangle\right|^2\delta(E_\lambda - E_{\lambda'} + E - E') \tag{3.10}$$

The expression can be simplified further when considering that the nuclear force is short ranged and the potential can be considered to be a delta function. As shown in refs (70; 72) a nuclear scattering potential known as the Fermi pseudopotential can be used which is shown in equation (3.11).

$$V(\mathbf{Q}) = \frac{2\pi\hbar^2}{m_{\mathrm{n}}} b \tag{3.11}$$

In equation (3.11), V is the scattering potential with a scattering length b. $\mathbf{Q} = k - k'$ is the neutron's momentum transfer. The next step is to sum over final states, using the assumption that during an experiment there is nothing selecting a particular energy, while keeping the initial states fixed. This is followed by a thermal averaging of the initial states with an assumed Boltzman distribution.

$$\frac{d\sigma}{d\Omega dE'} = \frac{k'}{k} \sum_{\lambda,\lambda'} P(\lambda) \left| \langle \lambda' \left| b \sum_j e^{i\mathbf{Q}\cdot\mathbf{R}_j} \right| \lambda \rangle \right|^2 \delta(E_\lambda - E_{\lambda'} + E - E') \tag{3.12}$$

In equation (3.12) $\mathbf{R}_j$ is the position of the jth nucleus and $P(\lambda)$ is the probability that the system starts out in state λ. As discussed in (72), through the use the integral representation of the delta function $\delta(E_\lambda - E_{\lambda'} E - E') = \frac{1}{2\pi\hbar} \int_{-\infty}^{\infty} \exp(i(E_\lambda - E_\lambda)t/\hbar)\exp(-i\omega t)dt$, the time-dependent Heisenberg operator $\mathbf{R}_i(t) = \exp(iHt/\hbar)\mathbf{R}_i\exp(-iHt/\hbar)$ where E_λ are eigen values of H, $\hbar\omega = E - E'$ (the energy transfer of the neutron), and through the use of the thermal average operator $\langle A \rangle = \sum_\lambda P(\lambda) \langle\ \lambda\, |A|\, \lambda \rangle$ the differential cross section can be re-expressed as equation (3.13).

$$\begin{aligned} \frac{d\sigma}{d\Omega dE'} &= N \frac{k'}{k} b^2 S(\mathbf{Q}, \omega) \\ S(\mathbf{Q}, \omega) &= \frac{1}{2\pi\hbar N} \sum_{j,j'} \int_{-\infty}^{\infty} \langle e^{(-i\mathbf{Q}\cdot\mathbf{R}_j(0))} e^{(i\mathbf{Q}\cdot\mathbf{R}_{j'}(t))} \rangle e^{-i\omega t} dt \end{aligned} \tag{3.13}$$

In equation (3.13), N is the number of nuclei. This is an important form of the partial differential cross section because it shows, for a known momentum and energy transfer, information about the atomic positions and motions is contained in the scattering function $S(\mathbf{Q}, \omega)$.

3.2.2.1 Coherent and incoherent scattering

The partial differential cross section is divided into two parts as shown in equation (3.14)

$$\frac{d^2\sigma}{d\Omega dE}_{\mathrm{total}} = \frac{d^2\sigma}{d\Omega dE}_{\mathrm{coh}} + \frac{d^2\sigma}{d\Omega dE}_{\mathrm{inc}} \tag{3.14}$$

For the coherent scattering length, one can consider a collection of atoms with an identical scattering length equal to $\bar{b}$ and for this mono-atomic system, the total cross section is $\sigma_{\text{coh}} = 4\pi\bar{b}^2$. As is seen in equation (3.13), the cross section depends on the correlations between atomic positions. For the case of coherent scattering, this will lead to interference effects. The incoherent scattering arises due the random variation of scattering lengths in the collection of atoms.

The incoherent term is added due to the fact that a real sample is a collection of isotopes and that the scattering length has a nuclear spin dependence which can randomly vary throughout a collection of atoms. This spin dependence comes from the interaction between the neutron and the nucleus, and whether or not the neutron spin is parallel are antiparallel to the nuclear spin. Because of the randomness of nuclear spin states above absolute zero and the isotopic distribution, nuclear states will not be correlated and will not lead to interference effects. The incoherent scattering will contribute a $\mathbf{Q}$ independent background in $\frac{d\sigma}{d\Omega}$ with a magnitude proportional to the variance of the scattering lengths ($\sigma_{\text{inc}} = (\sigma_{\text{total}} - \sigma_{\text{coh}}) = 4\pi(\overline{b^2} - \bar{b}^2) = 4\pi\overline{(b - \bar{b})^2}$).

3.2.3 Bragg scattering

The coherent scattering can provide information on atomic positions in a crystal system. The partial differential cross section can be expressed in terms of an atomic density operator $\rho_{\mathbf{Q}}(t) = \sum_j e^{(i\mathbf{Q}\cdot\mathbf{R}_j(t))}$ where the coherent scattering function is expressed as equation (3.15).

$$S(\mathbf{Q},\omega) = \frac{1}{2\pi\hbar N}\int_{-\infty}^{\infty} e^{-i\omega t}\langle\rho_{\mathbf{Q}}(0)\rho_{\text{-}\mathbf{Q}}(t)\rangle \tag{3.15}$$

For the case of coherent elastic nuclear scattering or Bragg scattering, the time average of the coherent scattering function can be used

$$S(\mathbf{Q},\omega) = \delta(\hbar\omega)\frac{1}{N}\langle\sum_{j,j'} e^{(-i\mathbf{Q}\cdot(\mathbf{R}_j - \mathbf{R}_{j'})}\rangle \tag{3.16}$$

For a Bravais lattice, $\frac{1}{N}\langle\sum_{j,j'} e^{(-i\mathbf{Q}\cdot(\mathbf{R}_j - \mathbf{R}_{j'})}\rangle = \frac{(2\pi)^3}{v_0}\sum_{\mathbf{G}}\delta(\mathbf{Q}-\mathbf{G})$ where $\mathbf{G}$ is a reciprocal lattice vector and v_0 is the unit cell volume. The coherent elastic cross section for a perfectly rigid monatomic lattice is shown in equation (3.17).

$$\frac{d\sigma}{d\Omega}_{\text{el,coh}} = N\frac{(2\pi)^3}{v_0}(\bar{b})^2 \sum_{\mathbf{G}} \delta(\mathbf{Q}-\mathbf{G}) \tag{3.17}$$

In reality, the atoms move around their equilibrium positions. This is accounted in the derivation of the phase factor averaging by adding the Debye-Waller factor e^{-2W} to equation (3.17) with $W = \frac{1}{2}\langle(\mathbf{Q}\cdot\mathbf{u})^2\rangle$ where $\mathbf{u}$ is the instantaneous position of the atom.

The systems covered in the work do not have a Bravais lattice but instead the unit cell is composed of a collection of different atoms which form a basis. Equation (3.18) shows the general case after the phase factor averaging with a non-Bravais lattice.

$$\frac{d\sigma}{d\Omega}_{\text{el,coh}} = N\frac{(2\pi)^3}{v_0} \sum_{\mathbf{G}} \delta(\mathbf{Q}-\mathbf{G}) \left|F_{\text{N}}(\mathbf{G})\right|^2 \tag{3.18}$$

$F_{\text{N}}(\mathbf{G})$ is the static nuclear structure factor. This function is shown in equation (3.19)

$$F_{\text{N}}(\mathbf{G}) = \sum_j \bar{b}_j e^{i\mathbf{G}\cdot\mathbf{d}_j} e^{-W_j} \tag{3.19}$$

In equation (3.19), $\bar{b}_j$ refers the average scattering length of a particular atom on site j and the sum is over all atoms in the basis. It is assumed that the unit cell repeats for all directions and the atomic positions $\mathbf{d}_j$ is the vector from the origin of the unit cell to an atom in the basis. In addition to information about the atomic positions, the mean-square displacements of each particular atom is found in the Debye-Waller factor. Through the measurement of large numbers of Bragg peaks, the crystal structure corresponding to the lattice parameters and positions of the basis atoms can be determined or verified.

3.3 Magnetic scattering

Because the neutron is a composite fermion, it has an intrinsic spin and therefore a magnetic dipole moment with a value represented as $-\gamma\mu_{\text{N}}\boldsymbol{\sigma}$ where $\gamma = 1.913$ is the gyromagnetic ratio, μ_{N} is the nuclear magneton, and $\boldsymbol{\sigma}$ is the spin operator. Through a dipole-dipole interaction between the neutron and an electron, neutron scattering is sensitive to the spin and angular momentum components of an electron moment.

An expression for the magnetic partial differential cross section similar to equation (3.9) can be expressed as equation (3.20) with the clear differences that the vector character of the dipole-dipole interaction requires that spin states are accounted for.

$$(\frac{d^2\sigma}{d\Omega dE'})_{\sigma\lambda\to\sigma'\lambda'} = \frac{k'}{k}(\frac{m_{\mathrm{n}}}{2\pi\hbar^2})^2 \left|\langle \mathbf{k}'\sigma'\lambda' \left|V_{\mathrm{m}}\right| \mathbf{k}\sigma\lambda\rangle\right|^2 \delta(E_\lambda - E_{\lambda'} + \hbar\omega) \tag{3.20}$$

The magnetic potential for a neutron with a dipole moment $\boldsymbol{\mu}_{\mathrm{N}}$ is shown in equation (3.21)

$$V_{\mathrm{m}} = -\boldsymbol{\mu}_{\mathrm{N}} \cdot \mathbf{B} = -\frac{\mu_0}{4\pi}\gamma\mu_{\mathrm{N}} 2\mu_{\mathrm{B}}\boldsymbol{\sigma} \cdot (\mathbf{W}_{\mathrm{S}} + \mathbf{W}_{\mathrm{L}}) \tag{3.21}$$

where $\mathbf{W}_{\mathrm{S}}$ and $\mathbf{W}_{\mathrm{L}}$ which are shown in equations (3.22) and (3.23)

$$\mathbf{W}_{\mathrm{S}} = \nabla \times (\frac{\mathbf{s}\times\hat{\mathbf{R}}}{R^2}) \tag{3.22}$$

$$\mathbf{W}_{\mathrm{L}} = \frac{1}{\hbar}\frac{\mathbf{p}\times\hat{\mathbf{R}}}{R^2} \tag{3.23}$$

are proportional to the magnetic fields associated the electronic spin and orbital momentum respectively. In these equations $\mathbf{s}$ is the spin angular momentum operator for the electron, $\mathbf{p}$ is the electron momentum, and $\mathbf{R}$ is a position relative to the electron where the magnetic field due to the electron spin and angular momentum is evaluated.

From this point on, the discussion will focus on spin-only scattering due to the fact that the analysis in the work considered spin-only scattering or the case where the angular momentum of the electron is small enough to be ignored. This is justified because the moment analyzed on $CaFe_2As_2$ and $Ba(Fe_{1-x}Co_x)_2As_2$ is a spin dominated moment from iron. (73)

A first step in the evaluation of equation (3.20) is the evaluation of $\langle k' \left|\mathbf{W}_{\mathrm{S}}\right| k\rangle$ is involves an integration over the space coordinates of the neutron. Through the use of the identity $\nabla \times (\frac{\mathbf{s}\times\hat{\mathbf{R}}}{R^2}) = \frac{1}{2\pi^2}\int \hat{\mathbf{q}} \times (\mathbf{s}\times\hat{\mathbf{q}})\exp(i\mathbf{q}\cdot\mathbf{R})d\mathbf{q}$ the matrix can be shown to be equation (3.24)

$$\langle k' \left|\mathbf{W}_{\mathrm{S}i}\right| k\rangle = 4\pi\exp(i\mathbf{Q}\cdot\mathbf{r}_i)(\hat{\mathbf{Q}} \times (\mathbf{s}_i \times \hat{\mathbf{Q}})) \tag{3.24}$$

where $\mathbf{r}_i$ is the location of the ith electron. It is convenient to define a magnetic interaction vector $\mathbf{S}_\perp$ which represents the interaction from all electron spins.

$$\begin{aligned}\mathbf{S}_\perp &= \frac{1}{4\pi}\sum_i \langle k'|\mathbf{W}_{Si}|k\rangle \\ &= \sum_i \exp(i\mathbf{Q}\cdot\mathbf{r}_i)(\hat{\mathbf{Q}}\times(\mathbf{s}_i\times\hat{\mathbf{Q}})) \\ &= \hat{\mathbf{Q}}\times(\mathbf{S}\times\hat{\mathbf{Q}}) \end{aligned} \tag{3.25}$$

where $\mathbf{S} = \sum_i \exp(i\mathbf{Q}\cdot\mathbf{r}_i)\mathbf{s}_i$ (70; 74) and is related to the spin magnetization as is shown in equation (3.26)

$$\begin{aligned}\mathbf{S} &= -\frac{1}{2\mu_{\mathrm{B}}}\mathbf{M}_{\mathrm{S}}(\mathbf{Q}) \\ \mathbf{M}_{\mathrm{S}}(\mathbf{Q}) &= \int \mathbf{M}_{\mathrm{S}}(\mathbf{r})\exp(i\mathbf{Q}\cdot\mathbf{r})d\mathbf{r}\end{aligned} \tag{3.26}$$

With the help of Fig. 3.2, it is can be observed that $\mathbf{S}_\perp = \mathbf{S} - (\mathbf{S}\cdot\hat{\mathbf{Q}})\hat{\mathbf{Q}}$. Using this expression a simplified expression of $\mathbf{S}_\perp \cdot \mathbf{S}_\perp$ is shown in equation (3.27) which will be needed for the evaluation of the cross section.

$$\begin{aligned}\mathbf{S}_\perp\cdot\mathbf{S}_\perp &= (\mathbf{S}-(\mathbf{S}\cdot\hat{\mathbf{Q}})\hat{\mathbf{Q}})\cdot(\mathbf{S}-(\mathbf{S}\cdot\hat{\mathbf{Q}})\hat{\mathbf{Q}}) \\ &= \mathbf{S}\cdot\mathbf{S}-(\mathbf{S}\cdot\hat{\mathbf{Q}})(\mathbf{S}\cdot\hat{\mathbf{Q}}) \\ &= \sum_{\alpha\beta}(\delta_{\alpha\beta}-\hat{Q}_\alpha\hat{Q}_\beta)S_\alpha S_\beta\end{aligned} \tag{3.27}$$

In equation (3.27), α and β refer to x, y, or z coordinates, and $\delta_{\alpha\beta}$ is the Kronecker delta function. After summing over final spin states, averaging over initial spin states, and using the result in equation (3.27), the partial differential cross section for magnetic scattering can be expressed as equation (3.28)

$$\frac{d^2\sigma}{d\Omega dE} = (\gamma r_0)^2\frac{k'}{k}\sum_{\alpha\beta}(\delta_{\alpha\beta}-\hat{Q}_\alpha\hat{Q}_\beta)\sum_{\lambda\lambda'}p_\lambda\langle\lambda|S_\alpha|\lambda'\rangle\langle\lambda'|S_\beta|\lambda\rangle\delta(E_\lambda - E_{\lambda'}+\hbar\omega) \tag{3.28}$$

In addition to the magnitude and orientation of the spin, the state $|\lambda\rangle$ depends on the position of the nucleus $\mathbf{R}_{ld}$ in the lattice, where l refers to a particular unit cell and d refers

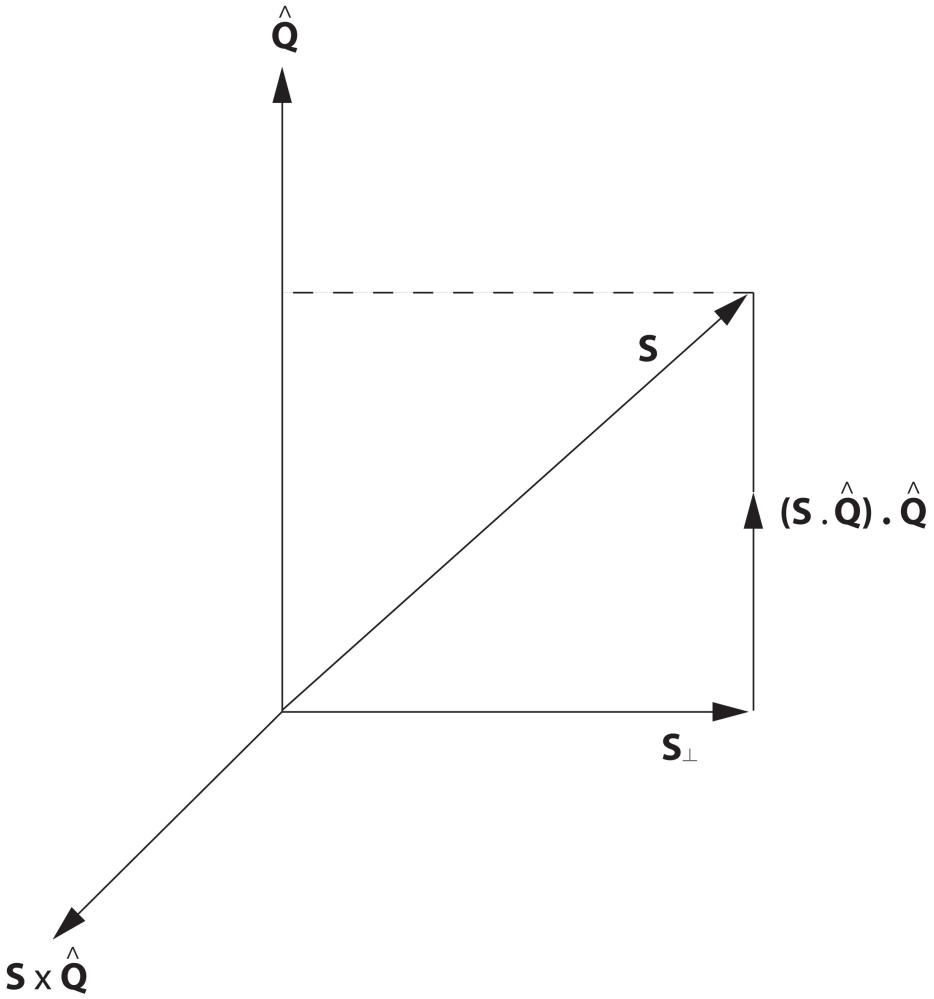

Figure 3.2 Relation between $\mathbf{S}$ and $\mathbf{S}_{\perp}$. (reproduction from ref (70))

to an atom in the unit cell, as well as the position of the electron relative to the nucleus $\mathbf{r}_\nu$ which represents the distance from atom d. It follows that the matrix element $\langle \lambda' | \mathbf{S} | \lambda \rangle$ can be re-expressed as equation (3.29).

$$\langle \lambda' | \mathbf{S} | \lambda \rangle = \langle \lambda' \left| \exp(i\mathbf{Q} \cdot \mathbf{R}_{ld}) \sum_\nu \exp(i\mathbf{Q} \cdot \mathbf{r}_\nu) \mathbf{s}_\nu \right| \lambda \rangle \tag{3.29}$$

The sum over ν takes into account all unpaired electrons. The energy of the neutron is not energetic enough to changes the space state of electrons. Under the assumption that all electrons are located close to the atom or that $\mathbf{r}_\nu$ is small and is roughly the same for all atoms. Therefore, the initial and final states only depend on the spin orientation and the location of the nucleus. The integration with respect to electron position can be can be carried out and the result is shown in equation (3.30)

$$\langle \lambda' | \mathbf{S} | \lambda \rangle = F_d(\mathbf{Q}) \langle \lambda' | \exp(i\mathbf{Q} \cdot \mathbf{R}_{ld}) \mathbf{S}_{ld} | \lambda \rangle \tag{3.30}$$

The function $F_d(\mathbf{Q})$ is magnetic form factor which provides information about the unpaired electron density around an atom at site d.

Using a procedure which is similar to what was done for nuclear scattering, the spin interaction operators in magnetic cross section can be expressed in terms of time-dependent Hamiltonian operators and integral representation of conservation of energy can be used. This is followed by a thermal averaging of the spin operator in order to arrive to equation (3.31) for the case of a Bravais lattice.

$$\begin{aligned} \frac{d\sigma^2}{d\Omega dE} &= \frac{(\gamma r_0)^2}{2\pi\hbar} \frac{k'}{k} N (\frac{g}{2} F(\mathbf{Q}))^2 \sum_{\alpha\beta} (\delta_{\alpha\beta} - \hat{\mathbf{Q}}_\alpha \hat{\mathbf{Q}}_\beta) \sum_l \exp(i\mathbf{Q} \cdot \mathbf{l}) \\ &\times \int_{-\infty}^{\infty} \langle \exp(-i\mathbf{Q} \cdot \mathbf{u}_0(0)) \exp(i\mathbf{Q} \cdot \mathbf{u}_l(t)) \rangle \langle \mathbf{S}_0^\alpha(0) \mathbf{S}_l^\beta(t) \rangle \exp(-i\omega t) dt \end{aligned} \tag{3.31}$$

In equation (3.31), $u_l(t)$ describes the time dependence of atomic displacements from their equilibrium positions for a monatomic system. The constant r_0 is the classical radius of an electron and g is the Landé splitting factor. The scattering processes in (3.31) including elastic magnetic scattering, magneto-vibrational which involves scattering by phonons through a mag-

netic interaction that leaves the spin unchanged, inelastic magnetic scattering, and scattering which involves a combination of lattice and magnetic dynamics.

3.3.1 Elastic magnetic scattering

The elastic-magnetic cross section is derived from the infinite time limit of the correlations between atoms and spins shown in equation (3.31) for example. For the case when the scattering is only due to interaction with electronic spin, the partial differential cross section for magnetic scattering can be expressed as equation (3.32).

$$(\frac{d^2\sigma}{d\Omega dE'})_{\text{el}} = r_0^2 \frac{k'}{k} \delta(\hbar\omega) \langle \mathbf{S}_\perp(0) \cdot \mathbf{S}_\perp(\infty) \rangle \tag{3.32}$$

And after the integration over energy for the case of elastic scattering where $\omega = 0$ and $k' = k$, the differential cross section is shown in equation (3.33).

$$\frac{d\sigma}{d\Omega} = r_0^2 \langle \mathbf{S}_\perp \rangle \cdot \langle \mathbf{S}_\perp \rangle \tag{3.33}$$

To arrive at this equation, one must consider that there are no correlations between processes well separated in time or a that $\langle \mathbf{S}_\perp \cdot \mathbf{S}_\perp(\infty) \rangle = \langle \mathbf{S}_\perp \rangle \langle \mathbf{S}_\perp(\infty) \rangle$ and the system is stationary or that for any time t, $\langle \mathbf{S}_\perp(t) \rangle = \langle \mathbf{S}_\perp(0) \rangle = \langle \mathbf{S}_\perp \rangle$. An expression for $\langle \mathbf{S}_\perp \rangle$ is shown in equation (3.34) which uses equation (3.25).

$$\langle \mathbf{S}_\perp \rangle = \int \exp(i\mathbf{Q} \cdot \mathbf{r}) \hat{\mathbf{Q}} \times (\mathbf{s}(\mathbf{r}) \times \hat{\mathbf{Q}}) d\mathbf{r} \tag{3.34}$$

Using the fact that $\mathbf{s}(\mathbf{r})$ is periodic and that you only have to integrate over the unit cell volume, the integration can be expressed as equations (3.35).

$$\int_{v_0} \exp(i\mathbf{Q} \cdot \mathbf{r}) \mathbf{s}(\mathbf{r}) d\mathbf{r} = \frac{(2\pi)^3}{v_0} \sum_{\boldsymbol{\tau}} \delta(\mathbf{Q} - \boldsymbol{\tau}) \overrightarrow{\mathcal{F}}(\boldsymbol{\tau}) \tag{3.35}$$

The sum is taken over the magnetic reciprocal lattice vectors $\boldsymbol{\tau}$. The function $\overrightarrow{\mathcal{F}}(\boldsymbol{\tau})$ is known as the magnetic unit-cell vector structure factor and is analogous to the scalar structure factor from nuclear Bragg scattering.

With the assistance of equations (3.33)-(3.35), the differential cross section becomes

$$\frac{d\sigma}{d\Omega} = r_0^2 N \frac{(2\pi)^3}{v_0} \sum_{\boldsymbol{\tau}} \delta(\mathbf{Q} - \boldsymbol{\tau}) \left| \hat{\mathbf{Q}} \times (\overrightarrow{\mathcal{F}}(\boldsymbol{\tau}) \times \hat{\mathbf{Q}}) \right|^2 . \tag{3.36}$$

An expression for the magnetic unit-cell vector structure factor is shown in equation (3.37) which takes into account the possibility that the spin can vary on atomic sites is shown in equation (3.37)

$$\overrightarrow{\mathcal{F}}(\boldsymbol{\tau}) = \sum_d \exp(i\boldsymbol{\tau} \cdot \mathbf{d}) \exp(-W_d) \frac{g}{2} \langle S_d \rangle F_d(\boldsymbol{\tau}) \hat{\mathbf{s}}_d(\boldsymbol{\tau}) \tag{3.37}$$

In equation (3.37) $\exp(-W_d)$ is the Debye-Waller factor, F_d is the form factor, $\langle S_d \rangle$ is the spin magnitude and $\hat{\mathbf{s}}_d$ is the spin direction at site d. The combined expression for the coherent magnetic cross section is shown in equation (3.38)

$$\begin{aligned} \frac{d\sigma}{d\Omega} &= r_0^2 N \frac{(2\pi)^3}{v_0} \sum_{\boldsymbol{\tau}} \delta(\mathbf{Q} - \boldsymbol{\tau}) \\ &\times \left| \sum_d \exp(i\boldsymbol{\tau} \cdot \mathbf{d}) \exp(-W_d) \frac{g}{2} \langle S_d \rangle F_d(\boldsymbol{\tau}) \{ \hat{\boldsymbol{\tau}} \times (\hat{\mathbf{s}}_d \times \hat{\boldsymbol{\tau}}) \} \right|^2 \end{aligned} \tag{3.38}$$

3.4 Spin waves and relaxational dynamics

This section will include a discussion of the low energy magnetic spectrum ($\hbar\omega < 15$ meV) that has been extensively studied using neutron scattering. These excitations have been described as originating from a crystal system where the magnetic moment is due to unpaired electrons which are located near the ions in the crystal lattice. In this case, the excitations are known as spin-waves which are excitations associated with the long range ordered magnetic lattice. In addition, the magnetic moment has been postulated to originate in the semi-metallic iron arsenides due to correlation of band or itinerant electrons. A Fermi-liquid model based on the band structure has been used to understand the heavily damped spin excitations in this picture. This model has also been used to model spin fluctuations in the paramagnetic state. Finally, below T_{c}, a peak in the low energy spin excitation spectrum known as the spin resonance mode has been observed through the use of neutron scattering. The following subsections describe how neutron scattering can be used to observe these phenomenon.

3.4.1 Scattering function using the generalized dynamic magnetic susceptibility

When only considering the inelastic magnetic component of equation (3.31), the partial differential cross section can be expressed as equation (3.39)

$$\frac{d\sigma^2}{d\Omega dE} = (\gamma r_0)^2 \frac{k'}{k} N (\frac{g}{2} F(\mathbf{Q}))^2 \exp(-2W) \sum_{\alpha\beta} (\delta_{\alpha\beta} - \hat{\mathbf{Q}}_\alpha \hat{\mathbf{Q}}_\beta) \mathcal{S}^{\alpha\beta}(\mathbf{Q}, \omega)$$
$$\mathcal{S}^{\alpha\beta}(\mathbf{Q}, \omega) = \frac{1}{2\pi\hbar} \sum_{ld} \exp(i\mathbf{Q} \cdot \mathbf{R}_{ld}) \int_{-\infty}^{\infty} \langle S_0^\alpha(0) S_{ld}^\beta(t) \rangle \exp(i\omega t) dt \tag{3.39}$$

where $\mathcal{S}^{\alpha\beta}(\mathbf{Q}, \omega)$ is known as the scattering function which describes the spin-spin correlations for the system.

The linear response of the magnetization is shown in equation (3.40)

$$\delta M_\alpha(\mathbf{Q}, \omega) = \chi_{\alpha\beta}(\mathbf{Q}, \omega) H_\beta(\mathbf{Q}, \omega) \tag{3.40}$$

where $\delta M_\alpha(\mathbf{Q}, \omega)$ refers to a change in the magnetization, $H_\alpha(\mathbf{Q}, \omega)$ refers a Fourier component of an applied magnetic field and $\chi_{\alpha\beta}(\mathbf{Q}, \omega)$ is the generalized magnetic susceptibility which describes the electronic magnetization's response to the magnetic field H (24). Again, the response is assumed to be linear which is only applicable for small fields. $\chi(\mathbf{Q}, \omega)$ is composed of real and imaginary parts as shown in equation (3.41).

$$\chi(\mathbf{Q}, \omega) = \chi'(\mathbf{Q}, \omega) + i\chi''(\mathbf{Q}, \omega) \tag{3.41}$$

The imaginary part of $\chi(\mathbf{Q}, \omega)$ describes the reactive or dissipative response to H and through the fluctuation-dissipation theorem, and can be related to the response function as shown in equation (3.42).

$$\mathcal{S}^{\alpha\beta}(\mathbf{Q}, \omega) = \frac{1}{\pi(g\mu_{\mathrm{B}})^2} \frac{1}{1 - e^{(\frac{-\hbar\omega}{k_{\mathrm{B}}T})}} \chi''_{\alpha\beta}(\mathbf{Q}, \omega) \tag{3.42}$$

Equation (3.42) describes the scattering function for scattering which involves neutron energy loss. Describing the scattering with the use of the generalized magnetic susceptibility allows for the direct comparison of neutron scattering data with theory. In the next section

will discuss examples of response functions used to describe the neutron scattering measurements in this work.

3.4.1.1 Spin waves

In ordered magnets, the low energy spin excitations are collective modes known as quantized spin waves or magnons. A simple physical picture of a spin wave is shown in Fig. 3.3 for a simple ferromagnet. In this picture, the spin excitations involve rotations of spins around the static moment direction. These collective excitations are commonly modeled thorough the use of a damped harmonic oscillator where the response function for a damped harmonic oscillator is shown in equation (3.43).

$$\chi(\mathbf{Q},\omega) = \chi'(\mathbf{Q},0)\frac{\omega_{\mathbf{Q}}^2}{\omega_{\mathbf{Q}}^2 - \omega^2 - i\gamma\omega} \tag{3.43}$$

In equation (3.43), $\omega_{\mathbf{Q}}$ is the spin-wave dispersion relation and γ indicates the level of damping.

The Heisenberg spin Hamiltonian for the 122 iron-arsenides which describes a local moment system was developed by Ewings *et al.* (75) which is based on a lattice of interacting spin moments. The arrangement of spins is shown in Fig. 3.4 where the ground state arrangement of spins involves an antiferromagnetic coupling along the orthorhombic **a**-direction, a ferromagnetic coupling along the **b**-direction, and an antiferromagnetic arrangement along the **c**-direction. Equation (3.44) shows this Hamiltonian for the case were nearest neighbor and next-nearest spin neighbors are considered. Single ion anisotropy, or the effects the surrounding crystalline field creates an energy cost of $D(S_z^2)$ for the spins flip 90° to point along **c** while (**a**-**b**) plane anisotropy is ignored.

$$\mathcal{H} = J_{1a}\sum_{\langle ij\rangle a}\mathbf{S}_i\cdot\mathbf{S}_j + J_{1b}\sum_{\langle ij\rangle b}\mathbf{S}_i\cdot\mathbf{S}_j + J_2\sum_{\langle ik\rangle ab}\mathbf{S}_i\cdot\mathbf{S}_k + J_c\sum_{\langle il\rangle c}\mathbf{S}_i\cdot\mathbf{S}_l + \sum_i D(S_z^2)_i \tag{3.44}$$

In equation (3.44) J_{1a} represents the spin coupling along the a-direction, J_{1b} represents coupling along b, J_2 is the next-nearest neighbor coupling, and J_c is coupling along c. The spin arrangement and the coupling constants are shown in Fig. 3.4. The sums are taken over spin pairs such as $\langle ij\rangle$ along either the **a**, **b**, the diagonal $\langle \mathbf{a},\mathbf{b}\rangle$, and **c** directions.

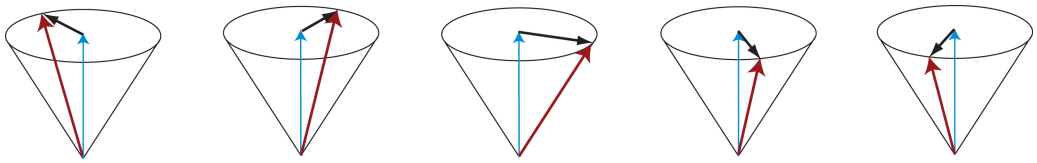

Figure 3.3 Physical picture of a spin wave where the static moment direction is perpendicular to the plane which includes the spin motions represented as the circular trajectory. (reproduction from ref (70))

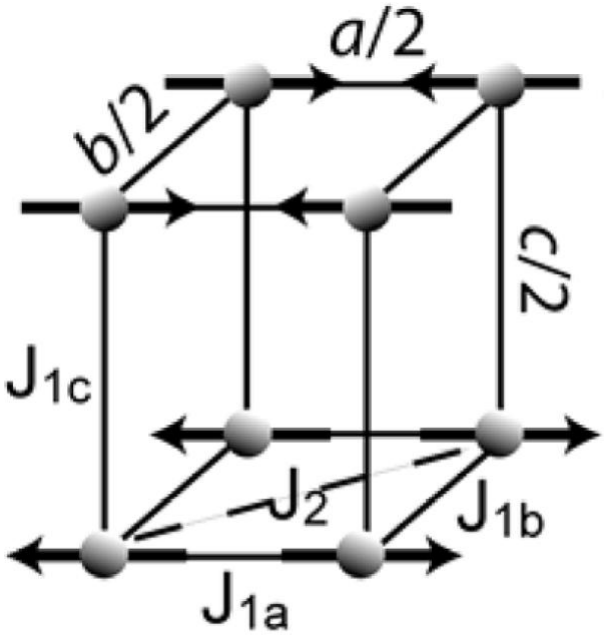

Figure 3.4 The spin arrangement and the coupling constants used in the Heisenburg spin Hamiltonian (Taken from ref (76))

Diagonalization of the Hamiltonian shown in equation (3.44) (75) leads to a spin dispersion shown in equation (3.45).

$$\hbar\omega(\mathbf{Q}) = \sqrt{A_{\mathbf{Q}}^2 - B_{\mathbf{Q}}^2} \tag{3.45}$$

where the functions $A_{\mathbf{Q}}$ and $B_{\mathbf{Q}}$ shown in equations (3.46) and (3.47) are expressed in terms of an effective spin $S = \frac{\mu}{g\mu_{\mathrm{B}}}$, where μ is the ordered moment, as well as the spin coupling constants.

$$A_{\mathbf{Q}} = 2S\{J_{1b}[\cos(\frac{\mathbf{Q}\cdot\mathbf{b}}{2}) - 1] + J_{1a} + 2J_2 + J_c + D\} \tag{3.46}$$

$$B_{\mathbf{Q}} = 2S\{J_{1a}\cos(\frac{\mathbf{Q}\cdot\mathbf{a}}{2}) + 2J_2\cos(\frac{\mathbf{Q}\cdot\mathbf{a}}{2})\cos(\frac{\mathbf{Q}\cdot\mathbf{b}}{2}) + J_c\cos(\frac{\mathbf{Q}\cdot\mathbf{c}}{2})\}. \tag{3.47}$$

The scattering function $\mathcal{S}^{\alpha\beta}(\mathbf{Q},\omega)$ for this system was calculated in the linear spin wave approximation in ref (75) based on work by Yao and Carlson (77). It is assumed that the spin magnitude does not change so the only components of this scattering function that contribute to the cross section are when $\alpha = \beta$ where these α or β correspond to x,y, or z components of spin. As is shown in Fig. 3.4, the moments are along the x-direction so the only components that contribute are $\mathcal{S}^{yy}$ and $\mathcal{S}^{zz}$ which can be assumed to be identical for the case of small single-ion anisotropy. Based on ref (75), the neutron energy loss scattering function for the case of small or no single ion anisotropy is shown in equation (3.48).

$$\mathcal{S}^{\alpha\alpha}(\mathbf{Q},\omega) = \mathcal{S}(\mathbf{Q},\omega) = S\frac{A_{\mathbf{Q}} - B_{\mathbf{Q}}}{\omega_{\mathbf{Q}}}\frac{1}{1 - e^{(\frac{-\hbar\omega}{k_{\mathrm{B}}T})}}\delta(\omega - \omega_{\mathbf{Q}}) \tag{3.48}$$

Equation (3.48) does not include damping which can be accounted for by substituting the delta function (which represents the energy dependence in equation (3.48)) with a Lorentzian function as is the case for the imaginary component of the damped harmonic oscillator $\chi(\mathbf{Q},\omega)$ shown in equation (3.43). The scattering function then becomes

$$\mathcal{S}(\mathbf{Q},\omega) = S\frac{A_{\mathbf{Q}} - B_{\mathbf{Q}}}{\omega_{\mathbf{Q}}}\frac{1}{1 - e^{(\frac{-\hbar\omega}{k_{\mathrm{B}}T})}}\frac{\omega_{\mathbf{Q}}^2\gamma\omega}{(\omega_{\mathbf{Q}}^2 - \omega^2)^2 + \gamma^2\omega^2} \tag{3.49}$$

where $\omega_0 = \omega_{\mathbf{Q}}$. Through the use of this form of $\mathcal{S}(\mathbf{Q},\omega)$, neutron scattering measurements can provide information about the strength and sign of the spin coupling as well as the level of spin-wave damping.

A visualization of $\mathcal{S}(\mathbf{Q},\omega)$ is shown in Fig. 5 where the parameters are chosen match results from ref (53) where $Ba(Fe_{0.953}Co_{0.047})_2As_2$. The dispersion is represented by the solid lines. The significant amount of intensity in regions above and below the dispersion is due to the significant damping that exists for the case of $Ba(Fe_{0.953}Co_{0.047})_2As_2$.

Using Figs. 3.5 and 3.6, some important features of the dispersion can be highlighted. First, the degree of dispersion and the corresponding zone boundary values are quite different along $[hh1]_T$ and $[\frac{1}{2}\ \frac{1}{2}\ l]_T$ or $[h01]_{\mathrm{O}}$ and $[10l]_{\mathrm{O}}$ due to the significantly larger J_{1a} as compared to J_c which is typical for this layered compound. The non-zero value of $\omega_{\mathbf{Q}}$ at the minima of the dispersion is called the spin-wave energy gap Δ_{AFM}. Due to the steepness of the dispersion such as in Fig. 5a, it is common when measuring low energy spin excitations to use a simplified conical dispersion as shown in equation (3.50) which assumes tetragonal symmetry.

$$\omega_{\mathbf{Q}} = \sqrt{\Delta_{\mathrm{AFM}}^2 + v_{ab}^2((q_x - q_{x0})^2 + (q_y - q_{y0})^2) + v_c(q_z - q_{z0})^2} \tag{3.50}$$

where $\mathbf{q}_0 = \mathbf{Q}_{\mathrm{AFM}}$ such that the dispersion relation has a value of Δ_{AFM} at $\mathbf{Q} = \mathbf{Q}_{\mathrm{AFM}}$. The velocities $v_{ab} = \frac{d\omega_{\mathbf{Q}}}{dq_x} = \frac{d\omega_{\mathbf{Q}}}{dq_y}$ and $v_c = \frac{d\omega_{\mathbf{Q}}}{dq_x}$ are clearly related to the steepness of the cone as shown in Fig 6. Through a Taylor series expansion of equation (3.45), a relationship between the spin-wave velocities and the axial anisotropy can be shown to be

$$\begin{aligned} v_{ab} &= aS(J_{1a} + 2J_2)\sqrt{1 + J_{1c}/(2J_2 + J_{1a})} \\ v_c &= cSJ_c\sqrt{1 + (2J_2 + J_{1a})/J_{1c}} \\ \Delta_{\mathrm{AFM}} &= 2S\sqrt{D[D + 2(2J_2 + J_{1a} + J_c)]} \end{aligned} \tag{3.51}$$

where a and c are lattice parameters. The use of equation (3.51) in the analysis of low energy spin-wave analysis can provide insight into the spin gap as well as the anisotropy between in-plane and out-of-plane spin couplings.

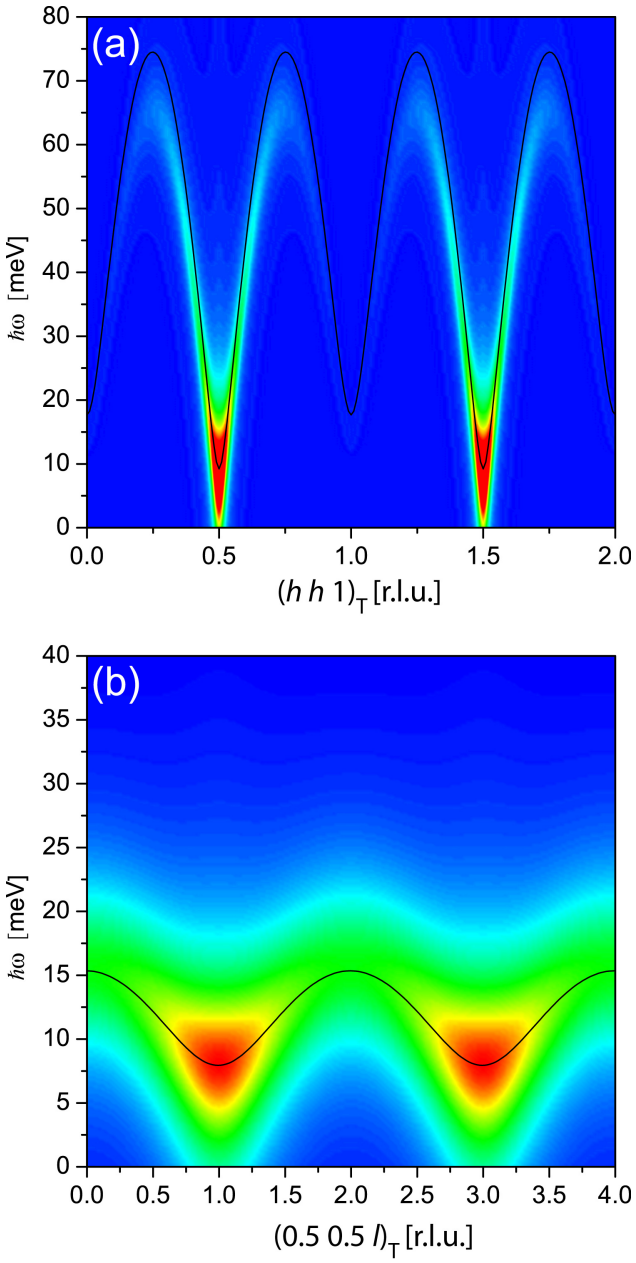

Figure 3.5 Contour plot of $\mathcal{S}(\mathbf{Q},\omega)$ based on measurements on $Ba(Fe_{0.953}Co_{0.047})_2As_2$ along the (a) $(h01)$ and (b) $(10l)$ directions. The sold lines represent the spin-wave dispersion. Please note the different energy scales.

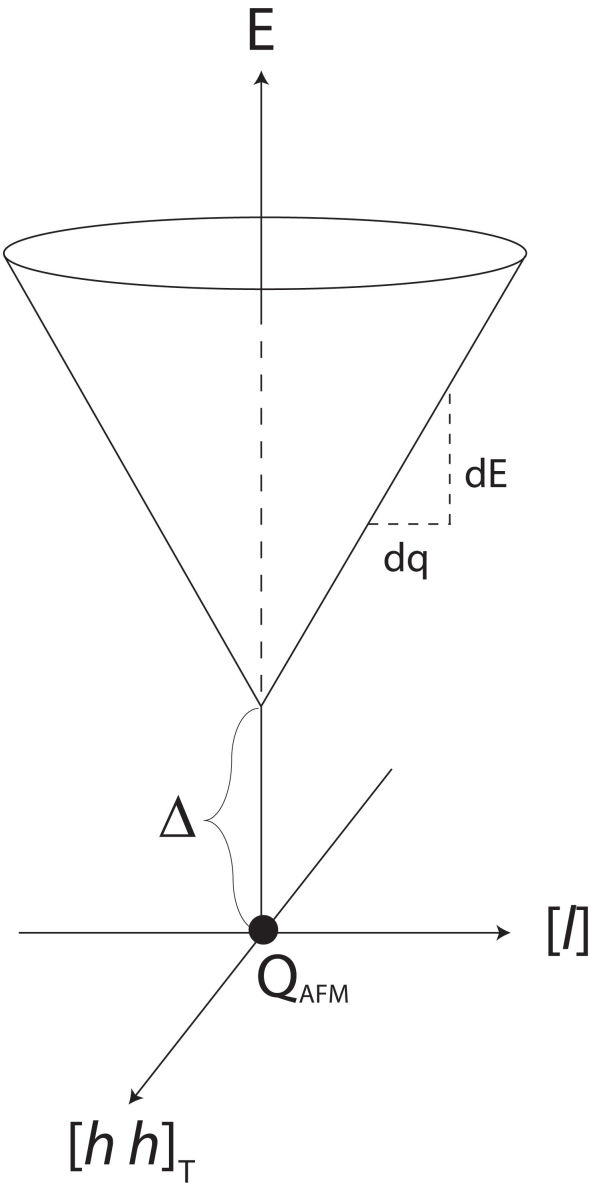

Figure 3.6 Conical Dispersion

3.4.1.2 Nearly antiferromagnetic Fermi liquid model

For the case of $Ba(Fe_{0.953}Co_{0.047})_2As_2$ which was studied in this work, fits to the local moment Heisenberg model resulted in a damping energy $\Gamma \approx 10$ meV which was greater than $\Delta_{\mathrm{AFM}} \approx 8$ meV causing intensity to be observed down to the elastic point in Fig. 5. This will discussed further in chapter 5. This motivated an alternative explanation for the low energy spin excitations. This large damping observed using inelastic neutron scattering could be due to short ranged and short lived spin-correlations of itinerant conduction electrons. This picture was further motivated by studies of paramagnetic spin fluctuations in the optimally doped compound(78)

Unlike local moment systems where the electron can be said to be on the atomic site and have a state localized in space, the itinerant picture involves conduction electrons which undergo strong scattering at a particular momentum transfer or a momentum localized in **q**-space (nesting). For the case of the iron arsenides itinerant magnetism can result from a nesting at $\mathbf{Q}_{\mathrm{AFM}}$ which separates the hole and electron bands.

The nearly antiferromagnetic fermi liquid model has been applied to inelastic neutron scattering data to analyze the spin-fluctuation spectrum for the case of itinerant electron systems (79). The expression *nearly antiferromagnetic* refers to the situation where the system is close to an antiferromagnetic transition or instability while he expression *fermi liquid* is a generic term for a quantum mechanical liquid of fermions such as electrons in a metal. This model is used to describe a paramagnetic system in the vicinity magnetic transition as well as to systems which have enhanced spin fluctuations due to magnetic frustration. As for the application of this model to $Ba(Fe_{0.953}Co_{0.047})_2As_2$, the latter explanation is applicable due to the fact that the measurements taken were in the AFM ordered state.

An expression for χ'' for a nearly antiferromagnetic Fermi liquid is shown in equation (3.52) (79; 78).

$$\chi''(\mathbf{Q},\omega,T) = \frac{\chi(T)\Gamma(T)\omega}{\omega^2 + \Gamma^2(T)(1+\xi^2(T)\left|\mathbf{Q}-\mathbf{Q}_{\mathrm{AFM}}\right|^2)^2} \tag{3.52}$$

In equation (3.52), the parameter $\chi(T) = \chi_0(T+\Theta)^{-1}$ is the Curie-Weiss law for uniform

susceptibility and is a temperature dependent scaling factor which represents the strength of the AFM correlations. The damping function is $\Gamma(\mathrm{T})=\Gamma_0(T+\Theta)$, the magnetic correlation length is $\xi(\mathrm{T})==\xi_0(T+\Theta)^{-1/2}$, and Θ refers to the Curie-Weiss temperature.

As for the analysis in this work, the temperature dependence was not studied and does not apply due to the fact that the system is not paramagnetic. This analysis was performed to show that the observed intensity can be interpreted both in a local moment picture as well as an itinerant electron picture and to provide evidence from the scattering to substantiate either picture. The damping and correlations along the orthorhombic a and c directions were analyzed through the measurements of $\mathbf{Q}_{\mathrm{AFM}} = (1\ 0\ 1)_{\mathrm{O}}$ (in reciprocal lattice units) through $(h\ 0\ 1)_{\mathrm{O}}$ and $(1\ 0\ l)_{\mathrm{O}}$ scans for the case of $Ba(Fe_{0.953}Co_{0.047})_2As_2$ using the equations in (3.53).

$$\begin{aligned}\chi''((\frac{2\pi h_{\mathrm{O}}}{a},0,1),\omega) &= \frac{\chi\Gamma\omega}{\omega^2+\Gamma^2(1+\xi_a^2\left|\frac{2\pi}{a}(h_{\mathrm{O}}-1)\right|^2)^2}\\ \chi''((1,0,\frac{2\pi l_{\mathrm{O}}}{c}),\omega) &= \frac{\chi\Gamma\omega}{\omega^2+\Gamma^2(1+\xi_c^2\left|\frac{2\pi}{c}(l_{\mathrm{O}}-1)\right|^2)^2}\end{aligned} \tag{3.53}$$

The $(1,0,\frac{2\pi l_{\mathrm{O}}}{c})$ analysis using this method showed that the correlation lengths for $Ba(Fe_{0.953}Co_{0.047})_2As_2$ were similar to those found in optimal doped samples in which no long range AFM order is present. This suggests that overdamping of spin fluctuations may be due to the relaxational processes (i.e. electron-electron scattering or electron-phonon scattering) associated with an itinerant character of the electrons responsible for magnetism in these systems.

3.4.2 Superconducting resonance

From an experimental point of view, the spin resonance refers to an observed redistribution of inelastic neutron scattering intensity from measurement of energy spectrum when the system is cooled below the superconducting transition temperature T_c. The SC spin-resonance has been observed in compounds where SC is believed to be unconventionally mediated (not phonon mediated) such as, layered copper oxide superconductors, heavy fermion superconductors, and in the iron-arsenide superconductors (15; 53; 80)

The superconducting resonance has been interpreted in several ways (81) but a promising

candidate is known as the spin-exciton model. The spin exciton refers an electron-hole bound state where the electron and hole may have either parallel or anti-parallel spins. Measurements of the resonance in the compound $FeSe_{0.4}Te_{0.6}$ in a field up to 14 Tesla has provided evidence of the spin-exciton model where the resonance was clearly split into three peaks providing evidence of a spin-triplet state when spin-hole system has parallel spins(82). However this experiment was repeated by Shiliang Li *et al.*(83) and the splitting was not observed shedding some doubt on this picture.

Calculations of the dynamical susceptibility in the spin-exciton model have indicated that the enhanced intensity is caused by an unconventional superconducting gap. In particular, it is required that the superconducting gap have a **q**-dependent phase factor which allows it to have both positive and negative values. This applies to the d-wave symmetry seen in the cuprates and the sign reversing s-wave or (s+-) which is believed to be present in iron based superconductors. Therefore, the observation of a superconducting spin resonance by inelastic neutron scattering has provided important clues about the symmetry of the superconducting gap of unconventional superconductors. The appropriate form of generalized susceptibility is shown in equation (3.54).

$$\chi(\mathbf{Q},\omega) = \frac{\chi_0(\mathbf{Q},\omega)}{1 - V(\mathbf{Q})\chi_0(\mathbf{Q},\omega)} \tag{3.54}$$

In equation (3.54), $\chi_0(\mathbf{Q},\omega)$ is known as the bare susceptibility in the SC state. The form of $\chi_0(\mathbf{Q},\omega)$ is model dependent but it commonly describes the generalized susceptibility for a fermi gas and can be expressed in terms of the density of states and the appropriate band structure which is gapped by SC. $V(\mathbf{Q})$ is also model dependent but this function can represent an additional electron-electron or spin-spin interaction. Examples of $V(\mathbf{Q})$ include interband Coloumb repulsion (Hubbard U) or a Hund's rule based coupling commonly represented as J which is a spin-spin interaction. This form of $\chi(\mathbf{Q},\omega)$ allows for an susceptibility enhancement (divergence) when $1 - V(\mathbf{Q})\chi_0(\mathbf{Q},\omega) = 0$ where $\omega \neq 0$.

The following provides an explanation for how the resonance can occur when superconductivity is "turned on" in this model. Below T_c the electronic density of states below the superconducting gap $2\Delta_{SC}$ and therefore $\chi_0(\mathbf{Q},\omega)$ goes to zero because there are no states to

excite to in this region. Below T_c, an abrupt step up in $\chi_0''(\mathbf{Q},\omega)$ forms at 2Δ. As discussed in ref (84), through the use of Kramers-Kronig relations, it is shown that this causes $\chi_0'(\mathbf{Q},\omega)$ to have a logarithmic divergence at 2Δ but has finite values above and below. This is shown in Fig. 3.7. The condition for $1 - V(\mathbf{Q})\chi_0(\mathbf{Q},\omega) = 0$ is met below $2\Delta_{SC}$ at the resonance energy ω_{res} when $\chi'(\mathbf{Q},\omega) = 1/V(\mathbf{Q})$ while $\chi_0''(\mathbf{Q},\omega)$ simultaneously equals zero.

As will be discussed in chapter 5, this resonance was observed in superconducting samples $Ba(Fe_{1-x}Co_x)_2As_2$ with x = 0.047 (T_c = 17K) and 0.08 (where T_c = 22K). It is clear in both of these samples that the resonance condition is met for a continuum of $\mathbf{Q}$ values.

3.5 The triple axis spectrometer

3.5.1 Elements of the triple axis spectrometer

So far there has been discussion of the cross sections for various physical phenomena covered in the work but there has not been any indication of how these measurement are actually performed. In this section, the instrumental tool used in this work , the triple axis spectrometer will be explored. Fig. 3.8 shows a basic schematic of the triple axis spectrometer where the three axes are located on the monochromator cyrstal, the sample, and the analyzer.
As well be discussed further in section 3.5.1.2 and as is shown in Figure 3.8, during a triple axis experiment, the control of the monochromator crystal's orientation allows for the selection of the incident energy of the neutrons. The sample rotation axis along with the ability to place the detector arm at the appropriate scattering angle (2θ) allows for the selection of a specific momentum transfer vector and finally, the analyzer crystal orientation control allows for the selection the final energy of the neutron. The precise orientation of these elements allows elastic and inelastic processes can be selected. In what follows, a discussion of these components and other important elements of the triple axis experiment shown in Fig. 3.8 will be summarized.

3.5.1.1 The source of neutrons

For all neutron scattering studies covered in this work, the source of neutrons was nuclear reactor based where the neutrons are a product of the fission process. The reactor based sources

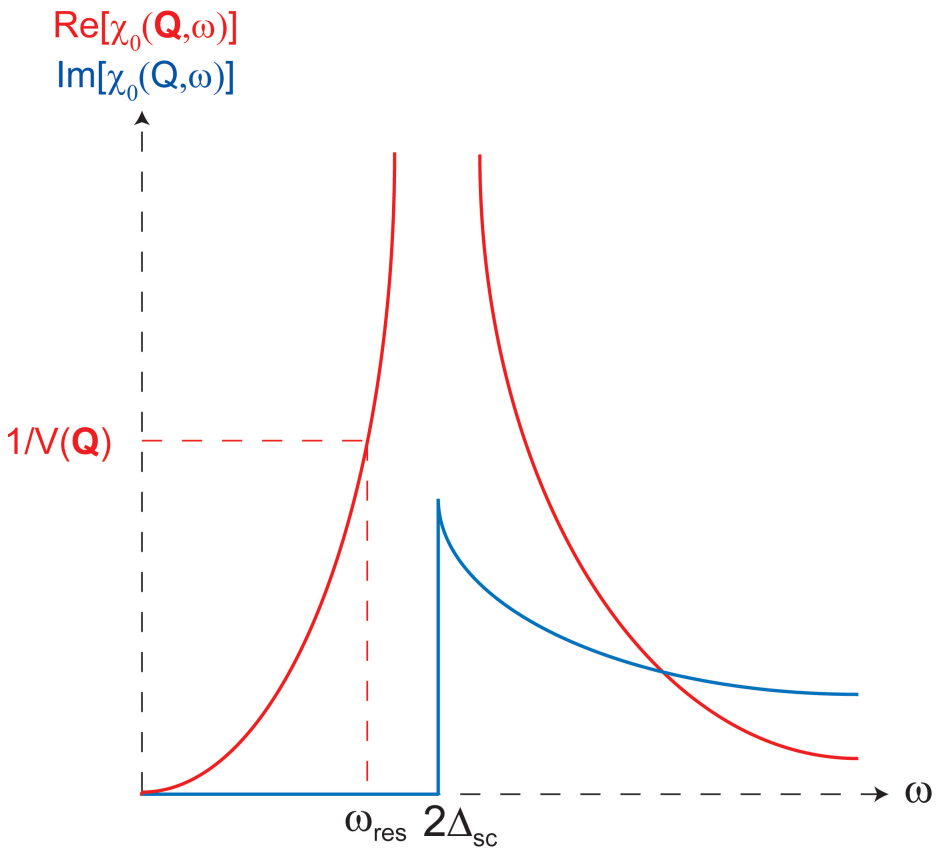

Figure 3.7 This schematically shows the effect of SC on $\chi_0''(\mathbf{Q},\omega)$ along with the resulting trend of $\chi_0'(\mathbf{Q},\omega)$ as determined from Kramers-Kronig relations. A condition for the resonance peak at ω_{res} in the RPA $\chi_0(\mathbf{Q},\omega)$ is that $\chi_0'(\mathbf{Q},\omega) = 1/\text{V}(\mathbf{Q})$ while $\chi_0''(\mathbf{Q},\omega)$ simultaneously equals zero.

used include the High Flux Isotope Reactor (HFIR) at Oak Ridge National Laboratory in Oak Ridge TN, the NIST Center for Neutron Research (NCNR) in Gaithersburg MD, the High Flux Reactor at the Institute Laue-Langevin (ILL) in Grenoble France, and the University of Missouri Research reactor (MURR) in Columbia MO. These reactor sources create a continuous flux of neutrons with high flux reactors such as HFIR producing 1×10^{15} neutrons/cm^{2}s with a Maxwellian energy distribution. As shown in Fig. 3.9, where the cylinders correspond to the nuclear fuel, the neutrons resulting from fission processes pass through a moderating material such as H_20 at $T \approx 350K$. The neutrons are then guided through beam ports toward the spectrometer. Neutrons achieve thermal equilibrium with the moderator with an energy distribution of $5 - 100$ meV or wavelength of $1 - 4\mathring{A}$. This wavelength range allows for the probing of common distances in crystal structures in condensed matter by diffraction.

3.5.1.2 The monochromator and analyzer

The beam of neutrons from the reactor source is composed of a wide range of energies ("white beam"), however a monochromatic beam is desired for the diffraction from a crystalline sample. Bragg scattering from the monochromator crystal is used to select the incident neutron energy (or wavelength). A typical monochromator is composed of a single crystal or collection of single crystals oriented to the incoming beam such that the Bragg condition is met. The relation between the wavelength and the monochromator angle is given by Bragg's law (55).

$$\lambda = d_{hkl} \sin(\theta_{\mathrm{M}}) \tag{3.55}$$

where d_{hkl} is the spacing between parallel planes of atoms in the crystal and $2\theta_{\mathrm{M}}$ is angle between the incident white beam and final monochromated beam. The reflectivity for a Bragg peak is related to the efficiency of producing a monochromatic beam and can be expressed as equation (3.56),

$$\begin{aligned} \mathcal{R}_p &= \frac{\mathcal{R}_0}{1 + \mathcal{R}_0} \\ \mathcal{R}_0 &= \frac{F_{\mathrm{N}}^2 \lambda^3 t_0}{v_0^2 \sqrt{2\pi}\eta \sin(2\theta_{\mathrm{M}}) \sin(\theta_{\mathrm{M}})} \end{aligned} \tag{3.56}$$

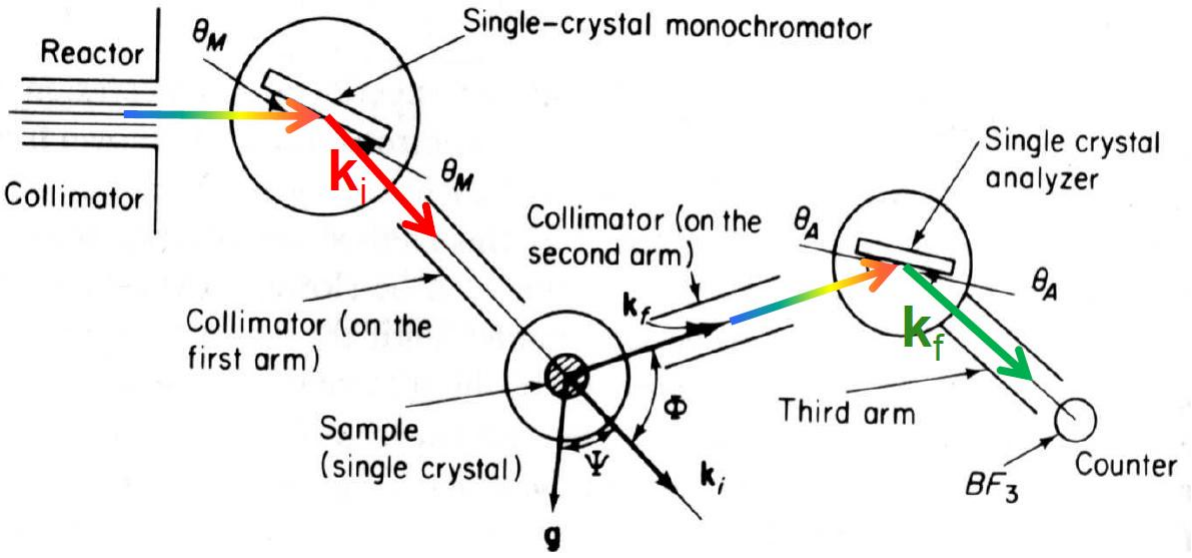

Figure 3.8 Schematic of a triple axis spectrometer

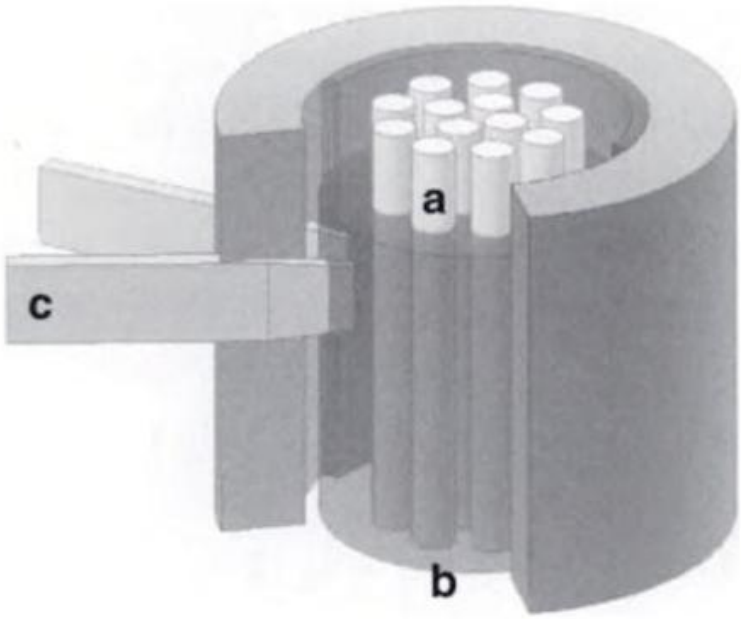

Figure 3.9 Schematic of a nuclear reactor that produces thermal neutrons (taken from ref (85)

where F_{N} is the nuclear structure factor, λ is the neutron wavelength t_0 is the thickness of the filter, v_0 is the density of unit cells and η is the crystal mosaic. It is important to note that it is useful to have a slightly imperfect crystal to minimize what is known as extinction. Extinction can be understood when considering the case of a perfect crystal where $\eta \approx 0$. For this case, when the Bragg scattering condition is met inside a crystal, because of the perfectly aligned planes throughout the crystal, there is a high probability of the same scattering condition to be encountered again as the neutron travels through the crystal and is scattered again. This can cause the neutron to be scattered out of the path toward the experiment which causes the intensity of the scattered beam to decreases. On the other hand for $\eta > 0$, there are misaligned grains in the crystal and theses misalignments of the scattering planes decrease the probability of additional scattering to take place and the beam intensity can increase. But as equation (3.56) suggests, there reaches a point where the increase in intensity due to the release of extinction related to a non zero η is dominated by the drop in intensity as the grains become further misaligned. Therefore a material where one can control η to find an appropriate balance between these effects would be ideal. Pyrolytic (ordered) graphite (PG) is commonly used because of this ability to control the mosaic spread while reflection off of the (002) reflection in the range of 4-40 meV has been shown to have reflectivies near 80% (86) This makes PG useful for thermal neutron scattering. Other common monochromator materials include Si, Ge, and Be. Due to the small lattice spacing in Be, the ratio (F_{N}^2/v_0) in equation (3.56) is large for the (002) reflection which makes a Be monochromator useful for high incident energies such as $E_{\mathrm{i}} > 50$ meV.

After the neutrons scatter from the sample under investigation, the beam is no longer monochromatic as neutrons gain or lose energy due to inelastic processes. This process is represented by the multi-colored arrow in Fig. 3.8. Through the use of an analyzer crystal, which is a second monochromator in the beam path after the sample, the final neutron energy can be selected and a monochromatic beam can be guided to the detector system. This allows for the study of elastic processes ($E_{\mathrm{i}} = E_{\mathrm{f}}$) which provides information about static crystal structure. Additionally, the energy spectrum associated with a particular momentum transfer can be probed through the selection of non zero energy transfers ($E_{\mathrm{i}} \neq E_{\mathrm{f}}$).

3.5.1.3 Collimation

Neutrons emerge from the reactor moving in all directions and need to be guided to the experiment. While lengthy beam tubes (which are labeled by the letter c in Fig. 3.9) provide a limit on the potential horizontal angular divergence of the beam, it is useful to further control the angular divergence of the beam. This can be done with the use of a Soller collimator. A Soller collimator consists of a rectangular frame which holds equally spaced and parallel vertical plates aligned parallel with the beam which are coated with a neutron absorbing material such as cadmium or gadolinium oxide. The angular divergence of the beam is controlled by adding plates and therefore changing the distance between plates. It is common to have collimators located before the monochromator, between the monochromator and sample, between the sample and analyzer, and between the analyzer and neutron detectors. Tightening the angular divergence using collimators improves the resolution of the spectrometer with the cost of a decreased neutron beam intensity. The correct balance of intensity and resolution will depend on the purpose of an experiment.

3.5.1.4 Filters

As discussed earlier, a monochromator selects the energy of the incident beam but unfortunately, higher energy neutrons are also selected because for a given monochromator reflection indexed (h, k, l), higher order reflections (or harmonics) (nh, nk, nl) where n is an integer will also pass and have an associated wavelength $\frac{\lambda}{n}$ where λ is the desired initial neutron wavelength. These higher energy neutrons can produce additional observed peaks which can easily be misinterpreted. Therefore, it is important to employ filters to minimize the presence of higher order wavelengths.

For thermal neutrons, the use of an oriented PG filter is commonly used. The PG is oriented such that the PG crystal's c-axis is oriented along the neutron beam. Investigations into PG filters (87) showed that for such an oriented filter, the largest cross section occurs for $1.17\mathring{A}$ neutrons. Therefore the $\frac{\lambda}{2}$ higher harmonic for $\lambda = 2.36\mathring{A}$ ($E_{\mathrm{i}} = 14.7$ meV) is significantly attenuated. It was also shown (88) that there is a maximum attenuation of $\frac{\lambda}{3}$ near 14 meV

making the range of 14-15 meV an ideal range of initial energies to employ PG filters.

3.5.1.5 Neutron detection

The ^{3}He proportional counter is useful for detection of thermal neutrons because ^{3}He large neutron cross section. Because neutrons do not directly ionize atoms, they are detected indirectly through a process that produces charged particles. For ^{3}He proportional counters, this involves the reaction $^3\mathrm{He} + {}^1_0\mathrm{n} \rightarrow {}^3\mathrm{H} + {}^1_1\mathrm{H} + +0.77$ MeV. The ${}^3_1$H and ${}^1_1$H ions are counted and the ion detection rate is proportional to the neutron flux.(89).

3.5.2 Triple axis data analysis

3.5.2.1 Bragg diffraction

The triple axis spectrometer has proven to be an extremely useful tool for the measurement of elastic scattering due to the highly reflective analyzer crystals which select the condition that $E_\mathrm{f} = E_\mathrm{i}$. This selection reduces the background from inelastic processes which improves the signa-noise ratio making it possible to measure small single crystals where the intensity may be low. It is optional to remove the analyzer crystal from the beam path and convert the triple axis to a 2-axis spectrometer. The two configurations are shown in Fig. 3.10. In this arrangement, the detector will pick up the entire spectrum of "white" beam from the crystal consisting of intensity from both elastic and inelastic processes. One advantage of the 2-axis mode is that the integrated intensity from a longitudinal scan through a Bragg Peak is related to the structure factor through the use of equation (3.57). The scan path for a longitudinal scan is shown in Fig. 3.11.

$$\mathcal{I} \propto \frac{|F(h,k,l)|^2}{\sin(2\theta_\mathrm{S})} \tag{3.57}$$

In equation (3.57), the structure factor could describe nuclear scattering as equation (3.19) or the magnetic scattering as in equation (3.37). The factor $\frac{1}{\sin(2\theta_\mathrm{S})}$ is known as the Lorentz factor and this factor depends on the geometry of the experiment The simple form of the Lorentz factor can be used for triple axis experiments because both incoming and outgoing

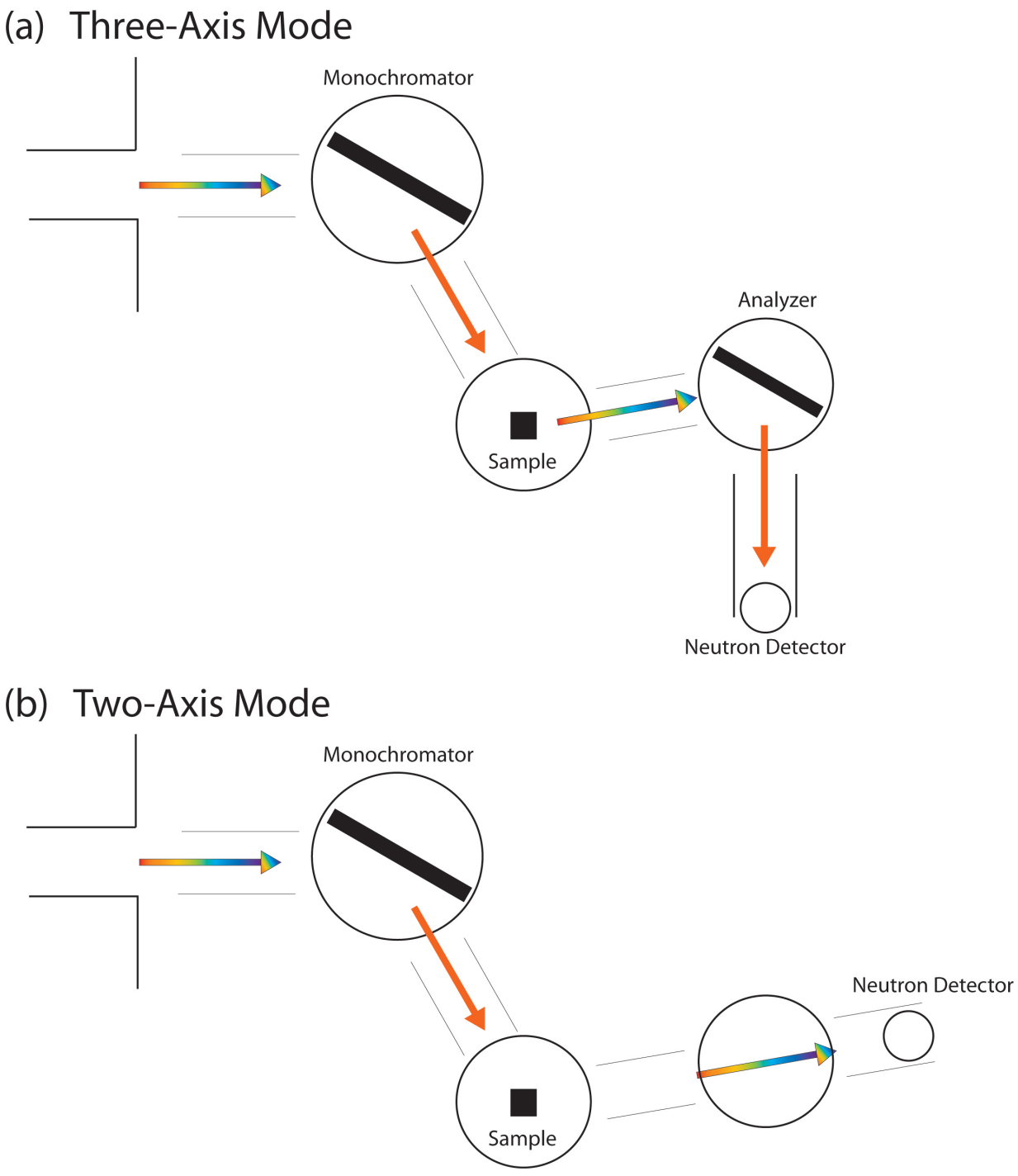

Figure 3.10 The triple axis spectrometer configuration in (a) Three-axis mode and in (b) Two-axis mode

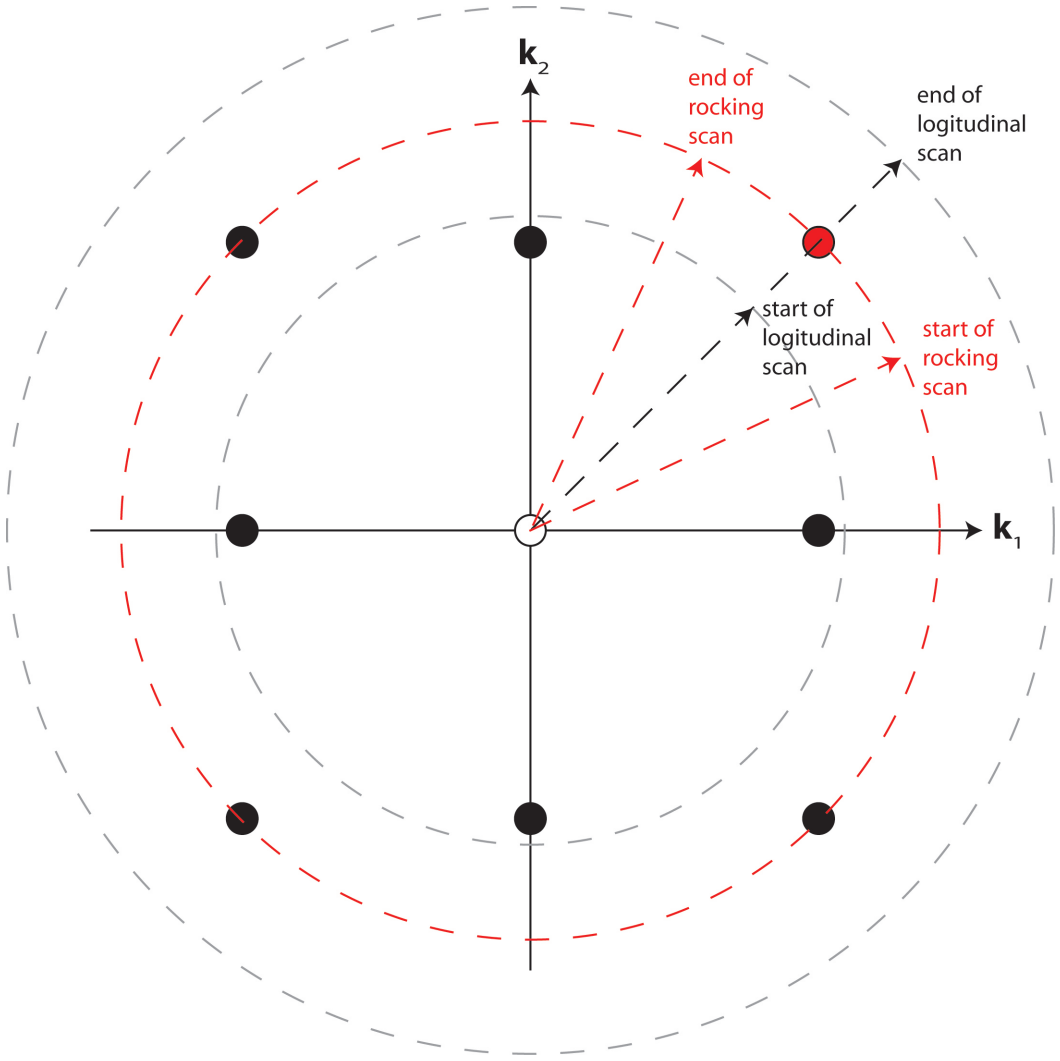

Figure 3.11 The path in reciprocal space followed during longitudinal scans and rocking scans which are commonly performed during a triple-axis experiment

beams coincide with the scattering plane probed (90). It was shown by R. Pynn (91) that for samples with mosaic widths below $60'$, there is little deviation from the integrated intensity of longitudinal scans when comparing 2-axis and 3-axis modes. On the other hand if scans where the crystal is rotated or rocked through the Bragg peak are performed which can be visualized using figure Fig 3.10, significant deviation is observed with comparing 2-axis and 3-axis modes for any sample mosaic width(91).

Equation (3.57) was commonly employed during experimentation as a test to confirm that the crystals studied had the expected crystal structure. For example, the magnetic structure of the $Ba(Fe_{1-x}Co_x)_2As_2$ was verified thorough the measurement of the $(\frac{1}{2}\ \frac{1}{2}\ 1)_{\mathrm{T}}$ and $(\frac{1}{2}\ \frac{1}{2}\ 3)_{\mathrm{T}}$ magnetic Bragg peaks. The ratio of the integrated intensities of the two magnetic peaks shown in equation (3.58) was found during experiments and compared to the expected value from structure factor calculations using the magnetic structure found by Goldman *et al.* (92).

$$\frac{\mathcal{I}(\frac{1}{2}\frac{1}{2}3)}{\mathcal{I}(\frac{1}{2}\frac{1}{2}1)} = \frac{\left|\mathcal{F}^2(\frac{1}{2}\frac{1}{2}3)\right| \sin(2\theta_{\frac{1}{2}\frac{1}{2}1)})}{\left|\mathcal{F}^2(\frac{1}{2}\frac{1}{2}1)\right| \sin(2\theta_{\frac{1}{2}\frac{1}{2}3)})} \tag{3.58}$$

3.5.2.2 Inelastic scattering - resolution convolution

The utility of a modern triple axis spectrometer is the ease of reaching very accurate points as well as traversing specific paths in $\mathbf{Q}$-ω space. This is due to the development over many years of mathematical formalism and computer software which to calculate the relative angular positions of the components of the spectrometer as well as accurately control the motors which position the components. The users of the triple axis spectrometer have the ability easily scan regions of reciprocal space and measure data that can be directly analyzed.

One draw back of measuring an inelastic scattering when compared to elastic scattering is the signals can be orders of magnitude smaller. This can be dealt through the measurement of large samples as well as using collimators with large angular divergence which allow higher neutron flux through the sample. Commonly both large single crystals and angular divergent beam are required. This spreading of intensity $(\Delta\mathbf{Q}, \Delta\omega)$ about some target position $(\mathbf{Q}_0, \omega_0)$ due to the angular divergence is not only due to collimation but due to the mosaic spread of the monochromator, the sample, and the analyzer crystals. The resulting intrinsic intensity

connected to a physical process in side the sample is convoluted with this spread and therefore during a measurement the intensity is a function of both. In other words, the spread of intensity is a signature of the resolution of the spectrometer $R(\mathbf{Q}-\mathbf{Q}_0)$. The intensity observed during a measurement $I(\mathbf{Q},\omega)$ is a convolution of this resolution function with the scattering function $S(\mathbf{Q},\omega)$.

The sizable 4-D resolution of the spectrometer related to the intensity transmission distribution of each of the components and approximate numerical calculations of the resolution can be performed under the assumption that each of the components and the sample transmit a gaussian distribution of intensity. The overall resolution function is related to a product of all the Gaussian distributions which have a FWHM equal to the angluar allowance for the case of the collimator or the crystal mosaic for the monochromator, sample, and analyzer. The shape, orientation and volume of this 4-D resolution function was first described by Cooper and Nathans (93) and Chesser and Axe (94). In practice, the size and orientation of the resolution function can be calculated with the assistance of the Matlab programing language and interactive environment to execute programs such as Reslib (95) and Rescal (96). Fig. 3.12 shows an example of a constant contour representation of the "resolution ellipsoid" where horizontal mosaic spread of the PG(002) (where (002) refers to the reflecting plane in ordered graphite) were set to $24'$ and the collimators were assumed to have $20'$ angular allowance. The shape is commonly referred to as a flattened cigar.

Through the use of the Maltab program Reslib, the effects of resolution on the intrinsic scattering signal from the sample $S(\mathbf{Q},\omega)$ can be analyzed. Reslib has the ability to calculate the resolution function appropriate to each data point or position in ($\mathbf{Q}$,ω)-space by inputting the experimental parameters such as the collimator divergences, monochromator, sample, and analyzer mosaics, the crystallographic information of the crystal, and incident neutron energy. Reslib can then numerically convolute a model cross section such as the one shown in equation (3.49), and fit the resulting convoluted cross section to the observed data by varying the parameters from the model (95). This was done to extract information about $S(\mathbf{Q},\omega)$ during inelastic measurements discussed in chapter 5. An example convolution is shown in Fig. 3.13 where data was fit to a scattering function model shown in equations (3.49) and (3.50). Fig.

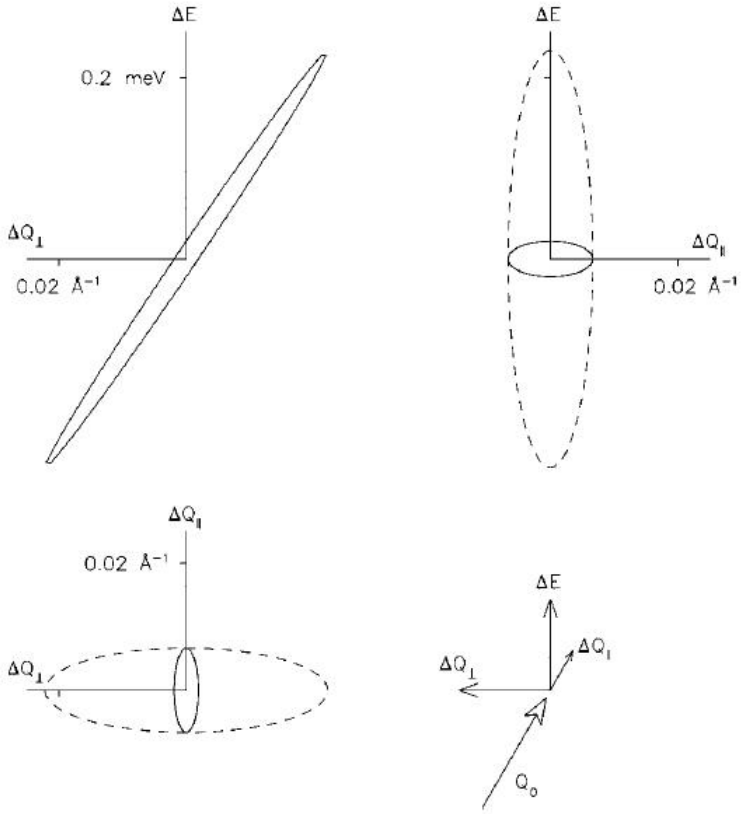

Figure 3.12 Example resolution ellipsoid where the solid lines represent the cross section of the ellipse in plane and the dashed lines show the projection into the plane. The spectrometer parameters are discussed in the text. This figure was taken from ref (88)

3.13 shows both the fitting results for S($\mathbf{Q}$,ω) along with the actual observed intensity with a curve through the data which represents S($\mathbf{Q}$,ω) convoluted with the resolution function. In this example, the resulting intensity for this scan suggests that the actual excitation spectrum is quite broad in energy resulting in similar peak widths between the actual dispersion and convoluted observations. The main effect is the reduction in intensity caused by renormalization of the intensity due to a sizable resolution volume.

The orientation of the resolution ellipsoid during can have a dramatic effect on the observed intensity and width of an excitation, and if possible, it is important to consider the orientation of the ellipsoid relative to the excitation dispersion $\omega(\mathbf{Q})$. As shown in Fig. 3.14, if the long axis of the resolution ellipse is parallel to the dispersion, the spectrometer is focused in that region of $(\mathbf{Q}, \omega)$ space. When focusing is achieved, the resolution will traverse the dispersion in a small range of $\Delta\mathbf{Q}$ or ΔE and because of this, the intensity will be sharp and intense. On the other hand, if the spectrometer is unfocused, the resulting intensity will be spread out because of the resolution convolution and in extreme cases may be unobservable (97). Fig. 3.15 demonstrates the effect of focusing. Lattice excitations or phonons were measured near $\mathbf{Q} = (2\ 2\ \pm 0.6)_{\mathrm{T}}$ in reciprocal lattice units and at neutron energy loss of $\hbar\omega = 5.4$ meV. A clear difference in the intensity distribution is observed between the focused region of reciprocal space near $(\mathbf{Q}, \hbar\omega) = ((2\ 2\ -0.6)_{\mathrm{T}}, 5.4$ meV) and the defocused region near $(\mathbf{Q}, \hbar\omega) = ((2\ 2\ 0.6)_{\mathrm{T}}, 5.4$ meV).

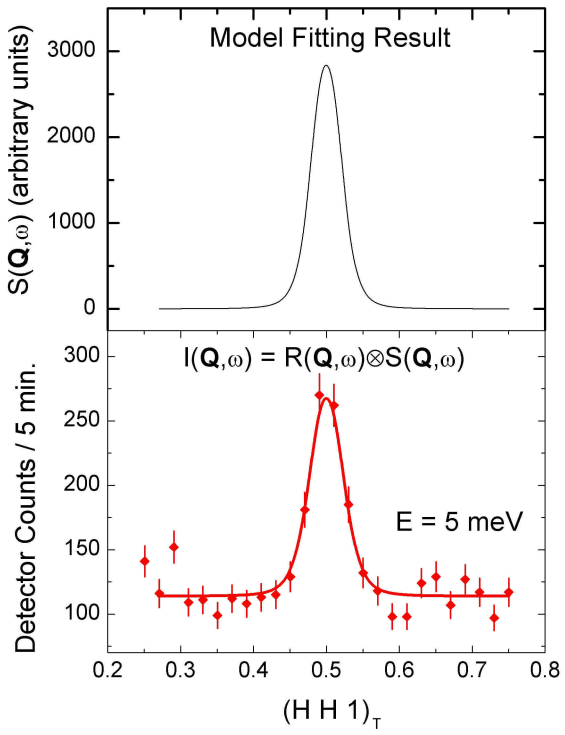

Figure 3.13 (a) The resulting S(**Q**,ω) from a fitting a magnetic excitation in using Reslib (b) The observed intensity along with the curve representing the resolution convolution with the results shown in (a).

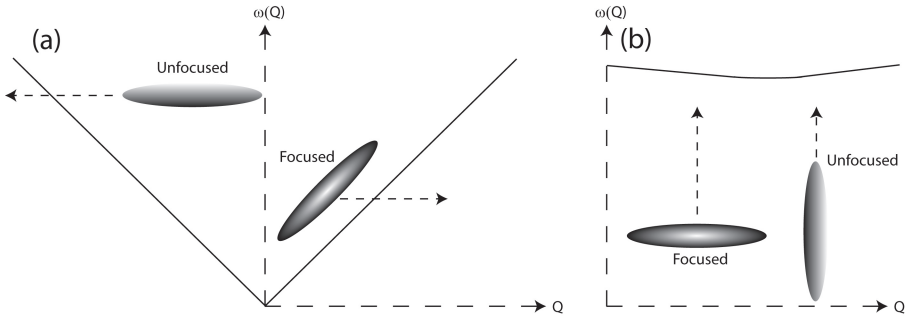

Figure 3.14 Focused and unfocused (a) **Q** scans and (b) energy scans.

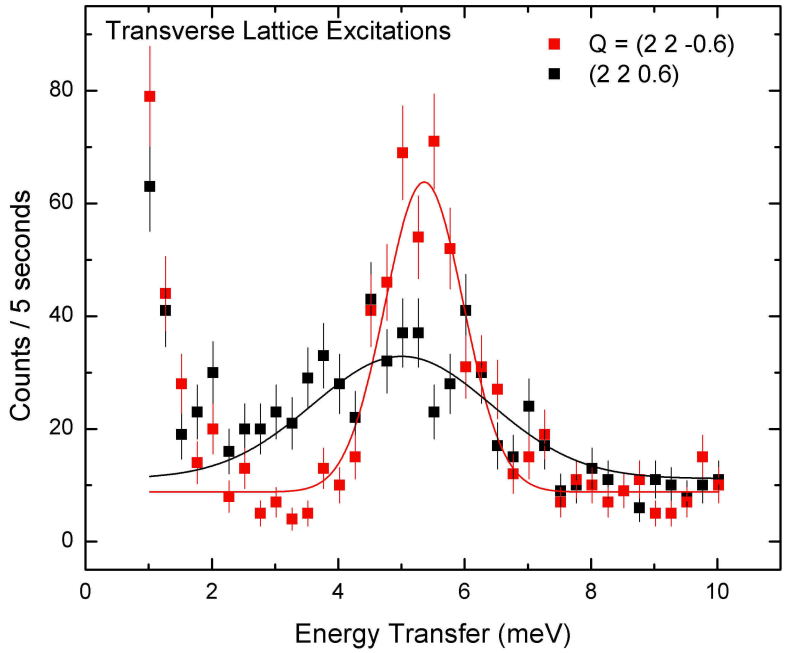

Figure 3.15 Transverse lattice excitations (motion transverse to the (1 1 0) direction) were measured in regions of -space where the triple axis was focused ($\mathbf{Q} = (2\ 2\ -0.6)_{\mathrm{T}}$) and defocused ($\mathbf{Q} = (2\ 2\ 0.6)_{\mathrm{T}}$). The lines are guides to the eye.

CHAPTER 4. Effects of pressure application on structure and magnetism in $CaFe_2As_2$

4.1 Introduction

Prior to the work described in this thesis, it was believed that pressure application had the same effect of doping in that it suppressed the structural and magnetic phases observed at ambient pressure sufficiently such that the conditions for SC can occur. The suppression of the resistive signature associated with the magnetic transition was observed in $CaFe_2As_2$ to be suppressed from 170 K at ambient pressure to 128 K at 0.35 GPa and SC was observed from 2.3 to 8.6 kbar (4). This was an exciting observation because it has been established in the copper oxide high temperature superconductors (HTSC) that the suppression of AFM order is necessary for SC to develop. Studies of the development of SC in the HTSC iron arsenides had the benefit that the induced disorder (which is expected to occur after chemical substitution) does not occur and pressure potentially provided a much cleaner way to study the development of superconductivity.

As is discussed in this chapter the details of the p-T diagram are dependent on the pressure application method. Early experiments used fluid pressure medium which solidified at high pressures. This placed the samples in complicated pressure gradients which placed different pressures on the different faces of the crystals (non-hydrostatic pressure)(4; 6; 7). Only through the use of a He gas medium (maximizing hydrostatic pressure) was a clear and a consistent picture of the p-T phase diagram developed. Eventually it became clear that under hydrostatic pressure, the cT phase seems to disrupt the development of SC.

Neutron powder diffraction measurements using a He gas pressure cell discovered that $CaFe_2As_2$ stood out amongst the other 122 superconductors as it transitioned to what is known

as a collapsed tetragonal (cT) phase with very modest pressures (5). It was also shown in this work that the established long range antiferromagnetic structure discussed in chapter 2 which consisted of antiferromagnetic stripe ordering (AF2 structure) was absent in the collapsed tetragonal phase. However, theoretical calculations by T. Yildrim (67) have suggested that the cT phase is in fact magnetic and new magnetic structures need to be explored to settle this issue. T. Yildrim suggested that an additional antiferromagnetic moment arrangement was possible which can be described as each iron plane having a spin-checkerboard structure (AF1 structure). The checkerboard spin structure could be antiferromagnetically coupled along the c-direction (also known as AF1-G) or ferromagnetically coupled along the c-direction (AF1-C). The ambient pressure AF2 magnetic structure and the two possible AF1 structures are shown in Figure 4.1.

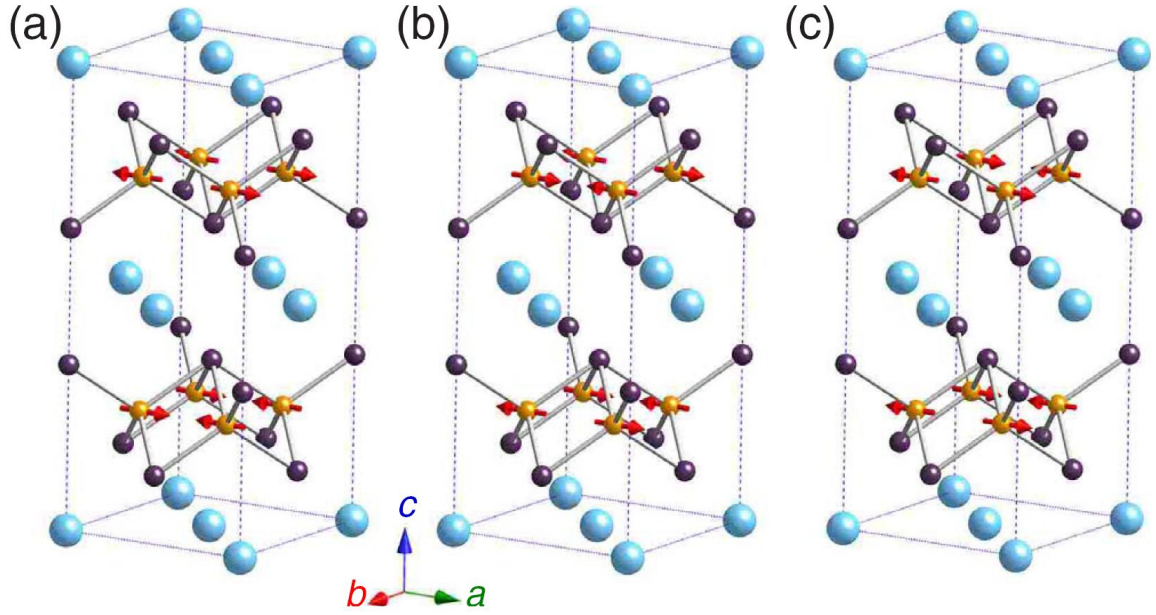

Figure 4.1 Magnetic structures for $CaFe_2As_2$ shown in the orthorhombic unit cell to facilitate comparison. (a) The AF2 magnetic structure realized at ambient pressure below 170 K (92). (b) Representation of the AF1 G-type antiferromagnetic structure with antiferromagnetic ordering along the **c** axis. (c) Representation of the AF1 C-type antiferromagnetic structure with ferromagnetic ordering along the c axis.

It is important to settle this issue of whether or not the cT phase was magnetic as it could provide an explanation for the disruption of SC. In this chapter, we will demonstrate through

the study of single crystal samples where the p-T phase diagram is thoroughly mapped under hydrostatic pressure, that the likely scenario of the none of the proposed magnetic order in the cT phase exist. Also, studies of paramagnetic fluctuations show that the moment is completely suppressed in the cT phase providing another clue as to why SC is absent in the scenario that SC is mediated by paramagnons. In the last section, a study of $CaFe_2As_2$ under maximized non-hydrostatic pressure provided that pressure SC does develop in a high pressure stabilized non-collapsed tetragonal phase.

4.2 The pressure-temperature (p-T) phase diagram

Neutron scattering measurements (at the NIST Center for Neutron Research (NCNR) on the BT-7 diffractometer) were performed in a double-axis mode using a wavelength of $\lambda = 2.36$ Å and two pyrolytic graphite filters to reduce higher harmonic content of the beam. A 10 mg single crystal (3 X 3 X 0.2 mm^3) wrapped in Al foil was secured to a flat plate and cooled using a closed-cycle refrigerator. An Al-alloy He-gas pressure cell was used which was connected to a pressurizing intensifier through a high-pressure capillary that allowed continuous monitoring and adjusting of the pressure. Using this system, the pressure could be varied at fixed temperatures (above the He solidification line) or the temperature could be scanned at nearly constant pressure. A helium reservoir allowed the pressure to remain relatively constant as the temperature was changed. The finite size of the reservoir, however, results in some change in pressure over the temperature range measured on the order of 15% for the highest pressures (≈0.6 GPa).The sample was oriented so that the $(h\ h\ l)_{\mathrm{T}}$ reciprocal lattice plane was coincident with the scattering plane of the diffractometer.

The p-T phase diagram for $CaFe_2As_2$ was explored by monitoring selected crystallographic and magnetic Bragg peaks as the sample environment was cycled along a series of paths in the p-T phase diagram. These paths included isobars where the sample was cooled or heated at a selected starting pressure, or isotherms as we pressurized and depressurized to cross a phase line at a constant temperature. The results are shown in Fig 4.2 (a-i).

Starting with the high-temperature-tetragonal to orthorhombic (T-O) transition, both the $(2\ 2\ 0)_{\mathrm{T}}$ and $(1\ 1\ 2)_{\mathrm{T}}$ structural peaks were monitored to observe the peak splitting or broad-

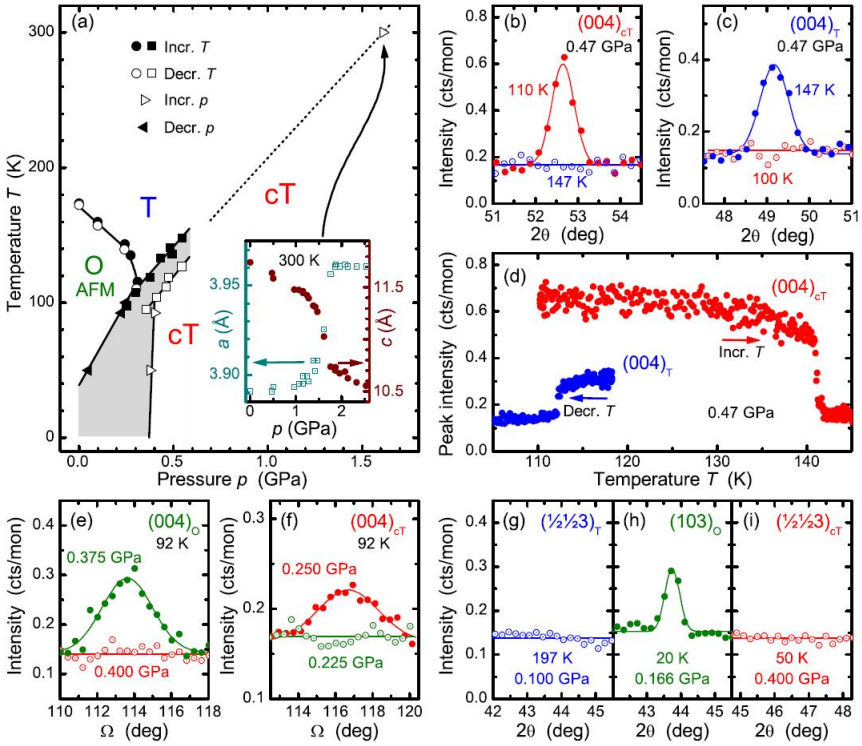

Figure 4.2 (a) Pressure-temperature phase diagram of $CaFe_2As_2$ under hydrostatic pressure. Filled and open circles (squares) denote phase boundaries determined upon heating and cooling at a set pressure for the O-T (cT-T) phase transition. Filled and open triangles denote phase boundaries determined upon decreasing and increasing pressure at a fixed temperature. The shading denotes hysteresis. The inset of (a) shows the lattice constants near the T-cT transition at 300 K. In (b)(i), the color codes denote measurements of the T phase (blue), O phase (green), or cT phase (red) diffraction peak positions. (b) Ω-2θ scans of the $(0\ 0\ 4)_{\mathrm{cT}}$ peak at 0.47 GPa on increasing temperature. (c) Ω-2θ scans of the $(0\ 0\ 4)_{\mathrm{T}}$ peak at 0.47 GPa on decreasing temperature. (d) Temperature dependence of the peak intensities of the $(0\ 0\ 4)_{\mathrm{T}}$ as the temperature is decreased at p=0.47 GPa and the $(0\ 0\ 4)_{\mathrm{cT}}$ as the temperature is increased at p=0.47 GPa. (e) Ω scans through the $(0\ 0\ 4)_{\mathrm{O}}$ peak at 92 K as the pressure is increased from 0.375 to 0.400 GPa. (f) Ω scans through the $(004)_{\mathrm{cT}}$ peak at 92 K as the pressure is decreased from 0.250 to 0.225 GPa. (g) Ω-2θ scans through the expected position of the $(\frac{1}{2}\ \frac{1}{2}\ 3)_{\mathrm{T}}$ magnetic peak in the tetragonal phase. (h) Ω-2θ scans through the observed position of the $(1\ 0\ 3)_{\mathrm{O}}$ magnetic peak. (i) Ω-2θ scans through the expected position of the $(\frac{1}{2}\ \frac{1}{2}\ 3)_{\mathrm{cT}}$ magnetic peak.

ening associated with the orthorhombic distortion. This provided a clear indication of a sharp transition. In Fig. 4.2a, the location of these transitions in the phase diagram are represented as open circles for isobaric cooling through the phase line (T-O transition) and filled circles for warming through the phase line (O-T transition). A small hysteresis of 2-3 K was observed which is related to the first order nature of this transition.

The collapsed tetragonal-to-tetragonal (cT-T) transition was monitored by warming the sample at high pressure while measuring the 2θ values of the $(0\ 0\ 4)_{\mathrm{cT}}$ and $(0\ 0\ 4)_{\mathrm{T}}$ peaks. In Fig. 4.2a, the transitions upon warming are labeled with black squares (cT-T transition) while the transitions observed upon cooling are labeled with open squares (T-cT transition). As mentioned in section 4.1, a large change in the length of the c lattice parameter is expected for any transition to, or from, the cT phase which results in a large change in the 2θ values for any Bragg peak with non zero 'l'. As can be seen in Fig. 4.2b and 4.2c, there is a clear difference 2θ values of $(0\ 0\ 4)_{\mathrm{cT}}$ and $(0\ 0\ 4)_{\mathrm{T}}$ peaks found at 52.7° and 49.2° (where $\lambda_{\mathrm{i}} = 2.36$ Å) respectively. This change 2θ corresponds to a 7% increase of the c lattice parameter when transitioning at $p = 0.47$ GPa and 147 K which is comparable to the 9% change in the c lattice parameter observed previously (5). Fig. 4.2d shows a set of measurements conducted while traversing the isobar at $p = 0.47$ GPa and the large pressure hysteresis involved in this transition is apparent. Upon heating, a sharp cT-T transition was observed at 141K while upon cooling, a sharp T-cT was observed at 112 K. The grey shading in Fig. 4.2(a) highlights the region where hysteresis is observed either in pressure or temperature during the different paths taken through the p-T phase diagram. Additionally, as can be observed in Fig. 4.2b and 4.2c, the $(0\ 0\ 4)_{\mathrm{cT}}$ peak is more intense and has a smaller peak width in comparison to the $(0\ 0\ 4)_{\mathrm{T}}$ after one cycle through the cT-T transition. This increase in mosaic was observed in subsequent transitions through this phase line indicating this first order transition causes irreversible damage to the crystal.

The (O-cT) transition was measured isothermally at selected temperatures. In Fig 4.2a, the transitions observed when pressurizing are labeled with open triangles (O-cT transition) and upon depressurizing by filled triangles (cT-O transition). A transition was again observed through a large change in the c lattice parameter determined by the change in 2θ position

between the $(0\ 0\ 4)_{\mathrm{cT}}$ and $(0\ 0\ 4)_{\mathrm{O}}$ crystallographic peaks. Fig. 4.2e shows a rocking scan of the $(0\ 0\ 4)_{\mathrm{O}}$ peak taken prior to pressurizing across the phase boundary at 92K. After pressurizing, in 0.025 GPa increments, up to 0.400 GPa the sample transformed from O to cT. By comparing the rocking scan in Fig. 4.2e with Fig 4.2f, one can again see that the mosaic has increased as the sample is damaged further by the transition to the cT phase. Upon decreasing the pressure at the same temperature (92 K), the transition back to the O phase did not occur until 0.225 GPa, revealing a large pressure hysteresis ($\Delta p = 0.175$ GPa) at this temperature. Upon cooling to 50 K, a similar set of scans revealed an even larger hysteresis of $\Delta p = 0.325$ GPa. Again the expected region of hysteresis is shaded grey in Fig. 4.2a. This highlighted hysteresis range, both in temperature and pressure, provides an explanation for the discrepancies in reported phase diagrams mentioned in the introduction of this chapter.

To explore the phase diagram in more detail and to verify the findings of H. Lee *et al.* (7), which claim the existence of a new phase that may exist above 0.75 GPa, high energy x-ray measurements were performed at the Advanced Photon Source (APS) and full details of the measurements are described in reference (8). Diffraction patterns, using x-rays with energies of 100 keV ($\lambda = 0.124$ Å), were recorded on a MAR345 image plate system using a detector rocking technique which allowed for the measurements of reciprocal lattice planes in a single measurement (113). The highest pressures reached using the He gas pressure medium was 0.6 GPa, therefore a Merrill-Bassett diamond anvil pressure cell was employed at room temperature using a mixture of ethanol and methanol as a pressure medium. Entire reciprocal lattice planes, namely $(h\ h\ l)_{\mathrm{T}}$ and $(h\ 0\ l)_{\mathrm{T}}$, were imaged allowing us to track the lattice parameters, as well as any changes in crystal symmetry, through the loss or appearance of Bragg peaks. The only observed changes at 300 K were consistent with a transformation from the T-to-cT phase at 1.6 GPa, with the collapse of the c lattice parameter and expansion of the a lattice parameter as shown in the inset of Fig 4.2a. No other indications of a new phase were observed for pressures up to 2.5 GPa ant 300 K.

4.2.1 Magnetism

The magnetic ordering in the O phase at ambient pressure was established during single crystal studies (92), but one of the most interesting results of the original report of a cT phase from neutron powder diffraction measurements (5) is the disappearance of Fe magnetic ordering. Nevertheless, theoretical calculations by T. Yildrim (67) have suggested that the cT phase remains magnetic, but has a different structure. The following discusses measurements performed at the NCNR which looked into the known and theorized magnetic structures.

The AF2 magnetic structure that is observed at ambient pressure, as shown in Fig 4.2(a), consists of spin stripes along the **b** direction which are AF coupled along **a** and **c** which can be monitored from measurements of the magnetic Bragg peak [$(\frac{1}{2}\ \frac{1}{2}\ l)$ in T or cT reciprocal lattice units, or $(1\ 0\ l)_{\mathrm{O}}$ in the orthorhombic unit cell with $l = 1$ and 3]. To maximize the intensity of the magnetic scattering relative to the substantial background from the pressure cell, these data were taken on a composite of eight single crystals, attached to an Aluminum support plate using Fomblin oil, with the diffractometer operated in triple-axis mode using a PG(002) analyzer. The single crystals (combined mass of approximately 60 mg) were co-aligned so that their common $(h\ h\ l)_{\mathrm{T}}$ plane was aligned in the scattering plane. The mosaic of the composite sample with respect to the $(h\ h\ 0)_{\mathrm{T}}$ and $(0\ 0\ l)_{\mathrm{T}}$ directions was approximately 1° full width at half maximum(FWHM). Selected Bragg peaks were measured after each parameter change. The sample first was cooled to 75 K at ambient pressure, which transformed the sample from the T phase to the O phase, and then pressurized up to 0.45 GPa with 0.05 GPa steps, which transformed the sample from the O phase to the cT phase. The sample was then cooled to 50 K and then the pressure was released with increments of 0.05 GPa until ambient pressure was reached.

The results for measurements upon pressurizing at 75 K are shown in the upper panel of Fig. 4.3 while the lower panel summarizes the results for depressurizing at 50 K. The phase volume fraction of the O and cT phases were found using equation (1)

$$VF_i = I_{004i}/(I_{004_{\mathrm{O}}} + I_{004_{\mathrm{cT}}}), i = \mathrm{O,cT} \tag{4.1}$$

where VF_i represents the volume fraction of either the O or cT phase at given temperature and pressure while I_{004i} is the integrated intensity of the (0 0 4) O or cT nuclear Bragg peak. Also shown in Fig. 4.3, the integrated intensity of the magnetic peak is shown in the top panel as the sample is pressurized at T = 75 K, and in the bottom panel as the sample is depressurized at T = 50 K.

Upon increasing pressure in the O phase at 75K, a transition is observed at 0.4 GPa. At this pressure, intensity was observed at both (0 0 4) O and cT positions indicating a roughly equal volume fraction of O and cT phases. Also, roughly half of the magnetic intensity was lost which is consistent with the volume fraction. Upon depressurizing from 0.5 GPa at 50K, a transition back to the O phase was observed at 0.75 GPa. The phase coexistence was observed in the measurements on a single crystal within our steps of 0.025 GPa and this can be explained by considering that the crystal assembly was held in alignment with Fomblin oil which is constraining the sample as the oil freezes. In addition to the fact that the transition is first order, the additional pressure gradients caused by the oil may be responsible for the extended range of observed coexistence. An incomplete transition occurs as ambient pressures are reached and phase coexistence is present due to sample constrains in frozen oil.

Fig 4.3. demonstrates that the magnetic Bragg intensity associated with the AF2 order is completely lost upon complete transformation to the cT phase, consistent with previous measurements by Kreyssig *et al.* (5). Theoretical calculations by T. Yildrim (67) have suggested that the presence of an AF1 ordering along with a 40% reduction of the iron moment can explain the lattice parameter changes observed in the cT phase. Even though neutron powder diffraction measurements, which discovered the cT phase, did not report any additional magnetic peaks, the signal to noise ratio may have been too low due to a significantly reduced moment. This motivated a search for new magnetic order from single crystal measurements. The possible AF1 structures are shown in Fig. 4.1b and 4.1c. The AF1-G type structure as shown in Fig 4.1b consists of spins antiferromagnetically correlated in all three dimensions and will produce magnetic Bragg peaks at $(h\ 0\ l)_{\mathrm{cT}}$ positions with h and l being odd. These peaks are coincident with allowed nuclear peaks and, therefore, are difficult to observe in general, especially if the moment is small. The AF1-C type structure as shown in Fig 4.1c consists

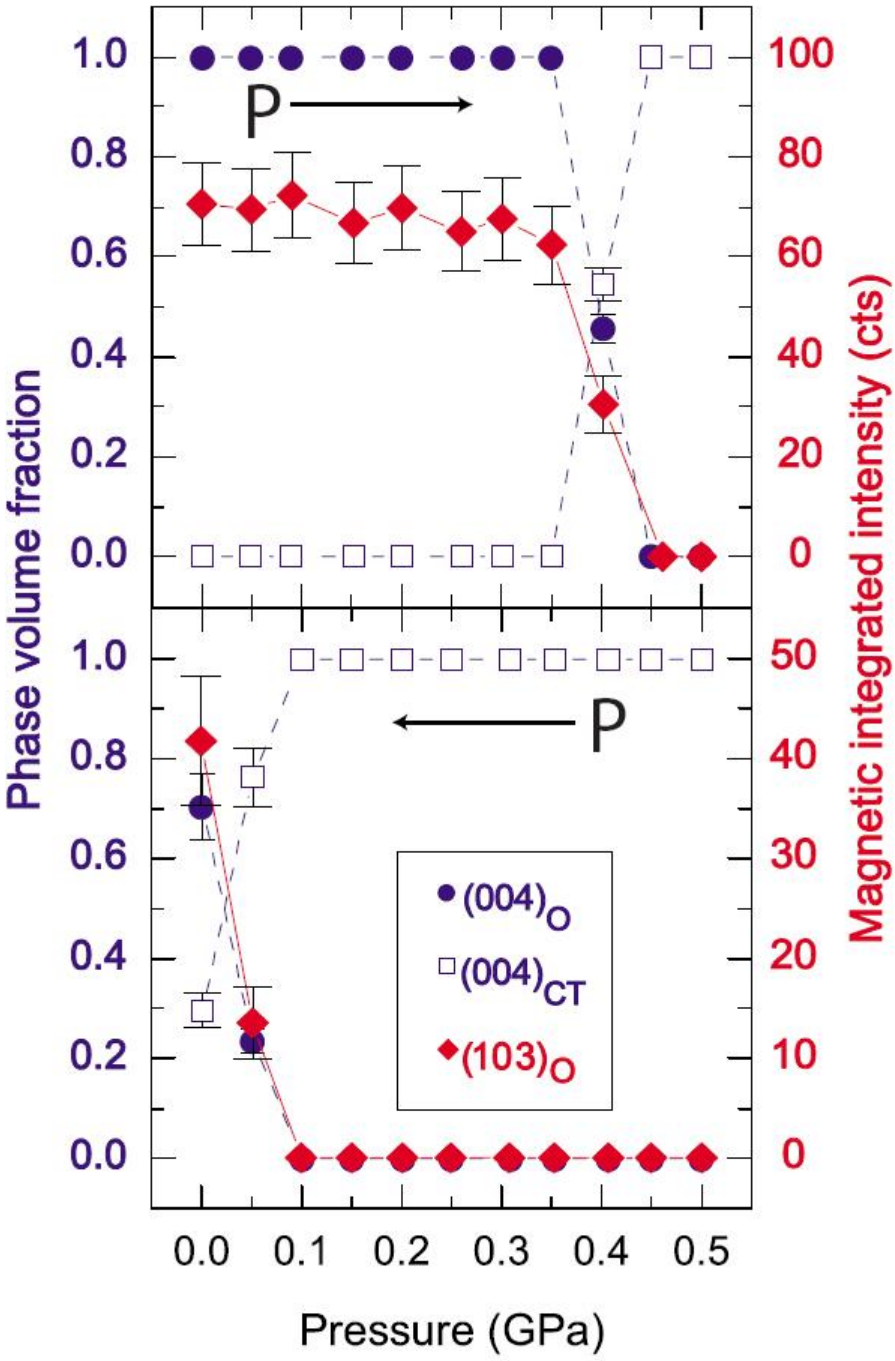

Figure 4.3 Phase fractions of the O and cT phases as a function of pressure upon increasing pressure (top panel) at 75 K and decreasing pressure (bottom panel) at 50 K. The integrated intensity of the magnetic $(1\ 0\ 3)_O$ reflection remains constant in the O phase. Uncertainties are statistical in origin and represent one standard deviation.

of spins antiferromagnetically ordered in the plane but ferromagnetically ordered along the c direction, and will produce magnetic Bragg peaks at (h 0 l)$_{\mathrm{cT}}$ positions with h odd and l even. The potential (1 0 l) with AF1-C magnetic peaks are located at forbidden nuclear Bragg peaks. Therefore, even with a small moment, it should be straight forward to determine if this magnetic ordering is present.

Neutron scattering measurements were performed with a crystal oriented in the (h 0 l)$_{\mathrm{cT}}$ plane associated with the proposed AF1 structure using the same diffractometer conditions described at the beginning of this section. For these measurements, a 70 mg single crystal, grown in an FeAs flux and annealed at 500 °C for 24 h, was wrapped in Al foil and secured with Fomblin oil to a flat plate within the Al-alloy He-gas pressure cell. The crystal mosaic of this sample was measured to be approximately 1° (FWHM). The sample was initially measured at ambient pressures and $T = 167$ K as a reference. These peaks were measured again in the cT phase at $p = 0.62$ GPa and $T = 50$ K. There was no observed magnetic intensity at the (1 0 0)$_{\mathrm{cT}}$ and (1 0 2)$_{\mathrm{cT}}$ positions. Additionally, the (1 0 1)$_{\mathrm{cT}}$ peak was measured from 50 K and 0.41 GPa in 10 K steps up to the transition cT-T transition temperature around 135 K and 0.49 GPa and little or no temperature dependence was observed. These results suggest that neither the AF1 C or G type static magnetic ordering exists in the cT phase.

4.3 Investigation of magnetism in the cT phase with polarized neutron scattering

Based on structure factor calculations of the magnetic intensity from a AF1-C type magnetic structure, the magnetic Bragg peaks appear at the same momentum transfer as allowed nuclear refection. A major benefit of performing a polarized neutron experiment is the ability to separate nuclear scattering from magnetic scattering. For a system with a large moment where the scattering intensities from the nuclear and magnetic lattice is similar, the development of the moment will be clearly observable as the intensity due to the combined nuclear and magnetic scattering will be temperature dependent above T_{N}. On the other hand, if the moment is small, the nuclear scattering can be orders of magnitude larger than the magnetic scattering

which makes the separation of these scattering sources through polarized neutron scattering necessary.

In order to get an estimate of the upper limit of the moment for the proposed AF1 order (67), an experiment was performed at the NIST Center for Neutron Research (NCNR) on BT-7 were the neutron beam was polarized using a ^{3}He polarizer such that the neutron polarization was perpendicular to the scattering plane and a spin flipper was used before the sample. The He pressure cell described earlier was used to reach pressures up to 0.6 GPa and the samples were cooled using a closed-cycle refrigerator. The triple axis spectrometer was operated in a 2-axis mode with a collimation configuration 120'-50'-50'-120'. Two samples, each with a mass of approximately 30 mg, were mounted on a sample stick and displaced vertically. The lower sample was oriented for access to the $(h\ 0\ l)_{\mathrm{T}}$ plane and the upper sample was mounted for access to the $(h\ h\ l)_{\mathrm{T}}$ plane. Elevation controls in the triple axis setup allowed for access to both samples as they were pressurized and cooled. The $(0\ 0\ 4)_{\mathrm{O,cT}}$ peak was measured for monitoring the O-to-cT phase transition. In the cT phase, the $(1\ 0\ 1)_{\mathrm{cT}}$ and $(1\ 0\ 5)_{\mathrm{cT}}$ peaks were measured and peak intensities were compared to calculated intensities from the predicted magnetic structure. The guide field, which is parallel to the neutron polarization, was oriented in the vertical direction (perpendicular to the scattering plane) and a spin flipper was placed before the sample. For this case where $\mathbf{Q}\cdot\mathbf{P_0}=\mathbf{0}$, the partial cross sections are (74),

$$\frac{d\sigma^{\pm\pm}}{d\Omega}=\sum_{i,j}e^{i\mathbf{Q}(\mathbf{r_i}-\mathbf{r_j})}(b_ib_j^*\mp(b_ip_j^*S_{\perp zj}^*+b_j^*p_iS_{\perp zi})+p_ip_j^*S_{\perp zi}S_{\perp zj}^*) \tag{4.2a}$$

$$\frac{d\sigma^{\pm\mp}}{d\Omega}=\sum_{i,j}e^{i\mathbf{Q}(\mathbf{r_i}-\mathbf{r_j})}(p_ip_j^*S_{\perp yi}S_{\perp yj}^*) \tag{4.2b}$$

which describes the correlation between atoms at r_i and r_j with a coherent nuclear scattering length b and magnetic scattering amplitude p. The atomic-spin components $S_{\perp zi}$ and $S_{\perp yi}$ are perpendicular to the $\mathbf{Q}$ in a right handed coordinate system defined such that $\mathbf{Q}$ is collinear with the x-direction and $\mathbf{P_0}$ is collinear with the z-direction. The spin flipper before the sample allowed for measurement of $\frac{d\sigma^{--}}{d\Omega}$ and $\frac{d\sigma^{+-}}{d\Omega}$. The other cross sections were constrained in the analysis such that $\frac{d\sigma^{--}}{d\Omega}=\frac{d\sigma^{++}}{d\Omega}$ and $\frac{d\sigma^{-+}}{d\Omega}=\frac{d\sigma^{+-}}{d\Omega}$.

Because of the presence of domains, each of the terms in equations (2a) will potentially contribute to the observed scattering. The advantage of this setup is that the spin-flip scattering represented in equation (2b) is entirely magnetic while being sensitive to the component of the spin moment which is both perpendicular to $\mathbf{Q}$ and $\mathbf{P_0}$. The presence of magnetic order or upper limit magnitude can be determined from these measurements.

Magnetic moment estimation requires the calculation of intensities from the known crystallographic and magnetic structures. For a double axis spectrometer equation, (3) can be used (91).

$$I \propto \frac{1}{\sin 2\theta}|F|^2 \tag{4.3}$$

In equation 4.3, 2θ is the scattering angle and F is the structure factor for either magnetic or nuclear Bragg reflection. The equations for nuclear and spin only magnetic scattering are given by

$$F_{\mathrm{N}} = \sum_i \bar{b_i} e^{i\mathbf{G}\cdot\mathbf{d_i}} e^{-W_i} \tag{4.4}$$

$$F_{\mathrm{M}} = \sum_i p_i S_\perp e^{i\mathbf{G_M}\cdot\mathbf{d_i}} e^{-W_i} \tag{4.5}$$

where in equation (4) b_j is the nuclear coherent scattering length for an atom at a position d_j at the jth site in the unit cell, $\mathbf{G}$ refers to a reciprocal lattice vector of the nuclear reciprocal lattice and e^{-W_i} is the Debye-Waller factor. In equation (5) $\mathbf{G_M}$ refers to a magnetic reciprocal lattice vector. Expressions for p_i and $S_\perp$ are provided in equations (6) and (7),

$$S_\perp = S \sin\alpha \tag{4.6}$$

$$p_i = \pm g f(Q)(0.2695 \times 10^{12} cm) \tag{4.7}$$

where, in equation, (6) S is the spin magnitude and α is the angle between the magnetization and the momentum transfer. In equation (7), g is the Lande splitting factor, and $f(\mathrm{Q})$ is the magnetic form factor (114). The expression gS represents the spin moment in units of μ_{B} and this has been determined in $CaFe_2As_2$ from refinement of neutron diffraction powder patterns to be 0.8(5) μ_{B} at ambient pressures (92)

For the sample oriented in the $(h\ h\ l)_{\mathrm{T}}$ plane with the moment direction along in the (h h) direction, the component $S_{\perp yi}$ from equation (2b) will entirely encompass $S_{\perp}$ because it is perpendicular to the polarization direction therefore the magnetic scattering in the spin flip channel will be described by equations 4.3 and 4.5. As long as the magnetic scattering is weak in comparison to the nuclear scattering, the non spin flip scattering will be dominated by nuclear scattering which can be described by equations 4.3 and 4.4.

A comparison of calculated intensities for the AF2 magnetic structure and crystal structure to our measurements can provide some confidence in our ability to predict an upper limit moment value for AF1 phases. The data was corrected for the inefficiency in the spin flipper and analyzer as well as for a time-dependence of the ^{3}He-neutron-spin-filters using the *pbcor* software (115) and the corrected data for the nuclear (0 0 4) (- - channel) and magnetic $(1\ 0\ 1)_{\mathrm{O}}$ (+ - channel) peaks is shown in Fig. 4.4. Table 1 shows the results of the analysis where the measured values are integrated intensities of Gaussian peaks fits to $\theta - 2\theta$ scans shown in Fig 4.4. The calculated nuclear intensity came from the use of equations (3) and (4) and the magnetic intensities were calculated using equations 4.3, 4.5, 4.6 and 4.7 where $f(\mathbf{Q})$ for Fe^{2+} was used with $gS = 0.8\ \mu_B$. From Table 1, one can see that the magnetic scattering intensity is almost an order of magnitude smaller than nuclear intensities, justifying ignoring any magnetic contribution in the non spin-flip channel. The ratio of intensity I(004)/I(101) from both observation and calculation is shown in the last row of Table 4.1 and they are in agreement.

Table 4.1 Results of moment prediction in O-AFM phase

$\mathbf{Q^P}$	Measured Intensity (counts/min)	Calculated Intensity (fm^2)
$(004)^{--}_{\mathrm{O}}$	217958 ± 7368	3267
$(101)^{+-}_{\mathrm{O}}$	6368 ± 613	89
Ratio	$\mathrm{I}(004)/\mathrm{I}(101) = 34 \pm 4$	$\mathrm{I}(004)/\mathrm{I}(101) = 37$

An example of our measurement in the cT phase is shown in Fig. 4.5 at a position where an expected $(1\ 0\ 1)_{\mathrm{O}}$ AF1-G type peak may exist. Both the $(0\ 0\ 4)_{\mathrm{cT}}$ and $(1\ 0\ 1)_{\mathrm{cT}}$ nuclear peaks are allowed and intense Bragg peaks are observed in the non spin flip channel. Intensity present at $\mathbf{Q} = (1\ 0\ 1)_{\mathrm{cT}}$ in the spin flip channel is suggestive of the presence of G-type

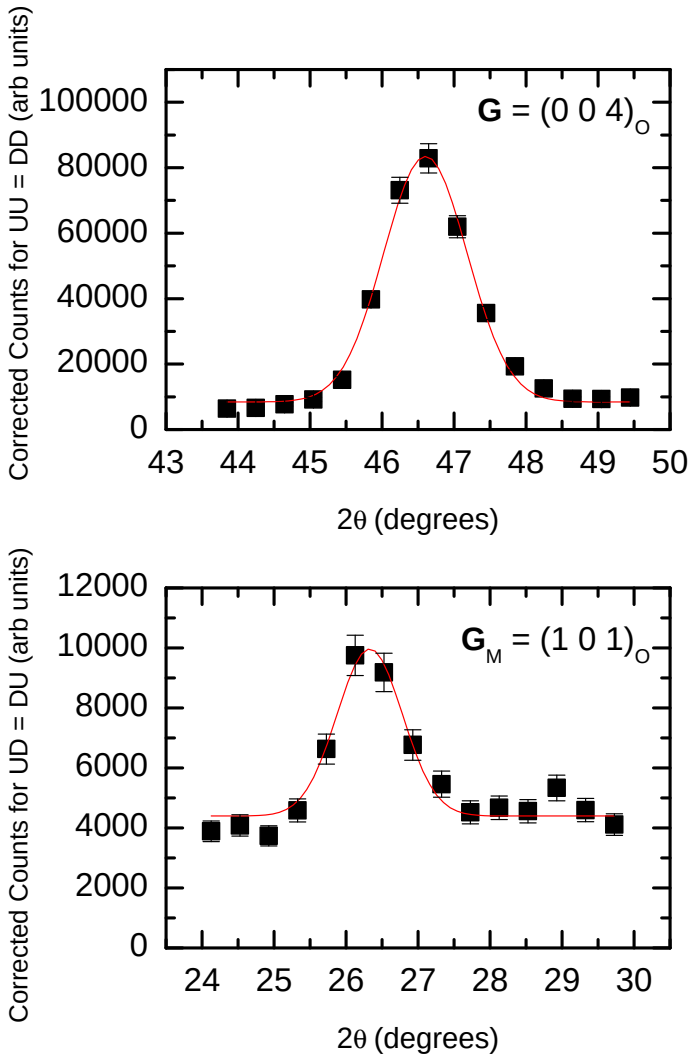

Figure 4.4 (top panel) θ-2θ scan through the nuclear $(0\ 0\ 4)_{\mathrm{O}}$ peak in the non spin-flip channel. (bottom panel) θ-2θ scan through the magnetic $(1\ 0\ 1)_{\mathrm{O}}$ peak in the spin-flip channel.

magnetic ordering. However, this peak is not likely to arise from $CaFe_2As_2$, but may be due to an impurity phase. From Fig. 4.5, an offset of 0.5° in the peak position between the nuclear $(1\ 0\ 1)_{cT}$ and the suspected magnetic $(1\ 0\ 1)_{cT}$ peak exists. Further, a similar peak was observed in the orthorhombic phase at the exact scattering angle which indicates that this intensity is likely from another phase. Additionally, there is no ϕ dependence indicating that this is related to a powder. Because FeAs is used as a precursor in the growth of the $CaFe_2As_2$ single crystals, this magnetic impurity could be present and it is ordered magnetically at 77 K. FeAs has an expected magnetic reflection associated with a reported d spacing of 3.71 Å (116) which is comparable to the d-spacing of 3.76 Å associated with the $(1\ 0\ 1)_{cT}$ peak and, due to the resolution condition, the intensity from this magnetic powder ring may be present. Unfortunately, magnetization measurements on the sample studied showed no evidence of an FeAs impurity so its existence was not confirmed. But, even if we cannot verify the identity of an impurity signal, we have evidence that suggests this intensity is not linked to the $CaFe_2As_2$ crystal and can be treated as additional background.

The first moment estimate was performed using a "fast" method, in which the integrated intensity of the rocking curve was found from a measurement where the counting rate was 30 seconds per point. The $(1\ 0\ 1)^{--}_{cT}$ and $(1\ 0\ 1)^{+-}_{cT}$ peak intensities were compared to calculations of $F(101)_N/F(101)_M$ for the moment estimation, even though non spin flip intensity observed at (101) may include magnetic scattering which will add to the uncertainty of this estimate. Because the proposed moment direction in the cT phase was rotated 45° from the moment direction in the O phase, an additional factor of $\sqrt{2}/2$ (or $\frac{1}{2}$ of the intensity due to $\cos(\beta)^2$ dependence of intensity where β is the angle between $\mathbf{S}_\perp$ and $\mathbf{P_0}$ from a single domain) was added.

The corrected non spin flip scan clearly shows the presence of a peak which was fit to a Gaussian peak shape. As shown in Fig. 4.6, the non spin flip channel did not show clear evidence but a Gaussian fit to the data was performed where the peak position and full width at half maximum was fixed to the fitted value from non spin flip channel. This resulted in a measured ratio of $F(101)_N/F(101)_M \sim 7.2 \pm 5.6$ (2σ) which corresponds to a moment of $0.5 \pm 0.6\mu_B$.

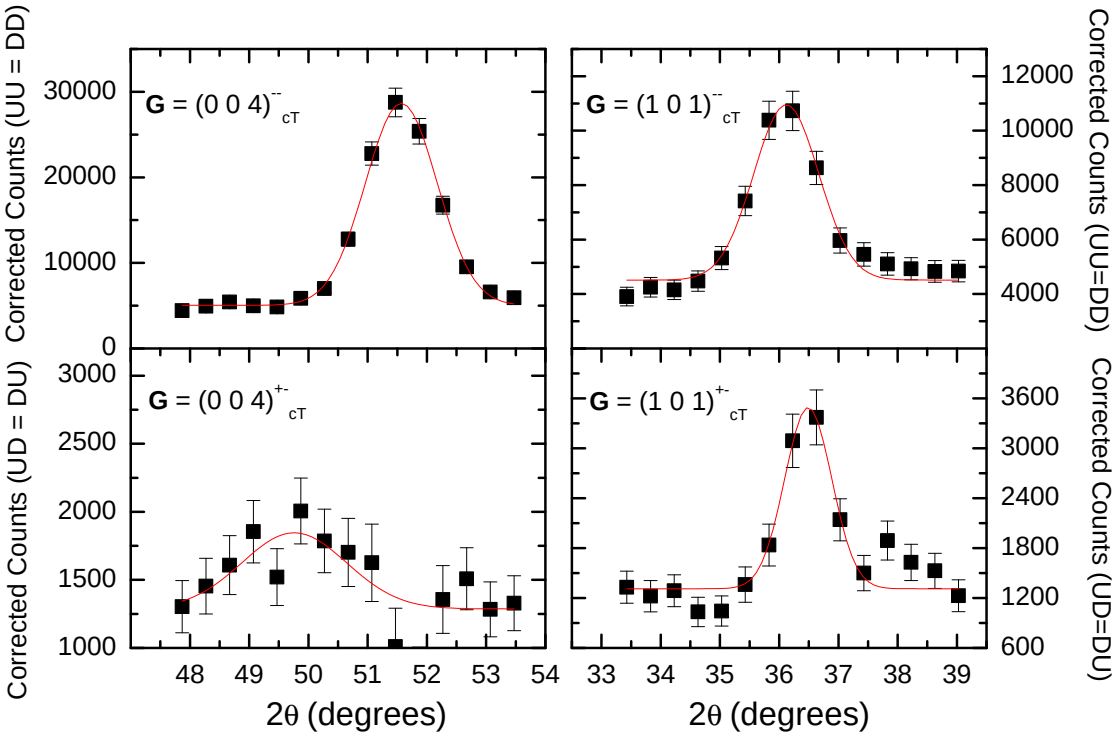

Figure 4.5 (top left) Corrected θ-2θ scan through the nuclear $(0\ 0\ 4)_{\mathrm{cT}}$ peak in the non spin-flip channel. (bottom left) Corrected θ-2θ scan through the nuclear $(0\ 0\ 4)_{\mathrm{cT}}$ peak in the spin-flip channel. Not that the counts are at background level. (top right) θ-2θ scan through the nuclear $(1\ 0\ 1)_{\mathrm{cT}}$ peak in the non spin-flip channel. (bottom right) θ-2θ scan through the proposed magnetic $(1\ 0\ 1)_{\mathrm{cT}}$ peak in the spin-flip channel. This peak is clearly displaced from the nuclear $(1\ 0\ 1)_{\mathrm{cT}}$ peak which is suggestive that this is an impurity peak.

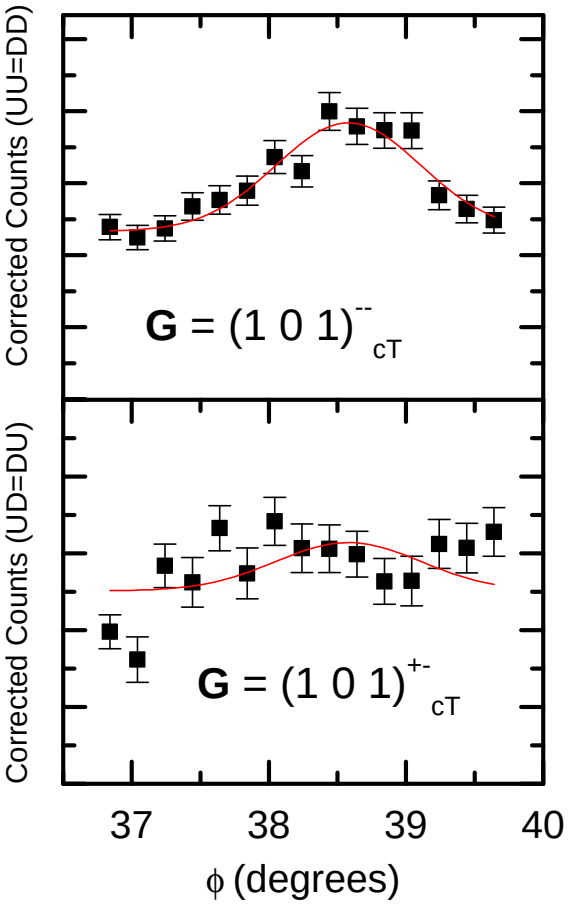

Figure 4.6 (top panel) Rocking scans through the nuclear $(1\ 0\ 1)_{\mathrm{cT}}$ peak in the non spin-flip channel. (bottom panel) Rocking scans through the proposed magnetic $(1\ 0\ 1)_{\mathrm{cT}}$ in the spin-flip channel. These scans provide allow for"fast" estimate of an upper limit of the proposed magnetic moment magnitude.

A second, more intensive procedure for moment estimation was performed which involved measuring the scattering intensity for as long as an hour at the proposed magnetic wave vector $(1\ 0\ 5)_{\mathrm{cT}}$ in both the non spin flip and spin flip channels as well as at a position shifted in ϕ and 2θ away from the peak for a background measurement. The peak position was measured for 1 hour and the background was measured for 15 min. This same procedure was performed for the $(0\ 0\ 4)_{\mathrm{cT}}$ peak and these were the only peaks measured. The moment value was adjusted in the calculation of $F(004)/F(105)$ such that this ratio matched observations. These experimental results and the moment estimate are shown in Table 2 which suggests a limit on the moment of

Table 4.2 Results of moment prediction in cT phase

$\mathbf{Q^P}$	Measured Intensity (counts/hour)	Calculated Intensity (fm^2)	Moment μ_B
$(004)^{--}_{\mathrm{cT}}$	$2.42047 \times 10^6 \pm 122923$	3053	-
$(105)^{+-}_{\mathrm{cT}}$	10017 ± 24395	7.34	0.34 ± 0.44
Ratio	$\mathrm{I}(004)/\mathrm{I}(105) = 415 \pm 1012$	$\mathrm{I}(004)/\mathrm{I}(101) = 415$	-

$m < 0.34\ \mu_{\mathrm{B}}$. It must be noted that one complication involved in using the $(1\ 0\ 5)_{\mathrm{cT}}$ peak for the moment estimation is that it is approximately 6° in 2θ from an aluminum powder ring which is likely causing additional background signal. A magnetic moment approaching the upper limit should have allowed G-type order to be inferred from powder diffraction experiments. This experiment has clearly shown that even though the $(1\ 0\ 1)_{\mathrm{cT}}$ and $(1\ 0\ 5)_{\mathrm{cT}}$ peaks have the highest intensities relative to the allowed nuclear peaks, the high backgrounds increase uncertainty in the result which should motivates future measurement of additional magnetic peaks. The successful prediction of the known magnetic structure in the O phase based both ϕ and $\theta - 2\theta$ scans of the nuclear $(0\ 0\ 4)_{\mathrm{O}}$ and magnetic $(1\ 0\ 1)_{\mathrm{O}}$ intensities provided some confidence in the procedure but careful measurements using all four polarization states, longer counting times, verification of impurities and again more potential magnetic peaks will allow for improved refinement and understanding the potential magnetic order the cT phase.

4.4 Pressure medium dependence of the *p-T* phase diagram

Disparity in the result of recent experiments under pressure using a variety of pressure cells and pressure media has highlighted the difficulty of achieving true hydrostatic pressure or

pressure application which is uniform across the sample. In particular, for $CaFe_2As_2$, initial experiments which measured electrical properties of this material indicated that superconductivity is observed in the p-T phase diagram (6; 4; 7). In all these references, the authors attempted to achieve hydrostatic pressure through the use of fluid pressure medium pressurized by a clamp type cell. Silicon oil was used in ref (6) and ref (7) while Florinert FC-75 was used in ref (4) which have pour points (or the lowest temperature at which the oil will pour or flow) of approximately 130K and 170 K respectively at ambient pressures and these pour points decrease with pressure. This indicates a limitation of these fluid medium cells to truly apply hydrostatic pressure over a broad range of temperatures and pressures where the interesting ground states such as SC occur. Clear differences in the published p-T phase diagrams such as the pressure ranges where superconductivity occurs and seem to depend on the pressure application methods. Additionally, muon spin relation (μSR) measurements on $CaFe_2As_2$ using a Daphine oil 7373 pressure medium (117) has supported phase coexistence in the p-T phase diagram (118). Measurements on Ca doped Sr ruthenate and MnSi (119) has demonstrated ability of μSR technique to determine the volume fractions of phase separated regions with and without long range magnetic order. Similar studies on $CaFe_2As_2$ show a paramagnetic phase co-existing with AFM phases at T= 2K within the pressure regions where SC is reported to exist. These observations are in contrast to our observations in Fig. 4.2 where a He gas pressure medium was used. Single phase $CaFe_2As_2$ was observed throughout the p-T phase diagram except for narrow ranges of pressure near the phase lines. We also observe coexistence of phases at ambient pressures and low temperatures after substantial damage to the crystals occurred as a result of multiple cycles to and from the cT phase.

To further test the pressure medium dependence of the phase diagram, samples grown at Ames Laboratory were measured on the E4 double axis spectrometer and are described in detail in reference (8). A 10 mg sample was oriented in the $(h\ h\ l)_{\mathrm{T}}$ scattering plane. These measurements involved pressure application using a Be-Cu pressure cell and a 1:1 mixture of Florinert 77 and Florinert 70 as a pressure medium. The pressure was monitored with the use of a manganin pressure sensor as well as in-situ by tracking the lattice constants of NaCl crystals as the sample was cooled from room temperature to 2K. Fig. 4.7 shows the temperature

dependence of the (0 0 2) peak at a pressure of 0.83 GPa which was set at room temperature. At approximately 120 K and 0.66 GPa, which is below the Florinert pour point, it is likely this pressure medium cannot provide hydrostatic pressure to the sample. While a phase transition is clearly observed in Fig 4.7 by the c-lattice parameter shift, a phase co-existence is observed and the multiple lattice parameters indicate the co-existence of the O and cT phases.

The coexistence of a non magnetic cT phase and an AFM ordered O phase observed is in agreement with μSR measurements and explains that the different reports on the response of $CaFe_2As_2$ to pressure and the observed phase coexistence depend critically on the method used to apply pressure. Again, both the E4 neutron and μSR measurements were performed with liquid pressure medium which begin to solidify at or below $\sim$150 K. The solidifying pressure media can apply non uniform pressure gradients across the sample volume which can lead to the existence of multiple phases. Undoubtedly, the He pressure apparatus can apply true hydrostatic pressure in a much broader range of temperatures and our results show sharp phase transitions to and from the cT phase with co-existence in a narrow pressure range. Earlier reports such as ref (4) for example showed that when liquid pressure medium were used, a sharp jump in resistivity is observed upon cooling at ambient pressure but upon pressure application, the upturn was broad in temperature and became much less apparent. The first evidence for the cT phase was indicated by a very broad downturn in resistivity upon cooling at high pressures. The results in ref (120) where hydrostatic pressure was used during resistivity and susceptibility measurements showed instead the T-O as well as the cT-T transition remained sharp and clearly first order in nature and in addition the SC which has been reported in this compound using liquid pressure medium was not found during the hydrostatic pressure experiment. These findings further support this picture of a complex pressure environment which is unavoidable when fluid pressure medium are used to study a materials behavior at low temperatures and high pressures.

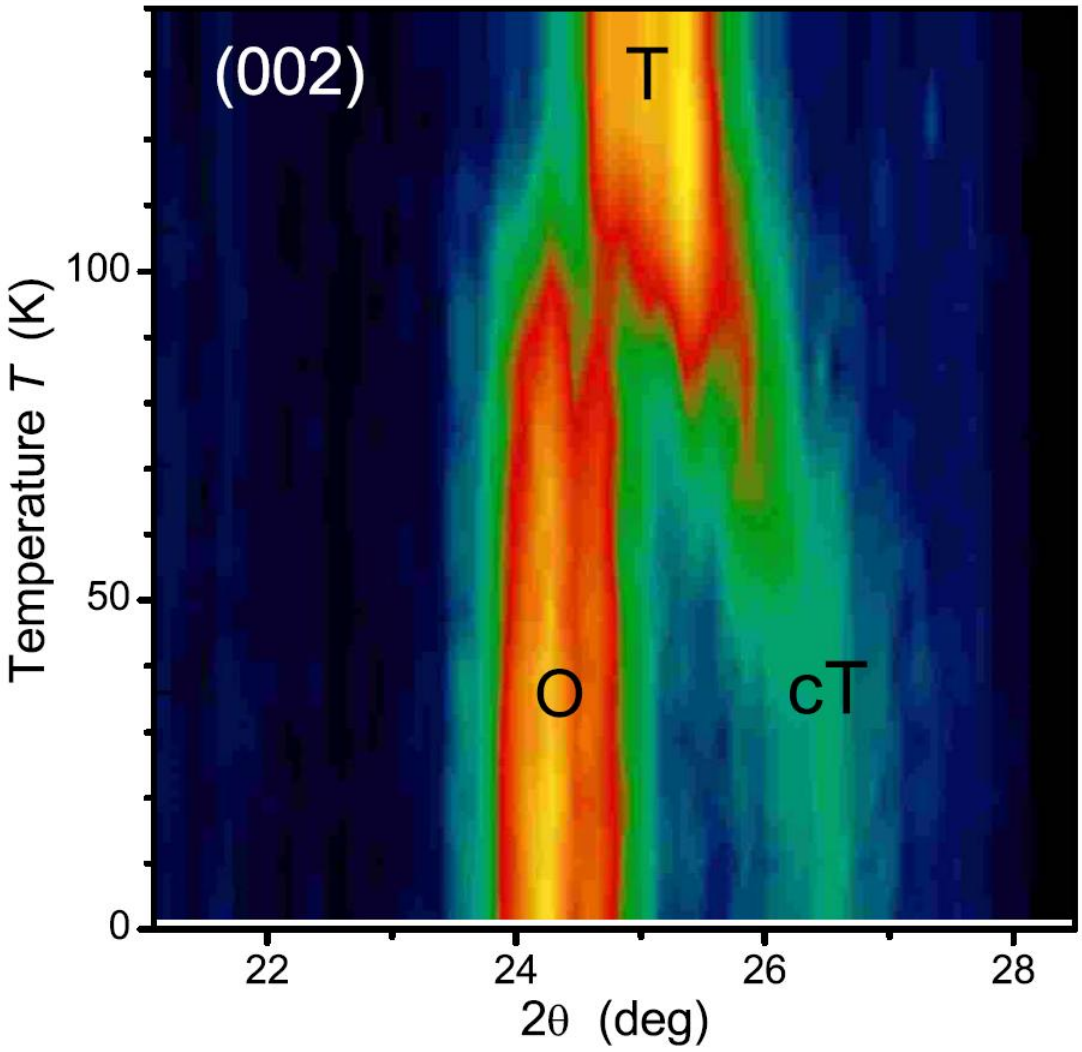

Figure 4.7 Measurement of the (0 0 2) nuclear reflection from $CaFe_2As_2$ with an area detector on the E4 diffractometer using a Be-Cu clamp-type cell. For an initial pressure of 0.83 GPa, at room temperature, the T phase transforms to a mixture of the cT and O phases below approximately 100 K.

4.5 Evidence from neutron diffraction for superconductivity in the stabilized tetragonal phase of $CaFe_2As_2$ under uniaxial pressure

Multiple experiments have shown that SC is in fact present in $CaFe_2As_2$ under pressure using fluid pressure media but exactly where in the phase diagram (65) this occurs is still under debate. The results presented in ref (120) which measured resistivity using a He pressure cell to maximize hydrostatic pressure clearly show that SC is not present in either the O or cT phases. Since these are the only observed states at low temperatures, what conditions must be met to stabilize SC in $CaFe_2As_2$? It was postulated that non hydrostatic conditions involving freezing pressure medium may support a metastable SC phase. This section will summarize a work lead by K. Prokeŝ (129) which attempted to answer this question and found some compelling evidence that a new phase exists where SC is stabilized by non-hydrostatic pressure conditions.

The experiments were performed using high quality single crystals weighing between 8-12 mg with typical dimensions of 2 X 3 X 0.2 mm which were grown out a Sn flux as described in ref (9). Further details of the sample preparation are described in ref (129). The samples were clamped between two ZrO_2 pistons and uniaxial pressure was applied along the **c**-axis to maximize non-hydrostatic conditions while the only force restricting the expansion of the **a**-**b** plane is the friction along the sample surface due to the pressure between the sample and the pistons. Neutron diffraction measurements were performed at the E4 double axis spectrometer at Helmhotz-Zentrum Berlin as well as at the D10 diffractometer at the Institute Laue Langevin (ILL). Both measurements used two-dimensional area detectors to gather intensity over a range of 2θ and rocking angle ϕ. Refer to (129) for full details of diffraction experiments.

The measurements on E4, which monitored all intensity in the vicinity of the $(0\ 0\ 2)_T$ Bragg reflection, showed that at a modest pressure of 0.075 GPa, as the sample was cooled below T = 170 K, multiple phases clearly existed by appearance of two peaks separated in 2θ. One of the 2θ values was consistent with the existence of the O phase. The location of the second peak around $T = 170$ K was not consistent with the known lattice parameter of cT phase. The data suggests there is a continuous evolution in the c_T lattice parameter found from the $(002)_T$ peak and the T phase is coexisting with the O phase. As the sample was cooled further, a third

co-existing peak appeared discontinuously. Both the discontinuous appearance of the third peak and its 2θ value were consistent with the appearance of the cT phase. It is important to note that all integrated intensity observed in the original tetragonal phase was accounted for in the three co-existing phases. Fig. 4.8 (129) shows the temperature dependence integrated intensity distribution as well the trend in 2θ (in the inset) of the $(0\ 0\ 2)_{\mathrm{T}}$ peak (which provides information about the trend of the c-lattice parameter) as the sample is cooled.

The discontinuous and first order change in lattice parameters at the T-O and T-cT transition is shown in the inset. There appears to be a continuous change in the lattice parameter of the high temperature tetragonal phase and this newly reported phase (labeled T') arises due to the uniaxial pressure and is therefore stabilized in this non-hydrostatic pressure condition. This experiment was repeated at D10 which tracked the magnetic $(1\ 0\ 3)_{\mathrm{O}}$ peak with temperature and pressure. The ratio of the measured $I(103)_{\mathrm{O}}/I(002)_{\mathrm{O}}$ peak was in agreement with a predicted ratio using reported magnetic structure and moment of 0.8 μ_{B}. The measurements on D10 show that the magnetic scattering intensity at each pressure is proportional to the fraction of the O phase and no clear evidence of an ordered moment in the T' phase was observed.

To determine if uniaxial pressure will create the conditions necessary for SC, simultaneous ac two-probe resistivity was measured across the **a**-**b** plane and neutron diffraction measurements of the (002) reflection along 2θ were measured at $p = 1$ GPa as the sample was cooled to $T =$ 1.7 K. The results are shown in Figure 4.9 (a)-(c) which was taken from ref (129). Fig. 4.9(a) shows the diffraction results as a function of temperature where the O, T', and cT phases are present at the lowest temperatures.

Fig 4.9(b) shows the resulting intensity after heating up through the transitions. These plots show evidence of hysteresis and a broadening associated with the irreversible damage to the sample upon transitioning to or from the cT phase, both of which were also observed in ref (8). Fig. 4.9(c) shows both the in plane resistivity in the main plot with the lower inset showing the low temperature region which shows the onset of SC at around 10 K. Unfortunately, due to the residual resistivity of the two-probe method, it is not possible to observe zero resistance. The upper inset shows the volume fraction of the T' phase at the lowest measured temperatures for the pressures associated with the green data points and the line is a guide to the eye.

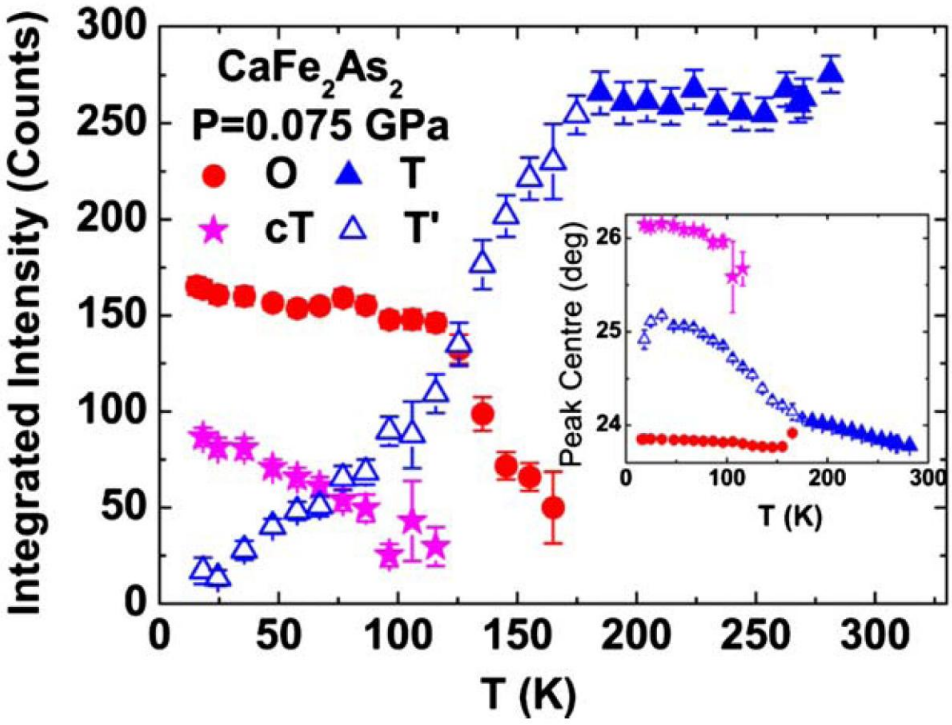

Figure 4.8 (Taken from K. Prokěs *et al.* (129)) Temperature dependence of the integrated intensity around the (0 0 2) position in the T (filled triangles), T' (open triangles), O (filled circles), and cT (filled stars) phases.

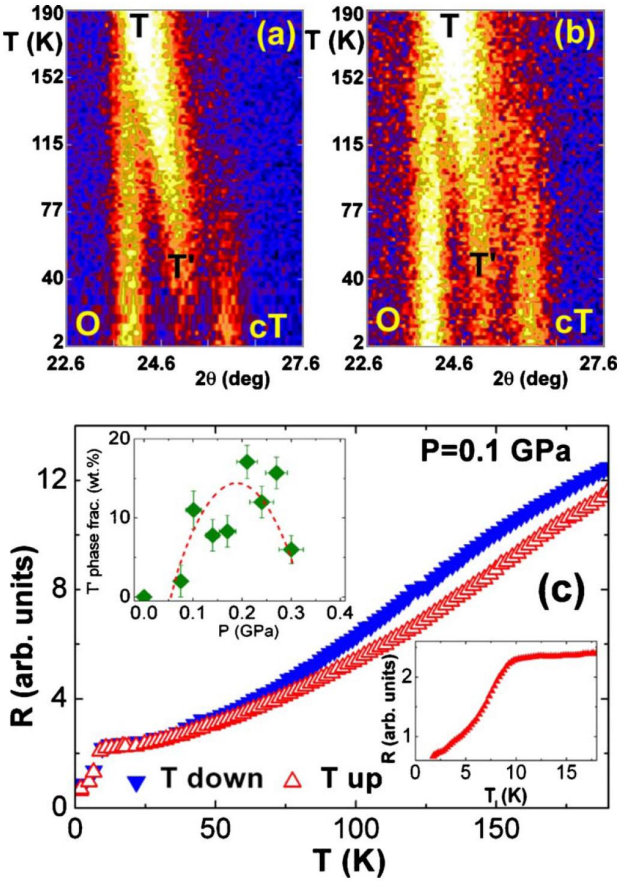

Figure 4.9 (Taken from K. Prokěs *et al.* (129)) Color map showing the intensity near the (002) reflection of CaFe2As2 under uniaxial pressure (0.1 GPa) upon (a) cooling and (b) warming. It is important to note that the color map intensity in (a) ranges from 20-260 while in (b) the range is 60-220. (c) Two probe resistance measurements taken simultaneously with diffraction measurements upon cooling (filled triangles) and warming (open triangles). The lower right inset shows a low temperature range highlighting the onset of SC at ∼10 K. The panel on the upper left shows the weight fraction of the stabilized T' phase as pressure is varied. The dotted line is a guide to the eye.

Interestingly, the onset of the T' phase occurs coincidentally with pressures associated with the onset of SC when uniaxial pressure is used (130).

To summarize, for the pressure range of $0.075 < 0.3$ GPa, an unreported phase has been observed in $CaFe_2As_2$ which is stabilized by non-hydrostatic pressure application. Both measurements of the temperature dependence of AFM order under pressure in this study and previous characterization measurements show that the O and cT phases do not support SC, simultaneous resistivity-neutron diffraction measurements have demonstrated that through the use of non-hydrostatic pressure, the stabilized T' phase appears to support SC. Although it is possible an un-detected phase, or a non-hydrostatic pressure modified O or cT phase may support SC, the fact that both SC and the T' phase exist over a limited pressure range and both vanish with hydrostatic pressure provides compelling evidence that the newly discovered T' phase is the host of SC in $CaFe_2As_2$.

4.6 Electronic density of states and $\chi(q)$ calculations in T and cT phases

The existence of a cT phase has been observed in compounds that crystallize in the $ThCr_2Si_2$ such as in the phosphide compounds $SrRh_2P_2$ (121), $EuRh_2Pd_2$ (121), $SrNi_2P_2$ (122), $EuCo_2P_2$ (122), and $EuFe_2P_2$ (107). Through the application of as low as 0.4 GPa this phase is observed in $CaFe_2As_2$ (5) and at much higher pressures such as 8 GPa in $EuFe_2As_2$ (123), and 20 GPa in $BaFe_2As_2$ (124). Reference (66) alluded to the possibility of a cT phase and qualitatively discussed that As-As bond length, which closely related to the c-lattice parameter length will depend heavily on the competition of the preferred alkaline earth packing and Madelung energy as well as the degree of As-As bonding. In this same reference, it is suggested that for a small cation such as Ca, it is energetically favorable to for a shortened As-As bond which can be realized in the cT phase. A transition in the bonding character of the As-As bond and the realization of a cT phase was also suggested by T. Yildrim (67) where both ref (67) and ref (66) show the details of the band structure are closely linked to the Fe_2As_2 layer spacing. Changing this spacing can have dramatic effects on the electronic and magnetic ground states. An example of this is $EuCo_2P_2$ where the cT phase causes a filling of the Co 3d orbital and results in an increase in the density of states (DOS) at the Fermi level leading to the formation

of a magnetic moment on the Co sites (107). In addition, band structure calculations by C. Krellner et. al. (125) shows that slight changes to z_{As} changes the population of the $3d_{x^2-y^2}$ Fe orbital which has a significant contribution to states at the Fermi level and therefore influences magnetic behavior.

To further investigate the impact of the cT transition of the electronic DOS and magnetism of $CaFe_2As_2$, Y. B. Lee of Ames Laboratory performed band-structure calculations of the generalized susceptibility $\chi(\mathbf{q})$ for both the T and cT phases. (8) These calculations were performed using the full-potential linearized augmented plane wave (LAPW) method with $R_{\mathrm{MT}}K_{\mathrm{max}}$=8 and R_{MT}=2.2, 2.0, and 2.0 a.u. for Ca, Fe, and As, respectively. The numbers of k points in the irreducible Brillouin zone are 550 for the self-consistent charge, 828 for the DOS calculation, and 34 501 for the $\chi(\mathbf{q})$ calculation. For the local density functional, the Perdew-Wang 1992 functional (126) was employed. The convergence criterion for the total energy was 0.01 mRy/cell. The structural parameters for the T and cT phases were obtained from experiment. (5) The density of states, obtained with the tetrahedron method, has been broadened with a Gaussian of width 3 mRy. Fig 4.10a shows the calculated DOS within 2 eV of the Fermi energy for both tetragonal phases. The Fe states overwhelmingly (>95%) contribute in this region, with significant As hybridization (bonding) occurring at lower energies and Ca contributions appearing at higher energies. The most significant change in the collapsed phase is the dramatic lowering of the DOS at the Fermi energy associated, primarily, with a shift to lower energies of the Fe $3d_{x^2-y^2}$ and Fe $3d_{xz-yz}$ orbitals. This is also demonstrated in the corresponding $\chi(\mathbf{q})$ calculations shown in Fig. 4.10b for the two phases.

The intraband contribution to $\chi(\mathbf{q}=0)$ is exactly the density of states at E_{F}, with a large value favoring ferromagnetic ordering (Stoner criteria). We note that the DOS at E_{F} of 2.8 states/eV Fe is comparable to that of pure Fe (3.0 states/eV Fe). The considerably larger peak in $\chi(\mathbf{q})$ at the zone boundary for the T phase, however, is an indication that the magnetic instability is antiferromagnetic, with ordering observed upon a small orthorhombic distortion. (92) The small DOS at E_{F} for the cT phase shown in Fig. 4.10a is apparently not sufficient to induce magnetic ordering, and the essentially featureless $\chi(\mathbf{q})$ (note the offset) in Fig. 4.10b and along other high-symmetry directions (not shown) for the cT phase indicates that magnetic

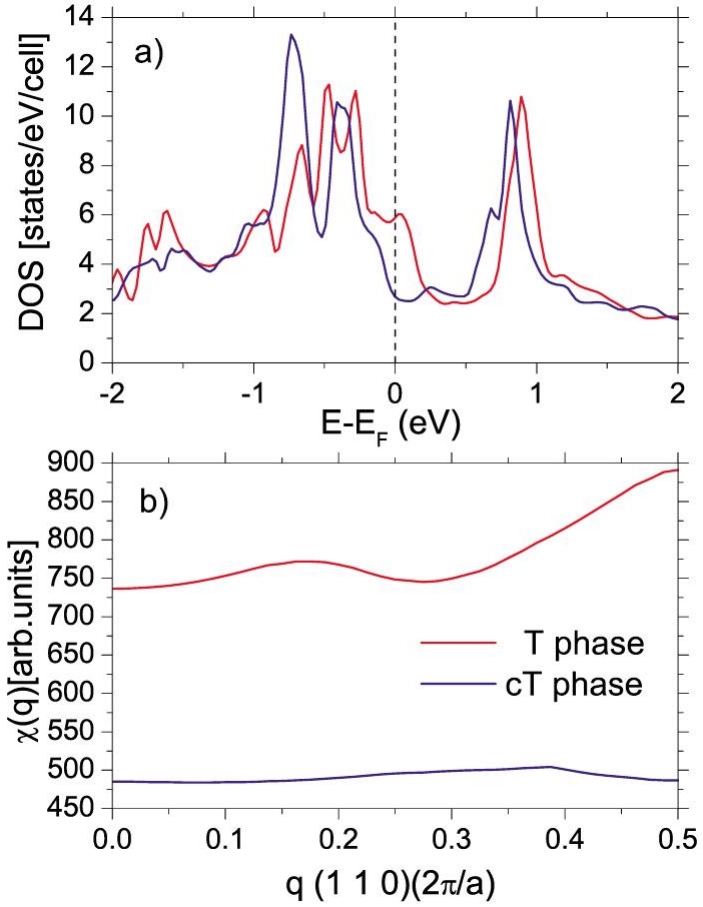

Figure 4.10 (a) Calculated DOS near the Fermi energy for the T (red line) and cT (blue line) phases of $CaFe_2As_2$. (b) The generalized susceptibility $\chi(\mathbf{q})$ for the T (red line) and cT (blue line) phases of $CaFe_2As_2$.

ordering is unlikely at any **q**.

These calculations clearly support the notion of a depressed Fe 3d density of states at E_F, which is consistent with previous work (67; 125) as well as the suppression of magnetism in the cT phase. The suppression of the DOS realized in these calculations is, however, surprising in light of the strong reduction in the resistivity of $CaFe_2As_2$ found upon transformations into the cT phase.(4; 6) This suggests that scattering effects are greatly reduced in the cT phase in comparison to the T phase and call for further investigation of the spin-fluctuation spectrum of the cT phase in particular which will be discussed in the next section.

4.7 Suppression of antiferromagnetic spin fluctuations in the cT phase of $CaFe_2As_2$

Superconductivity has been reported in the parent compounds AFe_2As_2 (A = Ca, Sr, Ba)using liquid pressure medium (4)(127), however measurements on $CaFe_2As_2$ under hydrostatic conditions (120) have shown that superconductivity does not exist in the O or cT phases and the authors of ref (120) suggested that a non-hydrostic component of pressure may cause the formation of domain walls which may have a variety of ground state properties including superconductivity. From the point of view of elastic neutron scattering, the cT phase is not magnetically ordered. All measurements of resistivity show a decrease of resistance upon traversing to the cT phase or an increase of conductivity which is inconsistent with DOS calculations which show that the states at the Fermi level dramatically drop (60% decrease of the DOS) when the system transforms to having a cT structure. While even though there are fewer charge carriers, the lack of scattering from spin on the Fe site is consistent with the increased conductivity. This motivated a study of spin dynamics in the cT phase.

Inelastic neutron scattering measurements were performed in order to investigate the presence of paramagnetic spin fluctuations in the cT phase of $CaFe_2As_2$. Approximately 300 Sn-flux grown single crystals (shown in Figure 4.11(a)) of $CaFe_2As_2$ (9) with a total mass of 1.5 grams were co-aligned on both sides of a set of aluminum plates such that their common $[h\ h\ 0]_T$ and $[0\ 0\ l]_T$ axes were coincident with the scattering plane. One of the challenges in this measure-

ment lies in the nature of the T-cT transition in $CaFe_2As_2$. Our experience has shown that because $CaFe_2As_2$ is quite soft, constrained samples exhibit an extended coexistence between the cT and O or T phases which is a problem if we want to measure the magnetic properties of the cT phase only. This coexistence is exacerbated when non-hydrostatic pressure is applied. (8) Therefore, only a light coating of fluorine-based (Fomblin) oil was used to maintain contact between the Al plates and the crystals. However, we have also found that this method can lead to changes in the alignment of crystals or the detachment and loss of some crystals at the cT transition. The Al plates holding the samples were stacked and placed in the well of an Al-alloy He-gas pressure cell described earlier to ensure hydrostatic pressure conditions. Using this system, the pressure could be varied at fixed temperatures for $T > 50$ K (above the He solidification line), or the temperature could be changed at nearly constant pressures. The inelastic neutron scattering measurements were performed on the IN8 triple-axis spectrometer at the Institut Laue-Langevin at a fixed final energy of 14.7 meV employing a double focusing Si(111) monochromator, a double focusing PG(002) analyzer and open collimation. A graphite filter was used after the sample to reduce harmonic contamination of the beam. The energy resolution in this configuration, measured using a vanadium standard, was 1.1 meV full-width-at-half-maximum (FWHM). The sample mosaic with respect to both the $[h\ h\ 0]_{\mathrm{T}}$ and $[0\ 0\ l]_{\mathrm{T}}$ directions was initially 1.6 deg FWHM at ambient pressure and increased slightly to 2 deg at $p = 0.5$ GPa. The pressure cell was loaded into an ILL Orange-type cryostat allowing temperature control from 300 K down to approximately 2 K.

Figures 4.11 (a) and (b) describe the regions of reciprocal space and the p-T phase diagram investigated during the spin-excitation measurements. The inelastic scattering was studied primarily around the $(\frac{1}{2}\ \frac{1}{2}\ 1)_{\mathrm{T}}$ antiferromagnetic wave vector (using the indices appropriate to the tetragonal unit cell). Constant energy **q**-scans were measured at several energies along both the $[h\ h\ 0]_{\mathrm{T}}$ and $[0\ 0\ l]_{\mathrm{T}}$ directions in order to characterize the spin fluctuations at selected temperatures and pressures.

The sequence of measurements is depicted in Fig. 4.11(c). Since we have already established that crossing the phase boundaries into the cT phase from either the O or T phase can significantly increase the mosaic of the sample (128), care was taken to first measure the

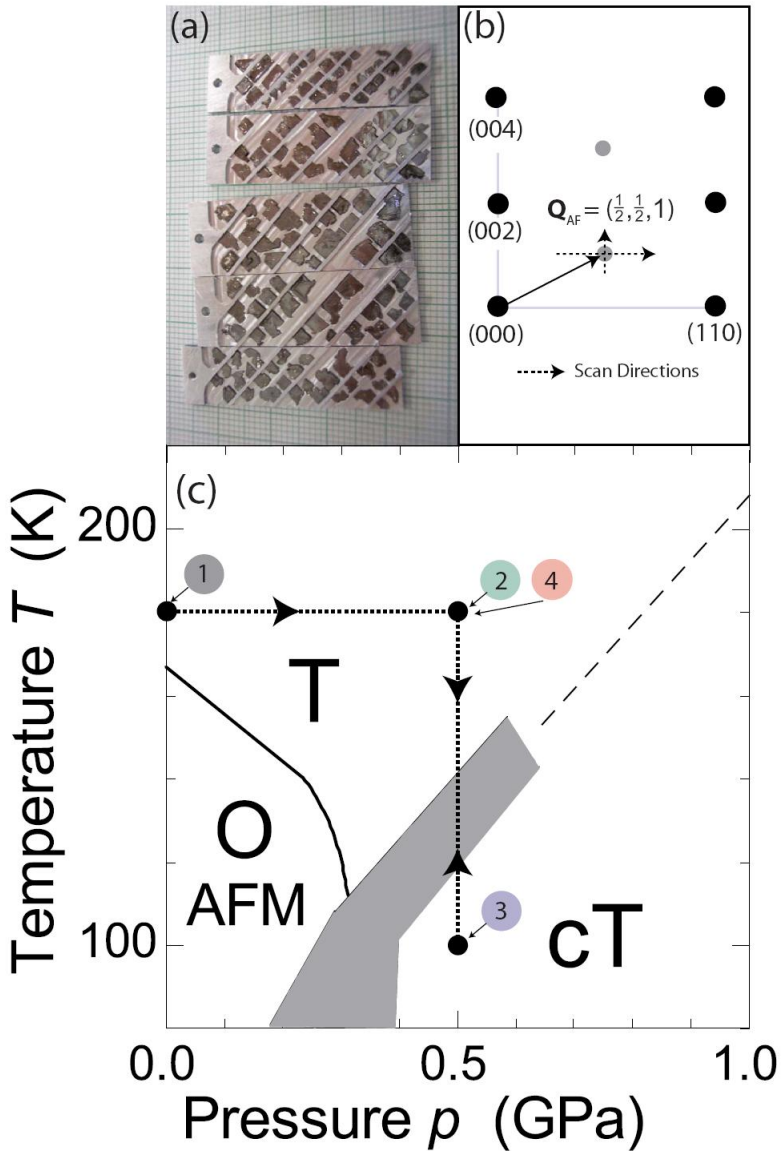

Figure 4.11 (a) Coaligned single crystals of $CaFe_2As_2$. Approximately 300 crystals were mounted on both sides of five Al plates that were stacked to produce the measurement sample (shown on a millimeter grid). (b) Schematic of the reciprocal lattice plane probed in these measurements. The dashed lines denote scans along the $[h\ h\ 0]_T$ and $[0\ 0\ l]_T$ directions. (c) The p-T phase diagram of $CaFe_2As_2$ (after ref. (8)). The shaded area represents hysteretic regions, and the numbers correspond to the measurement sequence as described in the text.

inelastic scattering at point 1 (ambient pressure in the tetragonal phase) and point 2 ($p = 0.5$ GPa but still in the tetragonal phase) before lowering temperature and crossing over into the cT phase itself (point 3). The scans at $p = 0.5$ GPa were repeated using the same pressure cell containing only the aluminum slides coated with the fluorine-based oil and the He pressure medium to determine the background contribution to the observed scattering. Measurements of the spin wave dispersion in the O phase at ambient pressure ($T = 140$ K) were also done prior to pressurizing the system and are consistent with results of previous measurements by McQueeney et al (76). Furthermore, no evidence of static magnetic order at the antiferromagnetic Bragg point in the T or cT phases was observed, consistent with previous results. (5; 8; 76)

Fig. 4.12 displays the raw data from constant energy **q**-scans through the $(\frac{1}{2}\ \frac{1}{2}\ 1)_{\mathrm{T}}$ reciprocal lattice position along the $[h\ h\ 0]_{\mathrm{T}}$ direction at $\hbar\omega = 3$ and 7 meV energy loss. This is the same wave vector where correlated spin fluctuations have been observed in the Co- and Ni-doped $BaFe_2As_2$ compounds.(18)(150) The open squares in this figure denote the measured, empty can, background data. Figures 4.12(a) and (b) clearly show the presence of correlated spin fluctuations in the tetragonal phase centered on the AF $(\frac{1}{2}\ \frac{1}{2}\ 1)_{\mathrm{T}}$ wave vector for both 3 and 7 meV. As temperature was lowered, at a constant pressure of 0.5 GPa, the sample transformed from the higher temperature T phase to the lower temperature cT phase at approximately 120 K. The absence of a clear signal above the empty can background in Figs. 4.12(c) and (d) indicates that the antiferromagnetic spin fluctuations in the cT phase (point 3 in Fig. 4.11(c)) are strongly suppressed, if not completely absent. Unfortunately, in the process of transforming from the T to the cT phase, there was an unavoidable increase in the sample mosaic from approximately 2 deg FWHM at 180 K and 0.5 GPa, to nearly 5 deg FWHM at 100 K and 0.5 GPa. Furthermore, the integrated intensity of the nuclear peaks measured in rocking scans decreased by approximately 40%, indicating that at least a portion of the sample was either dislodged or tilted well beyond the measured mosaic (verified by visual inspection after the experiment). Therefore, the temperature was increased back to 180 K (point 4), to investigate the impact of the broadened mosaic and decreased sample volume on our ability to observe the spin fluctuations. Crossing the cT-T phase line again increased the sample mosaic

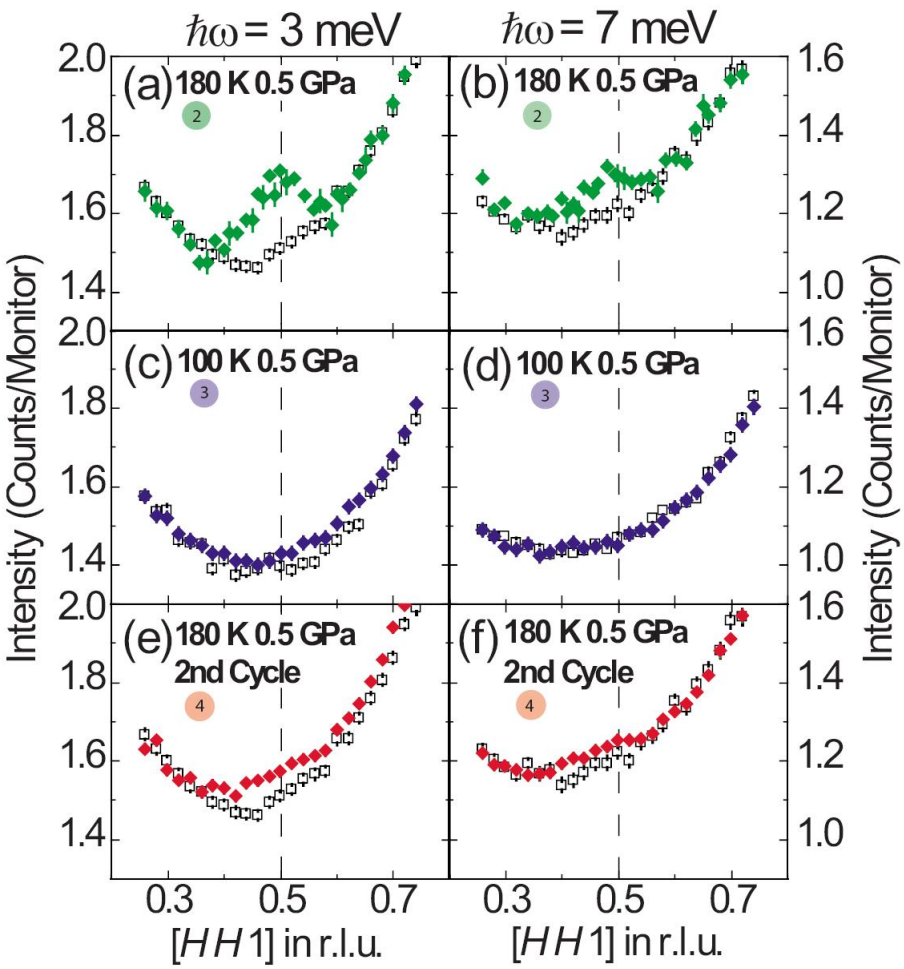

Figure 4.12 Constant energy **q** scans at 3 and 7 meV energy transfer through the $(\frac{1}{2}\ \frac{1}{2}\ 1)_{\mathrm{T}}$ antiferromagnetic wave vector along the in-plane $[h\ h\ 0]_{\mathrm{T}}$ direction at T=180 K and p= .5 GPa for (a) and (b); T=100 K and p=0.5 GPa for (c) and (d). Panels (e) and (f) show the data taken at T=180 K and p =0.5 GPa after passing through the T-cT transition twice (upon cooling and warming). The open squares denote the empty can background measurements. The dashed vertical line denotes the position of the $(\frac{1}{2}\ \frac{1}{2}\ 1)_{\mathrm{T}}$. Each data point in this figure represents 6 min of counting time (8000 monitor counts).

to nearly 6.5 deg but did not affect the integrated intensities of the nuclear peaks. Figs. 4.12(e) and (f) demonstrate that although the magnetic scattering is broadened and decreased relative to the first measurement at 180 K and 0.5 GPa, it remains clearly in evidence, re-affirming that the correlated spin fluctuations in the T phase of $CaFe_2As_2$ are strongly suppressed or absent in the cT phase.

In Fig. 4.13 we compare the inelastic scattering data taken at ($\frac{1}{2}$ $\frac{1}{2}$ 1), along both the $[h\ h\ 0]_T$ direction and the $[0\ 0\ l]_T$ direction, after subtracting the empty can background, at points 2, 3 and 4. We also show the ambient pressure data taken at 180 K (point 1) in Fig. 4.11(c) where the background was estimated from the wings of the constant energy **q**-scan along $[h\ h\ 0]_T$. Using a single Gaussian line shape to fit the data in Fig. 4.13(a) we obtain a dynamic spin correlation length of 25 $\pm$ 5 Å at 3 meV along $[h\ h\ 0]_T$, quite similar to the value obtained from similar measurements on $Ba(Fe_{0.92}Co_{0.08})_2As_2$. (18) The corresponding scan along $[0\ 0\ l]_T$ (Fig. 4.13(b)) is approximately 50% broader implying spin correlations perpendicular to the Fe-As planes with a shorter correlation length, again consistent with the findings of Lumsden et al (18). Upon increasing the pressure to 0.5 GPa at 180 K (Fig. 4.13(c) and (d)), both constant energy **q**-scans evidence additional broadening, beyond that due to the small increase (0.4 deg) in the sample mosaic, indicating that the range of antiferromagnetic spin correlations decreases with increasing pressure. Figs. 4.13(e) and (f) show the background subtracted constant energy **q**-scans at 100 K in the cT phase (blue diamonds) and after heating the sample back to 180 K in the T phase (red diamonds). No clear structure is observed in the cT phase data along the $[h\ h\ 0]_T$ direction (Fig. 4.13(e)), while a reduced and broadened peak at ($\frac{1}{2}$ $\frac{1}{2}$ 1) is apparent in the re-measured data at 180 K. The increased width of the peak and reduced intensity is consistent with the increased sample mosaic and loss in sample volume. The corresponding re-measured scan along $[0\ 0\ l]_T$ at 180 K (Fig. 4.13(f)) is nearly transverse and, therefore, affected more by the increased sample mosaic. Nevertheless, scattering above the background (or the cT phase data) can still be seen.

The observation of antiferromagnetically correlated spin fluctuations in the T phase, and their strong suppression or complete absence in the cT phase, provides interesting new perspectives concerning both the physical properties of $CaFe_2As_2$ and, more generally, supercon-

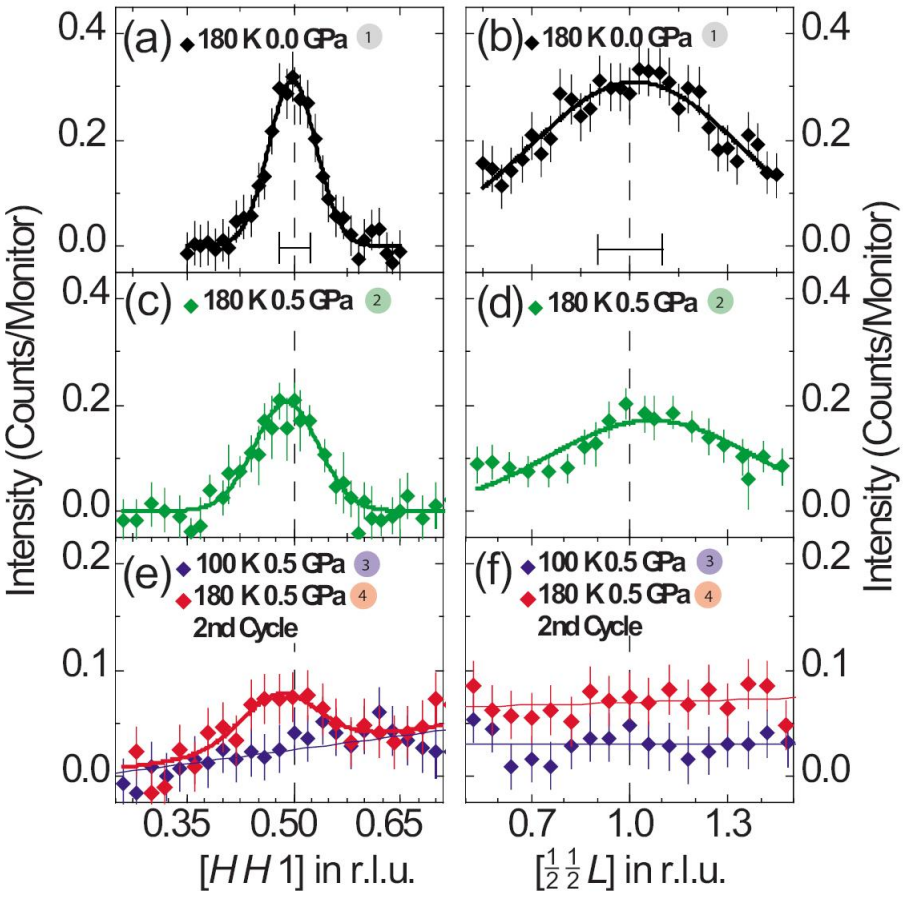

Figure 4.13 Constant energy **q** scans, after background subtraction, at 3 meV energy transfer through the $(\frac{1}{2}\ \frac{1}{2}\ 1)_{\mathrm{T}}$ antiferromagnetic wave vector along the $[h\ h\ 0]_{\mathrm{T}}$ [panels (a), (c), and (e)] and the $[0\ 0\ l]_{\mathrm{T}}$ directions [panels (b), (d), and (f)]. The numbers in the shaded circles correspond to the points indicated in Fig. 4.11(c). The heavy lines through the data are fits to a single Gaussian line shape. The thin lines provide a guide to the eyes. The dashed vertical line denotes the position of the $(\frac{1}{2}\ \frac{1}{2}\ 1)_{\mathrm{T}}$). The instrumental resolution is shown at the bottom of panels (a) and (b).

ductivity in the iron arsenides. Previous elastic neutron scattering studies (5; 8) have already provided strong evidence for the absence of static magnetic ordering in the cT phase. Total energy calculations (5) have shown that the Fe moment in the cT phase should be quenched. Our results are consistent with the absence of static order and low-energy magnetic fluctuations in the cT phase at $(\frac{1}{2}\ \frac{1}{2}\ l)_{\mathrm{T}}$ for l odd. The possibility that these low-energy spin fluctuations are redistributed to other locations in momentum space can not be excluded, and deserves further exploration through both experiment and theory.

4.8 Summary

In summary, neutron diffraction measurements performed using a hydrostatic pressure has revealed the phase lines between the paramagnetic tetragonal phase, antiferromagnetic orthorhombic, and the non-magnetic cT phases of $CaFe_2As_2$ with no other phases observed up to 2.5 GPa and 300 K. We saw a clear loss of the magnetic scattering in the cT phase at $\mathbf{Q} = (\frac{1}{2}\ \frac{1}{2}\ 3)_{\mathrm{T,cT}}$ which is associated with the reported AF2 structure where the spins are along the a-direction and a strip spin pattern running along b which is antiferromagnetic along c. Additionally, no evidence was found for proposed AF1-G and C type structures (67) in the cT phase. Polarized neutron experiments were performed to provided an upper limit of the proposed moment in the cT phase and, these measurements did not provide compelling evidence of a magnetic moment in the cT phase. Further work is needed to refine the upper limit.

Significant hysteresis was observed both upon transitioning to or from the cT phase while only a slight hysteresis is observed for transitions between the T and O phases. Unlike measurements with fluid pressure media, we observe only small ranges of phase co-existence which provides a clear indication that pressure media is causing additional pressure gradients which much be considered when interpreting the resulting phase diagram. Non-hydrostatic pressure gradients caused by both the freezing of the pressure medium and the extremely non uniform character of a transition to the cT phase can provide a range of pressure environments inside the sample and therefore separate phases can exists. This phase separation was confirmed by μSR measurements which provided evidence for co-existing paramagnetic/nonmagnetic and magnetically ordered state in $CaFe_2As_2$. Further evidence from neutron scattering measure-

ment on the E4 spectrometer at the Helmholtz center in Berlin using a liquid pressure medium provided clear evidence of the complex pressure conditions. A clear co-existence of the cT and O phases was found in contrast to experiments were He gas was used to transmit pressure which has proven to be the best method when hydrostatic pressure is desired due to the large range of temperatures and pressures where Helium can flow uniformly around a sample.

The cT phase has been shown to be nonmagnetic with the loss of magnetic ordering and spin fluctuations upon transforming into the cT phase. The loss of resistivity in the cT phase which does not seem to be consistent with DOS calculations in the cT phase due to a lowered DOS at the Fermi level can be explained by charge carrier coupling to the spin fluctuations and the loss of spin fluctuations can explain the trend in transport properties which show an increase of conductivity in the cT phase. In addition, in light of transport measurements that show that, under hydrostatic pressure conditions, the cT phase itself does not support bulk superconductivity (120), the observed suppression or absence of both static antiferromagnetic order and dynamic spin fluctuations in the cT phase of $CaFe_2As_2$ lends support to the notion that spin fluctuations play a role for iron arsenide superconductivity.

Finally, an important clue into the microscopic conditions which support SC in $CaFe_2As_2$ was shown in ref (129). Through the use of uniaxial pressure an additional phase (labeled T') was found to co-exist with the O and cT phases at low temperatures and in the range of pressures from 0.075 to 0.3 GPa. Simultaneous neutron diffraction and resistivity showed an onset of SC when a 0.1 GPa uniaxial pressure was applied along the c-axis. Also, the fact that pressure range where the new T' phase exist is coincident with the pressure range were SC is observed using uniaxial pressure (130) provides compelling evidence that this new phase stabilized by uniaxial pressure is the host of SC in $CaFe_2As_2$.

CHAPTER 5. Investigation of structure, magnetic excitations, and superconductivity in $Ba(Fe_{1-x}Co_x)_2As_2$

5.1 Introduction

The work in this chapter along with several other reported studies has been instrumental for our understanding that in the RFeAsO and $AeFe_2As_2$ compounds, superconductivity (SC) appears as the transition to an orthorhombic and antiferromagnetic (AFM) ordered state is suppressed by chemical doping (20; 104; 131; 69; 10). Detailed studies of the evolution of structural, magnetic, and SC properties as a function of chemical doping have revealed more complex behavior for compositions close to the boundary between (or coexistence region of) the AFM and SC phases. In the (1111) SC $CeFeAsO_{1-x}F_x$ (31), the phases appear to be mutually exclusive. However, in other cases such as $Ba_{1-x}K_xFe_2As_2$ (139), $Ba(Fe_{1-x}Co_x)_2As_2$ (69),(10), and $SmFeAsO_{1-x}F_x$ (132), regions of the phase diagram indicate a coexistence of AFM and SC. Coexistence of AFM and SC has been observed in other magnetic superconductors such as the Chevrel phases (RMo_6S_8) (133), borocarbides (RNi_2B_2C) (134), and ruthenates ($RuSr_2GdCu_2O_8$) (135) where rare-earth magnetic ordering occurs independently of SC. However, in some compounds, both magnetism and SC evolve from the same electronic (conduction) bands. In these exceptional systems, such UPt_3 (136; 137) and UNi_2Al_3 (138), neutron and resonant x-ray diffraction measurements have shown clear coupling between AFM and SC order parameters. The iron arsenide compounds belong to the latter category of magnetic superconductors, since both AFM and SC originate from the same Fe d bands. Section 5.2 provides clear evidence of this competition as depression of the ordered moment is observed below T_c suggesting SC and AFM order compete for the same electrons.

Section 5.4 discusses a systematic study of this competition with doping. The observed

suppression of the long range magnetic order with doping has allowed for an indirect theoretical connection between the observed co-existence and competition of phases and a sign changing unconventional Cooper pair wavefunction as discussed in chapter 2.. This conclusion may apply to many if not all of the superconducting iron arsenide compounds.

Section 5.5 provides further evidence that the SC wavefunction is sign changing through the observation of a superconducting magnetic resonance. Theoretical descriptions of the resonance require that the dynamical process connected to the resonance involve a momentum transfer that connects two points of the SC gap in k-space with different signs. Through this study, connection between SC and AFM order is further solidified. The resonance appears only after the sample is superconducting and it is observed at a momentum transfer associated with magnetism. It is also clear that the resonance provides information about the dimensionality of these systems. These layered systems are often approximated as 2-dimensional due to the weak interaction between Fe planes along the **c**-direction. However, our results show a clear dispersion of the SC resonance along the **c**-direction, providing motivation for theoretical descriptions to consider the 3-dimensional character when describing these systems.

5.2 Experimental details of the of neutron and x-ray scattering measurements on $\mathbf{Ba(Fe_{1-x}Co_x)_2As_2}$

5.2.1 Neutron and x-ray diffraction measurements $\mathbf{Ba(Fe_{1-x}Co_x)_2As_2}$

A series of neutron diffraction measurements discussed in sections 5.3 and 5.4 were performed on the HB1A diffractometer at the High Flux Isotope Reactor at Oak Ridge National Laboratory on a series of high quality single crystals of $Ba(Fe_{1-x}Co_x)_2As_2$ with $x = 0$ to 0.063. The experimental configuration for each experiment was 48'-40'-40'-136' with $E_i = 14.7$ meV. The samples were aligned in the $(h\ h\ l)_T$ plane and mounted in a closed-cycle refrigerator for low temperature studies.

X-ray scattering measurements were performed on $Ba(Fe_{0.953}Co_{0.047})_2As_2$ at the Advanced Photon Source (APS) at Argonne National Laboratory with an incident photon energy of 99.5 keV. X-ray diffraction measurements of the $(2\ 2\ 0)_T$ reflection above and below T_S. Ad-

ditional temperature-dependent, high-resolution, single-crystal x-ray diffraction measurements were performed at Ames Laboratory on a four-circle diffractometer using Cu K_α radiation from a Rigaku rotating Cu-anode Ru-300 system, selected by a germanium (1 1 1) monochromator. For these measurements, a plate-like single crystal of $Ba(Fe_{0.962}Co_{0.038})_2As_2$ was attached to a flat copper sample holder on the cold finger of a closed-cycle displex refrigerator. The diffraction data were obtained as a function of temperature between room temperature and 30 K.

5.2.2 Inelastic neutron scattering measurements on $Ba(Fe_{0.953}Co_{0.047})_2As_2$

The inelastic neutron-scattering measurement discussed in section 5.5 was performed on the HB3 spectrometer at the High Flux Isotope Reactor at Oak Ridge National Laboratory on single crystals of $Ba(Fe_{1-x}Co_x)_2As_2$ with $x = 4.7\%$. The sample consisted of nine co-aligned crystals with a total mass of 1.88 g and a total mosaic width of 1.5°. All samples were grown under identical conditions and show the tetragonal-orthorhombic transition of T_S=60 K, the Néel transition T_N=47 K, and SC transition temperatures at T_c=17 K, consistent with crystals used in previous studies. (140) Although the measurements were made below T_S where the sample is orthorhombic, in what follows we describe the scattering vector relative to the high temperature tetragonal (I4/mmm) cell. The sample was aligned in the $(h\ h\ l)_T$ plane and mounted in a closed-cycle refrigerator for low-temperature studies. Measurements were performed with 48'-60'-80'-120' collimation and a fixed final energy of E_f=14.7 meV. A pyrolytic graphite (PG) monochromator and analyzer were employed. One PG filter was used after the sample for inelastic measurements while two filters were used for elastic measurements to reduce the signal from higher-order harmonics.

5.3 Coexistence and competing antiferromagnetic and superconducting phases in the underdoped $Ba(Fe_{0.953}Co_{0.047})_2As_2$ compound studied by x-ray and neutron scattering techniques

In this section, neutron and x-ray diffraction measurements on $Ba(Fe_{0.953}Co_{0.047})_2As_2$ are presented which clearly show a large decrease in the AFM order parameter below T_c. In addition, the intensity of gapless spin wave excitations observed above T_c becomes redistributed at low energies in the SC state. Taken together, the results provide compelling evidence for strong competition between the AFM and SC phases and stress the important role that magnetism plays in superconductivity in the iron arsenides.

The series of Co-doped $Ba(Fe_{1-x}Co_x)_2As_2$ has been studied systematically by heat capacity, magnetization, resistivity (69; 10), and thermal expansion (141) measurements on single crystals grown in self-flux. With the addition of Co, the temperature of the first-order transition from the tetragonal (T) phase to the orthorhombic (O) and AFM ordered phase decreases and the transition either broadens or splits into separate transitions. Although it is suspected that the transition has structural and/or magnetic character, no microscopic determination of these phases has been reported until now. Nonetheless, evidence of the purported magnetic and structural transitions can be observed up to $x = 0.06$ (69; 10). At compositions above $x = 0.03$, SC first appears and exhibits a region between $x \sim 0.03$ and 0.06 where it is conjectured that the SC phase and the orthorhombic AFM phase (called underdoped compositions) coexist (69; 10). Beyond $x = 0.06$, the magnetic and structural transitions appear completely suppressed, and the SC transition temperature reaches a maximum of 23 K for $x = 0.074$ (69; 10). Figures 5.1(a) and 5.1(b) show the magnetization and resistivity data for an underdoped sample with $x = 0.047$. The data clearly show a superconducting transition at $T_c = 17$ K. Using the criteria in ref. (69) to determine transition temperatures, two higher temperature anomalies corresponding to the split transition are also identified. Upon cooling from high temperatures, the magnetization and resistivity undergo a change in slope near 60 K with temperature derivatives in Figs. 5.1(a) and 5.1(b) showing the anomaly more clearly. This is followed by another transition near 47 K. In analogy with the RFeAsO series of compounds where the magnetic and structural transitions

are split (142), it has been speculated that the strong resistivity anomaly at 60 K is associated with the T-O transition and the lower one (47 K) to AFM ordering. We undertook neutron and x-ray diffraction experiments to determine if the transitions separate and, if so, to identify the structural and magnetic phases in the underdoped region. It is also interesting to study how the AFM ordering, if present, evolves into the SC phase. Diffraction experiments were performed on a single crystal of underdoped $Ba(Fe_{0.953}Co_{0.047})_2As_2$ that were grown under identical conditions as those samples used in the bulk measurements in Figs. 5.1(a) and 5.1(b) and described in detail in ref. (9). The temperature dependence was studied at several nuclear Bragg peak positions and at $\mathbf{Q}_{\rm AFM} = (\frac{1}{2}\ \frac{1}{2}\ l = \text{odd})_{\rm T}$ positions corresponding to the AFM ordering in the parent $BaFe_2As_2$ compound (23).

Figure 5.1(c) shows the evolution of the integrated intensity of the $(2\ 2\ 0)_{\rm T}$ nuclear reflection with temperature. The (220) intensity starts to increase at about 80 K and grows gradually over a range of 20 K before increasing sharply at $T_{\rm S}$=60 K. This increase in intensity is ascribed to extinction release that occurs due to the formation of O twin domains at the structural transition. Although the resolution of neutron diffraction experiments was insufficient to determine the O splitting, we were able to confirm the orthorhombicity by performing high-energy single-crystal x-ray diffraction experiments using MUCAT sector 6-ID-D at the APS. X-ray diffraction measurements of the $(2\ 2\ 0)_{\rm T}$ reflection above and below $T_{\rm S}$ (Fig. 5.2) clearly show a very small O splitting [$(a$ - $b)/(a$ + $b)$= 0.12%] and twinning in the x = 0.047 sample. Given the full penetration of the x-rays, the results suggest that single phase O structure exists throughout the crystal.

We also studied a slightly lower composition of $x = 0.038$ which also shows a split transition and superconductivity, and the larger O splitting of 0.2% allows for clearer separation of twin reflections. Figure 5.2 shows the temperature evolution of the $(1\ 1\ 10)_{\rm T}$ reflection for x = 0.038 measured using a Rigaku rotating Cu-anode RU-300 system. The O splitting grows continuously below 76 K, and there does not appear to be any remaining T phase. While the evolution of the $(2\ 2\ 0)_{\rm T}$ intensity in the $x = 0.047$ neutron data is very sensitive to the structural transition, it arises from the formation of extrinsic twin domains and cannot be considered as the order parameter of the T-O structural transition. Despite the lack of strong

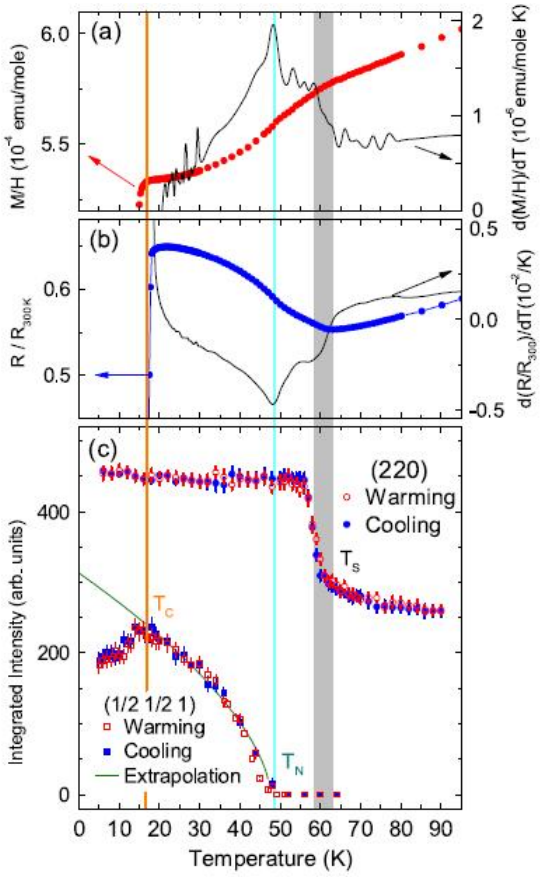

Figure 5.1 (a) Magnetization (dots) and its temperature derivative (line), and (b) resistivity and its temperature derivative for $Ba(Fe_{0.953}Co_{0.047})_2As_2$ as a function of temperature. (c) The integrated intensity of the $(2\ 2\ 0)_T$ nuclear reflection (circles) and the $(\frac{1}{2}\ \frac{1}{2}\ 1)_T$ magnetic reflection (squares) as a function of temperature. Hollow symbols indicate warming and filled symbols cooling. The solid line shows the power law fit to the magnetic order parameter. Vertical lines through all three panels indicate the structural (T_S), magnetic (T_N), and superconducting (T_c) transitions.

evidence for coexisting T and O phases (Fig. 5.2) and thermal hysteresis [Fig. 5.1(c)], we cannot determine if the T-O transition for the $x = 0.047$ composition is first or second order.

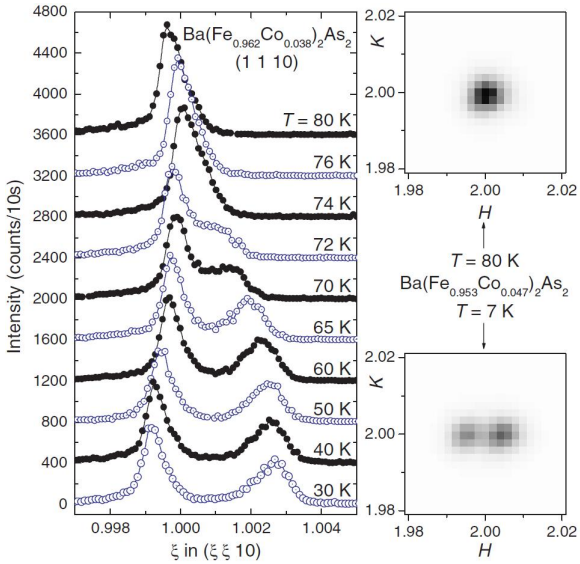

Figure 5.2 (Right) Images of the x-ray diffracted intensity of the $(2\ 2\ 0)_{\mathrm{T}}$ peak for $x = 0.047$ showing a single spot above T_{S} and two spots below T_{S} due to orthorhombic splitting. (Left) The temperature evolution of the $(1\ 1\ 10)_{\mathrm{T}}$ reflection for $x = 0.038$, showing T-O phase transition.

Figure 5.1(c) shows intensity gradually appearing at the $(\frac{1}{2}\ \frac{1}{2}\ 1)_{\mathrm{T}}$ magnetic Bragg position below $T_{\mathrm{N}} = 47$ K. The magnetic wave vector is identical to that for $BaFe_2As_2$ (23), indicating that the magnetic structure is likely the same AFM "stripe" structure observed in all of the AFM ordered Fe-As materials. The AFM squared order parameter was obtained from the integrated intensity of the $(\frac{1}{2}\ \frac{1}{2}\ 1)_{\mathrm{T}}$ peak. Below T_{N}, the integrated intensity can be fit to the form $(T - T_{\mathrm{N}})^{2\beta}$ with exponent $2\beta = 0.6$ and consistent with a second-order transition. Assuming that the full volume of the crystal is AFM ordered, an extrapolated zero-temperature magnetic moment of $0.2\pm0.1\mu_{\mathrm{B}}$ was estimated by comparison of the $(\frac{1}{2}\ \frac{1}{2}\ 1)_{\mathrm{T}}$ intensity to nuclear Bragg intensities and also to magnetic intensities of $CaFe_2As_2$ under similar experimental conditions. The moment is significantly reduced compared to the $x = 0$ moment of $0.87\mu_{\mathrm{B}}$, similar to the reduction observed in other doped FeAs compounds (31; 143). The evolution of the nuclear and magnetic intensities shown in Fig. 5.1(c) confirms that the single first-order transition in $BaFe_2As_2$ has split into two separate transitions with Co addition with the lower,

magnetic, transition appearing to be second-order in nature. Similar to the RFeAsO compounds (142), the structural transition occurs first upon cooling, followed by AFM ordering. Figure 5.3 identifies these states in the phase diagram for $Ba(Fe_{1-x}Co_x)_2As_2$.

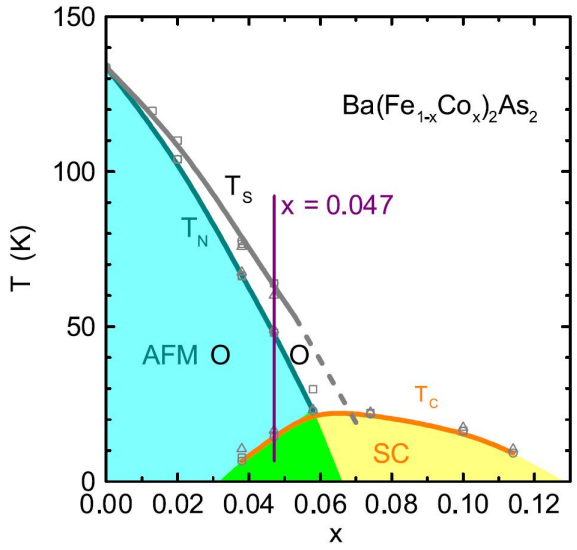

Figure 5.3 Phase diagram for $Ba(Fe_{1-x}Co_x)_2As_2$ showing paramagnetic tetragonal (T), paramagnetic orthorhombic (O), AFM ordered orthorhombic (AFM O), and superconducting (SC). AFM O and SC phases coexist between $x = 4\%$ and 6%. The vertical line shows the position of the $x = 0.047$ sample studied here. The data points for the phase lines have been taken from ref. (9).

The integrated AFM intensity is substantially reduced below T_c, as shown in Fig. 5.1(c). Meanwhile, the intensity ratio of the $(\frac{1}{2}\ \frac{1}{2}\ 1)_T$ and $(\frac{1}{2}\ \frac{1}{2}\ 3)_T$ reflections is unchanged [Fig. 5.4(a)], indicating that the moment direction and magnetic symmetry are unaffected by the onset of T_c. The partial suppression of $(\frac{1}{2}\ \frac{1}{2}\ 1)_T$ intensity shown in Fig. 5.4(a) therefore suggests a reduction in the average static Fe moment below T_c. In addition, inelastic energy scans at $(\frac{1}{2}\ \frac{1}{2}\ 1)_T$ [Fig. 5.4(b)] show that the low energy magnetic spectral weight is also suppressed. Above T_c, the excitations appear gapless, and constant energy cuts at 2.5 meV along the $[1\ 1\ 0]_T$ direction reveal a sharp peak [Fig. 5.4(c)] consistent with steep spin wave excitations (76). Below T_c, the intensity below 4 meV (and spin wave peak at 2.5 meV) are suppressed, suggesting that a gap forms in the spin wave excitations. This suppression is offset by an increase in the magnetic intensity above 4 meV. The redistribution of AFM spin excitations below T_c indicates a direct coupling between AFM and SC and is strong evidence in support

of the homogeneous coexistence of AFM and SC (see below). The behavior of the low energy spin excitations is similar to the development of a gap and resonance like feature below T_c in the optimally doped superconductor with $x = 0.1$ (18). However, at the optimal composition there is no long-range AFM order, and SC gaps the spectrum of short-ranged spin fluctuations that are much broader in momentum space. The resonance is discussed in detail in section 5.5.

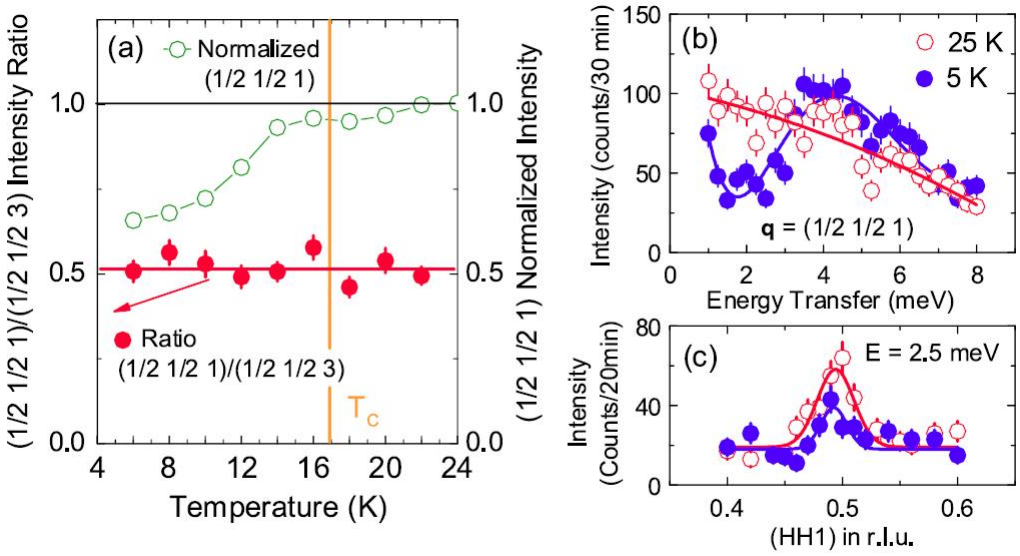

Figure 5.4 (a) The reduction in intensity of the $(\frac{1}{2}\ \frac{1}{2}\ 1)_T$ peak compared to the fit of the magnetic order parameter to a power law [shown in Fig. 1(c)] and the intensity ratio of $(\frac{1}{2}\ \frac{1}{2}\ 1)_T$ and $(\frac{1}{2}\ \frac{1}{2}\ 3)_T$ as a function of temperature. (b) Energy scan at $(\frac{1}{2}\ \frac{1}{2}\ 1)_T$ for T = 25 K (empty circles) and 5 K (solid circles). (c) Scans along [110] at 2.5 meV for 25 K and 5 K. Lines are guides to the eye.

Now, the question of homogeneity and the coexistence of the AFM, SC, and O phases in underdoped compositions will be addressed. Evidence from transport and thermodynamic measurements (69) and magnetic optical imaging of Meissner flux expulsion (144) supports homogeneous SC. x-ray measurements in Fig. 5.2 find only the twinned O structure in the SC phase, with no observable T phase. Thus, crystals appear to have crystallographic homogeneity from which one can conclude that SC occurs in the O structure. This is supported by the observation of a distinct difference in the anisotropy of H_{c2} in underdoped (orthorhombic) and optimally doped (tetragonal) samples (69). Neutron diffraction alone cannot provide direct evidence for homogeneity of AFM. However, as discussed above, suppression of the low energy

spin excitations together with the reduction of the static moment provides strong evidence that AFM and SC coexist homogeneously and are in competition with one another.

Competition between AFM and SC is natural when one considers that both originate from the multiple Fe conduction bands that cross the Fermi level. Fermi surface nesting giving rise to AFM or spin density wave ordering will gap only part of the Fermi surface. On the other hand, SC will (for example) gap the entire Fermi surface for an s-wave gap, or form line nodes for a d-wave gap. The (repulsive) interaction between spin density wave and SC order parameters then arises from competition over the shared electronic density of states common to both gaps, regardless of the microscopic origins of SC. This has been demonstrated using the two-band itinerant model for the iron arsenides where competing spin density wave and $s^{\pm}$ SC are shown to coexist over a range of doping (145). For the more general case of s-wave (147) or d-wave SC (146), the competition causes a reduction sublattice magnetization below T_c. This is described in more detail in the next section. In $Ba(Fe_{0.953}Co_{0.047})_2As_2$, the observed reduction in the ordered moment below T_c is substantially larger than that observed for UPt_3 (136) or UNi_2Al_3 (138), demonstrating an unusually strong interaction between AFM and SC in the iron arsenides.

5.4 Unconventional pairing in iron arsenide superconductors

In this section, we extend the measurements presented for $x = 0.047$ to other compositions to show how the coupling between SC and AFM evolve over a range of Co doping. The resulting x-T phase diagram, constructed, in part, from observations made during neutron scattering measurements of the under doped $BaFe_2As_2$ compounds will be shown. The theory described in this section discusses phenomenological and microscopic models describing the coupling of SC and AFM in Co doped $BaFe_2As_2$ system based on the work of R. Fernandes and J. Schmalian (159). The remarkable agreement of combined experimental and theoretical work provides the important conclusion that the Cooper pairing in the iron arsenides is unconventional.

5.4.1 Experimental results for $\mathbf{M}(x, T)$

Neutron-diffraction measurements were performed on the HB1A diffractometer at the High Flux Isotope Reactor at Oak Ridge National Laboratory on a series of $Ba(Fe_{1-x}Co_x)_2As_2$ single crystals using the same spectrometer configuration and data-analysis methods described in ref. (53). The magnetic integrated intensities were determined from rocking scans through the magnetic peak at $\mathbf{Q}_{\rm AFM} = (\frac{1}{2}\ \frac{1}{2}\ 3)_{\rm T}$ as a function of temperature and put on an absolute basis using the known mass of the samples and the magnetic diffraction from the parent compound, $BaFe_2As_2$, measured under identical conditions. The important observation is that at $T_{\rm c}$, a reduction of the moment is observed with the onset of SC and this reduction is maximized at the lowest temperatures when the SC gap is largest. This is clear evidence that as SC develops, electrons which were involved with AFM have formed Cooper pairs and no longer contributing to AFM order.

Fig. 5.5(a) shows the experimentally determined phase diagram based on observed magnetic neutron scattering to determine $T_{\rm N}$ as well as bulk thermodynamic and transport measurements to determine the structural transition $T_{\rm S}$. Fig. 5.5(b) shows the evolution of the magnetic moment as determined from neutron scattering measurements. For doping levels above $x = 0.038$, the reduction of the moment below $T_{\rm c}$ is clearly observed.

The magnetic moment at zero temperature in the absence of SC, $M(T = 0, x)$, where $M = |\mathbf{M}|$, was determined by extrapolating the measured order parameter $M(T, x)$ above $T_{\rm c}$ using a power-law fit to the data. An example extrapolation is shown in Fig. 5.6. As described in the next section, the values for $M(T = 0, x)$ will be compared to theoretically determined values. The ratios of the integrated intensities of the $(\frac{1}{2}\ \frac{1}{2}\ 1)_{\rm T}$ and $(\frac{1}{2}\ \frac{1}{2}\ 3)_{\rm T}$ magnetic reflections were monitored to ensure that there was no change in the moment direction as a function of temperature and composition x. No additional reflections, e.g., incommensurate magnetic satellites, were observed, in agreement with other work.(160)

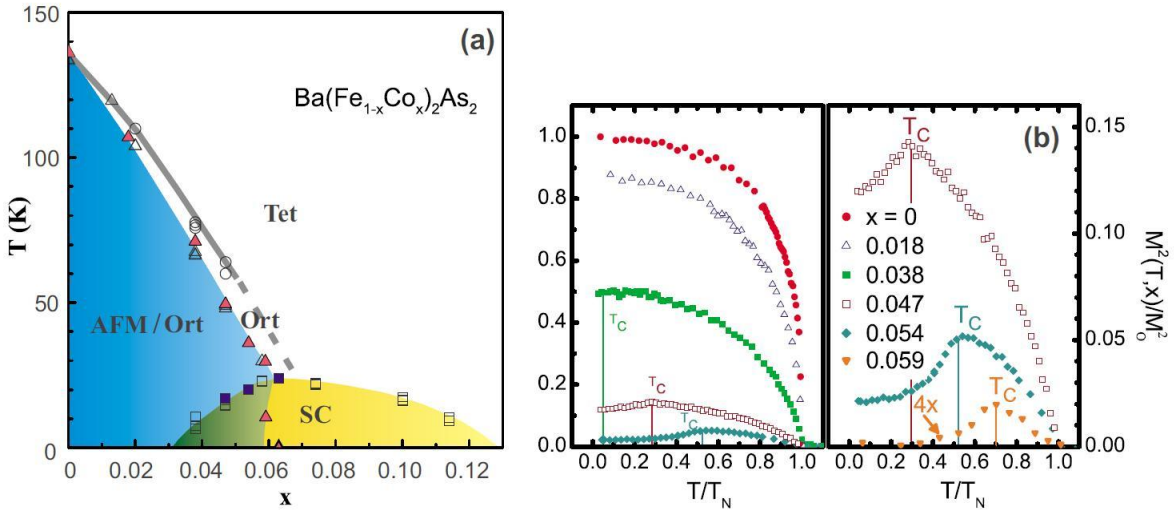

Figure 5.5 (a) Experimentally determined x-T phase diagram based on observed magnetic neutron and x-ray scattering as well as bulk thermodynamic and transport measurements. (b) The moment trend versus reduced temperature T/T_{N} The maximum moment value of the undoped compound is 0.87 μ_{B}(23)

5.4.2 Phenomenological model

The Ginsburg-Landau theory of coupled AFM and SC order parameters, can be used to describe the phase diagram of $Ba(Fe_{1-x}Co_x)_2As_2$. The free energy expansion which is shown as equation (1) consists of the SC order parameter (Δ) and the magnetic order parameter ($\mathbf{M}$).

$$F_{\mathrm{GL}}(\Delta,\mathbf{M}) = \int d^d r\left(\frac{a_{\mathrm{s}}}{2}|\Delta|^2 + \frac{u_{\mathrm{s}}}{4}|\Delta|^4 + \frac{\gamma}{2}|\Delta|^2\mathbf{M}^2 + \frac{a_{\mathrm{m}}}{2}\mathbf{M}^2 + \frac{u_{\mathrm{m}}}{4}\mathbf{M}^4\right) \tag{5.1}$$

The coefficients in 5.1 will be obtained in a microscopic theory described in the next section. The quadratic coefficients, a_{s} and a_{m}, for SC and AFM respectively, are defined such that $a_i = a_{i0}(T - T_{0i})$, $(i = \mathrm{s,m})$. T_{0i} is the transition temperature for the case where there is no coexistence or competition between AFM and SC (or $\gamma = 0$). A positive and non-zero γ from the SC-AFM coupling term indicates that there is coupling between order parameters. Therefore, for the rest of this discussion, γ will assumed to be positive. In the absence of coupling, the quartic coefficients u_{s} and u_{m} determine the order of the phase transition where a positive u_i indicates a second order transition will occur and a negative u_i is indicative of a first order phase transition.

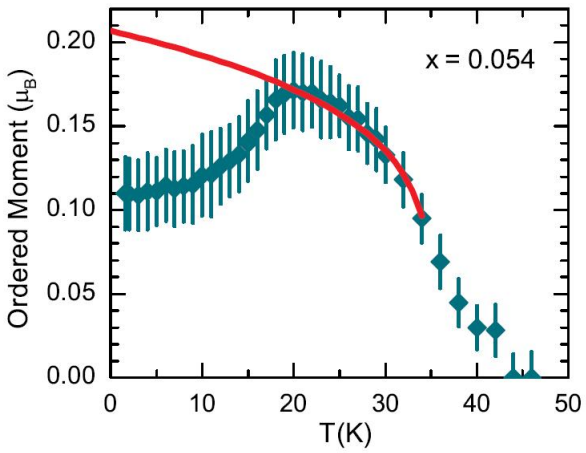

Figure 5.6 The experimentally determined moment trend with temperature for 5.4% Co doped $BaFe_2As_2$. The line shows an extrapolation to the T = 0 K moment value in the absence of SC.

Since we have observed experimentally that both SC and AFM transition temperatures depend on the level of Co-doping, $T_{0i}(x)$ will be assumed to have a doping dependence and, again, this will describes the transition temperature in the absence of coupling. For a given doping, x^*, where $T^* = T_{0m}(x^*) = T_{0s}(x^*)$ the system is in the proximity of a multi-critical point where both order parameters are small, and a simultaneous expansion of Δ and M shown in equation (1) is allowed.

It is useful to define a dimensionless quantity 'g' to describe the behavior in the phase diagram near (x^*,T^*).

$$g = \frac{\gamma^2}{u_s u_m} - 1 \tag{5.2}$$

For the range of γ where $g < 0$ ($0 < \gamma^2 < u_s u_m$), and quartic coefficients for each order parameter is positive, the transition to both AFM and SC will be second order and homogeneous phase coexistence will occur below a tetracritical point in the phase diagram as shown in figure 5.7(a). On the other hand, if $g > 0$ ($\gamma^2 > u_s u_m$), and the quartic terms are negative for AFM and SC, the transition to AFM or SC is first order and the phases will completely separate. Figure 5.7(b) shows the phase diagram in this case. A heterogenous coexistence is extended between the doping levels corresponding to x_1 and x_2, since there are two possible chemical potential values (for a given number of electrons) which correspond to either the existence of

SC or AFM. Thus, for values between x_1 and x_2 the SC and AFM phases coexist in separate regions of the sample. Doping above x_2 corresponds to the case where AFM is absent and the SC phase remains at $T = 0$.

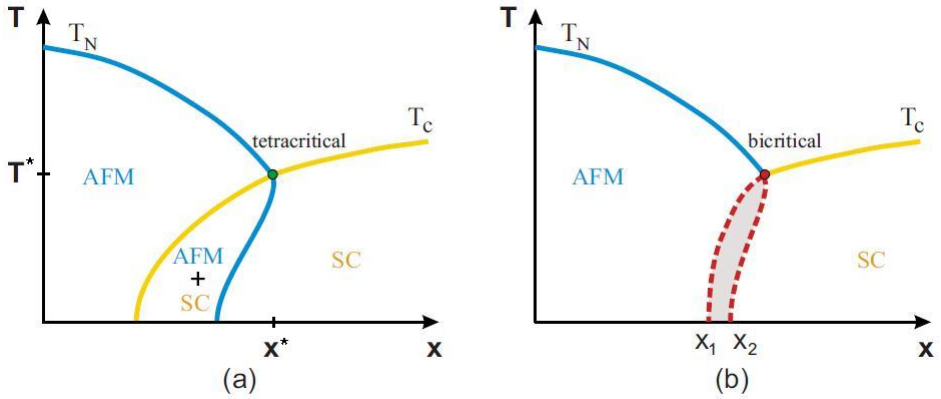

Figure 5.7 Schematic $x - T$ phase diagrams for the Co doped $BaFe_2As_2$ system with (a) homogeneous coexistence of SC and AFM and (b) heterogeneous coexistence of SC and AFM.

A reduction of T_N and back bending of the phase line in figure 5.7(a) can be inferred from the data and understood with a Ginsburg-Landau approach. For the simple case of a pure AFM phase, the solution to the order parameter (M) as a function of temperature meets the condition that $\frac{dM^2}{dT} < 0$ (forward bending) for all temperatures but this can change if two phases are competing. To illustrate this point, it was shown by Fernandes *et al.* for the case of homogenous co-existence, the magnetic order parameter for can be expressed as:

$$M^2(T) = \frac{a_{m,0}u_s(T_{N,0} - T) + a_{s,0}(T - T_{c,0})}{\sqrt{u_m u_s} - \gamma} \tag{5.3}$$

It follows that $\frac{dM^2}{dt} < 0$ if $a_{s0}\gamma > a_{m0}u_s$ and the ordered moment can decrease as temperature decreases below T_c due to competition of SC and AFM order. This behavior was observed experimentally as will be shown in section 5.4.3. The condition $a_{s0}\gamma > a_{m0}u_s$ also is an indication of a back bending of the phase line upon entering the SC state. To demonstrate why this is, consider the bare Néel temperature ($T_{N,0}$) near the doping levels just below the position in the phase diagram where $T_N = T_c$ or just below the critical doping x^*. In this region one can express the bare Néel temperature as $T_{N,0}(x) = T_{c,0}[1 + f(x)]$ with $\frac{dT_{N,0}}{dx} < 0$. The decrease of

$T_{N,0}(x)$ is connected to the detuning of the Fermi surface nesting of electron and hole pockets with doping. As $T_{c,0}$ is assumed to be constant near x^*, it must be true that $\frac{df(x)}{dx} < 0$. Using equation (3) at $T = T_N$, one can show $T_N = T_{c,0}[1 - f(x)\frac{a_{m,0}u_S}{a_{S,0}\gamma - a_{m,0}u_S}]$. Thus, the same condition which leads to a suppression of the moment with temperature ($a_{s0}\gamma > a_{m0}u_s$) also leads to a back bending of T_N in the region of phase coexistence. Both of these trends have been observed experimentally as will be shown in section 5.4.3

5.4.3 Microscopic model

The goal of the microscopic model is to determine the coefficients for the Ginzburg-Landau expansion based in part on electronic interactions in a two band model described earlier.

A two dimensional microscopic model was developed to further describe the interaction between SC and AFM states in electron doped $BaFe_2As_2$. In this section, the main components of the microscopic model will be summarized. This section does not show a complete development of this theory but is intended to provide the reader with some key ideas. For a more complete discussion of this model, refer to reference (159).

The microscopic model was motivated by ARPES measurements of $Ba(Fe_{1-x}Co_x)_2As_2$ (with $x = 0..0.14$)(27) where it was shown that two Fermi surface sheets exist with a hole pocket located at the zone center and an electron pocket displaced from the zone center by the magnetic ordering vector $\mathbf{Q} = (\pi, \pi)_T$ as was discussed in chapter 2. A schematic representation of the bands is shown in figure 5.8 which shows the dispersion of the hole and electron bands. It was shown in ref (27) that as the Co doping level was increased, the hole pocket decreased in size while the electron pocket grew larger as shown in figures 5.9(a) and 5.9(b). This occurs because in $Ba(Fe_{1-x}Co_x)_2As_2$, as the doping level increases, electrons are added to the system (Co adds one extra electron) and therefore the chemical potential (μ) increases. Eventually, for the case of large levels of Co doping, the hole pocket will disappear as the chemical potential rises above the top of the band.

The Hamiltonian is composed of three parts as shown in equation (4)

$$\mathcal{H} = \mathcal{H}_0 + \mathcal{H}_{AFM} + \mathcal{H}_{SC} \tag{5.4}$$

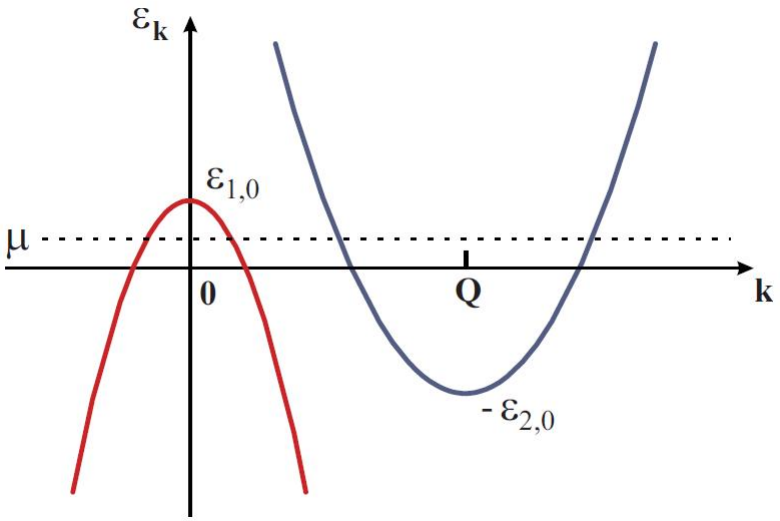

Figure 5.8 Schematic representation of the hole band at $\mathbf{k} = 0$ and the electron band at $\mathbf{k} = \mathbf{Q}$. The maxima of the hole bands and minima of the electron bands are labeled $\epsilon_{1,0}$ and $\epsilon_{2,0}$ respectively. The dashed line indicates the position of the chemical potential μ.

where $\mathcal{H}_0$ is the non interacting Hamiltonian describing the bands, $\mathcal{H}_{\mathrm{AFM}}$ describes the antiferromagnetic interaction, and $\mathcal{H}_{\mathrm{SC}}$ describes the pairing interaction.

Equation (5) is the non interacting Hamiltonian ($\mathcal{H}_0$) which has a form motivated by ARPES measurements and is shown schematically in figure 5.8.

$$\mathcal{H}_0 = \sum_{\mathbf{k},\sigma}(\epsilon_{1,\mathbf{k}} - \mu)c^{\dagger}_{\mathbf{k}\sigma}c_{\mathbf{k},\sigma} + \sum_{\mathbf{k}+\mathbf{Q},\sigma}(\epsilon_{2,\mathbf{k}} - \mu)d^{\dagger}_{\mathbf{k}\sigma}d_{\mathbf{k},\sigma} \tag{5.5}$$

The hole band is circular ($\epsilon_{1,\mathbf{k}} = \epsilon_{1,0} - \frac{k^2}{2m}$). The electron band is elliptical (($\epsilon_{2,\mathbf{k}+\mathbf{Q}} = -\epsilon_{2,0} + \frac{k_x^2}{2m_x} + \frac{k_y^2}{2m_y}$). The operator $c^{\dagger}_{\mathbf{k},\sigma}$, creates an electron with spin σ in the hole band while the operator $d^{\dagger}_{\mathbf{k},\sigma}$ creates an electron with spin σ in the electron band which is displaced from the hole band by the wave-vector $\mathbf{Q}$.

Introduction of scattering between bands by an interaction Hamiltonian can result in itinerant AFM (spin density wave) order under strong nesting conditions. The interaction term is defined as $\mathcal{H}_{\mathrm{AFM}} = I\sum_{i,j}\mathbf{S}_i \cdot \mathbf{S}_j$ where I is the inter-band Coulomb interaction, the spin in site i is $\mathbf{S}_i = \mathbf{S}_{i0}\mathrm{e}^{i\mathbf{Q}\cdot\mathbf{R}}$ with $\mathbf{R}$ being the inter-atomic spacing between iron atoms and $\mathbf{Q} = \mathbf{Q}_{\mathrm{AFM}}$ is the nesting vector between the two bands. Re-expressing $\mathcal{H}_{\mathrm{AFM}}$ in terms of creation

and annihilation operators yields equation (6)

$$\mathcal{H}_{\mathrm{AFM}} = I \sum_{\mathbf{k},\mathbf{k}',\mathbf{q}} \sum_{s,s'} c^{\dagger}_{\mathbf{k},s} \boldsymbol{\sigma}_{s,s'} d_{\mathbf{k}+\mathbf{q},s'} \cdot d^{\dagger}_{\mathbf{k}',s} \boldsymbol{\sigma}_{s,s'} c_{\mathbf{k}'-\mathbf{q},s'} \tag{5.6}$$

Using the mean field approximation, $\mathcal{H}_{\mathrm{AFM}}$ reduces to equation (7)

$$\mathcal{H}_{\mathrm{AFM}} = -\sum_{\mathbf{k},s} sM(c^{\dagger}_{\mathbf{k},s} d_{\mathbf{k}+\mathbf{Q},s} + d^{\dagger}_{\mathbf{k}+\mathbf{Q},s} c_{\mathbf{k},s}) \tag{5.7}$$

where the electronic AFM gap (M) is defined in terms of the staggered magnetization (m) as shown in equation (8).

$$M = \frac{1}{2N} \sum_{\mathbf{k},s} s < c^{\dagger}_{\mathbf{k},s} d_{\mathbf{k}+\mathbf{Q},s} >= Im \tag{5.8}$$

Finally, the term in the Hamiltonian which describes superconductivity ($\mathcal{H}_{\mathrm{SC}}$) includes an inter-band interaction $V_{\alpha\beta}= V(1-\delta_{\alpha\beta})$ with the indices (α or β) = 1 (hole band) or 2 (electron band). $\mathcal{H}_{\mathrm{SC}}$ for this case is shown in equation (9).

$$\mathcal{H}_{\mathrm{SC}} = V \sum_{\mathbf{k},\mathbf{k}',\mathbf{q}} c^{\dagger}_{\mathbf{k}+\mathbf{q},\uparrow} c^{\dagger}_{-\mathbf{k},\downarrow} d_{-\mathbf{k}'-\mathbf{q},\uparrow} d_{\mathbf{k}',\downarrow} \tag{5.9}$$

Using the mean field approximation, $\mathcal{H}_{\mathrm{SC}}$ can be simplified to the equation (10) with SC gaps shown in (11). As shown in ref (159) the SC order parameters on bands 1 and 2 involve an inter-band paring

$$\mathcal{H}_{\mathrm{SC}} = -\sum_{\mathbf{k}+\mathbf{Q}} \Delta_1 (c^{\dagger}_{\mathbf{k},\uparrow} c^{\dagger}_{-\mathbf{k},\downarrow} + c_{-\mathbf{k},\downarrow} c_{\mathbf{k},\uparrow}) - \sum_{\mathbf{k}} \Delta_2 (d^{\dagger}_{\mathbf{k},\uparrow} d^{\dagger}_{-\mathbf{k},\downarrow} + d_{-\mathbf{k},\downarrow} d_{\mathbf{k},\uparrow}) \tag{5.10}$$

$$\begin{aligned} \Delta_1 &= -V \sum_{\mathbf{k}+\mathbf{Q}} < d^{\dagger}_{\mathbf{k},\uparrow} d_{-\mathbf{k},\downarrow} > \\ \Delta_2 &= -V \sum_{\mathbf{k}+\mathbf{Q}} < c^{\dagger}_{\mathbf{k},\uparrow} c_{-\mathbf{k},\downarrow} > \end{aligned} \tag{5.11}$$

From equation (11), it becomes clear that size of $\Delta_1(\Delta_2)$ gaps formed on the hole (electron) band is determined by the density of states of the electron (hole) band. In this framework, competing theories describing the symmetry of the Cooper pair wave function with no angular dependence such as s++ and s+- (where figure 5.10 shows a representation of wavefunctions with these symmetries) can be explored by changing the sign of the inter-band coupling where $V < 0$ (attractive) results in s++ while $V > 0$ (repulsive interaction in unconventional SC) results in s+- symmetry. This can be seen after examining the gap equations at T_c in the absence of magnetism. As discussed in ref (159), at T_c, the gap equations can be simplified when one considers that only electrons around the Fermi surface are responsible for superconductivity and that the superconducting gaps are small. The resulting simplified gap equations are shown in equations (12),

$$\begin{aligned} \Delta_1 &= -V\rho_2\Delta_2 \ln\left(\frac{W\alpha}{T_c}\right) \\ \Delta_2 &= -V\rho_1\Delta_1 \ln\left(\frac{W\alpha}{T_c}\right) \end{aligned} \tag{5.12}$$

where ρ_i is the density of states at the Fermi level for band i, W is the upper cutoff energy for the pairing interaction, $\alpha = \pi e^{\frac{\gamma_E}{2}}$ and γ_E is Euler's constant. These coupled equations can be re-expressed in matrix form as shown in equation (13)

$$\begin{pmatrix} \Delta_1 \\ \Delta_2 \end{pmatrix} = \ln\left(\frac{W\alpha}{T_c}\right) \begin{pmatrix} 0 & -V\rho_2 \\ -V\rho_1 & 0 \end{pmatrix} \begin{pmatrix} \Delta_1 \\ \Delta_2 \end{pmatrix} \tag{5.13}$$

which has eigenvalues of $\lambda_\pm = \pm V\sqrt{\rho_1\rho_2}$ and eigenvectors $(\Delta_1, \Delta_2) \propto \frac{(\sqrt{\rho_2}, \mp\sqrt{\rho_1})}{\sqrt{\rho_1+\rho_2}}$. The largest λ value will indicate the most stable state with the largest T_c. If $V < 0$, the largest eigen value is λ_- and we can assign this state as s++ because the SC gaps have the same sign. If $V > 0$, the largest eigen value is λ_+ and we can assign this state as s+- because the SC gaps have opposite sign for this case. One can go beyond s wave symmetry and use more complicated d-wave symmetry by adding the appropriate directional dependence to $V(\mathbf{k})$. As will be discussed, the assumed inter-band coupling and the resulting SC and AFM order parameters will differ due to changes of the g-parameter (originating from the analysis of the quartic and coupling terms in the free energy) which, as was discussed earlier, determines whether or not the phases

coexist homogenously or heterogeneously. In ref (159) the free energy of the system described by the mean field Hamiltonian composed of the sum of equations (5), (7), and (8) is shown in equation (14),

$$f(M,\Delta_\alpha) = \frac{2}{I}M^2 - \frac{1}{V}(\Delta_1^*\Delta_2 + \Delta_2^*\Delta_1) - \frac{2T}{N}\sum_{k,a}\ln\left(2\cosh\frac{E_{a,k}}{2k_{\mathrm{B}}T}\right) \tag{5.14}$$

where $\mathrm{E}_{a,k}$ refers to the excitation energy of this system with simultaneous magnetic and superconducting order. Therefore, by design and as shown in equation (14), the resulting free energy in this theory is intimately linked to the band structure, SC, and AFM order.

In order to apply the Ginzburg-Landau theory, equation (14) below can be expanded to yield equation (16).

$$\delta f(M,\Delta_\alpha) = f(M,\Delta_\alpha) - f(0,0) \tag{5.15}$$

$$\delta f(M,\Delta_\alpha) = \frac{a_{\mathrm{m}}}{2}M^2 + \frac{u_{\mathrm{m}}}{4}M^4 + \sum_{\alpha,\beta}\frac{a_{\mathrm{s},\alpha\beta}}{2}\Delta_\alpha\Delta_\beta + \sum_{\alpha}\frac{u_{\mathrm{s},\alpha}}{4}\Delta_\alpha^4 + \sum_{\alpha\beta}\frac{\gamma_{\alpha\beta}}{2}M^2\Delta_\alpha\Delta_\beta \tag{5.16}$$

Now, the form of equation (16) can be compared to equation (1) shown in the phenomenological description. Expressions for the quadratic and quartic terms are shown in ref (159). When values for the magnetic interaction I, interband interaction V, and as well as values of the non interacting band structure (including $\epsilon_{\alpha 0}$, effective electron masses, and chemical potential assuming rigid bands) are known or can be estimated, the values of the Ginsburg-Landau parameters can be evaluated using the microscopic model and details of the phase diagram (e.g. homogenous or heterogeneous phase coexistence of SC and AFM) can be determined. It is important to note the term γ_{12} in (16) because it is related to the process in which Cooper pairs are scattered from one band to the other by static staggered magnetization. Since the SC gaps may differ from each other by a phase factor, this term will be sensitive to this phase and therefore provide the possibility that experimental studies of the phase diagram can lead to insight into the phase difference between Cooper pairs on each band.

5.4.4 Application to $Ba(Fe_{1-x}Co_x)_2As_2$

The microscopic model described in the last section is a rigid band model which assumes the density of states (DOS) of $Ba(Fe_{1-x}Co_x)_2As_2$ is unchanged by the addition of Co. Since each Co atom is a substitute for Fe which dominates the DOS at the Fermi surface, and Co is a neighbor to the right of Fe on the periodic table, a substitution of Co involves the addition of single electron to the bands. This raises the chemical potential of the system which is seen in equation (5). This change in the chemical potential will cause the electron and hole pockets which have similar areas for the un doped compound to change (a process known as detuning) such that electron pocket increase in size while the hole pocket becomes smaller. This has been observed in ARPES measurements (27). Therefore, in this model there is a direct connection to doping level (x) which we measure experimentally and μ.

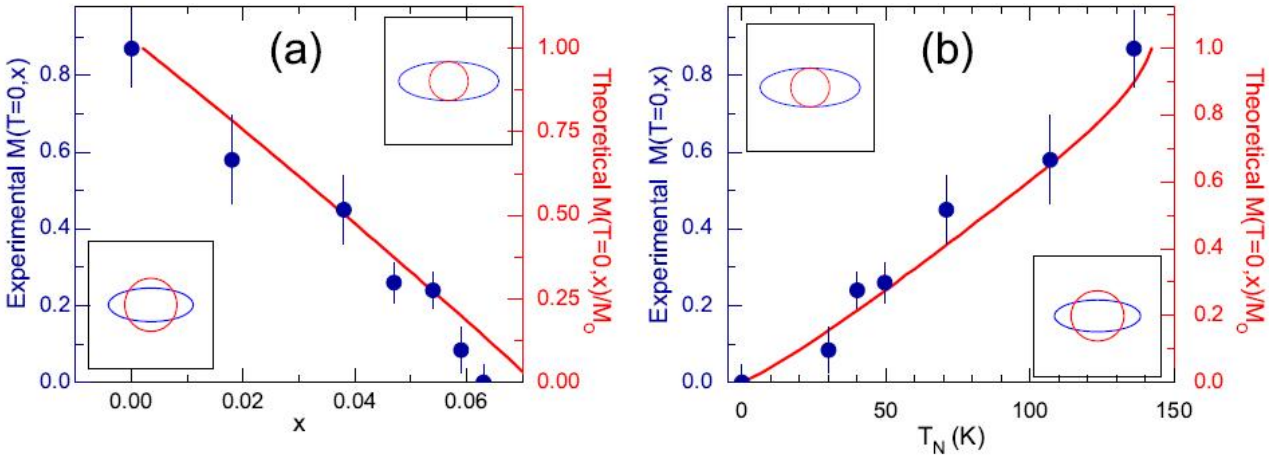

Figure 5.9 Extrapolated zero temperature ordered moment M(T=0,x) as function of doping x (panel a) and as function of T_N (panel b) for $Ba(Fe_{1-x}Co_x)_2As_2$. Points correspond to experimental data whereas the solid line is the result of the calculation described in the text. In the insets, the red circle (blue ellipse) denotes the hole (electron) Fermi pocket.

Theoretical calculations of the magnetic order in the absence of SC were performed by setting $\Delta_\alpha = 0$ but with a non-zero magnetic interaction I = 0.95 eV such that calculated $T_N = 140$ K when $x = 0$ to match the experimentally determined T_N. As shown in Fig

5.9, experimental and theoretical values are in good agreement showing again that as the Fermi surface pockets are detuned from each other as the doping level rises, magnetic order is suppressed. When magnetic order is completely suppressed, SC in the absence of AFM order can be theoretically switched on with the pairing interaction set to $|V| = 0.46$ eV such that T_c matches the experimentally observed $T_c = 25$ K at the doping level $x = 0.062$. The remaining parameter values are discussed in ref (159)

Now that the band structure, as well as the magnetic and pairing interaction, are properly calibrated with experimental observations, the competing SC and AFM order parameters can be calculated for any x which will allow for a theoretical phase diagram to be constructed to compare to experiment. These calculations were performed using the inter-band coupling used in equation (9) assuming either s++ ($V < 0$) or s+- ($V > 0$) symmetry. The experimental results showed in Fig. 5.10(a) and (b) can be directly compared to Figs. 5.10(c) and (d) where s+- symmetry is assumed and there is a remarkable agreement with the observed phase coexistence and competition observed experimentally with a second order phase transition is observed both at T_N and T_c. On the other hand, when s++ symmetry is assumed the theoretical phase diagram shown in Fig. 5.10(e) indicates that the phases are mutually exclusive and separated by a first order phase transition as shown in Fig 5.10(f).

5.4.5 Further theoretical investigations in superconducting gap symmetry

The model described in this section was also used to explore the effect of changing the band dispersions and pairing potentials. Each choice of parameter settings resulted in an appropriate g-parameter which is used to describe the free-energy in the region of the phase diagram were $T_N \approx T_c$. This analysis is similar to what was described in section 5.4.2 and can determine if competing phases coexist homogenously or heterogeneously based on the magnitudes of the quartic coefficients u_s, u_m, and γ in equation (16). For the various band settings and pairing potentials were explored, theoretical parameters were chosen such that the theoretical T_S and T_N matched experimentally determined values.

The first calculation assumed that there were identically shaped circular Fermi pockets with perfect nesting at the ordering vector $\mathbf{Q}_{AFM}$. The s++ ($V < 0$) state yields $g = 2$ which is

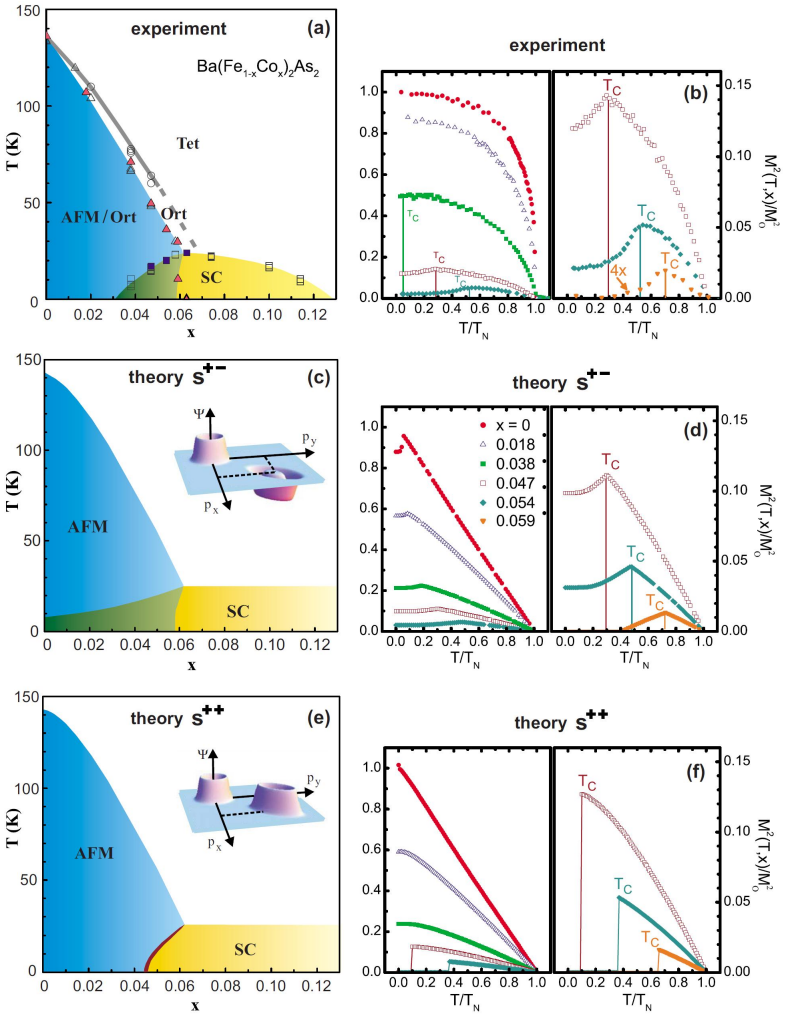

Figure 5.10 (a) Experimentally determined x-T phase diagram. (b) AFM order parameter squared determined by neutron scattering measurement. [(c) and (d)] Theoretically determined phase diagram and AFM order parameter squared for s+- pairing state. [(e) and (f)] Theoretically determined phase diagram and AFM order parameter squared for s++ pairing state.

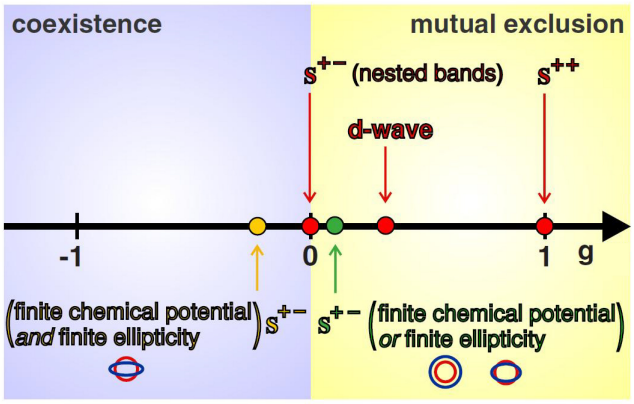

Figure 5.11 Summary of the resulting g-parameters which parameterize the band dispersions and SC states

far into a region of the phase diagram shown in Fig 5.11 where mutual exclusion takes place. On the other hand, with s+- ($V > 0$), $g = 0$ which is on the border mutual exclusion and co-existence.

The second set of calculations involved detuning of the bands either by (1) changing relative sizes of circular electron and hole Fermi pockets (i.e. changing the chemical potential), or (2) using a circular hole pocked and allowing the electron band to be elliptical while maintaining identical areas between pockets. For both cases, the results for s++ remain nearly unchanged with $g \approx 2$. For s+-, g becomes small but positive. Therefore chemical potential changes or ellipticity changes alone result in a first order transition at T_c and cannot explain the observed co-existence. On the other hand, if a finite chemical potential as well as a finite band ellipticity is assumed with effective masses and a chemical potential which result in a Fermi surface similar to what was observed in ARPES measurements (as was used in the last section), s++ again remains unchanged while for s+-, g is small but negative indicating that phase coexistence is possible. The negative g for s+- symmetry also holds when a small magnetic incommensurability is assumed.

Finally, a d-wave state with particle-hole symmetry was investigated and a resulting $g = \sqrt{\frac{8}{3}} - 1$. This shows that d-wave state is not very deep within the region of mutual exclusion as shown in Fig. 5.11 but is still away from the borderline where the s+- state is located for particle-hole symmetry. Yet, it is still possible that a set of parameters exists which allow the

d-wave state in theory to co-exist with AFM order making it difficult to rule out the existence d-wave state.

5.4.6 Conclusions from the unconventional pairing study

The iron-arsenide superconductors have proven to have a rich variety with some materials such as the electron doped $LaO_{1-x}F_xFeAs$ (161) and hole doped $Ba_{1-x}K_xFe_2As_2$ (162) showing heterogeneous phase coexistence while $Ba(Fe_{1-x}Co_x)_2As_2$ has clearly shown homogenous phase co-existence. Studies from $LaO_{1-x}F_xFeAs$ and $Ba_{1-x}K_xFe_2As_2$ therefore, cannot provide much insight using the theoretical work presented because s++, s+-, and d-wave symmetry can all show heterogeneous phase co-existence depending on the choice of model parameters. The most important outcome from this study is that the competition and homogenous coexistence observed in $Ba(Fe_{1-x}Co_x)_2As_2$ clearly suggests that SC symmetry cannot be s++, and therefore must be unconventional.

5.5 Dispersion of the SC resonance in $Ba(Fe_{0.953}Co_{0.047})_2As_2$

In the recently discovered iron pnictide compounds, magnetism and superconductivity (SC) seem to be intimately linked. SC appears after the antiferromagnetic (AFM) order observed in the parent compound is suppressed.(69; 140; 148; 10) However, the suppression of AFM order need not be complete and both SC and long-range AFM order can coexist in the so-called underdoped (UD) regions of the $Ba(Fe_{1-x}Co_x)_2As_2$ phase diagram.(69; 10) For these UD compositions, it has been shown that SC and static AFM order are in competition, characterized by a substantial reduction in the AFM order parameter below the superconducting transition temperature (T_c).(53),(149) In addition, inelastic neutron scattering has revealed a resonance in superconducting compositions of $Ba(Fe_{1-x}Co_x)_2As_2$ below T_c. As reported previously, (53) the data shows a resonance feature at $\mathbf{Q}_{AFM}$ that arises from the redistribution of magnetic intensity from low energies to high energies below T_c.

This resonance appears near the wave vector $\mathbf{Q}_{AFM}$ of the AFM ordered structure. The resonance has been observed in optimally doped (OD) compositions (defined as having a maximum T_c with no long-range AFM order) (Refs. (18; 150; 151; 78) as well as UD compounds

with AFM order.(53),(149) For both OD and UD compositions, the resonance is sharply peaked at $\mathbf{Q}_{\mathrm{AFM}}$ for momentum in the (**a**-**b**) plane (within Fe layers). (53),(149) On the other hand, the energy and intensity of the resonance vary only weakly along the c axis (perpendicular to the Fe layers) for optimal Co doping (18) and Ni doping,(150) suggesting nearly two dimensional (2D) behavior. Similar to the cuprates (152), the energy of the resonance mode in the OD iron pnictide compounds is in the range of 4 to 5 $\mathrm{k_B}T_{\mathrm{c}}$ and can be associated with the SC gap energy. (81)In UD compositions, where AFM order persists in the SC state, the effect of the AFM order on the resonance and the relationship between the resonance and spin-wave excitations must also be considered. Here we show that in the UD $\mathrm{Ba(Fe_{1-}}_x\mathrm{Co}_x)_2\mathrm{As}_2$ with x =4.7% (T_{N}=47 K and T_{c}=17 K) the resonance disperses quite strongly along the c axis (with an energy window of 4 to 8 meV), in contrast to the nearly dispersionless resonance found at approximately 9 meV for OD compositions (x =8% and T_{c}=22 K). This indicates that both the energy and bandwidth of the resonance are composition dependent (18) and suggests that AFM order leads to the resonance dispersion which bears some similarity to the AFM spin waves themselves.

Figure 5.12 summarizes several features of the neutron intensity [$I(\mathbf{Q},(\omega)$] above and below T_{c} in the AFM ordered state. In Fig. 5.12(a), the energy dependence of the scattering is shown at T=25 K above T_{c} and at T=5 K below T_{c} at $\mathbf{Q}$=$\mathbf{Q}_{\mathrm{AFM}}$=$(\frac{1}{2}\ \frac{1}{2}\ 1)_{\mathrm{T}}$. Figure 5.12(a) also shows estimates of the background [$\mathrm{C}(\omega)$] at both temperatures as obtained from scans at $\mathbf{Q}$=$(0.35\ 0.35\ 1)_{\mathrm{T}}$ and $(0.65\ 0.65\ 1)_{\mathrm{T}}$ which are far from magnetic intensity centered at $\mathbf{Q}_{\mathrm{AFM}}$ and display featureless energy response.

These data can be used to estimate the imaginary part of the magnetic susceptibility at $\mathbf{Q}_{\mathrm{AFM}}$ as shown in Fig. 5.12(b) using the equation

$$\chi''(\mathbf{Q}_{\mathrm{AFM}},\omega) = [I(\mathbf{Q}_{\mathrm{AFM}},\omega) - C(\omega)](1 - e^{-\hbar\omega/kT}) \tag{5.17}$$

The linear energy dependence of the normal-state susceptibility for $\hbar\omega < 6$ meV suggests gapless excitations although we cannot ascertain whether a small gap exists below 2 meV due to finite instrumental resolution. A comparison of $\chi''(\mathbf{Q}_{\mathrm{AFM}},\omega)$ at 25 and 5 K shows that the resonance exhibits an onset at 4 meV, a peak near 5 meV, and a long tail extending up to 10

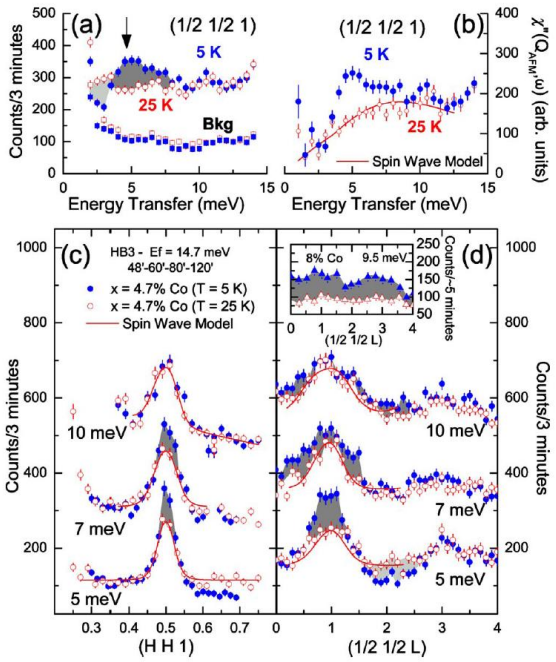

Figure 5.12 (a) Monitor-normalized neutron intensity I($\mathbf{Q}$,ω) for x =4.7% including background measurement for energy scans at $\mathbf{Q}_{\rm AFM}$=($\frac{1}{2}$ $\frac{1}{2}$ 1)$_{\rm T}$ both above (25 K, open circles) and below $T_{\rm c}$ (5 K, filled circles). The arrow shows the location of the resonance. The dark gray shading highlights regions of increased intensity related to the resonance while the light gray shading highlights a loss of intensity.(b) Energy dependence of $\chi''(\mathbf{Q}_{\rm AFM},\omega)$ at 5 and 25 K. The solid line is a fit to spin waves described in the text. (c) [h h 0]$_{\rm T}$ scans and (d) [0 0 l]$_{\rm T}$ scans through ($\frac{1}{2}$ $\frac{1}{2}$ 1) at 5, 7, and 10 meV. In (c) and (d) solid lines represent fits to the spin-wave model in the normal state. The inset to (d) shows [0 0 l]$_{\rm T}$ scans for x =8.0% both above (30 K, open triangles) and below $T_{\rm c}$ (10 K, filled triangles) at an energy transfer of 9.5 meV (close to the resonance peak) taken from Lumsden et al., Ref. (18).

meV.

Figures 5.12(c) and 5.12(d) explore the $\mathbf{Q}$ dependence of the magnetic scattering, showing constant energy scans at 5, 7, and 10 meV along the [h h 0]$_{\rm T}$ and [0 0 l]$_{\rm T}$ directions through $\mathbf{Q}_{\rm AFM}$. As expected for the ordered AFM state, the normal-state excitations along [h h 0]$_{\rm T}$ are sharply peaked at ($\frac{1}{2}$ $\frac{1}{2}$ 1)$_{\rm T}$ and appear to be consistent with the steep spinwave dispersion observed in parent compounds. The normal state line shapes are much broader along the l direction than in corresponding [h h 0]$_{\rm T}$ scans due to the relative weakness of the interlayer exchange. The normal-state spin excitations above $T_{\rm c}$ were fit using a damped spin-wave model

convoluted with the instrumental resolution function [lines in Figs. 5.12(c) and 5.12(d)]. The damped spin-wave response function used for analysis is

$$\chi''(\mathbf{q},\omega) = \frac{\Gamma\omega/\hbar}{\hbar^2(\omega^2 - \omega_{\mathbf{q}}^2)^2 + \Gamma^2\omega^2} \tag{5.18}$$

$$\hbar\omega_q = \sqrt{v_{ab}^2(q_x^2 + q_y^2) + v_c^2 q_z^2 + E_{\rm g}^2} \tag{5.19}$$

where $\mathrm{v}_{ab}/\hbar$ and $\mathrm{v}_c/\hbar$ are the in-plane and interplane spinwave velocities, $E_{\rm g} = \Delta_{\rm AFM}$ is the spinwave gap, Γ is a damping parameter, and the wave vector $\mathbf{q}$ is defined relative to the magnetic Brillouin-zone center at $\mathbf{Q}_{\rm AFM}$=($\frac{1}{2}$ $\frac{1}{2}$ 1). Fits to normal-state spin waves in the [h h 0]$_{\rm T}$ and [0 0 l]$_{\rm T}$ directions through $\mathbf{Q}_{\rm AFM}$, shown in Fig. 5.12, yielded spin-wave velocities of v_{ab} $\geq$123 meVÅ and v_c=43$\pm$9 meVÅ. The damping and the anisotropy-gap parameters were obtained by fits to both the linear dispersion in equation (5.19) as well as a more general Heisenberg model (not shown) and were found to be in the range of Γ=8 to 12 meV and $E_{\rm g}$=7 to 9 meV. Thus, despite an apparent finite value of the anisotropy gap, spectral weight persists down to the lowest measurable energies due to significant damping [Fig. 5.12(b)]. However, we note that the damping and anisotropy-gap parameters depend sensitively on estimates of the nonmagnetic background. The fits to a Heisenberg model were generally consistent with the published results for x =4.0%. (149)

Below $T_{\rm c}$, Figs. 5.12(c) and 5.12(d) show the $\mathbf{Q}$ dependence of the resonance which appears as a change in the intensity of the magnetic scattering below $T_{\rm c}$. Similar to other iron pnictides, the SC resonance is sharply defined for wave vectors in the (ab) plane (parallel to the Fe layer) near $\mathbf{Q}_{\rm AFM}$. The effect of SC on the spin excitations propagating along l is much more interesting. Measurements of the l dependence at the resonance peak energy at 5 meV show that it is narrowly defined at l=1, similar to reports for x =4.0%. (149) At a slightly higher energy of 7 meV, the intensity of the resonance appears to broaden or shift away from l=1. At 10 meV, the resonance intensity has weakened considerably and can be found only near the magnetic Brillouin-zone boundary at l=0 or 2. This is very different from the l dependence observed in the OD compound with x =8.0%, as determined by Lumsden *et al.* in Ref. (18),

where the intensity of the resonance peak (at 10 meV) is broadly distributed along l suggesting two-dimensional behavior(Fig. 5.12, inset).

These results suggest that the resonance observed in UD compositions has dispersion along the l direction. This dispersion is seen more clearly in energy scans measured at $\mathbf{Q}$=($\frac{1}{2}$ $\frac{1}{2}$ l)$_{\mathrm{T}}$ for several values of l and temperatures above and below T_{c}, as shown in Fig. 5.13(a). As l is increased away from $\mathbf{Q}_{\mathrm{AFM}}$, the resonance intensity shifts to higher energies with l and weakens, being nearly absent at l=2. Figure 5.13(b) compares the difference of intensities measured at 25 and 5 K and l=0, $\frac{1}{2}$, and 1 as compared to the OD data from Lumsden et al. (Ref. (18)), illustrating the distinctive behavior of compositions with and without AFM order. Figure 13(c) compares the l dispersion of the resonance peak for UD and OD samples. The UD resonance peak disperses from 5 meV at $\mathbf{Q}_{\mathrm{AFM}}$=($\frac{1}{2}$ $\frac{1}{2}$ 1)$_{\mathrm{T}}$ to 8 meV at the zone boundary whereas the resonance of the OD sample remains nearly dispersionless in the range of 8 to 9 meV.

The resonance dispersion can be fit to an empirical function $\Omega(l)$=Ω_0 + $W\left|\cos\frac{\pi l}{2}\right|$, where Ω_0 is the energy of the resonance at $\mathbf{Q}_{\mathrm{AFM}}$ and W is the bandwidth. For x =4.7%, W = 3 meV, and W/Ω_0=0.6, whereas W/Ω_0 <0.1 for x =8.0%, as shown in Fig. 5.13(c). This change in the relative bandwidth with doping suggests that the magnetic resonance is a three-dimensional (3D) feature when AFM and SC coexist and evolves to a 2D feature upon the loss of magnetic order.

We now discuss the possible origin of the resonance dispersion in the AFM ordered state. The magnetic resonance in iron-pnictide SC has been interpreted in the context of a spin-exciton model (153; 154) where the normal-state spin fluctuations arising from quasiparticle excitations become gapped below T_{c}. Within the random-phase approximation (RPA), the dynamical magnetic susceptibility in the SC state is given by

$$\chi(\mathbf{Q},\omega) = \frac{\chi_0(\mathbf{Q},\omega)}{1 - V(\mathbf{Q})\chi_0(\mathbf{Q},\omega)} \tag{5.20}$$

where $\chi_0(\mathbf{Q},\omega)$ is the noninteracting dynamical susceptibility in the SC state and V($\mathbf{Q}$) is an effective spin-spin interaction between itinerant electrons that can be nonlocal. (153) In the SC state, a resonance will appear in $\chi''(\mathbf{Q},\omega)$ at an energy where $V(\mathbf{Q})\chi_0(\mathbf{Q},\omega)$=1. In

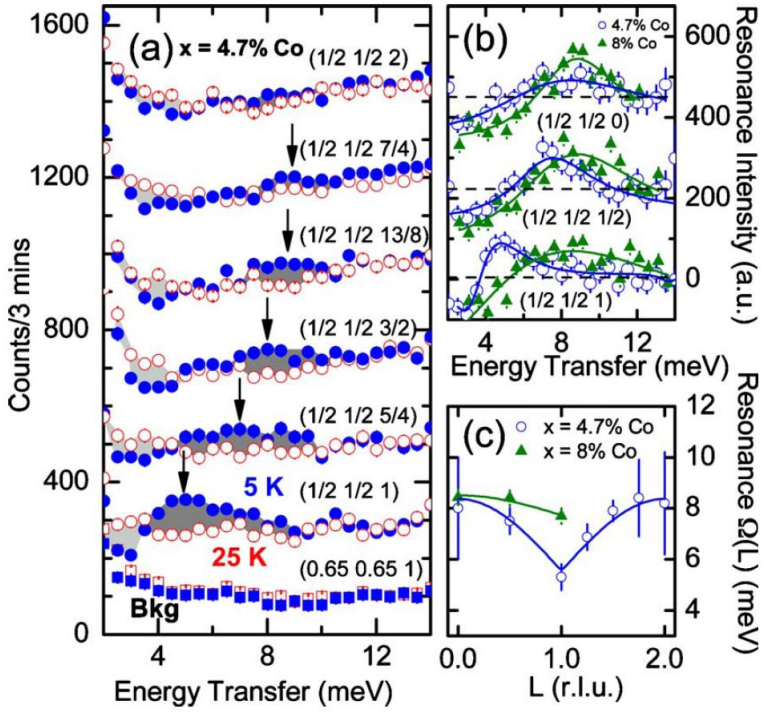

Figure 5.13 (a) Dispersion of the resonance shown by monitor-normalized constant-**Q** energy scans at $(\frac{1}{2}\ \frac{1}{2}\ l)_{\mathrm{T}}$ for x =4.7% for several values of l at temperatures above and below T_{c}. (b) Difference of scattering intensity between temperatures 5 K and 25 K above and below T_{c}, respectively, for both x =4.7% (open circles) and 8.0% (filled triangles) at l=0, $\frac{1}{2}$, and 1. (c) Comparison of the dispersion of the resonance peak energies along the l direction for x =4.7% and 8.0%. The x =8.0% data are taken from Ref. (18).

the pnictides $\chi_0(\mathbf{Q},\omega)$ is sharply peaked at $\mathbf{Q}_{\mathrm{AFM}}$ due to a near nesting of the quasi-2D Fermi surface and the resonance is sharply defined within the (ab) plane at $\mathbf{q}_0$. Along the l direction, the resonance condition is maintained as long as $V(\mathbf{q}_0+l\hat{z})\chi_0(\mathbf{q}_0+l\hat{z},\omega)$=1, which results in a nearly dispersionless resonance in the quasi-2D limit where both χ_0 and V vary weakly along l. Coherence factors in the SC state cause a strong enhancement of the resonance intensity when the SC order parameter has sign-reversing symmetry $\Delta_{\mathbf{k}}$=-$\Delta_{\mathbf{k}+\mathbf{q}_0}$. (153; 154) For an s-wave gap with this property (s+-), the RPA theory predicts that $\Omega_0 \approx 1.4\Delta$ for 2D spin fluctuations at $\mathbf{q}_0$. In OD composition, the observed energy and intensity of the resonance and its nearly dispersionless nature appears to support both the quasi-2D spin exciton picture and the s+- symmetry of the SC order parameter. (18)

The presence of 3D AFM order in UD samples requires the introduction of interlayer interactions that result in a stronger l dependence of V($\mathbf{Q}$) and/or $\chi_0(\mathbf{Q})$) due to Fermi-surface reconstruction. The resonance will remain sharply peaked at $\mathbf{q}_0$, however, interlayer interactions yield a 3D resonance that is peaked also at l=1, i.e., in the vicinity of the long-range magnetic ordering vector $\mathbf{Q}_{\rm AFM}$ =($\frac{1}{2}$ $\frac{1}{2}$ 1)$_{\rm T}$. The condition $V(\mathbf{q}_0+l\hat{z})\chi_0(\mathbf{q}_0+l\hat{z},\omega)$=1 causes dispersion of the resonance along the l direction. As either χ_0 or $V(\mathbf{Q})$ are maximum at l=1, the resonance energy will be minimum at $\mathbf{Q}_{\rm AFM}$ and increase along l, with the maximum energy bounded by the SC gap, $\Omega(l)\leq 2\Delta$. (153; 154) Even without long-range AFM order, the presence of pronounced short-range spin correlations along l has been used to explain the weaker resonance dispersion (W/Ω_0=0.26) observed in Ba(Fe$_{1-x}$Ni$_x$)$_2$As$_2$. (150)

Another hallmark of unconventional SC in quasi-2D antiferromagnets is that the ratio $\Omega_0/{\rm k_B}T_{\rm c}$ is usually found in the range from 4 to 5. (155) For x =4.7%, this ratio is only 3.5, which is somewhat smaller than expected. Even more surprising is that resonance observed in another UD composition with x =4.0% (Ω_0 ≈4.5 meV) (Ref. (149)) has a similar energy as x =4.7%. This is true despite the fact that $T_{\rm c}$=11 K for x =4.0%, whereas $T_{\rm c}$=17 K for x =4.7% indicating that there is no scaling between Ω_0 and $T_{\rm c}$. It is interesting to note that resonance dispersion is also observed in UPd_2Al_3 ($\Omega_0/{\rm k}T_{\rm c}$=2.8), where SC also appears within an AFM ordered state ($T_{\rm N}$=17 K and $T_{\rm c}$=2 K).(16; 17) $CeCoIn_5$ is not magnetically ordered, however, strong interlayer spin correlations exist resulting in an l-dependent resonance where $\Omega_0/{\rm k_B}T_{\rm c}$=3. (15)

The similar value of Ω_0 in UD 4.0% and 4.7% hints that Ω_0 in AFM ordered systems is influenced by another energy scale, such as the normal-state spin-wave dispersion, anisotropy gap, and/or Landau damping. Figure 5.14(a) shows a contour plot of the normal-state susceptibility as a function of l and $\hbar\omega$ with the fitted spin-wave dispersion superposed. The zone-boundary spin excitation is estimated to be 20 meV with substantial damping Γ=10 meV [a calculation of the damped spin-wave susceptibility is shown in Fig. 5.14(b)]. Figure 5.14(c) shows the measured susceptibility below $T_{\rm c}$ with both the resonance and spin-wave dispersion superposed on the image. Figure 5.14(d) shows the resonance dispersion as the difference of the SC and normal-state susceptibilities. The low-energy spin-wave dispersion along l, com-

bined with large damping, is suggestive of the magnon scenario for the resonance (156) where the SC gap acts to reduce the Landau damping and the subsequent sharpening of spin-wave modes near or below 2Δ yields a resonance-like feature. The magnon scenario has been used to describe the resonance in the electron-doped cuprates,(14) UPd_2Al_2,(157) and $CeCoIn_5$. (158)

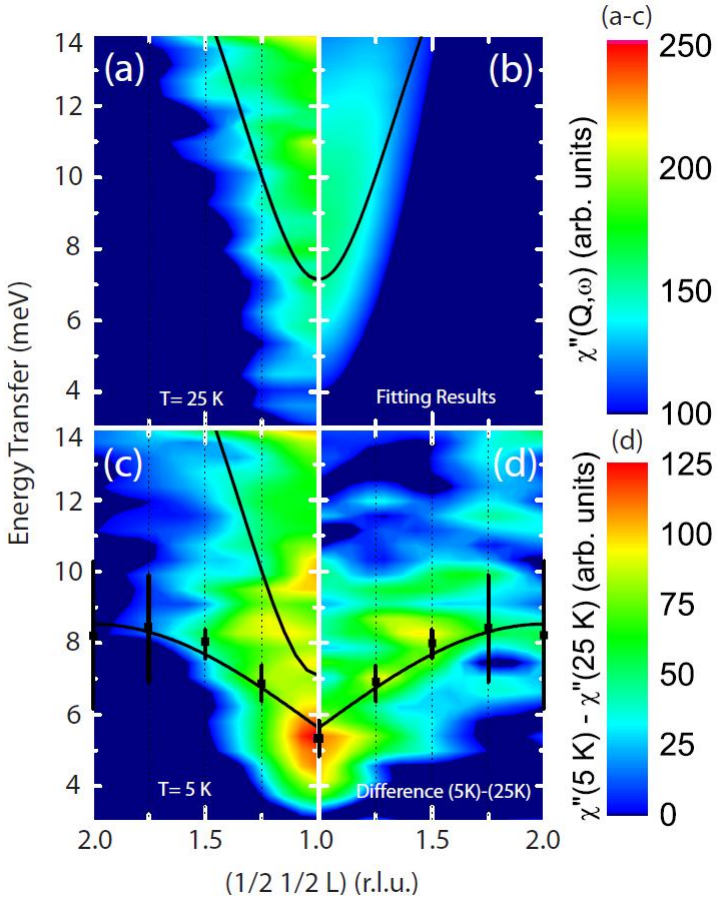

Figure 5.14 Contour plots of the magnetic susceptibility as a function of $\hbar\omega$ and l=1 to 2. (a) Measured data at 25 K. The line shows the fitted normal-state spin-wave dispersion. This line also appears in panels (b) and (c). (b) Normal-state damped spin-wave fitting results which have been convoluted with the experimental resolution. (c) Measured data below T_c at 5 K. The lower solid line is a fit to the square data points which represents the peak in the resonance. (d) The measured resonance susceptibility obtained from the difference of the data at 5 K [panel (c)] and 25 K [panel (a)].

In summary, the weakly dispersive magnetic resonance observed in the superconducting state of OD, paramagnetic, $Ba(Fe_{1-x}Co_x)_2As_2$ is quasi-2D, but develops significant dispersion along l for UD compositions where AFM and SC coexist (i.e., becomes more 3D). The resonance

energy at $\mathbf{Q}_{\mathrm{AFM}}$ does not appear to scale with T_{c} suggesting that the resonance may not have a simple or universal relationship to the SC gap when AFM order exists. The AFM order can be considered as a spin-density wave (SDW) that is stabilized by the gapping of the Fermi surface at $\mathbf{Q}_{\mathrm{AFM}}$ and the SDW and SC phases compete as the two gaps vie for the same electrons on the Fermi surface. (19) In this scenario, the interplay of SC and spin excitations, and consequently the resonance, is demonstrably more complex in the presence of AFM order.

CHAPTER 6. Summary and future work

6.1 Summary

A significant amount of progress has been made in the study of the effects of pressure application on $CaFe_2As_2$. Elastic neutron scattering measurements using He gas (hydrostatic pressure medium) to pressurize the samples has led to several important conclusions. First, modest pressurization up to ≈0.3 GPa will suppress the concomitant structural (tetragonal to orthorhombic) and magnetic (paramagnetic to antiferromagnetic) transition from 170 K to 110 K. Upon further pressurization, a new ground state exists which has become known as the collapsed tetragonal (cT) phase involving ≈5% decrease in unit cell volume. This new phase transition is clearly first order due to the extreme hysteresis that is observed upon transitioning to and from the cT phase. For compounds with the $ThCr_2Si_2$ structure, the presence of the cT phase depends on the competition between the preferred alkaline earth packing and Madelung energy as well as the degree of As-As bonding(66). In this same reference, it is suggested that for a small cation such as Ca, it is energetically favorable to for a shortened As-As bond which can be realized in the cT phase.

Studies of the p-T phase diagram involving pressure applications that maximize hydrostatic pressure (such as He gas pressurizers) or non-hydrostatic pressure in clamp type cells with or without pressure fluid pressure medium have proven to contradict each other. As discussed in chapter two, for non-hydrostatic pressure experiments, because the transitions are broadened, it is difficult to clearly place the phase lines as evidenced by the different published phase diagrams. On the contrary, studies of the phase diagram with hydrostatic pressure have shown that the phase transitions are sharp (first order) and the neutron scattering studies in this work have highlighted the large hysteresis both in temperature and pressure for transitions

involving the cT phase. Initial characterization measurements using non-hydrostatic pressure provide clear evidence for superconductivity in these compounds and the range of pressures where superconductivity is observed depends on pressure application measurements. The cT phase does not host superconductivity. Measurements using a clamp cell to maximize pressure along the crystallographic **c**-direction discovered a stabilized tetragonal phase co-existing with non superconducting orthorhombic and cT phases, providing an important clue that SC may occur under pressure in $CaFe_2As_2$ because of the presence of this new phase.

From our studies of magnetic ordering in the cT phase, we have concluded that the cT phase does not host long range magnetic order. In addition, inelastic neutron scattering data show that there is a loss of low energy magnetic excitations as well. Along with resistivity data showing that no superconductivity exists in the cT phase when using a He pressure intensifier, an important statement can be made that magnetic excitations seem to be an important ingredient for superconductivity to develop in the 122 iron arsenides.

Some significant conclusions developed from our systematic studies of the x-T phase diagram of $Ba(Fe_{1-x}Co_x)_2As_2$. First, it was demonstrated through neutron and x-ray diffraction studies that the simultaneous first-order transition to an orthorhombic and antiferromagnetic (AFM) ordered state in $BaFe_2As_2$ splits into two transitions with Co doping. This split transition was observed in the compound $Ba(Fe_{0.953}Co_{0.047})_2As_2$. In this compound, a tetragonal-orthorhombic transition was observed in x-ray scattering measurements at T_S=60 K where anomalies in resistivity and magnetization also occur. Following the structural transition, a second-order paramagnetic to AFM transition was observed at T_N=47 K in agreement with characterization measurements that again connect the microscopic changes to observations from bulk measurements.

We observed experimentally the co-existence and competition of antiferromagnetism and superconductivity. Neutron scattering measurements revealed a strong coupling between superconductivity and antiferromagnetism as we observed the clear decrease in elastic magnetic scattering as well as a redistribution of the low energy excitation spectrum at $\mathbf{Q}_{\mathrm{AFM}}$ below T_C. Magnetization, NMR, μSR (9; 11; 12) measurements which show the full mass of the samples are simultaneously magnetized and superconducting provide evidence for homogenous

co-existence of AFM and SC for a range of doping.

The observed loss of elastic magnetic scattering below $T_{\rm C}$ originates from AFM (spin density wave) and SC co-existing and competing for the electronic states at the Fermi surface. Free energy calculations were performed using two-band electronic model consisting of a circular hole and an elliptical electronic pockets observed at the Fermi surface. When electronic scattering related to AFM ordering and SC was introduced to this model, it was shown theoretically that AFM and SC can coexist in these materials only if Cooper pairs form an unconventional, sign-changing state. There was a particularly good agreement between theory and the experimental observations of a decrease in the ordered magnetic moment below $T_{\rm C}$ for all compounds where coexistence is observed when the sign changing SC s+- state is assumed. In fact, the theory predicted a re-entrance from the AFM state to the paramagnetic state, which was subsequently found.

The observation of a SC resonance has provided some important observations about the interplay of SC and AFM as they compete for electrons at the Fermi surface. For $T_{\rm C} < T < T_{\rm N}$ in the AFM normal state, $Ba(Fe_{1-x}Co_x)_2As_2$ with $x = 0.047$ appears to have gapless or nearly gappless damped spin excitations observed through inelastic neutron scattering. Below $T_{\rm C}$, a redistribution of spin excitations occur and the resonance peak rises out of the damped spin excitations. This resonance can be described by a dynamical magnetic susceptibility in the random phase approximation where additional interaction between spin or magnetic excitations and conduction electrons along with the sign changing superconducting gap causes an enhancement (or pole) the dynamical susceptibility which is observable by inelastic neutron scattering. For $Ba(Fe_{1-x}Co_x)_2As_2$ with $x = 0.047$, the resonance has a clear l dependence indicating a significant interaction between layers along the **c**-direction. This is unlike the resonance observed at higher doping levels of $x = 0.08$ where AFM order is absent and the resonance has little l dependence (i.e. it has a 2D nature). These results should motivate theoretical descriptions that consider the inter-layer spin correlations when attempting to understand the low energy spin excitations under doped compounds.

In sum, the experimental evidence of coexistence and competition in $Ba(Fe_{1-x}Co_x)_2As_2$ as well as the presence of a superconducting resonance presented in this thesis suggests unconven-

tional pairing may apply to the entire iron arsenide family. This conclusion is rather significant because it allows for the narrowing down of possible SC gap symmetries as well as SC pairing mechanisms. When combining the lessons from both $CaFe_2As_2$ and $Ba(Fe_{1-x}Co_x)_2As_2$, we have made a strong case that superconductivity in the iron arsenides is unconventional and mediated through spin fluctuations.

6.2 Future work

The descriptions of the magnetism in the arsenides has ranged from a local moment picture described by a Heisenberg model to models which describe the spin-correlations of itinerant conduction electrons. The small ordered magnetic moments measured ($< 1\mu_B$) also favor an itinerant description and detailed band structure calculations have shown that in the itinerant picture a the SDW instability is caused by details of Fermi surface nesting(168; 169). These calculations have also shown that the modulation of spin can be incommensurate (IC) and the magnetic propagation vector can change to $\boldsymbol{\tau} = \mathbf{Q}_{\mathrm{AFM}} + \boldsymbol{\epsilon}$ where $\boldsymbol{\epsilon}$ is a small incommensurability. As described in ref (170), systematic studies of parent as well as electron and hole doped $BaFe_2As_2$ has only found commensurate magnetic order with propagation vector $\mathbf{Q}_{\mathrm{AFM}}$. However, our recent neutron diffraction measurements demonstrate that IC magnetic order does indeed develop near optimally doped compositions of $Ba(Fe_{1-x}Co_x)_2As_2$ with $x \geq 0.056$, just before long-range magnetic ordering is completely suppressed at $x \approx 0.06$ (170) confirming the itinerant nature of magnetism in the iron arsenides.

It is important to continue to search for evidence that supports the role of Fermi surface nesting, as this is an important feature of the two band model involving of the competition of magnetism and superconductivity. This can be supported by the observation of IC spin density waves in other compounds (i.e. another doped of $BaFe_2As_2$ compound), where only commensurate order has been found, just as was done in $Ba(Fe_{1-x}Co_x)_2As_2$. Also, the discovery of lattice spacing modulations (strain wave) as well as a periodic charge modulation (charge density wave) that occurs in concert with SDW ordering will further support the itinerant picture. These phenomenon are also observed in Cr metal which have proven to be the best example of a compound that exhibits IC-SDW driven by Fermi surface nesting(108).

Gaining an understanding of the magnetic excitations normal state as well as the SC state in these itinerant electron systems is another important challenge. There is a need to develop a theoretical description of the excitations of a spin density wave and some possible modes of excitations include: spin waves, SDW amplitude fluctuations, and phason modes which involves a fluctuation of the spin-up and spin-down electron densities(171). It is possible that in these compounds that all of these modes and others yet described could prove to be important. Therefore, the experimental and theoretical challenge is to measure the excitation spectrum of a series of doped $BaFe_2As_2$ which exhibit IC-SDW order along with SC and demonstrate that the normal state excitations as well as the spectrum including a SC resonance can be best described using a model of itinerant electrons.

BIBLIOGRAPHY

[1] Yoichi Kamihara, Hidenori Hiramatsu, Masahiro Hirano, Ryuto Kawamura, Hiroshi Yanagi, Toshio Kamiya, and Hideo Hosono. Iron-Based Layered Superconductor: LaOFeP. *Journal of the American Chemical Society* **128**, 10012 (2006).

[2] Johnpierre Paglione and Richard L. Greene (2010). High-temperature superconductivity in iron-based materials. *Nature Physics* **6**, 645 (2010).

[3] Zhi-An Ren, Guang-Can Che, Xiao-Li Dong, Jie Yang, Wei Lu, Wei Yi, Xiao-Li Shen, Zheng-Cai Li, Li-Ling Sun, Fang Zhou, and Zhong-Xian Zhao. Superconductivity and phase diagram in iron-based arsenic-oxides $ReFeAsO_{1-\delta}$ (Re = rare-earth metal) without fluorine doping. *Europhysics Letters* **83**, 17002 (2008).

[4] M. S. Torikachvili, S.L. Bud'ko, N. Ni, and P. C. Canfield. Pressure induced superconductivity in $CaFe_2As_2$ *Physical Review Letters* **101**, 057006 (2008).

[5] A. Kreyssig, M. A. Green, Y. Lee, G. D. Samolyuk, P. Zajdel, J. W. Lynn, S. L. Bud'ko, M. S. Torikachvili, N. Ni, S. Nandi, J. B. Leão, S. J. Poulton, D. N. Argyriou, B. N. Harmon, R. J. McQueeney, P. C. Canfield, and A. I. Goldman. Pressure-induced volume-collapsed tetragonal phase of $CaFe_2As_2$ as seen va neutorn scattering. *Physical Review B* **78**, 184517 (2008).

[6] T. Park, E. Park, H. Lee, T. Klimczuk, E. D. Bauer, F. Ronning, and J. D. Thompson. Pressure-induced superconductivity in $CaFe_2As_2$. *Journal of Physics: Condensed Matter* **20**, 322204 (2008).

[7] H. Lee, E. Park, T. Park, V. A. Sidorov, F. Ronning, E. D. Bauer, and J. D. Thompson. Pressure-induced superconducting state of antiferromagnetic $CaFe_2As_2$. *Physical Review B* **80**, 024519 (2009).

[8] A. I. Goldman, A. Kreyssig, K. Prokeš, D. K. Pratt, D. N. Argyriou, J. W. Lynn, S. Nandi, S. A. J. Kimber, Y. Chen, Y. B. Lee, G. Samolyuk, J. B Leão, S. J. Poulton, S. L. Bud'ko, N. Ni, P. C. Canfield B. N. Harmon, and R. J. McQueeney. Lattice collapse and quenching of magnetism in $CaFe_2As_2$ under pressure: A single-crystal neutron and x-ray diffraction investigation. *Physical Review B* **79**, 024513 (2009).

[9] N. Ni, S. Nandi, A. Kreyssig, A. I. Goldman, E. D. Mun, S.L. Bud'ko, and P. C. Canfield. First-order structural phase transition in $CaFe_2As_2$. *Physical Review B* **78**, 014523 (2008).

[10] Jiun-Haw Chu, James G. Analytis, Chris Kucharczyk, and Ian R. Fisher. Determination of the phase diagram of the electron-doped superconductor $Ba(Fe_{1-x}Co_x)_2As_2$. *Physical Review B* **79**, 104506 (2009).

[11] M.-H. Julien, H. Mayaffre, M. Horvatic, C. Berthier, X. D. Zhang, W. Wu, G. F. Chen, N. L. Wang, and J. L. Luo. Homogeneous vs. inhomogeneous coexistence of magnetic order and superconductivity probed by NMR in Co- and K-doped iron pnictides. *Europhysics Letters* **87**, 37001 (2009).

[12] C. Bernhard, A. J. Drew, L. Schulz, V. K. Malik, M. R.össle, Ch. Niedermayer, Th. Wolf, G. D. Varma, G. Mu, H-H. Wen, H. Liu, G. Wu, and X. H. Chen. Muon spin rotation study of magnetism and superconductivity in $BaFe_{2-x}Co_xAs_2$ and $Pr_{1-x}Sr_xFeAsO$. *New Journal of Physics* **11**, 055050 (2009).

[13] I. I. Mazin and J. Schmalian. Pairing symmetry and pairing state in ferropnictides: Theoretical overview. *Physica C* **469**, 614 (2009).

[14] J.-P. Ismer, Ilya Eremin, Enrico Rossi, and Dirk K. Morr. Theory of magnetic excitons in the heavy-fermion superconductor UPd_2Al_3. *Physical Review Letters* **99**, 047005 (2007).

[15] C. Stock, C. Broholm, J. Hudis, H. J. Kang, and C. Petrovic. Spin Resonance in the d-Wave Superconductor $CeCoIn_5$. *Physical Review Letters* **100**, 087001 (2008).

[16] N. Bernhoeft, N. Sato, B. Roessli, N. Aso, A. Hiess, G. H. Lander, Y. Endoh, and T. Komatsubara. Enhancement of Magnetic Fluctuations on Passing below T_C in the Heavy Fermion Superconductor UPd_2Al_3. *Physical Review Letters* **81**, 4244 (1998).

[17] A. Hiess, N. Bernhoeft, N. Metoki, G. H. Lander, B. Roessli, N. K. Sato, N. Aso, Y. Haga, Y. Koike, T. Komatsubara, and Y. Onuki. Magnetization dynamics in the normal and superconducting phases of UPd_2Al_3: I. Surveys in reciprocal space using neutron inelastic scattering. *Journal of Physics: Condensed Matter* **18**, R437 (2006).

[18] M. D. Lumsden, A. D. Christianson, D. Parshall, M. B. Stone, S. E. Nagler, G. J. MacDougall, H. A. Mook, K. Lokshin, T. Egami, D. L. Abernathy, E. A. Goremychkin, R. Osborn, M. A. McGuire, A. S. Sefat, R. Jin, B. C. Sales, and D. Mandrus. Two-dimensional resonant magnetic excitation in $BaFe_{1.84}Co_{0.16}As_2$. *Physical Review Letters* **102**, 107005 (2009).

[19] Rafael M. Fernandes, Daniel K. Pratt, Wei Tian, Jerel Zarestky, Andreas Kreyssig, Shibabrata Nandi, Min Gyu Kim, Alex Thaler, Ni Ni, Paul C. Canfield, Robert J. McQueeney, Jörg Schmalian, and Alan I. Goldman. Unconventional pairing in the iron arsenide superconductors. *Physical Review B* **81**, 140501(R) (2010).

[20] Yoichi Kamihara, Takumi Watanabe, Masahiro Hirano, and Hideo Hosono. Iron-Based Layered Superconductor $La[O_{1-x}F_x]FeAs$ (x = 0.05-0.12) with $T_C = 26$ K. *Journal of the American Chemical Society* **130**, 3296 (2008).

[21] M. L. Cohen and P. W. Anderson. *Comments on the maximum superconducting transition temperature Superconductivity in d- and f-Band Metals.* ed. D. H. Douglass (1972) (New York: AIP) pp 1727.

[22] Shuichi Wakimoto, Katsuaki Kodama, Motoyuki Ishikado, Masaaki Matsuda, Ryoichi Kajimoto, Masatoshi Arai, Kazuhisa Kakurai, Fumitaka Esaka, Akira Iyo, Hijiri Kito, Hiroshi Eisaki, and Shin-ichi Shamoto Degradation of Superconductivity and Spin Fluctuations by Electron Overdoping in $LaFeAsO_{1-x}F_x$. *Journal of the Physical Society of Japan* **79**, 074715 (2010).

[23] Q. Huang, Y. Qiu, Wei Bao, M. A. Green, J. W. Lynn, Y. C. Gasparovic, T. Wu, G. Wu, and X. H. Chen. Neutron-Diffraction Measurements of Magnetic Order and a Structural Transition in the Parent $BaFe_2As_2$ Compound of FeAs-Based High-Temperature Superconductors. *Physical Review Letters* **101**, 257003 (2008).

[24] David C. Johnston. The puzzle of high temperature superconductivity in layered iron pnictides and chalcogenides. *Advances in Physics* **6**, 803 (2010).

[25] Jean-Pierre Mercier, Gérald Zambelli, Wilfried Kurz. *Introduction to materials science.* (2002) Elsevier.

[26] I. I. Mazin, D. J. Singh, M. D. Johannes, and M. H. Du. Unconventional Superconductivity with a Sign Reversal in the Order Parameter of $LaFeAsO_{1-x}F_x$. *Physical Review Letters* **101**, 057003 (2008).

[27] Chang Liu, Takeshi Kondo, Rafael M. Fernandes, Ari D. Palczewski, Eun Deok Mun, Ni Ni, Alexander N. Thaler, Aaron Bostwick, Eli Rotenberg, Jörg Schmalian, Sergey L. Budko, Paul C. Canfield, and Adam Kaminski. Evidence for a Lifshitz transition in electron-doped iron arsenic superconductors at the onset of superconductivity. *Nature Physics* **6**, 419 (2010).

[28] Andrea Damascelli. Probing the Electronic Structure of Complex Systems by ARPES. *Physical Review B* **T109**, 61 (2004).

[29] Vladimir Cvetkovic and Zlatko Tesanovic. Valley density-wave and multiband superconductivity in iron-based pnictide superconductors. *Physical Review B* **80**, 024512 (2009).

[30] Clarina de la Cruz, Q. Huang, J. W. Lynn, Jiying Li, W. Ratcliff II, J. L. Zarestky, H. A. Mook, G. F. Chen, J. L. Luo, N. L. Wang, and Pengcheng Dai. Magnetic order close to superconductivity in the iron-based layered $LaO_{1-x}F_xFeAs$ systems. *Nature* **453**, 899 (2008).

[31] Jun Zhao, Q. Huang, Clarina de la Cruz, Shiliang Li, J. W. Lynn, Y. Chen, M. A. Green, G. F. Chen, G. Li, Z. Li, J. L. Luo, N. L. Wang, and Pengcheng Dai. Structural and magnetic phase diagram of $CeFeAsO_{1-x}F_x$ and its relation to high-temperature superconductivity. *Nature Materials* **7**, 953 (2008).

[32] C. R. Rotundu, D. T. Keane, B. Freelon, S. D. Wilson, A. Kim, P. N. Valdivia, E. Bourret-Courchesne, and R. J. Birgeneau. Phase diagram of the $PrFeAsO_{1-x}F_x$ superconductor. *Physical Review B* **80**, 144517 (2009).

[33] Nikolay Plakida *High-Temperatures Cuprate Superconductors, Experiment, Theory, and Applications.* (Springer Series in Solid-State Sciences 166, 2010).

[34] N. F. Mott and R. Peierls. Discussion of the paper by de Boer and Verwey. *Proceedings of the Physical Society* **49**, 72 (1937).

[35] J. Orenstein and A. J. Millis. Advances in the Physics of High-Temperature Superconductivity. *Science* **288**, 468 (2000).

[36] Kouji Segawa, M. Kofu, S-H. Lee, I. Tsukada, H. Hiraka, M. Fujita, S. Chang, K. Yamada, and Yoichi Ando. Zero-doping state and electronhole asymmetry in an ambipolar cuprate. *Nature Physics* **6**, 579 (2010).

[37] M. Tinkham. *Introduction to Superconductivity.* (Dover Publications, 1996).

[38] J. Bardeen, L. N. Cooper, and J. R. Schrieffer. Microscopic Theory of Superconductivity. *Physical Review* **106**, 162 (1957).

[39] J. G. Bednorz and K. A. Muller. Possible High Tc Superconductivity in the Ba-La-Cu-O System. *Zeitschrift fr Physik B* **64**, 189 (1986).

[40] M. K. Wu, J. R. Ashburn, C. J. Torng, P. H. Hor, R. L. Meng, L. Gao, Z. J. Huang, Y. Q. Wang, and C. W. Chu. Superconductivity at 93 K in a new mixed-phase Y-Ba-Cu-O compound system at ambient pressure. *Physical Review Letters* **58**, 908 (1987).

[41] A. Schilling, M. Cantoni, J.D. Guo, and H.R. Ott. Superconductivity above 130 K in the Hg-Ba-Ca-Cu-O system. *Nature* **363**, 56 (1993).

[42] C. C. Tsuei and J. R. Kirtley. Pairing symmetry in cuprate superconductors. *Review of Modern Physics* **72**, 969 (2000).

[43] M. L. Kulic, S.-L. Drechsler, and O. V. Dolgov. Conventional superconductivity in Fe-based pnictides: The relevance of intra-band electron-boson scattering. *Europhysics letters* **85**, 47008 (2009).

[44] Charles Day. Iron Based Superconductors. *Physics Today* **62**, 36-40 (2009).

[45] Li Yu-ke, Lin Xiao, Tao Qian, Chen Hang, Wang Cao, Li Lin-Jun, Luo Yong-Kang, He Mi, Zhu Zeng-Wei, Cao Gang-Han, and Xu Zhu-An. Superconductivity and Transport Properties in Th and F Codoped $Sm_{1x}Th_xFeAsO_{1y}F_y$. *Chinese Physics Letters* **26**, 017402 (2009).

[46] N. D. Zhigadlo, S. Katrych, Z. Bukowski, S. Weyeneth, R. Puzniak, and J. Karpinski. Single crystals of superconducting $SmFeAsO_{1-x}F_y$. *Journal of Physics: Condensed Matter* **20**, 342202 (2008).

[47] Marianne Rotter, Marcus Tegel, and Dirk Johrendt. Superconductivity at 38 K in the Iron Arsenide $(Ba_{1-x}K_x)Fe_2As_2$. *Physical Review Letters* **101**, 107006 (2010).

[48] Paul C. Canfield and Sergey L. Bud'ko. FeAs-Based Superconductivity: A Case Study of the Effects of Transition Metal Doping on $BaFe_2As_2$. *Annual Reviews, Condensed Matter Phyics* **1**, 27 (2010).

[49] Joshua H. Tapp, Zhongjia Tang, Bing Lv, Kalyan Sasmal, Bernd Lorenz, Paul C. W. Chu, and Arnold M. Guloy. LiFeAs: An intrinsic FeAs-based superconductor with $T_{\mathrm{C}} = 18$ K . *Physical Review B* **78**, 060505 (2008).

[50] Dinah R. Parker, Matthew J. P. Smith, Tom Lancaster, Andrew J. Steele, Isabel Franke, Peter J. Baker, Francis L. Pratt, Michael J. Pitcher, Stephen J. Blundell, and Simon J. Clarke. A new Control of the Competition between a Magnetic Phase and a Superconducting Phase in Cobalt-Doped and Nickel-Doped NaFeAs Using Electron Count. *Physical Review Letters* **104**, 057007 (2009).

[51] Z. Deng, X. C. Wang, Q. Q. Liu, S. J. Zhang, Y. X. Lv, J. L. Zhu, R. C. Yu, and C. Q. Jin. A new "111" type iron pnictide superconductor LiFeP. *Europhysics Letters* **87**, 37004 (2009).

[52] Wei Bao, Y. Qiu, Q. Huang, M. A. Green, P. Zajdel, M. R. Fitzsimmons, M. Zhernenkov, S. Chang, Minghu Fang, B. Qian, E. K. Vehstedt, Jinhu Yang, H. M. Pham, L. Spinu, and Z. Q. Mao. Tunable ($\delta\pi$, $\delta\pi$)-Type Antiferromagnetic Order in α-Fe(Te,Se) Superconductors. *Physical Review Letters* **102**, 247001 (2009).

[53] D. K. Pratt, W. Tian, A. Kreyssig, J. L. Zarestky, S. Nandi, N. Ni, S. L. Budko, P. C. Canfield, A. I. Goldman, and R. J. McQueeney. Coexistence of Competing Antiferromagnetic and Superconducting Phases in the Underdoped $Ba(Fe_{0.953}Co_{0.047})_2As_2$ Compound Using X-ray and Neutron Scattering Techniques. *Physical Review Letters* **103**, 087001 (2009).

[54] Michael J. Pitcher, Dinah R. Parker, Paul Adamson, Sebastian J. C. Herkelrath, Andrew T. Boothroyd, Richard M. Ibberson, Michela Brunelli, and Simon J. Clarke. Structure and superconductivity of LiFeAs. *Chemical Communications* **45**, 5918 (2008).

[55] Safa O. Kasap, Peter Capper. *Springer handbook of electronic and photonic materials.* (Springer Science+Business Inc., 2006)

[56] S. V. Borisenko, V. B. Zabolotnyy, D. V. Evtushinsky, T. K. Kim, I. V. Morozov, A. N. Yaresko, A. A. Kordyuk, G. Behr, A. Vasiliev, R. Follath, and B. Bchner. Superconductivity without Nesting in LiFeAs. *Physical Review Letters* **105**, 067002 (2010).

[57] C.W. Chua, F. Chena, M. Goocha, A.M. Guloyd, B. Lorenza, B. Lvd, K. Sasmal, Z.J. Tangd, J.H. Tappd, and Y.Y. Xuea. The synthesis and characterization of LiFeAs and NaFeAs. *Physica C: Superconductivity* **469**, 326 (2009).

[58] Alaska Subedi, Lijun Zhang, D. J. Singh, and M. H. Du. Density functional study of FeS, FeSe, and FeTe: Electronic structure, magnetism, phonons, and superconductivity. *Physical Review Letters* **78**, 134514 (2008).

[59] Q. Huang, Jun Zhao, J. W. Lynn, G. F. Chen, J. L. Luo, N. L. Wang, and Pengcheng Dai. Doping evolution of antiferromagnetic order and structural distortion in $LaFeAsO_{1-x}F_x$. *Physical Review B* **78**, 054529 (2008).

[60] A. Martinelli, A. Palenzona, M. Tropeano, C. Ferdeghini, M. Putti, M. R. Cimberle, T. D. Nguyen, M. Affronte, and C. Ritter. Doping evolution of antiferromagnetic order and structural distortion in $LaFeAsO_{1-x}F_x$. *Physical Review B* **81**, 094115 (2010).

[61] Bumsung Lee, Seunghyun Khim, Jung Soo Kim, G. R. Stewart, and Kee Hoon Kim. Single-crystal growth and superconducting properties of LiFeAs. *European Physics Letters* **91**, 67002 (2010).

[62] Kalyan Sasmal, Bing Lv, Bernd Lorenz, Arnold M. Guloy, Feng Chen, Yu-Yi Xue, and Ching-Wu Chu. Superconducting Fe-Based Compounds $(A_{1-x}Sr_x)Fe_2As_2$ with A= K and Cs with Transition Temperatures up to 37 K. *Physical Review Letters* **101**, 107007 (2008).

[63] Nathalie C. Gresty, Yasuhiro Takabayashi, Alexey Y. Ganin, Martin T. McDonald, John B. Claridge, Duong Giap, Yoshikazu Mizuguchi, Yoshihiko Takano, Tomoko Kagayama, Yasuo Ohishi, Masaki Takata, Matthew J. Rosseinsky, Serena Margadonna, and Kosmas Prassides. Structural Phase Transitions and Superconductivity in $Fe_{1+\delta}Se_{0.57}Te_{0.43}$ at Ambient and Elevated Pressures. *Journal of the American Physical Society* **131**, 16944 (2010).

[64] Simon A. J. Kimber, Andreas Kreyssig, Yu-Zhong Zhang, Harald O. Jeschke, Roser Valent, Fabiano Yokaichiya, Estelle Colombier, Jiaqiang Yan, Thomas C. Hansen, Tapan Chatterji, Robert J. McQueeney, Paul C. Canfield, Alan I. Goldman, and Dimitri N. Argyriou. Similarities between structural distortions under pressure and chemical doping in superconducting $BaFe_2As_2$. *Nature Materials* **8**, 471 (2009).

[65] P.C. Canfield, S.L. Budko, N. Ni, A. Kreyssig, A.I. Goldman, R.J. McQueeney, M.S. Torikachvili, D.N. Argyriou, G. Luke, and W. Yu. Structural, magnetic and superconducting phase transitions in $CaFe_2As_2$ under ambient and applied pressure . *Physica C* **469**, 404 (2009).

[66] Roald Hoffmann and Chong Zheng. Making and breaking bonds in the solid state: the thorium chromium silicide ($ThCr_2Si_2$) structure. *Physical Review B* **89**, 4175 (1985).

[67] Y. Yildrim. Strong coupling of Fe-spin state and the As-As hybridization in iron-pnictide superconductors from first principles calculations. *Physical Review Letters* **102**, 037003 (2009).

[68] W. Yu, A. A. Aczel, T. J. Williams, S. L. Budko, N. Ni, P. C. Canfield, and G. M. Luke. Absence of superconductivity in single-phase $CaFe_2As_2$ under hydrostatic pressure. *Physical Review B* **79**, 020511 (2009).

[69] N. Ni, M. E. Tillman, J.-Q. Yan, A. Kracher, S. T. Hannahs, S. L. Budko, and P. C. Canfield. Effects of Co substitution on thermodynamic and transport properties and anisotropic H_{c2} in $Ba(Fe_{1-x}Co_x)_2As_2$ single crystals. *Physical Review B* **78**, 214515 (2008)).

[70] G. L. Squires. *Introduction to the Theory of Thermal Neutron Scattering.* (Cambridge University Press, 1996).

[71] George Edward Bacon. *Neutron diffraction.* (Clarendon Press, 1975).

[72] Stephen W. Lovesey. *The Theory of Neutron Scattering from Condensed Matter: Volume II (International Series of Monographs on Physics).* (Clarendon Press, Oxford 1984).

[73] K. Prokeš, A. Gukasov, D. N. Argyriou, S. L. Bud'ko, P. C. Canfield, A. Kreyssig, and A. I. Goldman. Magnetization distribution in the tetragonal $Ba(Fe_{1-x}Co_x)_2As_2$, $x = 0.066$ probed by polarized neutron diffraction. *Europhysics Letters* **93**, 32001 (2011).

[74] R. M. Moon, T. Riste, and W. C. Koehler. Polarization Analysis of Thermal-Neutron Scattering. *Physical Review* **181**, 920 (1969).

[75] R. A. Ewings, T. G. Perring, R. I. Bewley, T. Guidi, M. J. Pitcher, D. R. Parker, S. J. Clarke, and A. T. Boothroyd. High-energy spin excitations in $BaFe_2As_2$ observed by inelastic neutron scattering. *Physical Review B* **78**, 220501(R) (2008).

[76] R. J. McQueeney, S. O. Diallo, V. P. Antropov, G. D. Samolyuk, C. Broholm, N. Ni, S. Nandi, M. Yethiraj, J. L. Zarestky, J. J. Pulikkotil, A. Kreyssig, M. D. Lumsden, B. N. Harmon, P. C. Canfield, and A. I. Goldman. Anisotropic Three-Dimensional Magnetism in $CaFe_2As_2$. *Physical Review Letters* **101**, 227205 (2008).

[77] Dao-Xin Yao and E. W. Carlson. Magnetic excitations in the high- T_c iron pnictides. *Physical Review B* **78**, 052507 (2008).

[78] D. S. Inosov, J. T. Park, P. Bourges, D. L. Sun, Y. Sidis, A. Schneidewind, K. Hradil, D. Haug, C. T. Lin, B. Keimer, and V. Hinkov. Normal-state spin dynamics and temperature-dependent spin-resonance energy in optimally doped $BaFe_{1.85}Co_{0.15}As_2$. *Nature Physics* **6**, 178 (2010).

[79] T. Moriya. *Spin Fluctuations in Itinerant Electron Magnetism.* (1985) Springer.

[80] J. Rossat-Mignod, L.P. Regnault, C. Vettier, P. Bourges, P. Burlet, J. Bossy, J.Y. Henry, and G. Lapertot. Spin Resonance in the d-Wave Superconductor $CeCoIn_5$. *Physica C: Superconductivity* $\mathbf{185-189}$, 89 (1991).

[81] Matthias Eschrig. The effect of collective spin-1 excitations on electronic spectra in high-T_C superconductors. *Advances in Physics* **55**, 47 (2009).

[82] Wei Bao, A. T. Savici, G. E. Granroth, C. Broholm, K. Habicht, Y. Qiu, Jin Hu, Tijiang Liu, and Z.Q. Mao. A Triplet Resonance in Superconducting $FeSe_{0.4}Te_{0.6}$. *arχiv:*1002.1617v1 (2008).

[83] Shiliang Li, Xingye Lu, Meng Wang, Hui-qian Luo, Miaoyin Wang, Chenglin Zhang, Enrico Faulhaber, Louis-Pierre Regnault, Deepak Singh, and Pengcheng Dai. In-plane magnetic field effect on the neutron spin resonance in optimally doped $FeSe_{0.4}Te_{0.6}$ and $BaFe_{1.9}Ni_{0.1}As_2$ superconductors. *arχiv:*1105.4923v2 (2011).

[84] Ar. Abanov, Andrey V. Chubukova, and Jörg Schmalianb. Fingerprints of spin mediated pairing in cuprates. *Journal of Electron Spectroscopy and Related Phenomena* **117118**, 129 (2001).

[85] Jörg Fitter, Thomas Gutberlet, and John Katsaras. *Neutron scattering in biology: techniques and applications.* (Springer-Verlag Berlin Heidelberg, 2009).

[86] S.M. Shapiroa and N.J. Chesser. Characteristics of pyrolytic graphite as an analyzer and higher order filter in neutron scattering experiments. *Nuclear Instruments and Methods* **101**, 183 (1972).

[87] B. O. Loopstra. Neutron powder diffractometry using a wavelength of 2.6$\AA$. *Nuclear Instruments and Methods* **44**, 181 (1966).

[88] G. Shirane, S. M. Shapiro, and J. M. Tranquada. *Neutron Scattering with a Triple-Axis Spectrometer*. (Cambridge University Press, 2001).

[89] P. J. Brown. Thermal Neutron Detection. *International Tables for Crystallography*. **C**. 639 (1999).

[90] M. J. Buerger. The Correction of X-Ray Diffraction Intensities for Lorentz and Polarization Factors. *Physics* **26**, 637 (1940).

[91] R. Pynn. Lorentz factor for triple-axis spectrometers. *Acta Crystallographica Section B* **31**, 2555 (1975).

[92] A. I. Goldman, D. N. Argyriou, B. Ouladdiaf, T. Chatterji, A. Kreyssig, S. Nandi, N. Ni, S. L. Budko, P. C. Canfield, and R. J. McQueeney. Lattice and magnetic instabilities in $CaFe_2As_2$: A single-crystal neutron diffraction study. *Physical Review Letters* **78**, 100506(R) (2008).

[93] M. J. Cooper and R. Nathans. The resolution function in neutron diffractometry. I. The resolution function of a neutron diffractometer and its application to phonon measurements. *Acta Crystallographica* **23**, 357 (1967).

[94] N. J. Chesser and J. D. Axe. Crystal Physics, Diffraction, Theoretical and General Crystallography. *Acta Crystallographica Section A* **29**, 160 (1973).

[95] A. Zheludev. ResLib 3.4 - 3-axis resolution library for MatLab. http://neutron.ornl.gov/ zhelud/reslib/manual.pdf (2007).

[96] D.A. Tennant and D. F. McMorrow. Rescal for Matlab: a computational package for calculating neutron TAS resolution functions. http://xray.physics.ox.ac.uk/rescal/rescal.htm (1995).

[97] G. E. Peckham, D. H. Saunderson, and R. I. Sharp. Focusing conditions for a triple-axis neutron spectrometer. *British Journal of Applied Physics* **18**, 473 (1967).

[98] A. Chubukov, D. Pines, and J. Schmalian. *The Physics of Superconductors*, edited by K.-H. Bennemann and J. B. Ketterson, (Springer, New York, 2002).

[99] B. I. Zimmer, W. Jeitschko, J. H. Albering, R. Glaum, and M. Reehuis. The rate earth transition metal phosphide oxides LnFePO, LnRuPO and LnCoPO with ZrCuSiAs type structure. *Journal of Alloys and Compounds* **229**, 238 (1995).

[100] Carl S. Winslow. *New topics in Josephson junction and superconductivity research.* (Nova Science Publishers, 1997).

[101] Marcus Tegel, Marianne Rotter, Veronika Wei, Falko M Schappacher, Rainer Pöttgen, and Dirk Johrendt. Structural and magnetic phase transitions in the ternary iron arsenides $SrFe_2As_2$ and $EuFe_2As_2$. *Journal of Physics: Condensed Matter* **20**, 452201 (2008).

[102] Duang Feng and Guojun Jin. *Introduction to Condensed Matter Physics, Volume I.* (World Scientific, 2005).

[103] Lijun Zhang and D. J. Singh. Electronic structure of $Ba(Fe,Ru)_2As_2$ and $Sr(Fe,Ir)_2As_2$ alloys. *Physical Review B* **79**, 174530 (2009).

[104] Marianne Rotter, Marcus Tegel, and Dirk Johrendt. Spin-density-wave anomaly at 140 K in the ternary iron arsenide $BaFe_2As_2$. *Physical Review B* **78**, 020503(R) (2008).

[105] Walter Uhoya, Andrew Stemshorn, Georgiy Tsoi, Yogesh K. Vohra Athena S. Sefat, Brian C. Sales Kevin M. Hope, and Samuel T. Weir. Collapsed tetragonal phase and superconductivity of $BaFe_2As_2$ under high pressure. *Physical Review B* **82**, 144118 (2010).

[106] Walter O Uhoya, Jeffrey M Montgomery, Georgiy M Tsoi, Yogesh K Vohra, M A McGuire, Athena S Sefat, Brian C Sales, and Samuel T Weir. Phase transition and superconductivity of $SrFe_2As_2$ under high pressure. *Journal of Physics: Condensed Matter* **23**, 122201 (2010).

[107] B. Ni, M. M. Abd-Elmeguid, H. Micklitz, J. P. Sanchez, P. Vulliet, and D. Johrendt. Interplay between structural, electronic, and magnetic instabilities in EuT_2P_2 (T=Fe, Co) under high pressure. *Physical Review B* **63**, 100102(R) (2001).

[108] E. Fawcett. Spin-density-wave antiferromagnetism in chromium. *Review of Modern Physics* **60**, 209 (1988).

[109] X. F. Wang, T. Wu, G. Wu, H. Chen, Y. L. Xie, J. J. Ying, Y. J. Yan, R. H. Liu, and X. H. Chen. Structure and superconductivity of LiFeAs. *Physical Review Letters* **102**, 117005 (2009).

[110] Z. G. Chen, R. H. Yuan, T. Dong, and N. L. Wang. Optical spectroscopy of single-crystalline LaFeAsO. *Physical Review B* **81**, 100502 (2010).

[111] C. C. Homes, A. Akrap, J. S. Wen, Z. J. Xu, Z. W. Lin, Q. Li, and G. D. Gu. Electronic correlations and unusual superconducting response in the optical properties of the iron chalcogenide $FeTe_{0.55}Se_{0.45}$. *European Physics B* **81**, 180508 (2010).

[112] N. Tsoltanidis *Measurements and detection of radiation.* (Taylor and Francis Group, 1995).

[113] Y. Janssen, S. Chang, A. Kreyssig, A. Kracher, Y. Mozharivskyj, S. Misra, and P. C. Canfield. Magnetic phase diagram of Ce_2Fe_{17}. *Physical Review B* **76**, 054420 (2007).

[114] P. J. Brown. Magnetic form factors. *International Tables for Crystallography.* **C**. 454 (2006).

[115] W. Ratcliff. Neutron polarized-beam correction for triple-axis . http://code.google.com/p/tripleaxisproject (2011).

[116] Kari Selte and Arne Kjekshus. The Crystal Structure of FeAs. *Acta Chemica Scandinavica* **23**, 2047 (1969).

[117] Keizo Murata, Harukazu Yoshino, Hari Om Yadav, Yoshiaki Honda, and Naoki Shirakawa. Pt resistor thermometry and pressure calibration in a clamped pressure cell with the medium, Daphne 7373. *Review of Scientific Instruments* **68**, 2490 (1997).

[118] T. Goko, A. A. Aczel, E. Baggio-Saitovitch, S. L. Budko, P. C. Canfield, J. P. Carlo, G. F. Chen, Pengcheng Dai, A. C. Hamann, W. Z. Hu, H. Kageyama, G. M. Luke, J. L. Luo, B. Nachumi, N. Ni, D. Reznik, D. R. Sanchez-Candela, A. T. Savici, K. J. Sikes, N. L. Wang, C. R. Wiebe, T. J. Williams, T. Yamamoto, W. Yu, and Y. J. Uemura. Superconducting state coexisting with a phase-separated static magnetic order in (Ba,K)Fe_2As_2, (Sr,Na)Fe_2As_2 , and $CaFe_2As_2$. *Physical Review B* **80**, 024508 (2009).

[119] Y. J. Uemura, T. Goko, I. M. Gat-Malureanu, J. P. Carlo, P. L. Russo, A. T. Savici, A. Aczel, G. J. MacDougall, J. A. Rodriguez, G. M. Luke, S. R. Dunsiger, A. McCollam, J. Arai, Ch. Pfleiderer, P. Böni, K. Yoshimura, E. Baggio-Saitovitch, M. B. Fontes, J. Larrea, Y. V. Sushko, and J. Sereni. Phase separation and suppression of critical dynamics at quantum phase transitions of MnSi and $(Sr_{1-x}Ca_x)RuO_3$. *Nature Physics* **3**, 29 (2006).

[120] W. Yu, A. A. Aczel, T. J. Williams, S. L. Budko, N. Ni, P. C. Canfield, and G. M. Luke. Absence of superconductivity in single-phase $CaFe_2As_2$ under hydrostatic pressure. *Physical Review B* **79**, 020511(R) (2009).

[121] C. Huhnt, G. Michels, M. Roepke, W. Schlabitz, A. Wurth, D. Johrendt, and A. Mewis. First-order phase transitions in the $ThCr_2Si_2$-type phosphides ARh_2P_2 (A = Sr, Eu) . *Physica B: Condensed Matter* **240**, 26 (1997).

[122] C. Huhnt, G. Michels, M. Roepke, W. Schlabitz, A. Wurth, D. Johrendt, and A. Mewis. First-order phase transitions in $EuCo_2P_2$ and $SrNi_2P_2$. *Physical Review B* **56**, 13796 (1997).

[123] Walter Uhoya, Georgiy Tsoi, Yogesh K Vohra, Michael A McGuire, Athena S Sefat, Brian C Sales, David Mandrus and Samuel T Weir. Anomalous compressibility effects and superconductivity of $EuFe_2As_2$ under high pressures . *Journal of Physics: Condensed Matter* **22**, 292202 (2010).

[124] R. Mittal, S. K. Mishra, S. L. Chaplot, S. V. Ovsyannikov, E. Greenberg, D. M. Trots, L. Dubrovinsky, Y. Su, Th. Brueckel, S. Matsuishi, H. Hosono, and G. Garbarino. Ambient- and low-temperature synchrotron x-ray diffraction study of $BaFe_2As_2$ and $CaFe_2As_2$ at high pressures up to 56 GPa. *Physical Review B* **83**, 054503 (2011).

[125] C. Krellner, N. Caroca-Canales, A. Jesche, H. Rosner, A. Ormeci, and C. Geibel. Magnetic and structural transitions in layered iron arsenide systems: AFe_22As_2 versus RFeAsO. *Physical Review B* **78**, 100504(R) (2008).

[126] John P. Perdew and Yue Wang. Accurate and simple analytic representation of the electron-gas correlation energy. *Physical Review B* **45**, 13244 (1992).

[127] Patricia L Alireza, Y T Chris Ko, Jack Gillett, Chiara M Petrone, Jacqueline M Cole, Gilbert G Lonzarich, and Suchitra E Sebastian. Superconductivity up to 29 K in $SrFe_2As_2$ and $BaFe_2As_2$ at high pressures. *Journal of Physics Condensed Matter* **21**, 012208 (2009).

[128] Kazumi Igawa, Hironari Okada, Hiroki Takahashi, Satoru Matsuishi, Yoichi Kamihara, Masahiro Hirano, Hideo Hosono, Kazuyuki Matsubayashi, and Yoshiya Uwatoko. Pressure-Induced Superconductivity in Iron Pnictide Compound $SrFe_2As_2$. *Journal of the Physical Society of Japan* **78**, 025001 (2009).

[129] K. Prokeš, A. Kreyssig, B. Ouladdiaf, D. K. Pratt, N. Ni, S. L. Budko, P. C. Canfield, R. J. McQueeney, D. N. Argyriou, and A. I. Goldman. Evidence from neutron diffraction for superconductivity in the stabilized tetragonal phase of $CaFe_2As_2$ under uniaxial pressure. *Physical Review Letters* **81**, 180506(R) (2010).

[130] M. S. Torikachvili, S. L. Budko, N. Ni, P. C. Canfield, and S. T. Hannahs. Effect of pressure on transport and magnetotransport properties in $CaFe_2As_2$ single crystals. *Physical Review B* **80**, 014521 (2009).

[131] Athena S. Sefat, Rongying Jin, Michael A. McGuire, Brian C. Sales, David J. Singh, and David Mandrus. Superconductivity at 22 K in Co-Doped $BaFe_2As_2$ Crystals. *Physical Review Letters* **101**, 117004 (2008).

[132] R. H. Liu, G. Wu, T. Wu, D. F. Fang, H. Chen, S. Y. Li, K. Liu, Y. L. Xie, X. F. Wang, R. L. Yang, L. Ding, C. He, D. L. Feng, and X. H. Chen. Anomalous Transport Properties and Phase Diagram of the FeAs-Based $SmFeAsO_{1-x}F_x$ Superconductors. *Physical Review Letters* **101**, 087001 (2008).

[133] Ø. Fischer and M. B. Maple. *Topics in Current Physics, Vols. 32 and 34*. (Springer-Verlag, New York, 1983).

[134] P. C. Canfield, P. L. Gammel, and D. J. Bishop. New Magnetic Superconductors: A Toy Box For Solid-State Physicists. *Physics Today* **51**, No. 10 40 (1998).

[135] J. W. Lynn, B. Keimer, C. Ulrich, C. Bernhard, and J. L. Tallon. Antiferromagnetic ordering of Ru and Gd in superconducting $RuSr_2GdCu_2O_8$. *Physical Review B* **61**, R14964 (2000).

[136] G. Aeppli, E. Bucher, C. Broholm, J. K. Kjems, J. Baumann, and J. Hufnag. Magnetic order and fluctuations in superconducting UPt_3. *Physical Review Letters* **60**, 615 (1998).

[137] E. D. Isaacs, P. Zschack, C. L. Broholm, C. Burns, G. Aeppli, A. P. Ramirez, T. T. M. Palstra, R. W. Erwin, N. Stücheli, and E. Bucher. Antiferromagnetism and Its Relation to the Superconducting Phases of UPt_3. *Physical Review Letters* **75**, 1178 (1995).

[138] J. G. Lussier, M. Mao, A. Schröder, J. D. Garrett, B. D. Gaulin, S. M. Shapiro, and W. J. L. Buyers. Neutron-scattering study of incommensurate magnetic order in the heavy-fermion superconductor UNi_2Al_3. *Physical Review B* **56**, 11749 (1997).

[139] Marianne Rotter, Marcus Tegel, Inga Schellenberg, Falko M Schappacher, Rainer Pöttgen, Joachim Deisenhofer, Axel Günther, Florian Schrettle, Alois Loidl, and Dirk Johrendt. Competition of magnetism and superconductivity in underdoped $(Ba_{1-x}K_x)Fe_2As_2$. *New Journal of Physics* **11**, 025014 (2009).

[140] P. C. Canfield, S. L. Budko, Ni Ni, J. Q. Yan, and A. Kracher. Decoupling of the superconducting and magnetic/structural phase transitions in electron-doped $BaFe_2As_2$. *Physical Review B* **80**, 060501(R) (2009).

[141] S. L. Budko, N. Ni, S. Nandi, G. M. Schmiedeshoff, and P. C. Canfield. Thermal expansion and anisotropic pressure derivatives of T_C in $Ba(Fe_{1-x}Co_x)_2As_2$ single crystals. *Physical Review B* **79**, 054525 (2009).

[142] Michael A. McGuire, Andrew D. Christianson, Athena S. Sefat, Brian C. Sales, Mark D. Lumsden, Rongying Jin, E. Andrew Payzant, David Mandrus, Yanbing Luan and Veerle Keppens, Vijayalaksmi Varadarajan, Joseph W. Brill, Raphaël P. Hermann, Moulay T. Sougrati, Fernande Grandjean, and Gary J. Long. Phase transitions in LaFeAsO: Structural, magnetic, elastic, and transport properties, heat capacity and Mössbauer spectra. *Physical Review B* **78**, 094517 (2008).

[143] H. Chen, Y. Ren, Y. Qiu, Wei Bao, R. H. Liu, G. Wu, T. Wu, Y. L. Xie, X. F. Wang, Q. Huang, and X. H. Chen. Coexistence of the spin-density wave and superconductivity in $Ba_{1-x}K_xFe_2As_2$. *European Physics Letters* **85**, 17006 (2009).

[144] R. Prozorov, M.A. Tanatar, R.T. Gordon, C. Martin, H. Kim, V.G. Kogan, N. Ni, M.E. Tillman, S.L. Budko, and P.C. Canfield. Anisotropic London penetration depth and superfluid density in single crystals of iron-based pnictide superconductors. *Physica C* **469 – 673** (2009).

[145] A. B. Vorontsov, M. G. Vavilov, and A. V. Chubukov. Interplay between magnetism and superconductivity in the iron pnictides. *Physical Review B* **79**, 060508R (2009).

[146] Tanmoy Das, R. S. Markiewicz, and A. Bansil. Competing order scenario of two-gap behavior in hole-doped cuprates. *Physical Review B* **77**, 134516 (2009).

[147] Kazushige Machida. Spin Density Wave and Superconductivity in Highly Anisotropic Materials. *Journal of the Physical Society of Japan* **50**, 2195 (1981).

[148] N. Ni, A. Thaler, A. Kracher, J. Q. Yan, S. L. Budko, and P. C. Canfield. Phase diagrams of $Ba(Fe_{1-x}M_x)_2As_2$ single crystals (M =Rh and Pd). *Physical Review B* **80**, 024511 (2009).

[149] A. D. Christianson, M. D. Lumsden, S. E. Nagler, G. J. MacDougall, M. A. McGuire, A. S. Sefat, R. Jin, B. C. Sales, and D. Mandrus. Static and Dynamic Magnetism in Underdoped Superconductor $BaFe_{1.92}Co_{0.08}As_2$. *Physical Review Letters* **103**, 087002 (2009).

[150] Songxue Chi, Astrid Schneidewind, Jun Zhao, Leland W. Harriger, Linjun Li, Yongkang Luo, Guanghan Cao, Zhuan Xu, Micheal Loewenhaupt, Jiangping Hu, and Pengcheng Dai. Inelastic Neutron-Scattering Measurements of a Three-Dimensional Spin Resonance in the FeAs-Based $BaFe_{1.9}Ni_{0.1}As_2$ Superconductor. *Physical Review Letters* **102**, 107006 (2009).

[151] Shiliang Li, Ying Chen, Sung Chang, Jeffrey W. Lynn, Linjun Li, Yongkang Luo, Guanghan Cao, Zhuan Xu, and Pengcheng Dai. Spin gap and magnetic resonance in superconducting $BaFe_{1.9}Ni_{0.1}As_2$. *Physical Review B* **79**, 174527 (2009).

[152] Robert J. Birgeneau, Chris Stock, John M. Tranquada, and Kazuyoshi Yamada. Magnetic Neutron Scattering in Hole-Doped Cuprate Superconductors. *Journal of the Physical Society of Japan* **75**, 111003 (2006).

[153] M. M. Korshunov and I. Eremin. Theory of magnetic excitations in iron-based layered superconductors. *Physical Review B* **78**, 140509(R) (2008).

[154] T. A. Maier and D. J. Scalapino. Theory of neutron scattering as a probe of the superconducting gap in the iron pnictides. *Physical Review B* **78**, 020514(R) (2008).

[155] Yasutomo J. Uemura. Superconductivity: Commonalities in phase and mode. *Nature Materials* **8**, 253 (2009).

[156] A. Chubukov, D. Pines, and J. Schmailian *The Physics of Conventional and Unconventional Superconductors.* (Springer-Verlag, Berlin, 2002), p. 495.

[157] Jun Chang, I. Eremin, P. Thalmeier, and P. Fulde. Theory of magnetic excitons in the heavy-fermion superconductor UPd_2Al_3. *Physical Review B* **75**, 024503 (2007).

[158] A. V. Chubukov and L. P. Gorkov. Spin Resonance in Three-Dimensional Superconductors: The Case of $CeCoIn_5$. *Physical Review Letters* **101**, 147004 (2008).

[159] Rafael M. Fernandes and Jörg Schmalian. Competing order and nature of the pairing state in the iron pnictides. *Physical Review B* **82**, 014521 (2010).

[160] C. Lester, Jiun-Haw Chu, J. G. Analytis, S. C. Capelli, A. S. Erickson, C. L. Condron, M. F. Toney, I. R. Fisher, and S. M. Hayden. Neutron scattering study of the interplay between structure and magnetism in $Ba(Fe_{1-x}Co_x)_2As_2$. *Physical Review B* **79**, 144523 (2009).

[161] H. Luetkens, H.-H. Klauss, M. Kraken, F. J. Litterst, T. Dellmann, R. Klingeler, C. Hess, R. Khasanov, A. Amato, C. Baines, M. Kosmala, O. J. Schumann, M. Braden, J. Hamann-Borrero, N. Leps, A. Kondrat, G. Behr, J. Werner, and B. Büchner. The electronic phase diagram of the $LaO_{1-x}F_xFeAs$ superconductor. *Nature Materials* **8**, 305 (2009).

[162] J. T. Park, D. S. Inosov, Ch. Niedermayer, G. L. Sun, D. Haug, N. B. Christensen, R. Dinnebier, A. V. Boris, A. J. Drew, L. Schulz, T. Shapoval, U. Wolff, V. Neu, Xiaoping Yang, C. T. Lin, B. Keimer, and V. Hinkov. Electronic Phase Separation in the Slightly Underdoped Iron Pnictide Superconductor $Ba_{1-x}K_xFe_2As_2$. *Physical Review Letters* **102**, 117006 (2009).

[163] N. Katayama, S. Ji, D. Louca, S.-H. Lee, M. Fujita, T.J. Sato, J.S. Wen, Z.J. Xu, G.D. Gu, G. Xu, Z.W. Lin, M. Enoki, S. Chang, K. Yamada, and J.M. Tranquada. Investigation of the spin-glass regime between the antiferromagnetic and superconducting phases in $Fe_{1+y}Se_xTe_{1-x}$. *arXiv:* 1003.4525 (2010).

[164] Q. Si and E. Abrahams. Strong Correlations and Magnetic Frustration in the High T_C Iron Pnictides. *Physical Review Letters* **101**, 076401 (2008).

[165] D. J. Singh, D. J. and M.-H. Du. Density Functional Study of $LaFeAsO_{1-x}F_x$: A Low Carrier Density Superconductor Near Itinerant Magnetism. *Physical Review Letters* **100**, 237003 (2008).

[166] H.J. Gotsis, N. Russo, and E. Sicilia. Density functional calculations of the electronic structure and magnetism of the different phases of $BaFe_2As_2$. *Chemical Physics Letters* **498**, 281 (2010).

[167] S. A. J. Kimber, D. N. Argyriou, F. Yokaichiya, K. Habicht, S. Gerischer, T. Hansen, T. Chatterji, R. Klingeler, C. Hess, G. Behr, A. Kondrat, and B. Büchner. Magnetic ordering and negative thermal expansion in PrFeAsO. *Physical Review B* **78**, 140503 (2008).

[168] J. T. Park, D. S. Inosov, A. Yaresko, S. Graser, D. L. Sun, Ph. Bourges, Y. Sidis, Yuan Li, J.-H. Kim, D. Haug, A. Ivanov, K. Hradil, A. Schneidewind, P. Link, E. Faulhaber, I. Glavatskyy, C. T. Lin, B. Keimer, and V. Hinkov. Symmetry of spin excitation spectra in the tetragonal paramagnetic and superconducting phases of 122-ferropnictides. *Physical Review B* **82**, 134503 (2010).

[169] S. Graser, A. F. Kemper, T. A. Maier, H.-P. Cheng, P. J. Hirschfeld, and D. J. Scalapino. Spin fluctuations and superconductivity in a three-dimensional tight-binding model for $BaFe_2As_2$. *Physical Review B* **81**, 214503 (2010).

[170] D. K. Pratt, M. G. Kim, A. Kreyssig, Y. B. Lee, G. S. Tucker, A. Thaler, W. Tian, J. L. Zarestky, S. L. Budko, P. C. Canfield, B. N. Harmon, A. I. Goldman, and R. J. McQueeney. Incommensurate spin-density wave order in electron-doped $BaFe_2As_2$ superconductors. *Physical Review Letters* **106**, 257001 (2011).

[171] B. H. Grier, G. Shirane, and S. A. Werner. Magnetic excitations in chromium. II. *Physical Review B* **31**, 2892 (1985).